MAGNETOHYDRODYNAMICS OF THE EARTH'S CORE
1) STEADY, ROTATING MAGNETOCONVECTION
2) MAGNETIC ROSSBY WAVES

by

MICHAEL I. BERGMAN

B.A. Geophysics
Columbia University
(1986)

Submitted to the Department of Earth,
Atmospheric, and Planetary Sciences
in Partial Fullfillment of the Requirements
for the Degree of

DOCTOR OF PHILOSOPHY

at the

MASSACHUSETTS INSTITUTE OF TECHNOLOGY

September, 1992

Signature of Author _____
Department of Earth, Atmospheric, and Planetary Sciences
July 30, 1992

Certified by _____
Theodore R. Madden
Department of Earth, Atmospheric, and Planetary Sciences
Thesis Supervisor

Accepted by _____
Thomas H. Jordan
Department Chairman

MAGNETOHYDRODYNAMICS OF THE EARTH'S CORE
1) STEADY, ROTATING MAGNETOCONVECTION
2) MAGNETIC ROSSBY WAVES

by

MICHAEL I. BERGMAN

Submitted to the Department of Earth, Atmospheric, and Planetary Sciences
on July 30, 1992 in Partial Fulfillment of the Requirements
for the Degree of Doctor of Philosophy

Abstract

Geomagnetic and paleomagnetic data show that certain features of the Earth's internal magnetic field remain stationary for time scales longer than the presumed convective time scale of the core. This suggests external control by the mantle, with its much longer convective time scale. We review the evidence for core-mantle thermal coupling, which includes spatial correlation between the static magnetic field features, lateral thermal anomalies in the lower mantle, core-mantle boundary topography, and possibly virtual geomagnetic pole (VGP) paths during magnetic dipole reversals. However, questions remain about the resolution of the various data. Maps of the main magnetic field at the Earth's surface suggest that anomalous electrical currents may be present in the equatorial zone, with a large azimuthal wavenumber m = 1 contribution. To test this inference, we invert the surface magnetic field for the magnitude of ideal magnetic dipoles distributed in various ways throughout the outer core. We find a better, smoother fit with equatorial dipoles than with polar dipoles. The equatorial anomalies in the surface main field correlate with regions of high surface magnetic secular variation, further suggesting persistent motions in the core.

Although the convective equations are highly non-linear due to the high Rayleigh number of the Earth's core, so that time-dependent motions are certainly present, we are interested here in the possibility of steady motions that result from either free convection (laterally homogeneous boundary buoyancy conditions) or forced convection (laterally inhomogeneous boundary buoyancy conditions), and that might cause static features in the magnetic field. Our approach to the non-linear problem is therefore to look for finite-amplitude, time-independent convective solutions using an iterative finite-difference numerical method. Although we cannot be sure of the stability with respect to time perturbations of our solutions, our method has computational advantages over time-stepping that allow us to examine a large parameter space. We provide destabilization in our model by uniformly fluxing buoyancy across the bottom boundary with a concominant buoyancy sink at the top boundary. The Rayleigh number Ra is a measure of the destabilization.

We first apply our method to a non-rotating, electrically insulating, spherical fluid shell in order to demonstrate the method's viability. We then look for solutions in a rapidly rotating spherical fluid shell (high Taylor number Ta). We obtain axisymmetric polar modes, but not the non-axisymmetric equatorial modes (columns) predicted by linear theory, which require an azimuthal drift in spherical geometry. In an infinite annulus we have no difficulty obtaining columnar convection, and show that in this geometry, an imposed toroidal magnetic field actually inhibits convection.

We next return to the rotating spherical shell, impose a poloidal magnetic field, and look for the magnetic analog of the polar modes. When the Lorentz force is comparable to

the Coriolis force (Elsasser number El = O(1)), the modes fill the shell and most efficiently transport buoyancy. We show that it is the component of gravity parallel to the rotation axis, g_z, that is responsible for the modes' existence. Hence, for supercritical convection it is dynamically incorrect to omit g_z, especially for an electrically conducting fluid in which the polar modes are more efficient. In conjunction with the greater efficiency of convection near the inner spherical boundary than near the outer one, the non-linear interaction between the advectively-created toroidal magnetic field and the associated radial electrical current leads to a consistent bias towards equatorial upwelling flow in the core. Because of the lack of time-dependence, we cannot be sure of the stability of any particular converged solution, but we nevertheless believe that this non-linear result is a general feature of the ω-effect.

Finally, we study axisymmetric flows forced by a high buoyancy flux across the upper boundary near the equator and a low flux near the poles. In the absence of rotation and a magnetic field, we find converged solutions with local downwelling flow beneath the equator for a wide range of Ra, displaying the effect of the boundary condition. With rotation and a magnetic field we find similar results at low Ra, when conduction remains dominant. At higher Ra, however, when convection becomes dominant, we cannot induce equatorial downwelling because of the non-linear bias towards equatorial upwelling. Instead, we obtain equatorial upwelling reduced from that with a homogeneous boundary buoyancy flux. On the other hand, a high upper boundary buoyancy flux at the poles enhances the equatorial upwelling. The study of forced flows requires more work, including discerning the role of non-axisymmetry and time-dependence.

A second topic that we study in this thesis involves a possible consequence of compositional convection in the Earth's core: the formation of a stably stratified layer at the top of the outer core. The magnetic analog of Rossby (planetary) waves in this stable layer (the 'H' layer) may be responsible for a portion of the short-period secular variation. We adopt a thin shell model to examine the dynamics of the H layer. The stable stratification justifies the thin-layer approximations, which greatly simplify the analysis. The governing equations are then the Laplace's tidal equations, modified by the Lorentz force, and also the magnetic induction equation. We linearize the Lorentz force in the Laplace's tidal equations and the advection term in the magnetic induction equation, assuming a zeroth order dipole field as representative of the magnetic field near the insulating core-mantle boundary.

An analytical β-plane solution shows that a magnetic field can release the equatorial trapping that low frequency, non-magnetic planetary waves exhibit. A numerical solution to the 2-D spherical equations confirms that a sufficiently strong magnetic field can break the equatorial waveguide. Both solutions are highly dissipative, but this is essentially due to our neglect of $\partial b/\partial t$ in comparison with the advection and diffusion terms in the magnetic induction equation. Were one to include the time derivative of the magnetic field, which would necessitate relaxing the radial independence of the solutions, one would find magnetic planetary waves are considerably less damped. For the magnetic field strength appropriate for the H layer, the real part of the eigenfrequencies change little from their non-magnetic values. We estimate a phase velocity of the lowest westward propagating modes that is rather rapid compared with fluid speeds typically presumed in the core.

Thesis supervisor: Theodore R. Madden
Title: Professor of Geophysics

Table of Contents

Chapter 1

Historical Context

Soon after presenting his 1905 paper on special relativity, Einstein described the problem of the generation of the Earth's magnetic field as one of the five great unsolved problems of physics. Despite progress, the geodynamo problem remains unsolved. Larmor (1919a,b) was the first to suggest that fluid motions within astronomical bodies might be responsible for generating magnetic fields in a self-exciting dynamo process. However, Cowling (1934) demonstrated that a velocity field symmetric about an axis (such as the rotation axis) cannot maintain a magnetic field also symmetric about that axis. This first anti-dynamo theorem (see Moffatt, 1978 for more anti-dynamo theorems) therefore mandated that a sufficiently complex velocity field be present in the Earth's magnetofluid outer core, and was a harbinger of the difficulties ahead. In light of this anti-dynamo theorem, Blackett (1952) hypothesized that a rotating solid body might have a magnetic dipole moment inherently proportional to its angular momentum, so that astronomical bodies might exhibit large magnetic fields. However, in a laboratory experiment involving a rotating gold sphere and a sensitive magnetometer that he designed expressly for the experiment, he found no evidence of magnetic field generation.

Bullard and Gellman (1954) pressed forward with finding a solution to the kinematic dynamo problem. The kinematic dynamo problem consists of finding a velocity field that when inserted into the magnetic induction equation sustains magnetic field growth. It is simpler than the full hydromagnetic dynamo problem in that one is not concerned with dynamics, *i.e.*, one does not solve the Navier-Stokes equation with the non-linear Lorentz force coupling term. Questions remained about the convergence of Bullard and Gellman's (1954) solution, and Gibson and Roberts (1969) finally proved that it does not converge, but in the meantime Backus (1958) designed a kinematic dynamo with a time-varying velocity field that does converge. This demonstrated the viability of the

kinematic dynamo in a fluid sphere, without relying on wires, brushes, and other matter presumably foreign to planetary interiors. Along with advances in magnetohydrodynamics (MHD) by Alfven (1940) and Elsasser (1946a,b,1947), the success of these early kinematic dynamos propelled the study of dynamo theory, and indeed, no one has yet established a general anti-dynamo theorem. It is now generally presumed that a dynamo mechanism is responsible for the generation of the geomagnetic field.

The difficulty of the dynamo problem arises from several sources. Firstly, the governing equations are mathematically formidable. The equations governing the kinematic dynamo problem include Maxwell's equations,

$$\nabla \times \mathbf{B} = \mu \mathbf{J}, \tag{1.1}$$

$$\nabla \times \mathbf{E} = -\partial \mathbf{B}/\partial t, \text{ and} \tag{1.2}$$

$$\nabla \cdot \mathbf{B} = 0, \tag{1.3}$$

and Ohm's law,

$$\mathbf{J} = \sigma(\mathbf{E} + \mathbf{v} \times \mathbf{B}), \tag{1.4}$$

which combine to yield the magnetic induction equation,

$$\frac{\partial \mathbf{B}}{\partial t} = \chi \nabla^2 \mathbf{B} + \nabla \times (\mathbf{v} \times \mathbf{B}). \tag{1.5}$$

For the full hydromagnetic dynamo problem one must also solve the Navier-Stokes equation,

$$\frac{\partial \mathbf{v}}{\partial t} + (\mathbf{v} \cdot \nabla)\mathbf{v} + 2\Omega \times \mathbf{v} = -\nabla p + \nu \nabla^2 \mathbf{v} + c\mathbf{g} + \frac{1}{\mu \rho}(\nabla \times \mathbf{B}) \times \mathbf{B}, \tag{1.6}$$

as well as the continuity equation,

$$\nabla \cdot \mathbf{v} = 0, \tag{1.7}$$

and the buoyancy equation,

$$\frac{\partial c}{\partial t} + (\mathbf{v} \cdot \nabla) c = \kappa \nabla^2 c + \varepsilon. \tag{1.8}$$

In (1.1) - (1.8), $\mathbf{v}$ is the velocity field in the rotating reference frame, $\mathbf{B}$ is the magnetic field, $\mathbf{E}$ is the electric field, $\mathbf{J}$ is the electric current density, p is the pressure, c is the density deficit from the mean, μ is the magnetic permeability, σ is the electrical conductivity, $\chi = 1/\mu\sigma$ is the magnetic diffusivity, Ω is the rotation vector, ν is the fluid viscosity, $\mathbf{g}$ is the radial gravitational vector, ρ is the fluid density, κ is the density diffusivity, and ε is a density source term. In writing down (1.1) - (1.8) we have already made two assumptions, incompressibility and the Boussinesq approximation (Melchior, 1986). Solving a set of non-linear partial differential equations such as (1.5) - (1.8) in spherical geometry for the unknowns $\mathbf{B}$, $\mathbf{v}$, p, and c, subject of course to the proper boundary conditions, is very clearly a formidable task. Thus, it is not really feasible even on today's supercomputers to simply 'solve' the geodynamo without making further assumptions.

The second difficulty associated with the dynamo problem is our deficient knowledge concerning various parameters associated with the Earth's core. Although we know the values of μ (equal to its free space value μ_o, given the high temperature in the core) and Ω, and have good estimates for σ, ρ, and $\mathbf{g}$ (as a function of radius) in the core, we are less certain of the molecular values of ν and κ (see Table 1.1). Perhaps more glaring is our ignorance of the geodynamo's power source. Via viscous and Ohmic dissipation, the kinetic energy of the fluid motions and magnetic energy stored in the magnetic field gets

transferred to heat, which then escapes to the mantle. Against this energy loss, the geodynamo must have a power source. Although some (Malkus, 1968) have suggested other mechanisms such as precession, most work has concentrated on thermal or chemical (compositional) buoyancy as the power source. Thermal buoyancy might result from a distribution of radioactive heat sources in the fluid outer core or from latent heat of crystallization (Verhoogen, 1980). Latent heat results from the freezing of the core at the inner-outer core boundary (ICB), where the core freezing point curve intersects the temperature curve. Accompanying the latent heat and resulting thermal buoyancy may be a supply of chemical buoyancy that occurs with the release of gravitational energy (Braginsky, 1963). The gravitational energy results from pure iron preferentially freezing out, leaving the resulting melt slightly enriched in lighter impurities such as oxygen or sulfur (Ringwood, 1977).

Although some (Gubbins, 1977) argue that chemical buoyancy is more efficient than thermal buoyancy, we cannot yet be certain of the energy source for core convection and hence for the geodynamo. In any case, the equations that govern the distribution of temperature and of chemistry are the same, (1.8), and because of our uncertainty on the proper energy source, we use c to denote the density deficit due to either temperature or chemistry. Similarly, we use ε to denote either a thermal or chemical buoyancy source. However, although the governing equations are identical, the boundary conditions on c, the functional form of ε, and the value of κ might be very different depending on the driving force. For instance, the molecular value of κ for temperature is probably much greater than that for chemistry (Table 1.1). Moreover, we might expect ε to be uniform throughout the core for radioactive heat, but concentrated at the lower boundary for latent heat or gravitational energy. Similarly, the proper boundary conditions for thermal convection might be a fixed temperature or heat flux at the ICB and a fixed heat flux at the core-mantle boundary (CMB), whereas for chemical convection a fixed chemical flux at the ICB and zero flux at the CMB may be more appropriate.

A major part of the difficulty in evaluating the energy needs of core convection and the geodynamo is that we do not know the strength of the magnetic field in the Earth's core. Because the electrical conductivity of the mantle is several orders of magnitude lower than that of the core (though we do not know the details of the electrical conductivity profile in the mantle, particularly near the CMB (Merrill and McElhinny, 1983)), electrical currents cannot effectively flow in the mantle. In the limit that the entire mantle is electrically insulating, the toroidal magnetic field in the core must go to zero at the CMB. Hence, what we observe at the Earth's surface, the poloidal magnetic field, is only a part of the total in the core. Indeed, it is a feature of some dynamo models, the 'strong-field' models, that the toroidal field is as much as two orders of magnitude stronger than the poloidal field (Braginsky, 1964a,b). On the other hand, some models, the 'weak-field' models, exhibit a toroidal field comparable to the poloidal field (Busse, 1975). Although theory shows that the stability of the weak-field models is doubtful (Soward, 1979), and their energy requirements may be unreasonably large (Roberts, 1988), we have few observational constraints to guide us as to strength of the toroidal magnetic field.

Not definitively knowing the parameter range of interest within the core, we cannot always properly evaluate the assumptions that we must make if we are to attempt to solve the mathematically difficult problem. Although geomagnetic data can provide us with information on fluid flow at the top of the outer core, provided we make several assumptions (Bloxham, 1988), it is available only for the past few hundred years. Also, its spatial coverage is not generally ideal. Paleomagnetic data has shown us that the dipole magnetic field can reverse its polarity on an extremely rapid timescale (compared with the geologic timescale), and that the reversals are aperiodic, presumably demonstrating the high non-linearity of the problem. However, paleomagnetic data is often of low quality (with less spatial coverage and discontinuous temporal coverage) than geomagnetic data. Thus, besides the mathematical difficulty of the theory and the uncertain parameter range, we have

little observational evidence to guide us. This paucity of observational evidence compounds the challenge to connect data and theory.

Finally, the dominant forces are likely the Coriolis, pressure, and perhaps, Lorentz forces. The first arises due to the rapid rotation of the Earth, the last due to the magnetic field. These two forces are not generally within the realm of common experience, and are often counter-intuitive. Acting together, they can be counter-counter-intuitive, as we shall later see. Perhaps as much as any of the mathematical and observational problems, this lack of intuition makes the problem so difficult, but also so interesting. Of the many non-dimensional numbers that we will use through this work, the most certain may be the success parameter S defined by Roberts (1988), where

$$S = \frac{\text{number of successful models}}{\text{number of attempted models}}.$$

Needless to say, S is a small number.

Nevertheless, although we do not have a dynamically self-consistent dynamo operating at the parameter range approaching that likely found in the core, much progress has been made in understanding the generation of the Earth's magnetic field. One can attack the full hydromagnetic dynamo problem from two approaches. One, as described above, is the kinematic approach whereby one studies the magnetic induction equation (1.5). From this approach one can come to understand the kind of motions that are necessary to sustain magnetic field growth against the inevitable dissipative processes. An improvement to this approach is that where one also solves the Navier-Stokes equations (1.6) and the continuity equation (1.7), but one assigns the buoyancy force c and does not solve the buoyancy equation (1.8). Braginsky and Roberts (1987) used such an attack in their study of the model-Z dynamo. In addition, they employed an approach whereby one assigns the azimuthally averaged effects of interaction between the weakly non-axisymmetric velocity and magnetic fields (Braginsky, 1964a,b). The interaction is a means to produce an

'α-effect' (Parker, 1955), and the method allows one to reduce the dimension of the problem from three to two, at the cost of a somewhat artificially assigned electrical current. Alternatively, one can think of using the α-effect as employing a two-scale approach (Steenbeck *et al.*, 1966). The α-effect is central to modern kinematic dynamo theory, for it is the primary means to create a poloidal magnetic field from a toroidal one. Also important to kinematic dynamo theory is the 'ω-effect', which is the primary means to create a toroidal magnetic field from a poloidal one, but which can be axisymmetric and does not require averaging.

The second approach towards gaining an understanding of the geodynamo is to study the various instabilities that can occur in a rotating, electrically conducting fluid. This typically involves solving (1.5) - (1.8), but with some fixed basic state assigned *a priori*. For instance, one might examine the linear stability of a rotating, electrically conducting fluid shell, heated from below and cooled from above, and permeated by an assigned magnetic field and fluid shear. The study of linear convection and magnetoconvection has unearthed a plethora of instabilities that may play a role in the generation of the magnetic field and its secular variations (Chandrasekhar, 1961, Fearn *et al.*, 1988, see Chapter 3). Of course, because the assigned magnetic field and shear are fixed, one cannot speak of dynamo action. At the juncture of the two approaches lies the full hydromagnetic geodynamo problem, equations (1.5) - (1.8), with no magnetic fields or fluid shears assigned *a priori*, and with parameters, boundary conditions, and an energy source assigned in a geophysically realistic manner. A problem, of course, is that we do not always know what is geophysically realistic.

While mathematicians continue to make progress towards an understanding of the full hydromagnetic dynamo problem through advances in kinematic dynamo theory and studies of instabilities in electrically conducting, rotating fluids, geophysicists are making progress in determining the proper parameter range, boundary conditions, and energy sources under which the geodynamo operates. The challenge is to connect the two, which

is clearly a formidable task. Although the geophysical data is limited in quality and quantity, and although the subjects of kinematic dynamo theory and rotating magnetoconvection are still not fully mastered, we nevertheless believe that we can use the geophysical data to provide some insight into the dynamics of the lower mantle and core. In this thesis we therefore hope not only to further our understanding of magnetoconvection and magnetic instabilities in rotating fluids, but also to apply our findings to the real Earth.

In the second chapter of this thesis, we present the geophysical evidence that static features in the geomagnetic field may correlate with lateral thermal anomalies in the lower mantle. Although there remain questions about the resolution of the data, the suggestion of core-mantle thermal coupling (Bloxham and Gubbins, 1987) is intriguing. However, very little is known about the stationary motions in an electrically conducting, rotating fluid driven by a laterally inhomogeneous boundary buoyancy condition (forced convection) that might give rise to static features in the magnetic field. In the third and fourth chapters, we therefore develop an iterative method to study steady, finite-amplitude, rotating magnetoconvection. We will apply the method to both free convection (laterally homogeneous boundary buoyancy conditions), for which considerable prior work exists for comparison, and forced convection. Using our iterative method, we will study the influence of rotation, imposed magnetic field configuration, geometry, and non-linear effects. In chapter five, we examine a somewhat separate problem, that of magnetic Rossby waves in a hypothetical stably stratified layer beneath the CMB. We investigate the possibility that these waves might be responsible for a portion of the magnetic secular variation. Finally, in chapter six, we conclude.

Mean rotational frequency	7.2722×10^{-5} rad/s
Mean radius of the outer core[b]	3.48×10^{6} m
Mean radius of the inner core[b]	1.22×10^{6} m
Composition of the outer core[a]	primarily Fe, possibly a few percent Ni, 6-10% lighter elements such as O, S, Mg, Si
Mean density of the outer core[b]	1.2×10^{4} kg/m^3
Temperature at CMB[a,b]	2300 K < T < 5000 K, best estimate 3157 K
Temperature at ICB[a,b]	3000 K < T < 8000 K, best estimate 4168 K
Gravity at CMB[b]	10.68 m/s^2
Gravity at ICB[b]	4.40 m/s^2
Fluid viscosity of the outer core[a]	10^{-6} m^2/s < ν < 10^{5} m^2/s
Magnetic diffusivity of the outer core[a]	O(1) m^2/s
Thermal diffusivity of the outer core[b]	4.2×10^{-6} m^2/s
Chemical diffusivity of the outer core[b]	3×10^{-9} m^2/s
Rayleigh number[c]	>> 1, perhaps as large as 10^{30}
Taylor number[d]	>> 1, perhaps as large as 10^{30}
Elsasser number[d]	perhaps O(1)
Thermal Prandtl number[d]	O(1)
Chemical Prandtl number[e]	>>1
Magnetic Prandtl number[d]	O(10^{-6})

Source: [a]Merrill and McElhinny (1983), [b]Loper (1984), [c]Cardin and Olson (1992), [d]Roberts (1988), [e]Zhang (1991)

Table 1.1 Estimates for parameters and non-dimensional numbers of importance for rotating magnetoconvection in the Earth's core.

References

Alfven, H., *Cosmical Electrodynamics*, Oxford University Press (1940).

Backus, G.E., "A class of self-sustaining dissipative spherical dynamos", *Ann. Phys.* **4**, 372-447 (1958).

Blackett, P.M.S., "A negative experiment relating to magnetism and the Earth's rotation", *Phil. Trans. Roy. Soc. London A***245**, 309-370 (1952).

Bloxham, J., "The dynamical regime of fluid flow at the core surface", *Geophys. Res. Lett.* **15**, 585-588 (1988).

Bloxham, J., and Gubbins, D., "Thermal core-mantle interactions", *Nature* **325**, 511-513 (1987).

Braginsky, S.I., "Structure of the F-layer and reasons for convection in the Earth's core", *Dokl. Akad. Nauk SSSR* **149**, 8-10 (1963).

Braginsky, S.I., "Self-excitation of a magnetic field during the motion of a highly conducting fluid", *Sov. Phys. JETP* **20**, 726-735 (1964a).

Braginsky, S.I., "Theory of the hydromagnetic dynamo", *Sov. Phys. JETP* **20**, 1462-1471 (1964b).

Braginsky, S.I., and Roberts, P.H., "A model-Z dynamo", *Geophys. Astrophys. Fluid Dynam.* **38**, 327-349 (1987).

Bullard, E.C., and Gellman, H., "Homogeneous dynamos and terrestrial magnetism", *Phil. Trans. Roy. Soc. London A***247**, 213-278 (1954).

Busse, F.H., "A model of the geodynamo", *Geophys. J. R. Astron. Soc.* **42**, 437-459 (1975).

Cardin, P., and Olson, P., "Chaotic thermal convection in a rapidly rotating spherical shell: consequences for flow in the outer core", manuscript, (1992).

Chandrasekhar, S., *Hydrodynamic and Hydromagnetic Stability*. Dover Publications (1961).

Cowling, T.G., "The magnetic field of sunspots", *Mon. Not. Roy. Astr. Soc.* **94**, 39-48 (1934).

Elsasser, W.M., "Induction effects in terrestrial magnetism. 1. Theory", *Phys. Rev.* **69**, 106 (1946a).

Elsasser, W.M., "Induction effects in terrestrial magnetism. 2. The secular variations", *Phys. Rev.* **70**, 202 (1946b).

Elsasser, W.M., "Induction effects in terrestrial magnetism. 3. Electric modes", *Phys. Rev.* **72**, 821 (1947).

Fearn, D.R., Roberts, P.H., and Soward, A.M., "Convection, stability, and the dynamo", 60-324, In *Energy, Stability, and Convection*, eds. Straughan, B., and Galdi, G.P., Longmans (1988).

Gibson, R.D., and Roberts, P.H., "The Bullard-Gellman dynamo", 577-601, In *The Application of Modern Physics to the Earth and Planetary Interiors*, ed. Runcorn, S.K., Wiley (1969).

Gubbins, D., "Energetics of the Earth's core", *J. Geophys.* **43**, 453-464 (1977).

Larmor, J., "Possible rotational origin of magnetic fields of Sun and Earth", *Elec. Rev.* **85**, 412 (1919a).

Larmor, J., "How could a rotational body such as the Sun become a magnet", *Rep. Brit. Assoc. Adv. Sci.* **1919**, 159-160 (1919b).

Loper, D.E., "Structure of the core and lower mantle", *Adv. Geophys.* **26**, 1-34 (1984).

Malkus, W.V.R., "Precession of the Earth as the cause of geomagnetism", *Science* **160**, 259-264 (1968).

Melchior, P., *Physics of the Earth's Core*, Pergamon Press (1986).

Merrill, R.T., and McElhinny, M.W., *The Earth's Magnetic Field*, Academic Press (1983).

Moffatt, H.K., *Magnetic Field Generation in Electrically Conducting Fluids*, Cambridge University Press (1978).

Parker, E.N., "Hydromagnetic dynamo models", *Astrophys. J.* **122**, 293-314 (1955).

Ringwood, A.E., "Composition of the core and implications for the origin of the Earth", *Geochem J.* **11**, 111 (1977).

Roberts, P.H., "Future of geodynamo theory", *Geophys. Astrophys. Fluid Dynam.* **44**, 3-31 (1988).

Soward, A.M., "Convection driven dynamos", *Phys. Earth Planet. Inter.* **20**, 134-151 (1979).

Steenbeck, M., Krause, F., and Radler, K.H., "A calculation of the mean electromotive force in an electrically conducting fluid in turbulent motion, under the influence of Coriolis forces", *Z. Naturforsch.* **21**a, 369-376 (1966).

Verhoogen, J., *Energetics of the Earth's Core* National Academy of Science (1980).

Zhang, K.K., "Convection in a rapidly rotating spherical shell at infinite Prandtl number: steadily drifting rolls", *Phys. Earth Planet. Inter.* **68**, 156-169 (1991).

Chapter 2

Observational Evidence for Stationary Flow in the Earth's Core

2.1 Introduction

In Chapter 1 we discussed the difficulty of interpreting surface geomagnetic and other geophysical data to shed light on the workings of the Earth's dynamo; in this chapter we briefly illustrate some of the difficulty with regard to the subject of core-mantle thermal coupling. The usual geophysical problem of insufficient and defective data is extreme in matters concerning the lower mantle and core. Moreover, while the evidence is mounting that the mantle, with its long thermal time constant, plays a role in governing near-surface core motions, there remain problems with the interpretation of the observations. After reviewing the observational evidence for core-mantle thermal coupling, we will look critically at the claimed correlation of various geophysical data. Finally, we will simply examine maps of the magnetic field and its secular variation at the Earth's surface in an effort to gain further insight into the dynamics of the Earth's deep interior.

2.2 Evidence for core-mantle thermal coupling

In part because of efforts to obtain maps of the fluid flow at the CMB, considerable effort has been made to obtain maps of B_r and $\partial B_r/\partial t$ at the CMB. One can construct maps of the magnetic field at the Earth's surface using a least squares fit to a truncated spherical harmonic expansion (Barraclough *et al.*, 1978). However, constructing maps of the magnetic field at the CMB using a spherical harmonic analysis is a bit more problematic (Shure *et al.*, 1982, Gubbins, 1983). Firstly, small wavelength errors (and crustal contributions) in the magnetic field at the Earth's surface may dominate the field that is simply downward continued to the CMB. One could truncate the expansion at a low

degree, but this is somewhat arbitrary. Secondly, it is not possible to assign meaningful errors to the maps of the magnetic field at the CMB using a spherical harmonic analysis. This is especially important when one is using the maps quantitatively for finding fluid flow, and one would like to know the range of possible models.

Shure *et al.* (1982) and Gubbins (1983) developed alternate methods for modelling the geomagnetic field on the CMB, both, like the spherical harmonic analysis, assuming an insulating mantle. Shure *et al.* (1982) used harmonic splines to find the smoothest field consistent with the data. They assessed this smoothness using various norms on the integrated magnetic field on the core surface, such as the Ohmic dissipation. Gubbins (1983) used stochastic inversion to incorporate *a priori* knowledge to damp out spurious small scale features in the magnetic field at the CMB. By choosing similar *a priori* knowledge (such as minimizing the Ohmic dissipation), stochastic inversion gives results similar to harmonic splines, but it also gives error estimates. Gubbins and Bloxham (1985) reformulated their stochastic inversion in terms of a Bayesian formalism, which also enabled them to incorporate measurements such as total intensity (from satellites), and declination and inclination (from ship surveys) that depend non-linearly on the model. They find that the core fields they obtain are relatively insensitive to the damping level, but that the error bounds, especially at high degree, very much depend on the damping level.

Gubbins and Bloxham (1985), Bloxham and Gubbins (1985), Bloxham (1986), and Hutcheson and Gubbins (1990) used this formulation of the stochastic inverse to produce models of the magnetic field at the CMB as far back as the seventeenth century, with formal errors that represent the uncertainty in the field models. They found that their maps resolve small scale features that their error analysis indicates are real features of the core surface magnetic field. Figure 2.1 is one such map, for 1980. The maps show static patches of high magnetic flux at high positive and negative latitudes at longitudes of 120° E and 120° W (1 - 4 in Figure 2.1), and static patches of low magnetic flux at the poles (5 - 6), which is perhaps surprising since one would expect a maximum at the poles for a

dipole field. They also found rapidly westwardly drifting flux spots, primarily under the Atlantic region, as well as stationary, local magnetic field oscillations near the magnetic equator underneath Indonesia.

Gubbins and Bloxham (1987) tentatively identified the static high flux patch pairs 1 and 3, and 2 and 4 with the intersection of convection columns (Roberts, 1968, Busse, 1970, see Chapter 3, Figure 3.1) with the spherical surface at the CMB. Associated with each convecting column is downwelling flow induced by Ekman suction at the boundary (Greenspan, 1968) that concentrates the magnetic flux. In between (longitude = 180°) lies a pair of regions of low magnetic flux associated with a column containing upwelling flow. At 0° longitude a third pair of regions of high flux is missing; they ascribed this to the near core surface flow that is associated with the high secular variation under the Atlantic region. The static low flux patches near the poles they accredited to the dynamical effect of the inner core. In the absence of strong Lorentz forces this picture is appealing. However, the columns, if they represent free convection driven by a homogeneous boundary temperature or buoyancy flux, should drift in azimuth (Busse, 1970); they show no such drift.

Bloxham and Gubbins (1987) ascribed this lack of drift to core-mantle thermal coupling. The mantle, being much more viscous than the core, has a much longer convective time scale than the outer core. Hence, horizontal temperature differences in the lower mantle should persist over many core convective overturns, and force flow in the outer core via an inhomogeneous boundary heat flux (King and Hager, 1989, Zhang and Gubbins, 1992). (Note that because of the short thermal time scale of the outer core the proper thermal boundary condition on mantle convection remains an isothermal temperature.) Bloxham and Gubbins (1987) found evidence for core-mantle thermal coupling by finding a spatial correlation between static features in the magnetic field at the CMB, anomalies in the seismic P-wave velocity at the bottom of the mantle (Dziewonski, 1984), and CMB topography (Hager *et al.*, 1985). Figure 2.2 shows the P-wave velocity at the CMB and Figure 2.3 shows the CMB topography. Regions in the lower mantle that

Figure 2.1 Map of the radial component of the magnetic field at the core-mantle boundary for 1980 (reproduced from Gubbins and Bloxham, 1987, originally from Gubbins and Bloxham, 1985). The contour interval is 100 μT; solid contours represent positive radial field, dashed contours represent negative radial field, and bold contours represent zero radial field. The pairs 1-3 and 2-4 are patches of high (enhanced) magnetic flux and 5-6 are patches of low magnetic flux.

Figure 2.2 Map of the seismic P-wave velocity at the core-mantle boundary (reproduced from Bloxham and Gubbins, 1987, originally from Dziewonski, 1984). The contour interval is .5%. The minus signs corresponds to fast, *i.e.*, cold, mantle, and the plus sign to slow, or hot, mantle. The regions of cold mantle appear to correlate with the patches of high magnetic flux in Figure 2.1, suggesting downwelling core flow, while the region of hot mantle appears to correlate with the flux spots beneath southern Africa, suggesting upwelling flow.

Figure 2.3 Map of dynamic core-mantle boundary topography inferred from P-wave variations and constrained by the geoid, assuming a chemically uniform mantle with a ten-fold increase in viscosity beneath 670 km (reproduced from Bloxham and Gubbins, 1987, orginally from Hager *et al.*, 1985). The contour interval is 500 m. The minus signs correspond to regions of depressed CMB, or cold mantle, the plus sign to a region of elevated CMB, *i.e.*, hot mantle. Again, there is some correlation with Figure 2.1.

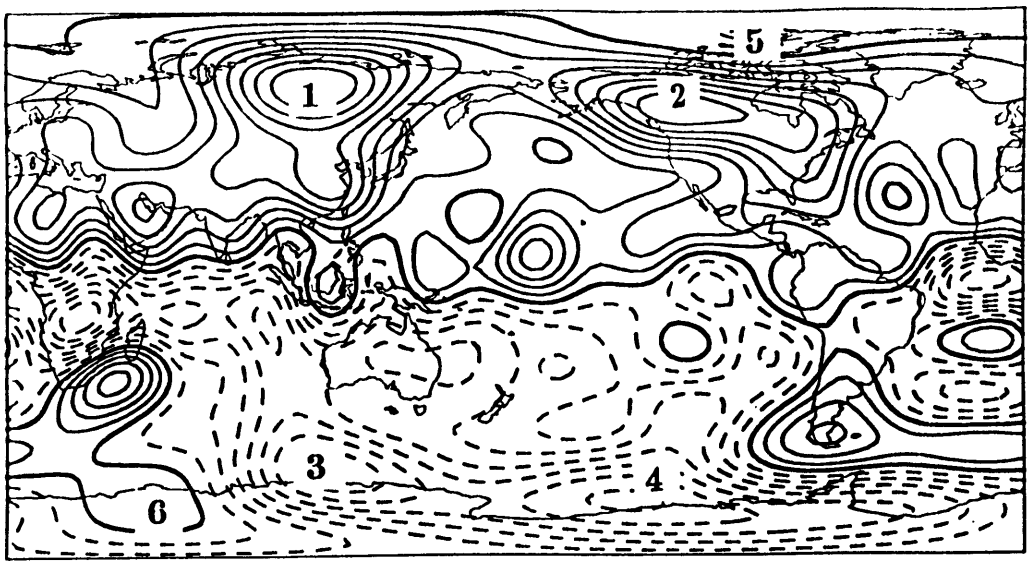
1
2
3
4
5
6

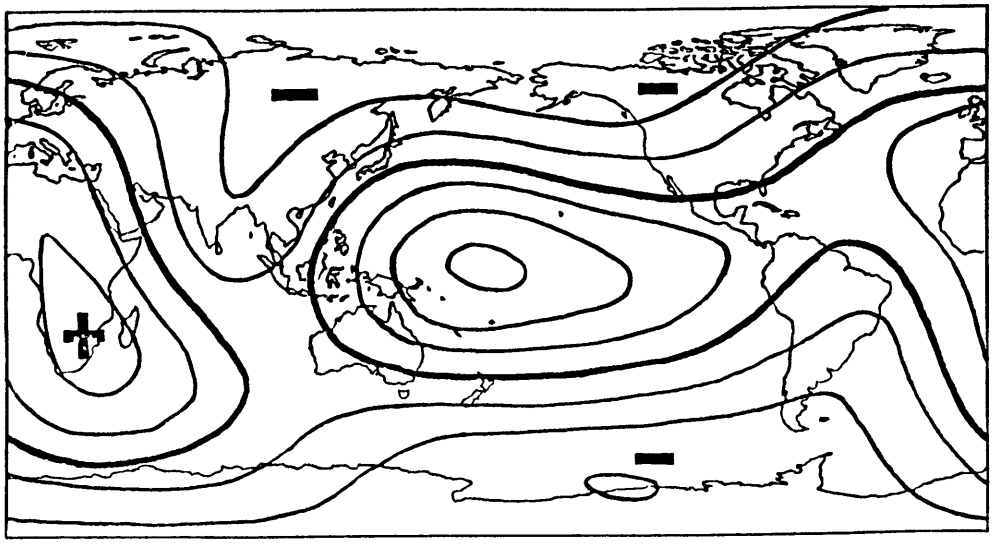

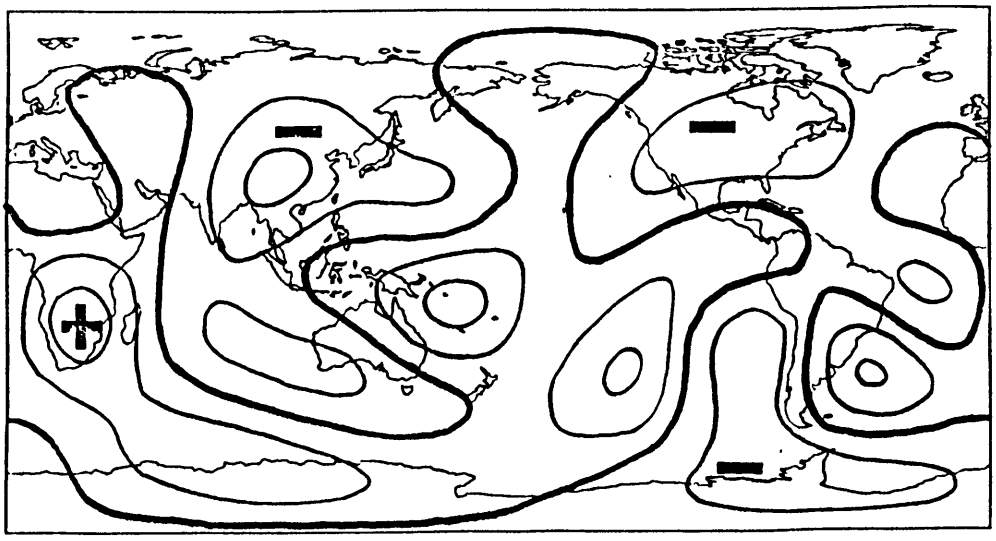

are cold should be seismically fast, with a dynamically maintained depressed CMB, and vice versa. Further, regions in the lower mantle that are cold might exhibit a high heat flux from the underlying region of the core, resulting from core fluid horizontally converging and then downwelling, which could also cause a static high magnetic flux patch. Although the correlation in Figures 2.1 - 2.3 is certainly suggestive of core-mantle thermal coupling, the resolution of the three plotted quantities is perhaps insufficient, as we shall shortly discuss.

During a magnetic dipole reversal it is unlikely that the field maintains a simple structure, *i.e.*, the dipole does not simply 'flip' (Merrill and McElhinny, 1983). If this were the case, one could define a single VGP path for each reversal that without control external to the core would vary for each reversal. If not the case, a VGP path is in theory a meaningless quantity, since there is no single north pole to define. Nevertheless, paleomagnetists have found that while each reversal does not trace out a single VGP path, it does often yield just two distinct longitudinal paths. This suggests that during a reversal a relatively simple, though not unique, field structure remains. One possibility (Clement and Kent, 1991) that gives rise to the observed equatorial symmetry is a magnetic field with a dominant h_3^1 Gauss coefficient. Clement and Kent (1991) and Clement (1991) state that the longitudes of the two VGP paths during the Matuyama-Brunhes magnetic dipole reversal (Figure 2.4) nearly coincide with the longitudes of the static patches of high magnetic flux at the CMB (Gubbins and Bloxham, 1987), but we later question this correlation. In any case, there is also evidence that VGP paths have preferred these two longitudes during other reversals (Tric *et al.*, 1991, Laj *et al.*, 1991), which further supports the idea that the mantle exerts control over core motions.

While these possible correlations between static magnetic flux patches, P-wave velocities in the lower mantle, CMB topography, and VGP paths during magnetic dipole reversals are certainly suggestive of coupling between core and mantle, the data are not without considerable uncertainty. Backus (1988) questioned the error estimates of Gubbins

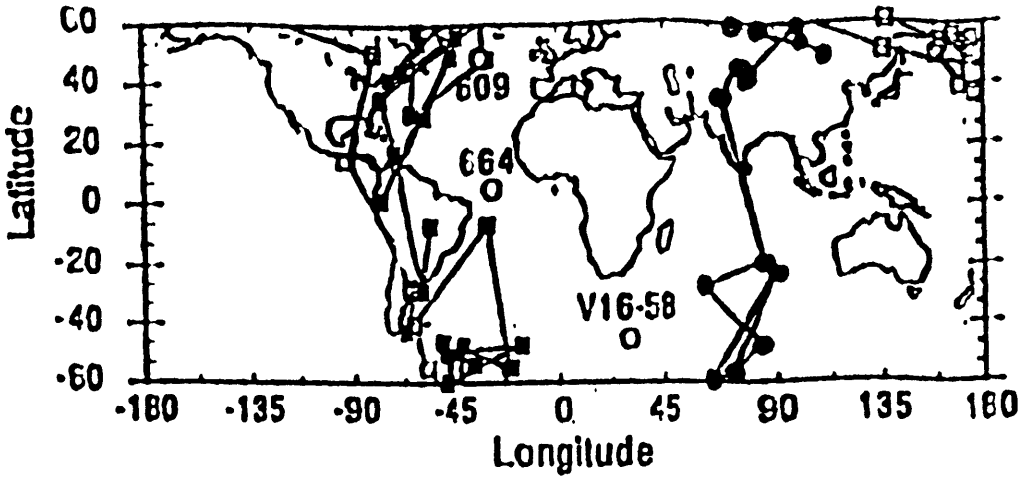

Figure 2.4 Virtual geomagnetic pole paths for the Matuyama-Brunhes dipole reversal (from Clement and Kent, 1991). Solid squares indicate pole positions for site V16-58, open squares for site 609, and solid circles for site 664, with the open circles indicating site positions. The mid-latitude sites yield VGP paths passing through the Americas, while the equatorial site yields a VGP path passing through Asia. The longitudes of the paths are nearly antipodal.

and Bloxham (1985), believing that their optimistic error estimates resulted from an overemphasis on the *a priori* information, *i.e.*, too much damping. Thus, the resolution of the small scale features (degree $\ell > 10$) of the magnetic field on the CMB of Bloxham and Gubbins (1985), Bloxham (1986), and Hutcheson and Gubbins (1990) is under question. However, maps produced with entirely different data sets (different epochs) and with a different inversion technique (a spherical harmonic analysis truncated at degree 14) produce similar looking maps (Gubbins, 1989), and in any case, the static flux patches are less than degree 10.

More severe doubts remain about our current ability to resolve aspherical seismic structure of the lower mantle for $\ell > 3$. Gudmundsson and Clayton (1991) discussed the low signal to noise ratio of the International Seismological Centre (ISC) Catalogue for tomographic inversions for lower mantle asphericity. In addition, the data set contains systematic errors and uneven geographical coverage. Significantly less unique than our maps of lower mantle P-wave velocity, and the inferred thermal structure, are our maps of CMB topography (Hide *et al.*, 1992). By using the surface geoid, and lateral seismic velocity variations to infer temperature (and hence density) variations in the mantle, and assuming a chemistry and viscosity structure in the mantle, one can obtain the dynamic CMB topography (Hager *et al.*, 1985). For a chemically uniform mantle with a ten-fold increase in viscosity beneath 670 km, this procedure predicts the CMB topography that we show in Figure 2.3, which has a peak-to-peak amplitude of about 3 km. However, we do not know the viscosity structure of the mantle, particularly in the D" layer directly above the CMB, and a low viscosity zone associated with an elevated temperature yields a smaller dynamically maintained CMB topography. For instance, for a 200 km thick D" layer with a viscosity 1/100 that of the lower mantle, the procedure predicts an amplitude less than 2 km (Hager and Richards, 1989). We show this topography in Figure 2.5 (from Hide *et al.*, 1992). Although the amplitudes differ between Figures 2.3 and 2.5, the spatial variation appears similar.

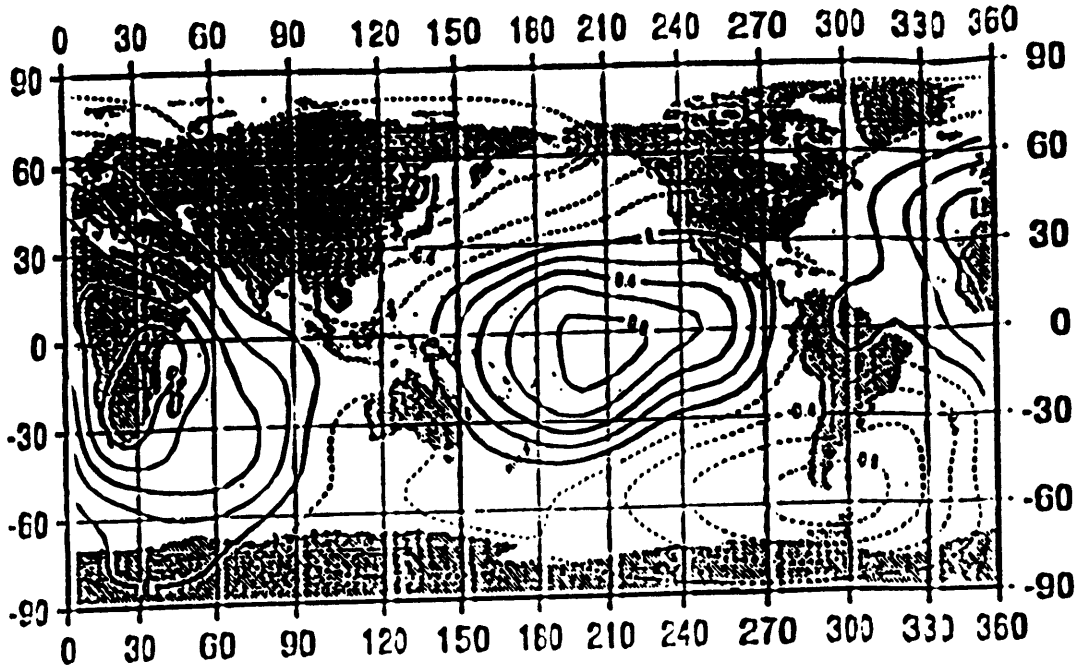

Figure 2.5 Map of dynamic core-mantle boundary topography inferred from P-wave variations and constrained by the geoid, assuming mantle model WL of Hager and Richards (1989) (reproduced from Hide *et al.*, 1992). The model allows for a low viscosity D". The contour interval is 200 m. Solid contours correspond to regions of elevated CMB, dashed contours to regions of depressed CMB. Although the amplitude differs from Figure 2.3, there is spatial correlation.

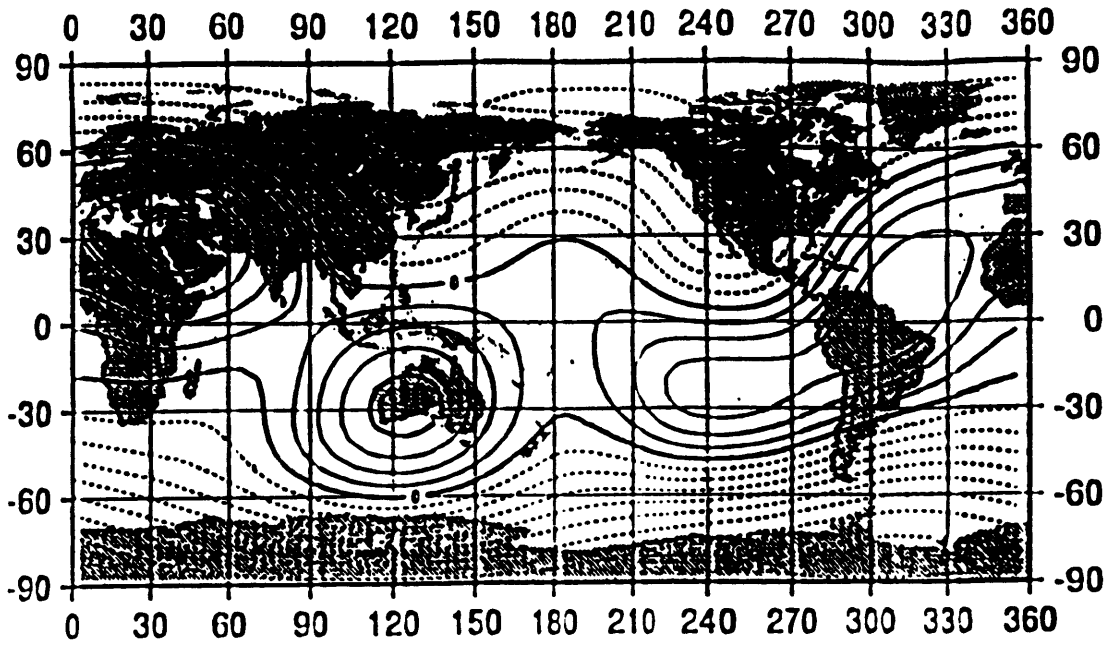

Figure 2.6 Map of core-mantle boundary topography inferred directly from P-wave variations, allowing for velocity variations in D" (reproduced from Hide *et al.*, 1992, originally from Gudmundsson and Clayton, 1992). The contour interval is 500 m. Solid contours correspond to regions of elevated CMB, dashed contours to regions of depressed CMB. Although the amplitude is much less than that inferred seismically by Creager and Jordan (1986) or Morelli and Dziewonski (1987), there is no azimuthal correlation with the dynamically inferred topography of Figures 2.3 and 2.5. On the other hand, Figures 2.2, 2.3, 2.5, and 2.6 all show an equatorial bias towards hot, upwarped mantle and a polar bias towards cold, downwarped mantle.

On the other hand, direct inversion of ISC travel-times of seismic phases that sample the CMB in different ways (reflection off the core surface, refraction through the uppermost core) yields maps of CMB topography that are different for different workers, and different and with larger amplitude than the maps of dynamically inferred topography. Creager and Jordan (1986) used PKP_{AB} and PKIKP phases for their study, which yielded a 20 km peak-to-peak amplitude. They hypothesized that the large amplitude and poor spatial correlation with the dynamically inferred topography could be explained by a chemical boundary layer (CBL) underneath the CMB, which would allow the seismic velocity to be uncorrelated with density. Morelli and Dziewonski (1987) used PKP_{BC} and PcP phases for their study, which yielded a 12 km amplitude. They again found poor spatial correlation with the dynamically inferred topography, which cannot be solely explained by a core-side CBL since PcP does not sample beneath the CMB. Figure 2.6 shows the CMB topography from an inversion of ISC PcP and PKP travel-times by Gudmundsson and Clayton (1992). They found a trade-off between horizontal variations of seismic velocity in the D" and the amplitude of CMB topography. Although the amplitude in Figure 2.6 is only about 5 km, it does not look similar to the dynamically inferred topography of Figure 2.5, at least in its azimuthal dependence. On the other hand, though they may disagree in their azimuthal dependence, Figures 2.2, 2.3, 2.5, and 2.6 all show an equatorial bias towards hot, upwarped mantle and a polar bias towards cold, downwarped mantle.

Valet *et al.* (1992) reanalyzed the paleomagnetic data, and found no statistical evidence for a simple magnetic field structure remaining during a single dipole reversal, nor for any preferred longitudes for VGP paths for different reversals. Hopefully, the addition of more transition records will alleviate the current paucity of VGP paths and resolve the question. In addition to the questionable statistical significance of the VGP paths, we do not understand how there can be a correlation between (m = 1) antipodal VGP paths and the presumed m = 3 symmetry that Gubbins and Bloxham (1987) inferred. The

interpretation of convecting columns (of the Busse (1970) type) in the core being thermally locked to the mantle also puzzles us. Free convective columns drift; according to Gubbins and Bloxham (1987) the inhomogeneous heat flux at the CMB keeps the columns stationary, presumably to transport heat most effectively from the lower core to the mantle. However, according to Figure 9 of Zhang (1991), free convection slightly above the critical Rayleigh number (the parameter regime at which convecting columns exist) primarily transports heat in the equatorial zone, with the heat flux negative in the polar regions. In other words, the primary means of heat transport of freely convecting columns is not motion parallel to the columns, so that it is not clear that an inhomogeneous boundary heat flux will fix convecting columns to align themselves with temperature anomalies in the mantle. Hence, while downwelling core flow due to cold mantle may well cause static patches of high magnetic flux on the CMB, the mechanism may not in essence be the Ekman flow of convection columns locked to the mantle. Zhang and Gubbins (1992) studied steady flows forced by a laterally variable CMB temperature, and found that rotation induces an azimuthal phase shift between the thermal boundary condition and the flow. Their model did not include free convection driven by bottom heating, however, and it assumed Lorentz forces are negligible, so it remains difficult to apply the results to the Earth's core.

Thus, while we find the basic concept of core-mantle thermal coupling intriguing, we need to understand better the steady motions that occur in an electrically conducting, rotating fluid shell driven by 1) a laterally homogeneous and 2) a laterally inhomogeneous boundary buoyancy flux. We will develop an iterative method to study steady, finite-amplitude motions in Chapter 3 and apply it to the Earth's core in Chapter 4. At the same time, the observational evidence needs strengthening. We can expect this as geomagnetism, paleomagnetism, seismology, and geodynamics advance. In the meantime, in the next section we examine maps of the surface magnetic field to look for further clues on the state of the Earth's deep interior.

2.3 Interpretation of surface magnetic field data

Figure 2.7 is a contour map of the north-south (X) component of the 1980 magnetic field at the Earth's surface, produced from the International Geomagnetic Reference Field (IGRF) Gauss coefficients up to degree and order 10 (Peddie, 1982). The 1980 IGRF uses data from MAGSAT and approximately 150 permanent magnetic observatories. If the field were purely dipolar, the contours would of course be parallel to lines of constant latitude. The largest deviation away from a dipole field appears to be an equatorial m = 1 anomaly, with additional north-seeking field beneath Indonesia and a deficit of north-seeking field beneath the northern coast of South America. Such an anomaly implies large electrical currents in the east-west and radial directions in the equatorial zone, *e.g.*, current loops parallel to but displaced from the rotaton axis.

To test this inference, we set up a small inverse problem for electrical currents in the outer core. We first place ideal magnetic dipoles, *i.e.*, infinitesimal current loops, spaced every forty degrees in longitude, at +/- 20^{o} latitude, and at four fixed depths in the core. At each of these 72 positions we allow for X (current loop with axis in the north-south direction), Y (axis in east-west direction), and Z (axis in radial direction) dipoles. For comparison we then change the location of the 72 ideal magnetic dipoles, placing them on the cylinder circumscribing the inner core, again at four depths and nine longitudes. For each geometry we invert all three components of the surface non-dipole field (from the coefficients of the 1980 IGRF) for the magnitudes of the 216 dipole components. We hope that this simple approach will yield some insight into the electrical current system associated with the poloidal magnetic field, though of course, the magnetic field maps contain the same information.

The expression for the magnetic field **B** due to an ideal magnetic dipole **m** is

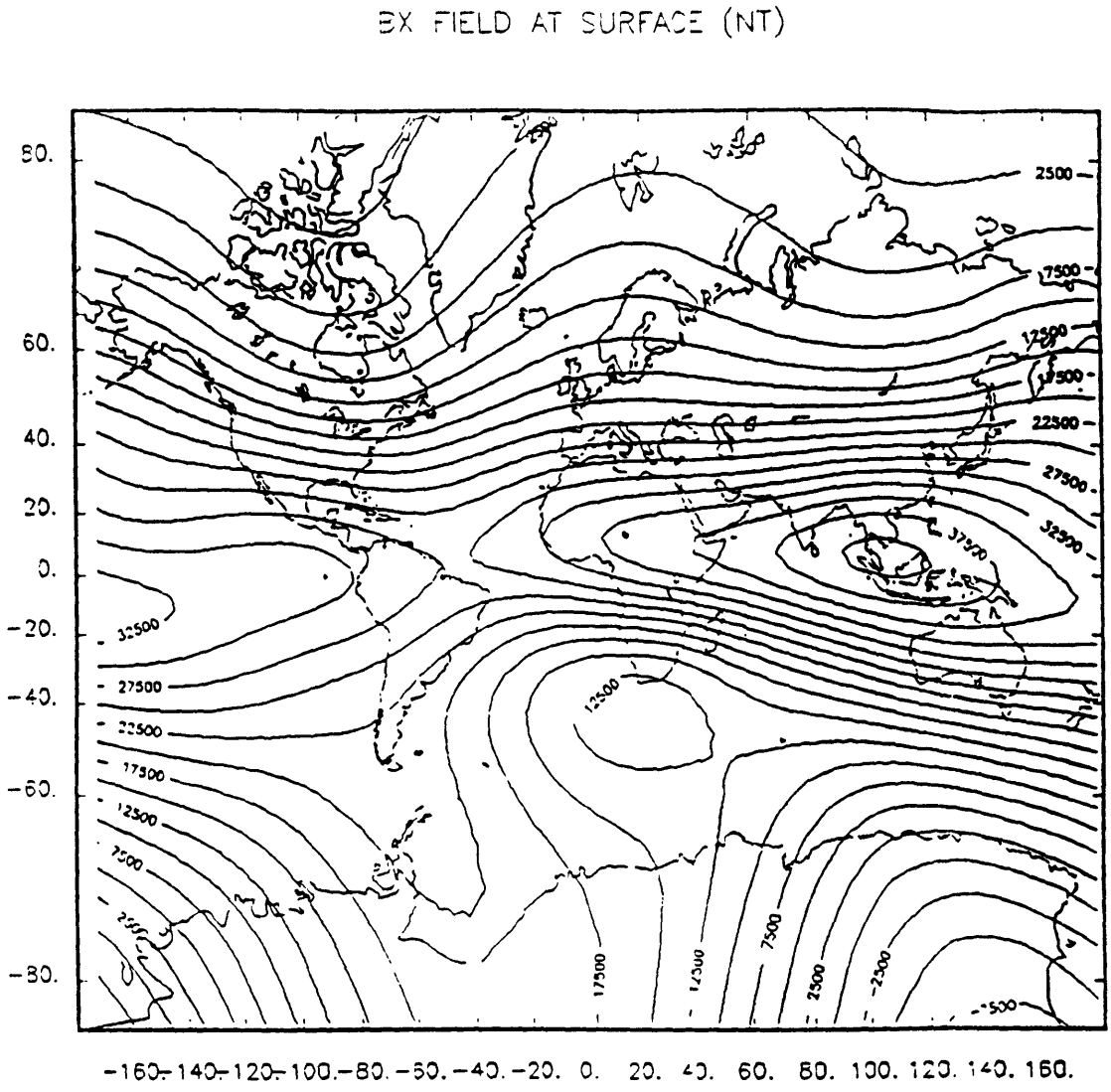

Figure 2.7 Map of the north-south (X) component of the magnetic field at the Earth's surface for 1980 produced from the IGRF Gauss coefficients up to degree and order 10 (Peddie, 1982). The contour interval is 2500 nT. The positive anomaly beneath southern Asia and the negative anomaly beneath the northern coast of South America are antipodal, and are suggestive of east-west and radial electrical currents in the equatorial zone.

$$\mathbf{B} = \frac{\mu_o}{4\pi}\frac{1}{r^3}[3(\mathbf{m}\cdot\hat{\mathbf{r}})\hat{\mathbf{r}} - \hat{\mathbf{m}}], \qquad (2.1)$$

where μ_o is the permeability of free space, r is the distance between the dipole and the observation point, $\hat{\mathbf{r}}$ is the direction between the dipole and the observation point, and $\hat{\mathbf{m}}$ is the orientation of the dipole (Jackson, 1962, and converting to the MKS system). We invert equation (2.1) using damped least squares, so that we solve

$$\mathbf{x} = (\mathbf{A}^T\mathbf{A} + \varepsilon^2\mathbf{I})^{-1} \cdot (\mathbf{A}^T\mathbf{b}). \qquad (2.2)$$

In (2.2) the model **x** consists of the magnitudes of the components of the 72 dipole moments **m**, the operator matrix **A** (with transpose $\mathbf{A}^T$) represents (2.1) in some coordinate system, and the data **b** consists of 432 evenly spaced point values of the components of the surface non-dipole magnetic field **B**, computed from the 1980 IGRF coefficients. The term $\varepsilon^2\mathbf{I}$ represents the damping.

For both the equatorial dipoles, which form a cone, and the polar dipoles, which lie on a cylinder, we position dipoles at depths of the CMB, CMB - 600 km, CMB - 1200 km, and CMB - 1800 km, and at nine longitudes. Figures 2.8 and 2.9 show the results of the inversions for the amplitudes of the X, Y, and Z components of the current loops, for damping with $\varepsilon^2 = 10^3$. In each figure, the upper four traces of each plot represent the amplitudes for one component in the northern hemisphere at the four fixed depths, the lower four in the southern hemisphere. The traces begin at 0° longitude and proceed eastwardly at intervals of 40°. The amplitude between traces is 10^{21} A-m^2. The number at the lower right of each plot is the fit of the plotted solution to the original set of equations $\mathbf{A}\cdot\mathbf{x} = \mathbf{b}$, or equation (2.1).

At this level of damping, $\varepsilon^2 = 10^3$, the fit for the equatorial dipoles, .99, is better than for the polar dipoles, .98. For the equatorial dipoles, the largest amplitudes occur for the X component, in accordance with our inference. The X component shows a strong

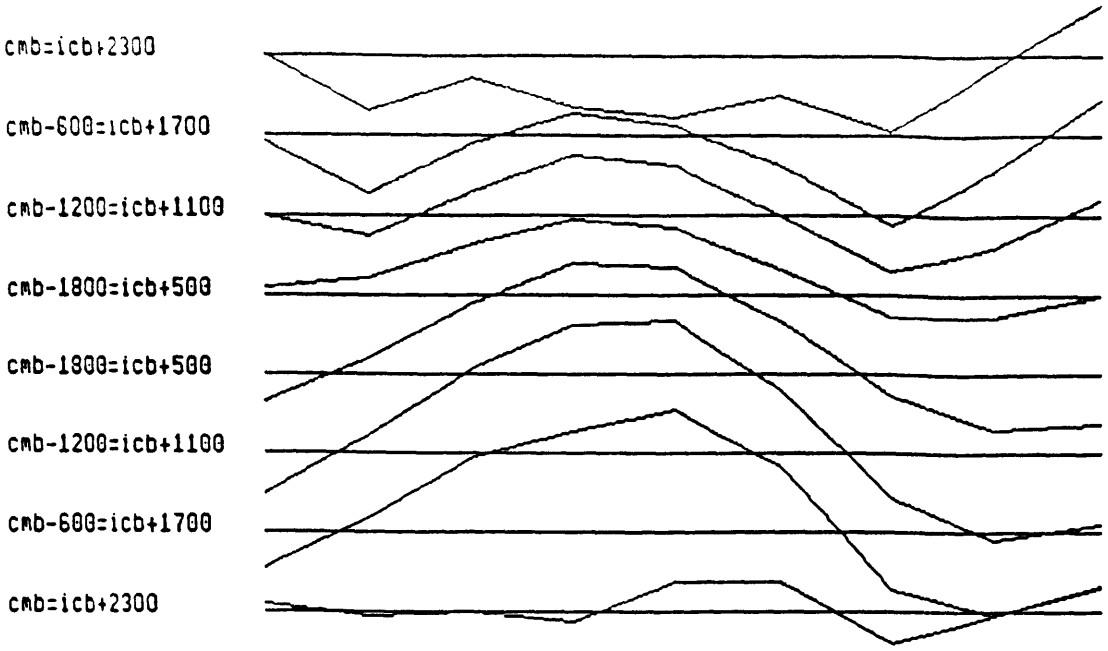

xmom.nd.20deg.1ep3 0.992146

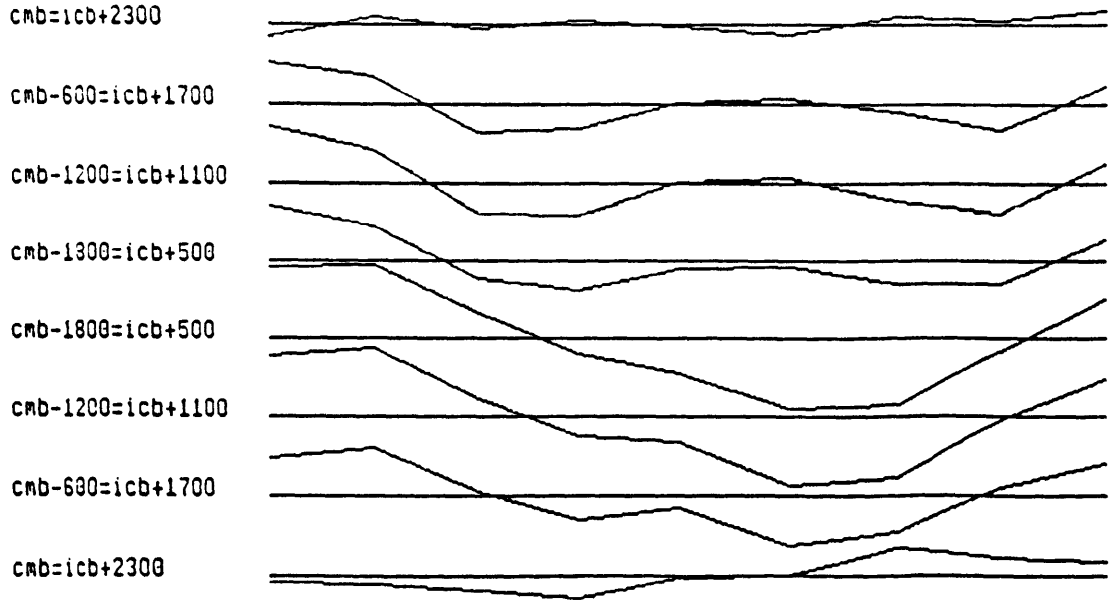

ymom.nd.20deg.1ep3 0.992146

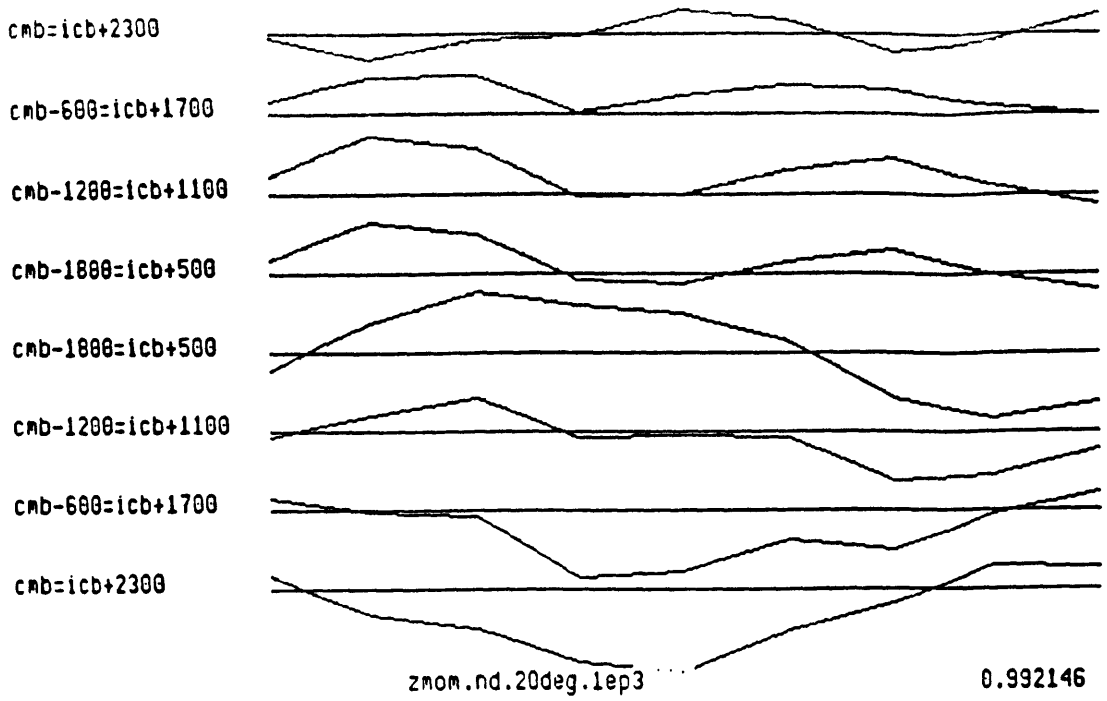

Figure 2.8 The amplitude (10^{21} A-m^2 between traces) of the ideal magnetic dipoles that fit the non-dipole part of Figure 2.7 through a damped least-squares inversion of equation (2.2). The damping level is $\varepsilon^2 = 10^3$, with a resulting fit of .99. The first four traces of each plot are at +20° latitude, the second four at -20°, at the indicated depths. Each trace begins at 0° longitude, and proceeds eastwardly at 40° intervals. Plot a) shows the amplitude of the X (current loop with axis in the north-south direction) component, b) shows the Y (east-west) component, and c) shows the Z (radial) component. X has the largest amplitude and shows a large m = 1 contribution.

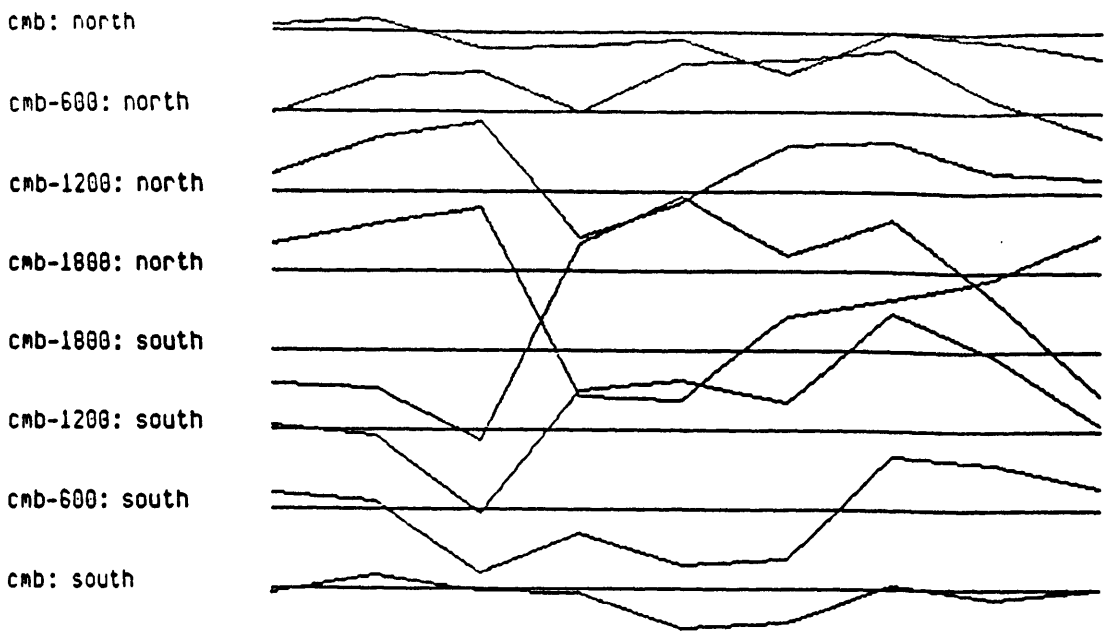
cmb: north
cmb-600: north
cmb-1200: north
cmb-1800: north
cmb-1800: south
cmb-1200: south
cmb-600: south
cmb: south
xmom.nd.cyl.1ep3
0.981455

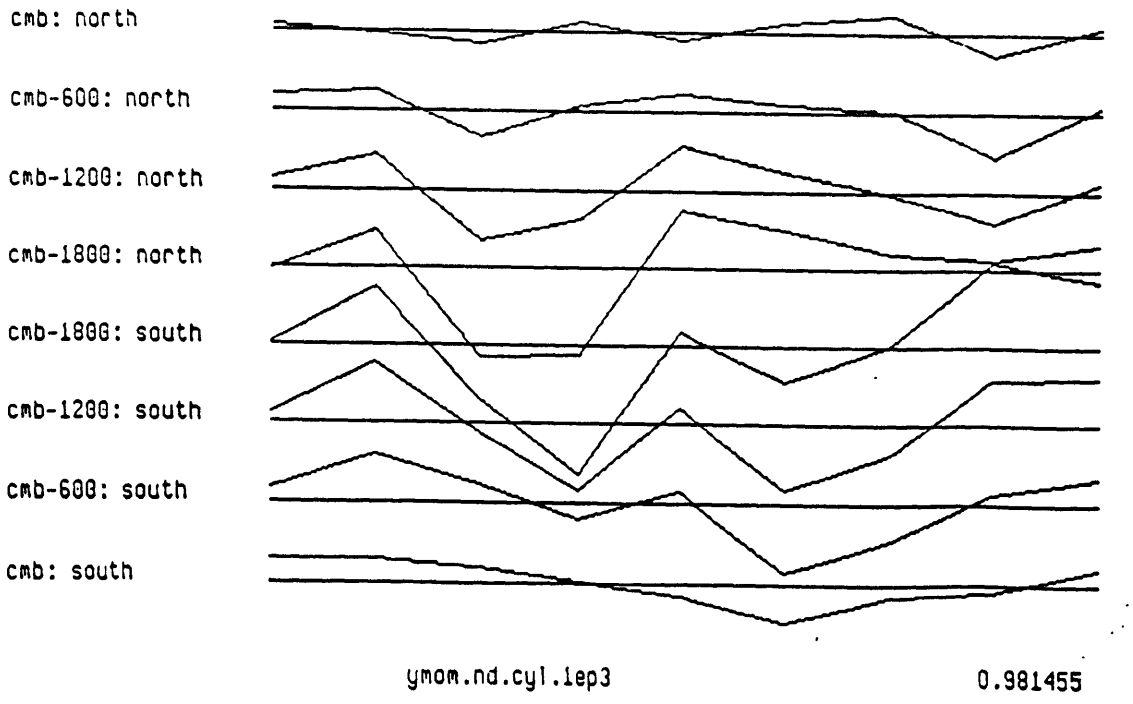
cmb: north
cmb-600: north
cmb-1200: north
cmb-1800: north
cmb-1800: south
cmb-1200: south
cmb-600: south
cmb: south
ymom.nd.cyl.1ep3
0.981455

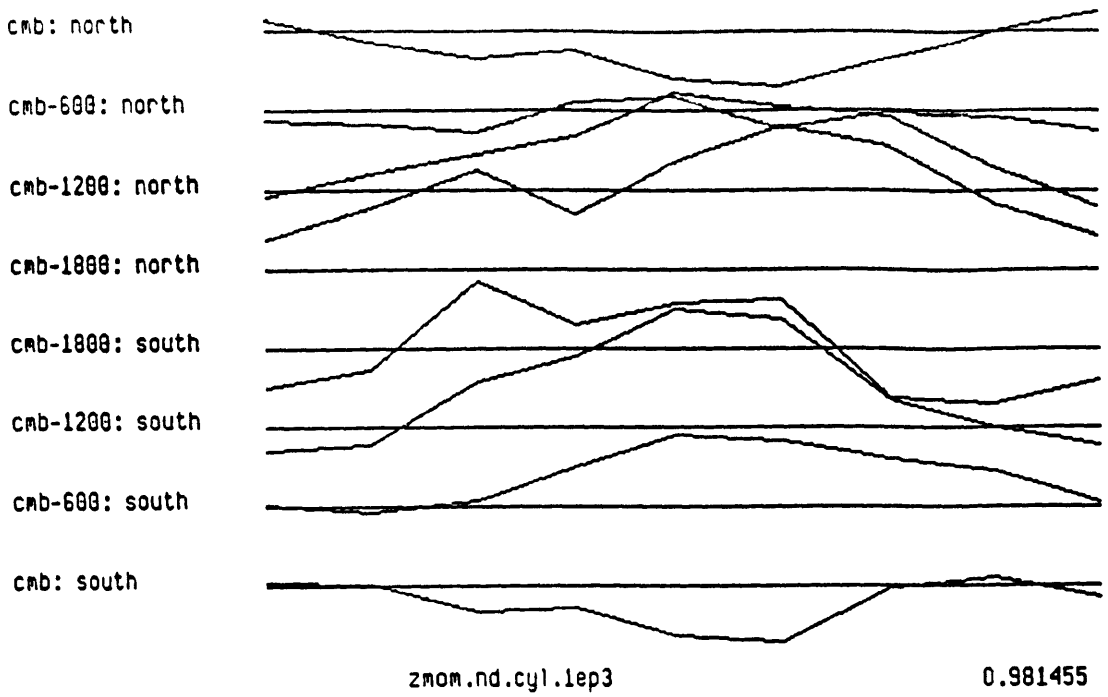

Figure 2.9 As for Figure 2.8, but with ideal dipoles on the cylinder circumscribing the inner core. The upper four traces of each plot are for northern hemisphere dipoles, the lower four for southern hemisphere dipoles. The solution is not as smooth as for the equatorial dipoles, and the fit is only .98.

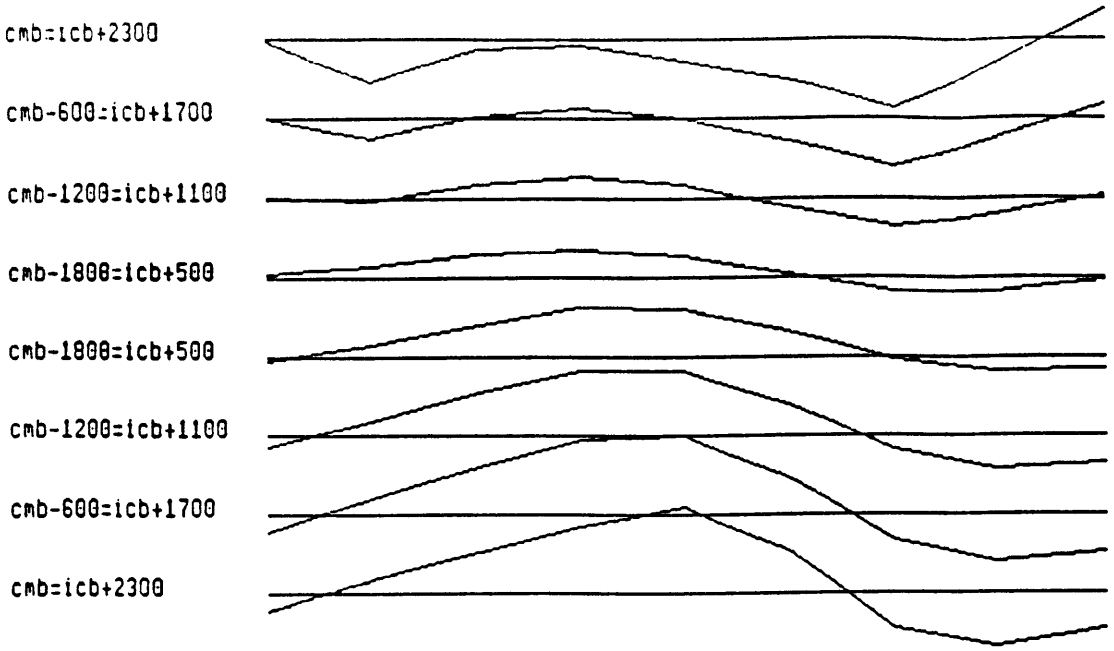

xmom.nd.20deg.1ep4 0.976729

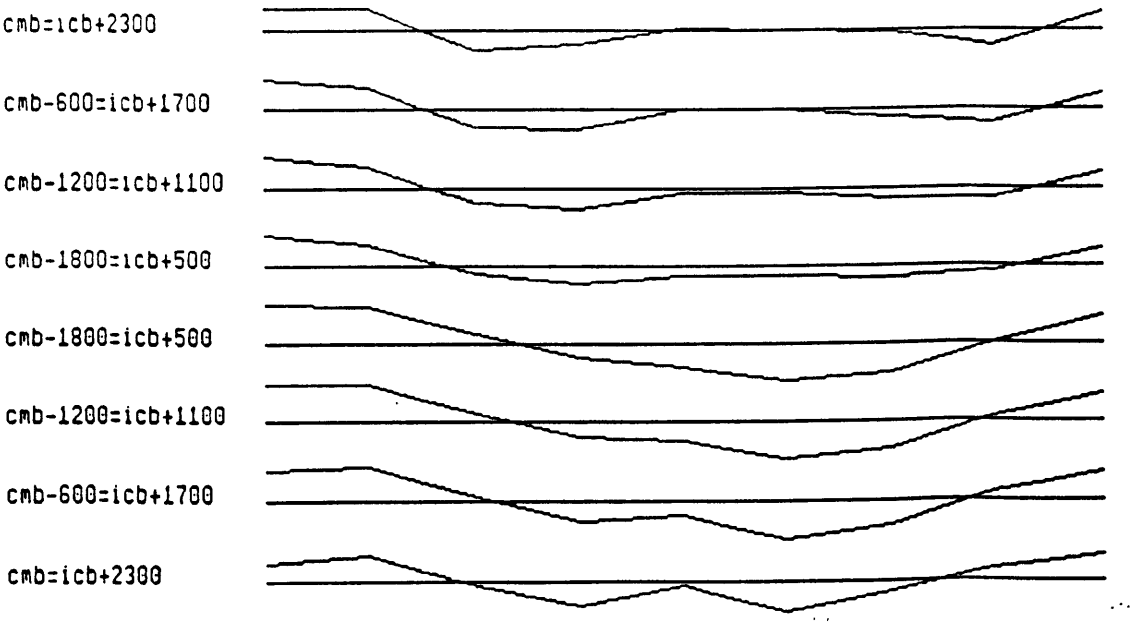

ymom.nd.20deg.1ep4 0.976729

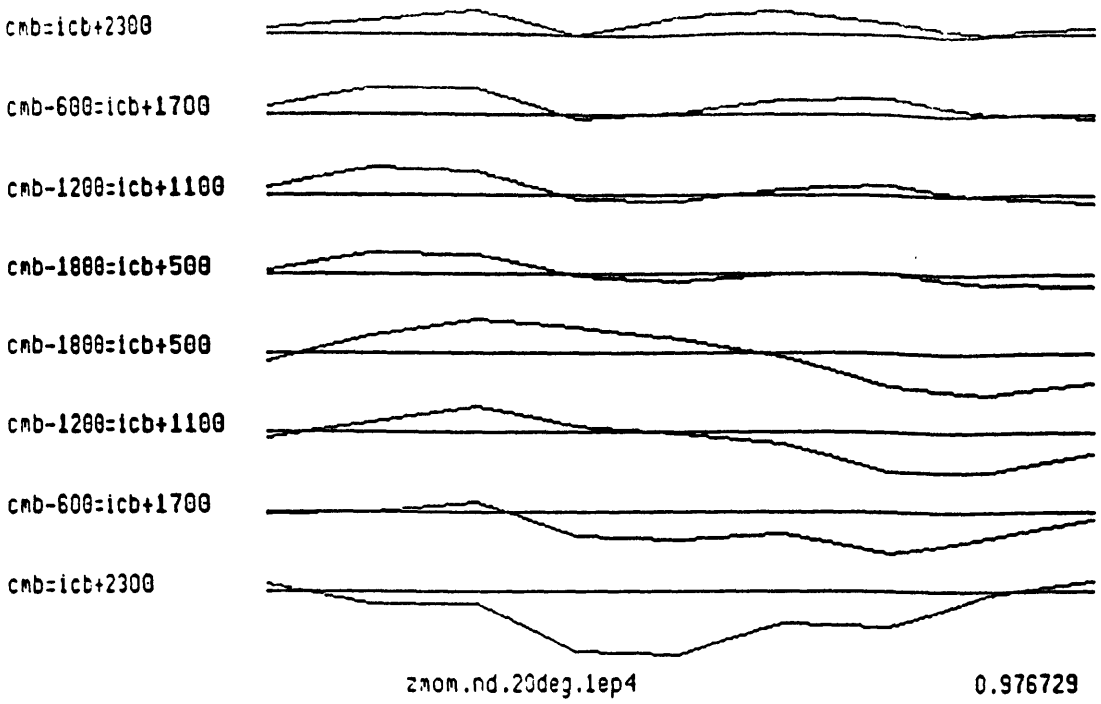

Figure 2.10 As for Figure 2.8, but with damping $\varepsilon^2 = 10^4$. The solution is smoother than that in Figure 2.8, but the fit is only .98.

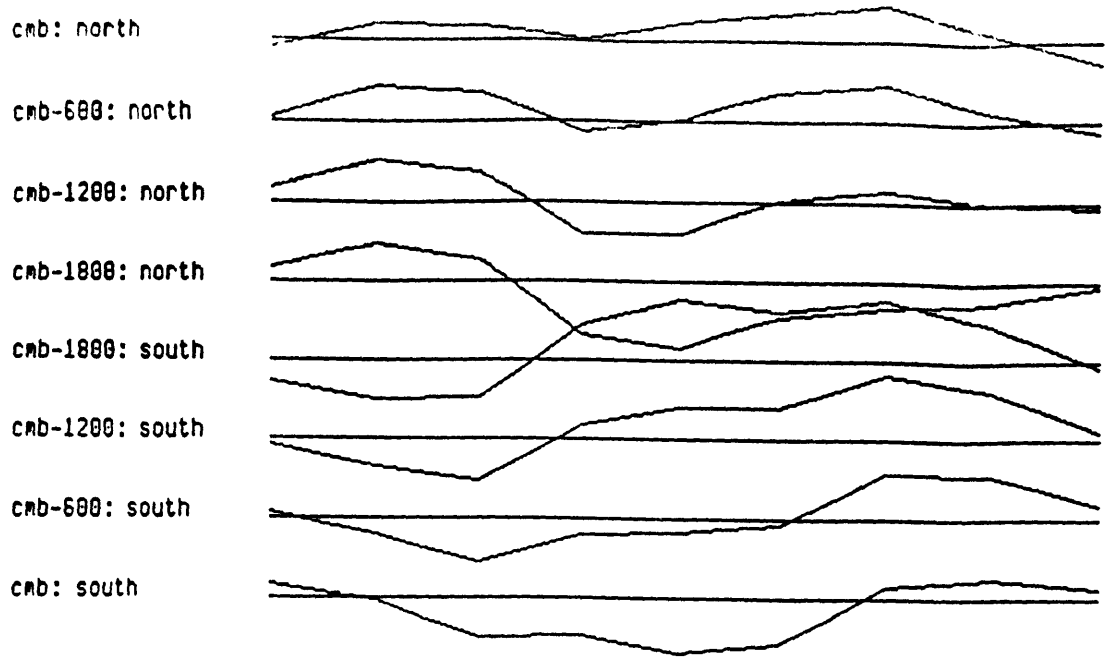
cmb: north
cmb-600: north
cmb-1200: north
cmb-1800: north
cmb-1800: south
cmb-1200: south
cmb-600: south
cmb: south
xmom.nd.cyl.iep4
0.938637

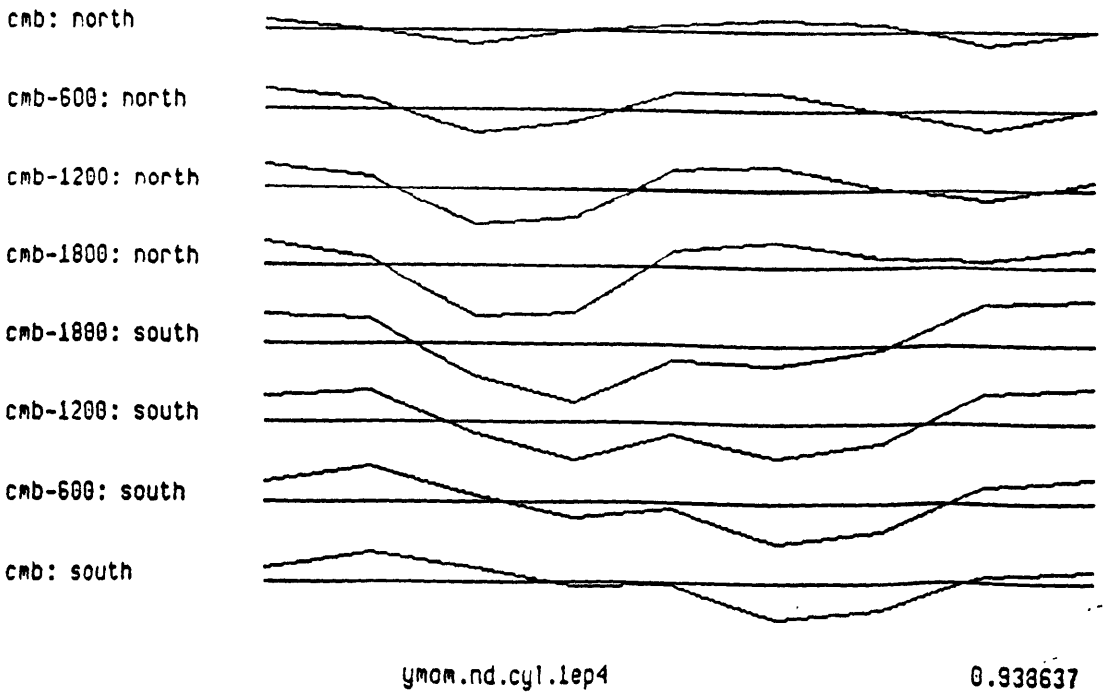
cmb: north
cmb-600: north
cmb-1200: north
cmb-1800: north
cmb-1800: south
cmb-1200: south
cmb-600: south
cmb: south
ymom.nd.cyl.iep4
0.938637

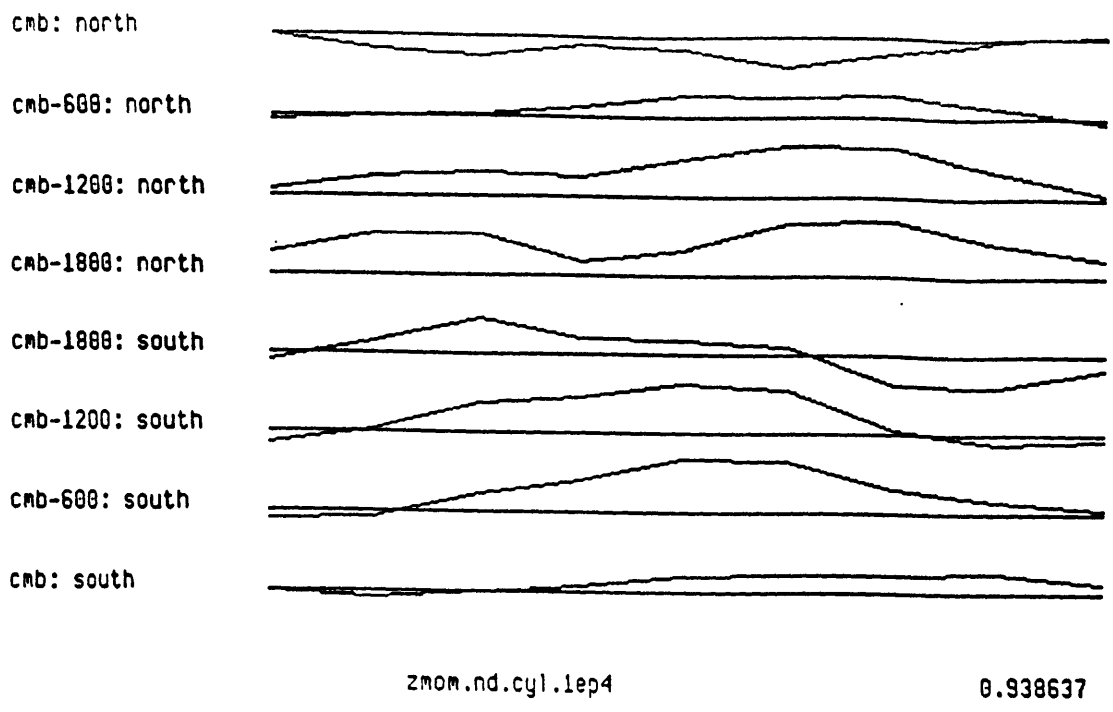

Figure 2.11 As for Figure 2.9, but with damping $\varepsilon^2 = 10^4$. The solution is smoother than that in Figure 2.9, but the fit is only .94.

m = 1 contribution, particularly for the dipoles at -20° latitude. On the other hand, the solution for the polar dipoles is very rough and requires large amplitudes in all three components. An m = 1 dominance is not obvious. A comparison of the two solutions, Figures 2.8 and 2.9, suggests that equatorial currents with a large m = 1 contribution account for much of the non-dipole field. With higher damping, $\varepsilon^2 = 10^4$, the equatorial dipoles achieve a .98 fit and the polar dipoles but a .94 fit. These solutions, Figures 2.10 and 2.11, are of course smoother, but at the expense of the fit, particularly for the polar dipoles. Thus, these figures convey a message similar to those of the rougher solutions.

While these inversions suggest that electrical currents in the equatorial zone may give rise to the anomalous m = 1 non-dipole field at the Earth's surface, they by no means constitute a proof. With damping $\varepsilon^2 < 10^4$, the fits are well over 90% for either equatorial or polar sources, but we prefer equatorial sources because of the slightly better fit and smoother solution. We have parameterized the currents sources with an assigned distribution of ideal dipoles; this parameterization is by no means unique, nor are the locations of the dipoles. Moreover, there is almost certainly a trade-off between the amplitudes of dipoles at different depths. Nevertheless, we believe that these inversions do support the notion that electrical currents in the equatorial zone are responsible for the anomaly in the X component of the surface magnetic field, Figure 2.7.

Figure 2.12 is a contour map of the radial (Z) component of the magnetic secular variation at the Earth's surface, also produced from the 1980 IGRF coefficients (Peddie, 1982). The geometry of this map is similar to that of Figure 2.7, in that the largest secular variation is present at low latitudes and at two azimuths. Interestingly, the azimuths of the largest anomalies in X and $\partial Z/\partial t$ are the same as for the apparent preferred VGP paths: the Americas and eastern Asia. Given the uncertainty in the VGP paths, we cannot be sure of the reliability of the correlation. However, the correlation between the main field and the secular variation is also suggestive of persistent high activity in those regions, which is perhaps evidence for long-period control by the mantle. Until we better understand the

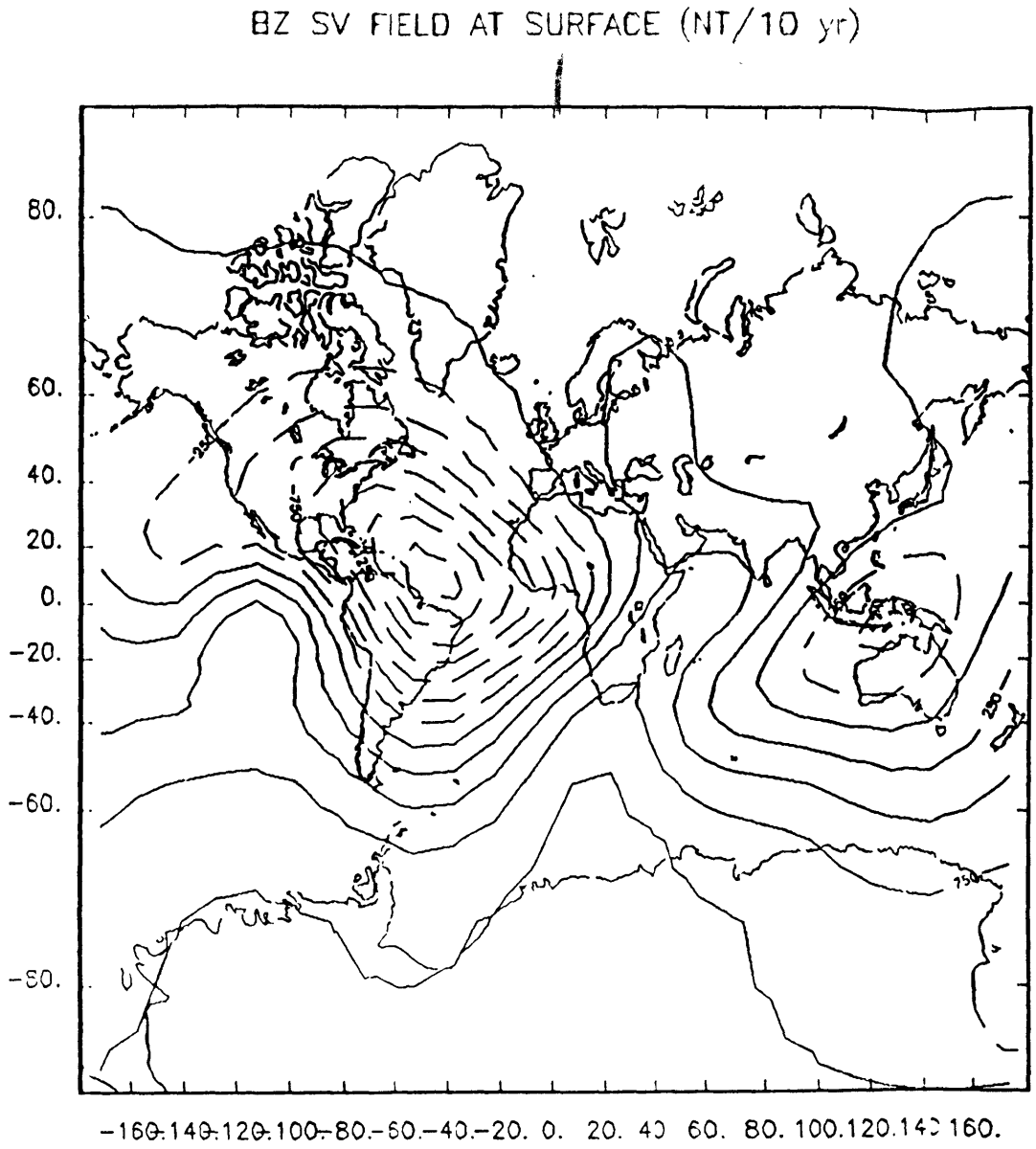

Figure 2.12 Map of the radial (Z) component of the magnetic secular variation at the Earth's surface for 1980 produced from the IGRF Gauss coefficients up to degree and order 8 (Peddie, 1982). The contour interval is 250 nT / 10 yr. The geometry of the map is similar to Figure 2.7.

steady, or mean, motions that can occur in an electrically conducting, rotating fluid shell, we cannot offer a specific explanation for this persistent activity. Thus, for instance, using the method of Chapter 3, we will find in Chapter 4 that cold mantle does not necessarily induce downwelling core flow. Although the observational evidence for stationary magnetic fields and persistent core flow remains somewhat under debate, we believe it is important to improve our scant understanding of free and forced steady motions.

References

Backus, G.E., "Bayesian inference in geomagnetism", *Geophys. J.* **92**, 125-142 (1988).

Barraclough, D.R., Harwood, J.M., Leaton, B.R., and Malin, S.R.C., "A definitive model for the geomagnetic field and its secular variation for 1965 - I. Derviation of model and comparison with IGRF", *Geophys. J. R. Astron. Soc.* **55**, 111-121 (1978).

Bloxham, J., "Models of the magnetic field at the core-mantle boundary for 1715, 1777, and 1842", *J. Geophys. Res.* **91**, 13,954-13,966 (1986).

Bloxham, J., and Gubbins, D., "The secular variation of Earth's magnetic field", *Nature* **317**, 777-781 (1985).

Bloxham, J., and Gubbins, D., "Thermal core-mantle interactions", *Nature* **325**, 511-513 (1987).

Busse, F.H., "Thermal instabilities in rapidly rotating systems", *J. Fluid Mech.* **44**, 441-460 (1970).

Clement, B.M., "Geographical distribution of transitional VGP's: evidence for non-zonal equatorial symmetry during the Matuyama-Brunhes geomagnetic reversal", *Earth Planet. Sci. Lett.* **104**, 48-58 (1991).

Clement, B.M., and Kent, D.V., "A southern hemisphere record of the Matuyama-Brunhes polarity reversal", *Geophys. Res. Lett.* **18**, 81-84 (1991).

Creager, K.C., and Jordan, T.H., "Aspherical structure of the core-mantle boundary from PKP travel times", *Geophys. Res. Lett.* **13**, 1497-1500 (1986).

Dziewonski, A.M., "Mapping in the lower mantle: determination of lateral heterogeneity in P velocity up to degree and order 6", *J. Geophys. Res.* **89**, 5929-5952 (1984).

Greenspan, H.P., *The Theory of Rotating Fluids*, Cambridge University Press (1968).

Gubbins, D., "Geomagnetic field analysis - I. Stochastic inversion", *Geophys. J. R. Astron. Soc.* **73**, 641-652 (1983).

Gubbins, D., "Implications of geomagnetism for mantle structure", *Phil. Trans. Roy. Soc. London A***328**, 365-375 (1989).

Gubbins, D., and Bloxham, J., "Geomagnetic field analysis - III. Magnetic fields on the core-mantle boundary", *Geophys. J. R. Astron. Soc.* **80**, 695-713 (1985).

Gubbins, D., and Bloxham, J., "Morphology of the geomagnetic field and implications for the geodynamo", *Nature* **325**, 509-511 (1987).

Gudmundsson, O., and Clayton, R.W., "A 2-D synthetic study of global traveltime tomography", *Geophys. J. Int.* **106**, 53-65 (1991).

Gudmundsson, O., and Clayton, R.W., "Some problems in mapping core-mantle boundary structure", *J. Geophys. Res., in press* (1992).

Hager, B.H., Clayton, R.W., Richards, M.A., Comer, R.P., Dziewonski, A.M., "Lower mantle heterogeneity, dynamic topography and the geoid", *Nature* **313**, 541-545 (1985).

Hager, B.H., and Richards, M.A., "Long-wavelength variations in Earth's geoid: physical models and dynamical implications", *Phil. Trans. Roy. Soc. London A* **328**, 309-327 (1989).

Hide, R., Clayton, R.W., Hager, B.H., Spieth, M.A., and Voorhies, C.V., "Topographic core-mantle coupling and fluctuations in the Earth's rotation", *IUGG Jeffreys Symposium Volume, submitted* (1992).

Hutcheson, K.A., and Gubbins, D., "Earth's magnetic field in the seventeenth century", *J. Geophys. Res.* **95**, 10,769-10,781 (1990).

Jackson, J.D., *Classical Electrodynamics*, Wiley (1962).

King, S.D., and Hager, B.H., "Coupling of mantle temperature anomalies and the flow pattern in the core: interpretation based on simple convection calculations", *Phys. Earth Planet. Inter.* **58**, 118-125 (1989).

Laj, C., Mazaud, A., Weeks, R., Fuller, M., and Bervera, E.H., "Geomagnetic reversal paths", *Nature* **351**, 447 (1991).

Merrill, R.T., and McElhinny, M.W., *The Earth's Magnetic Field*, Academic Press (1983).

Morelli, A., and Dziewonski, A.M., "Topography of the core-mantle boundary and lateral homogeneity of the liquid core", *Nature* **325**, 678-683 (1987).

Peddie, N.W., "International Geomagnetic Reference Field: the third generation", *J. Geomag. Geoelectr.* **34**, 309-326 (1982).

Roberts, P.H., "On the thermal instability of a rotating fluid sphere containing heat sources", *Phil. Trans. Roy. Soc. London A***263**, 93-117 (1968).

Shure, L., Parker, R.L., and Backus, G.E., "Harmonic splines for geomagnetic modelling", *Phys. Earth Planet. Inter.* **28**, 215-229 (1982).

Tric, E., Laj, C., Jehanno, C., Valet, J.P., Kissel, K., Mazaud, A., and Iaccarino, S., "High-resolution record of the Upper Olduvai transition from Po Valley (Italy) sediments: support for dipolar transition geometry?", *Phys. Earth Planet. Inter.* **65**, 319-336 (1991).

Valet, J.P., Tucholka, P., Courtillot, V., and Meynadier, L., "Paleomagnetic constraints on the geometry of the geomagnetic field during reversals", *Nature* **356**, 400-407 (1992).

Zhang, K.K., "Convection in a rapidly rotating spherical shell at infinite Prandtl number: steadily drifting rolls", *Phys. Earth Planet. Inter.* **68**, 156-169 (1991).

Zhang, K.K., and Gubbins, D., "On convection in the Earth's core driven by lateral temperature variations in the lower mantle", *Geophys. J. Int.* **108**, 247-255 (1992).

Chapter 3

Rotating Magnetoconvection: Development of a Numerical Technique to Find Steady Solutions

3.1 Introduction

As witnessed by aperiodic reversals of the dipole field as well as the short-period magnetic secular variation, convection and magnetic field generation in the Earth's core are clearly time-dependent. Nevertheless, we have noted in Chapter 2 that certain features of the magnetic field, and hence certain fluid motions in the core, may remain relatively stationary, or at least exhibit a mean, for much longer than the presumed core convective timescale of a few thousand years. In this chapter and the next, we therefore develop and employ a numerical method to study steady, rotating magnetoconvection. After a brief review of prior work on rotating magnetoconvection, we introduce our method and demonstrate its viability for studying non-rotating, non-magnetic free convection in a spherical shell. We next apply the method to study free convection in rotating systems, both non-magnetic and magnetic, in order to compare our solutions with those from previous work. We then study forced convection, for which very little prior work can guide us, but which may be of some interest if core-mantle thermal coupling is important.

The governing equations for the unknown velocity field $\mathbf{v}$, pressure p, density deficit c, and magnetic field $\mathbf{B}$ are (1.5) - (1.8). We will non-dimensionalize them by setting $\nabla=\nabla^*/L$, $t=t^*L^2/\kappa$, $v=v^*\kappa/L$, $p=p^*\kappa\nu/L^2$, $c=c^*(\Delta\rho/\rho)$, $\mathbf{B}=\mathbf{B}^*B(\mu_o\rho)^{1/2}$, $\mathbf{g}=g\hat{\mathbf{g}}$, and $\Omega=\Omega\hat{\Omega}$, where L is the characteristic length scale of the system, κ is the thermal or chemical diffusivity, $(\Delta\rho/\rho)$ is the magnitude of the density deficit from a mean density ρ, B is the magnitude of the magnetic field, μ_o is the magnetic permeability of free space, g is the magnitude of the gravity vector, Ω is the magnitude of the rotation vector, and $\hat{\mathbf{g}}$ and $\hat{\Omega}$ are unit vectors. Inserting these into (1.5) - (1.8) and dropping the *'s, we obtain

$$\frac{\partial \mathbf{B}}{\partial t} = q^{-1}\nabla^2\mathbf{B} + \nabla \times (\mathbf{v}\times\mathbf{B}), \tag{3.1}$$

$$Pr^{-1}\left\{\frac{\partial \mathbf{v}}{\partial t} + (\mathbf{v}\cdot\nabla)\mathbf{v}\right\} =$$

$$-\nabla p + \nabla^2\mathbf{v} - Ta^{1/2}\,\hat{\Omega}\times\mathbf{v} + Ra\, c\hat{\mathbf{g}} + \frac{Ta^{1/2}\,El}{q}(\nabla\times\mathbf{B})\times\mathbf{B}, \tag{3.2}$$

$$\nabla\cdot\mathbf{v} = 0, \text{ and} \tag{3.3}$$

$$\frac{\partial c}{\partial t} + (\mathbf{v}\cdot\nabla)c = \nabla^2 c, \tag{3.4}$$

where we have dropped the source term from (3.4). The non-dimensional numbers in (3.1) - (3.4) are the Prandtl number

$$Pr=\nu/\kappa, \tag{3.5}$$

the magnetic Prandtl number

$$q=\kappa/\chi, \tag{3.6}$$

the Rayleigh number

$$Ra=(\Delta\rho/\rho)gL^3/(\nu\kappa), \tag{3.7}$$

the Taylor number

$$Ta=4\Omega^2L^4/\nu^2, \tag{3.8}$$

and the Elsasser number

$$El=B^2/2\Omega\chi, \tag{3.9}$$

where ν is the fluid viscosity and $\chi=1/\mu_o\sigma$ is the magnetic diffusivity, with σ the electrical conductivity. The Rayleigh number is a measure of buoyancy to dissipative forces, the Taylor number a measure of the Coriolis force to viscous force, and the Elsasser number a measure of the Lorentz force to the Coriolis force. Table 1.1 contains estimates for various core parameters and non-dimensional numbers.

3.2 Early work on rotating mangetoconvection

Before we begin our search for steady solutions to (3.1) - (3.4) for various parameter ranges of (3.5) - (3.9), we will review prior work on rotating magnetoconvection. We begin with the classic treatise by Chandrasekhar (1961), who studied the linear stability of a variety of hydrodynamic and hydromagnetic systems. The first problem considered by Chandrasekhar that is of particular interest to us is his analysis of the stability of thermal conduction between two horizontal planes each in the (x,y) plane, with vertical gravity $\hat{\mathbf{g}} = -\hat{\mathbf{z}}$, rotation $\hat{\Omega} = \hat{\mathbf{z}}$, and impressed magnetic field $\mathbf{B} = \hat{\mathbf{z}}$. The system is heated from below, with the lower and upper planes held fixed at given temperatures. The non-dimensional number that characterizes the strength of the heating is the Rayleigh number, $Ra = (g\alpha\beta L^4)/(\kappa\nu)$, where $\alpha\beta L$ replaces $\Delta\rho/\rho$. For this problem L is the distance between the parallel planes, α is the coefficient of thermal expansion, and β is the uniform temperature gradient between the planes. As one increases the heating from below, β, and hence Ra, rises, and the fluid becomes increasingly gravitationally unstable. At the critical Rayleigh number, Ra_c, the conductive (diffusive) solution is no longer stable, and the fluid begins to convect.

The approach that Chandrasekhar developed to find Ra_c and the infinitesimal fluid motions that develop at Ra_c for a variety of fluid boundary conditions is to assume the conductive solution and linearize (3.4) by assuming $\nabla c = -\hat{\mathbf{z}}$ ($-\beta\hat{\mathbf{z}}$ in dimensional terms). All variables are then perturbations, which must satisfy

$$\frac{\partial \mathbf{B}}{\partial t} = q^{-1}\nabla^2\mathbf{B} + \nabla \times (\mathbf{v}\times\hat{\mathbf{z}}), \tag{3.10}$$

$$Pr^{-1}\frac{\partial \mathbf{v}}{\partial t} = - \nabla p + \nabla^2\mathbf{v} - Ta^{1/2}\,\hat{\mathbf{z}}\times\mathbf{v} + Ra\, c\hat{\mathbf{z}} + \frac{Ta^{1/2}\,El}{q}(\nabla\times\mathbf{B})\times\hat{\mathbf{z}}, \tag{3.11}$$

$$\nabla\cdot\mathbf{v} = 0, \text{ and} \tag{3.12}$$

$$\frac{\partial c}{\partial t} = w + \nabla^2 c, \tag{3.13}$$

where w is the velocity in the z-direction. Assuming normal mode solutions of the form exp i ($k_x x + k_y y + \omega t$), where (k_x,k_y) are the horizontal wavenumbers, and ω are the eigenfrequencies, Ra_c is that Ra at which there exists an $Im(\omega) < 0$, indicating positive growth rate. If $Re(\omega) = 0$ at Ra_c, one says 'the principle of the exchange of stabilities' is valid and the convection is stationary, else the convection sets in as overstability. The eigenfunction f(z) associated with this eigenfrequency gives the geometry of the solution at Ra_c but, being a linear analysis, no information on its amplitude.

When Ta and El are zero, Ra_c is independent of Pr (and obviously of q), and the convection is stationary at Ra_c. When El is zero, but Ta non-zero, the situation is more complicated. For Pr > O(1), the convection at Ra_c is also stationary, with Ra_c proportional to $Ta^{2/3}$ and $\mathbf{k}_c$ proportional to $Ta^{1/6}$ in the asymptotic limit that $Ta \rightarrow \infty$, where $\mathbf{k}_c$ is the horizontal wavevector of the convective cell patterns at Ra_c. When Pr < O(1), convection commences as overstability, provided Ta is large enough. The same asymptotic dependencies on Ta hold. Already for the plane layer, the complexity of the subject is becoming apparent. It is perhaps appropriate here to point out that we do not know the value of Pr in the Earth's core. Its molecular value is typically presumed to be much greater than one, but then, its eddy (turbulent) value is typically presumed to be order one (Zhang, 1991a).

To understand the dependence of Ra_c and $\mathbf{k}_c$ on Ta, we introduce the Taylor-Proudman theorem (Proudman, 1916, Taylor, 1921), central to the theory of rotating fluids. Consider (3.11) in the absence of inertial, viscous, buoyancy, and Lorentz forces. This yields the geostrophic balance,

$$-\nabla p = Ta^{1/2}\, \hat{\mathbf{z}} \times \mathbf{v}. \tag{3.14}$$

If we now take the curl of this equation, we obtain the Taylor-Proudman theorem, $\partial v/\partial z = 0$, so that the fluid has a tendency to move in columns, independent of the coordinate parallel to the rotation axis. To the extent that other forces are present, it is possible to break the strength of the theorem. We can now understand why Ra_c increases with increasing Ta: convective motions in a horizontal plane layer with vertical gravity and rotation must necessarily have a z-dependence so that to overcome rotation the fluid requires more buoyancy to commence convection. Similarly, the convective cells tend to become aligned with the z-axis in the interior of the fluid, bending only in the viscous (Ekman) boundary layers near the horizontal surfaces. This alignment results in a smaller horizontal wavelength with increasing rotation rate.

Similarly, in the absence of other forces, motion in the presence of a uniform magnetic field $\mathbf{B} = \hat{\mathbf{z}}$ also tends towards two-dimensionality, independent of the z-coordinate. Thus, in the limit that the Chandrasekhar number $Q = B^2L^2/(\nu\chi) \rightarrow \infty$, Ra_c is proportional to Q and $\mathbf{k}_c$ is proportional to $Q^{1/6}$, and the convective cells become elongated in the z-direction. For the magnetic Prandtl number $q < O(1)$, stationary convection commences at Ra_c, and for $q > O(1)$, overstability occurs provided Q is large enough. The molecular value of q in the Earth's core is probably much less than one, though again, there is the question of its eddy value (Fearn, 1979, Zhang, 1991a). Chandrasekhar (1961) also showed that if the impressed magnetic field **B** is inclined to the vertical, the isotropy of the two horizontal directions is lost, and convection commences most easily as longitudinal rolls in the direction of the horizontal component of **B**. Such rolls do not need to vary along the component of **B** that they are aligned with, and so they exhibit the minimum Ra_c. A similar effect occurs if Ω and **g** are not collinear.

Although acting separately rotation $\Omega\hat{\mathbf{z}}$ and an impressed magnetic field $B\hat{\mathbf{z}}$ each inhibit convection in a horizontal plane layer with gravity $-g\hat{\mathbf{z}}$, together they can actually promote it. To understand this, consider that by decreasing the Taylor number, increasing viscosity facilitates convection in a rotating fluid, and impressing a magnetic field on an

electrically conducting fluid is in some sense giving the fluid additional viscosity. The critical Rayleigh number Ra_c is a complicated function of Pr, q, Ta, and El (or Q), and the convection at Ra_c can be either stationary or overstable depending on the parameter values. The general pattern, however, is that for a given Ta, as Q increases from zero, Ra_c and $\mathbf{k}_c$ decrease until a minimum is reached, and then they begin to increase with further increase in Q. Not surprisingly, the minimum Ra_c and $\mathbf{k}_c$ occur when the Coriolis and Lorentz forces are comparable, or El = O(1).

Chandrasekhar (1961) next considered the linear stability of the thermal conduction solution in non-rotating, non-magnetic, internally heated fluid spheres and shells, primarily with constant radial gravity and basic state temperature gradients. He found the critical Rayleigh number for stationary convection as a function of spherical harmonic order ℓ for various fluid boundary conditions. He then examined the stability of a fluid sphere rotating about the z-axis, finding that Ra_c increases with increasing Ta, in analogy with the horizontal plane layer. Roberts (1965) showed that for this problem, Ra_c is proportional to $Ta^{2/3}$, as for the plane layer. However, these studies considered only convection symmetric about the rotation axis.

3.3 Recent developments in rotating magnetoconvection

Roberts (1968) realized that non-axisymmetric convection in a rotating fluid sphere might have a lower Ra_c than axisymmetric convection because non-axisymmetric convection could arrange itself in rolls (columns) parallel to the rotation axis, thereby not requiring that the buoyancy force break the constraint of the Taylor-Proudman theorem. Were it not for the spherical boundaries, such columnar convection could commence at the lower Rayleigh number associated with that of a non-rotating fluid. However, such columns must necessarily intersect the spherical boundaries, so that their effectiveness in transporting buoyancy is somewhat limited, as we shall later see. The tendency for rotation

to eliminate z-dependence and the strong z-dependence of the spherical boundaries conspire to limit the length scale of the rolls so that the azimuthal wave number m increases with $Ta^{1/6}$ and Ra_c with $Ta^{2/3}$ (though with a lower constant of proportionality than for the axisymmetric modes).

Busse (1970) re-examined the problem of convection in a rotating sphere and found that solutions with a different symmetry with respect to the equatorial plane had a lower Ra_c than Robert's solutions. Figure 3.1 is a sketch of the convective motions that occur in an internally heated, rotating sphere at Ra_c in the Roberts-Busse theory. The pattern of columns occurs not as stationary convection, but drifts eastwards as a Rossby wave (Busse, 1970, Gill, 1982). To understand this, consider Figure 3.2, in which a filament of fluid moves outwards from the rotation axis. As it does so, it acquires an anticyclonic vorticity relative to the ambient fluid in order to conserve potential vorticity. A nearby filament moving inwards acquires cylconic vorticity, and the motion that this pattern of vorticity induces causes a net eastward propagation of the pattern. Busse (1970) also observed that the non-linear interaction of Rossby waves can give rise to a mean azimuthal flow in the form of differential rotation.

Busse and Cuong (1977) studied convection in a spherical shell of inner radius η and outer radius 1. They noted the qualitative difference between convection in the region with cylindrical radius $s < \eta$ and that for $\eta < s < 1$ (Figure 3.3). In the former region, the rotation and gravity vectors tend to be parallel, so that the polar modes resemble convection in Chandrasekhar's (1961) horizontal plane layer rotating about a vertical axis with vertical gravity. In the latter region, the two vectors are nearly perpendicular, so that the equatorial modes resemble the columnar convection of Roberts (1968). The minimum Ra_c at all Prandtl numbers occurs for the equatorial modes, which Busse (1975) argued would arrange themselves in columns around the cylinder tangent to the inner core.

Gilman (1975) performed extensive linear numerical calculations on convection in a rotating spherical shell of inner radius $\eta = .8$ at $Pr = 1$ and Ta between 0 and 10^6. His

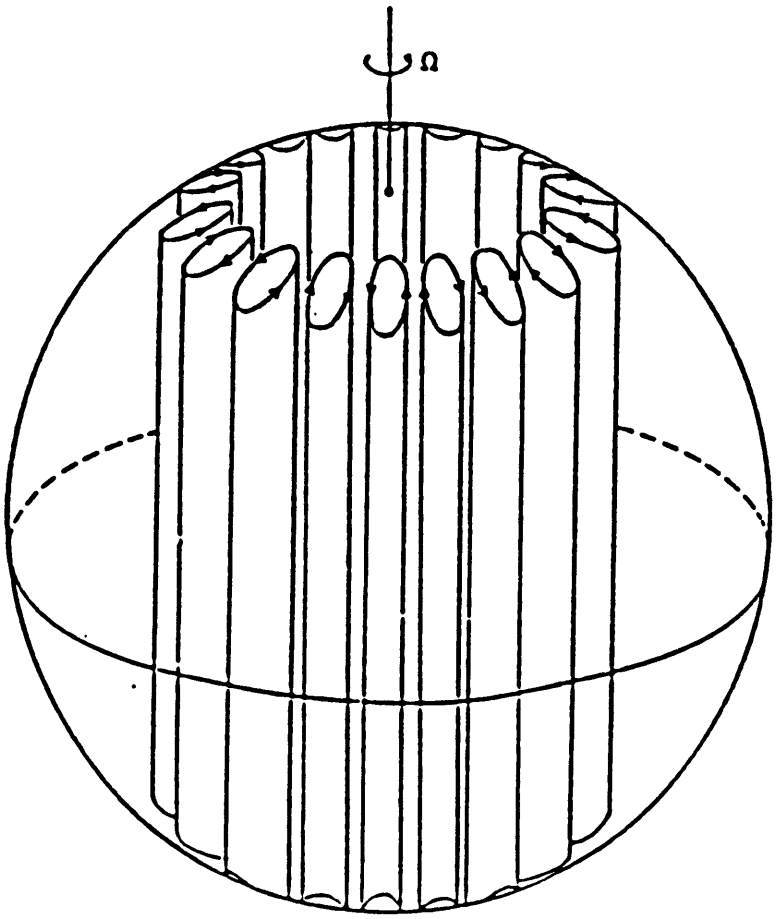

Figure 3.1 A sketch of the convective motions that occur at Ra_c in a rotating sphere with constant radial buoyancy gradient (from Busse, 1970).

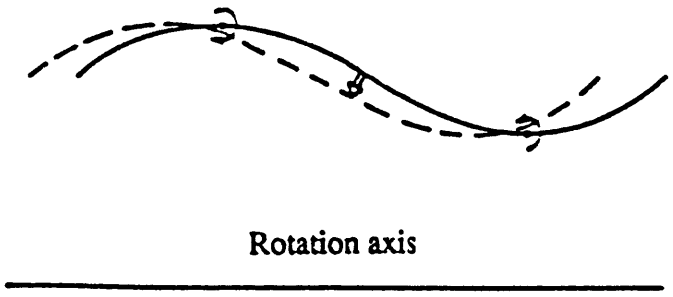

Figure 3.2 The mechanism for the eastward propagation of Rossby waves in a thick shell such as the Earth's core (adapted from Gill, 1982). A filament of fluid moving towards the rotation axis (on the right) experiences vortex stretching, and thus acquires cyclonic relative vorticity in order to conserve potential vorticity. The filament on the left, moving away from the rotation axis, conversely acquires anticyclonic relative vorticity. This pattern of relative vorticity causes the wave to propagate eastwardly, as indicated by the broad arrow. The Rossby wave mechanism is responsible for the azimuthal drift of the convective columns at Ra_c pictured in Figure 3.1.

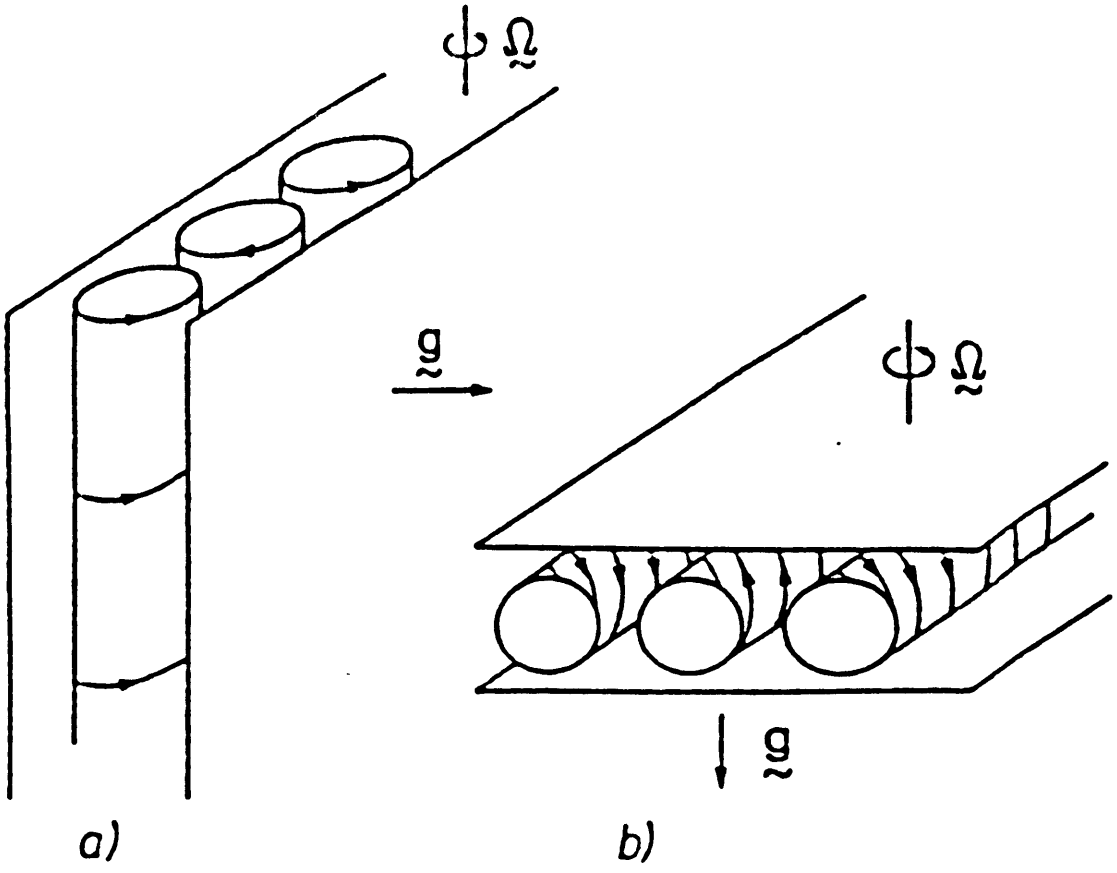

Figure 3.3 (from Busse and Cuong, 1977)

a) Convection in a layer with gravity and rotation perpendicular, as at the equator. In order not to violate the Taylor-Proudman theorem, the convective columns arrange themselves aligned parallel with the rotation axis. In the absence of spherical boundaries this columnar convection has the same critical Rayleigh number Ra_c as non-rotating convection.

b) Convection in a layer with gravity and rotation parallel, as at the poles. Convection must necessarily break the Taylor-Proudman theorem, thereby inhibiting convection and raising Ra_c. There is no preferred horizontal direction for the convective rolls.

calculations confirmed the analytical predictions that solutions with high azimuthal wave number m (up to m = 24) are most unstable in the equatorial zone and those with lower m are most unstable in the polar zone, with a mid-latitude gap. The calculations confirm that the equatorially symmetric equatorial modes are overall the most unstable, with Ra_c proportional to $Ta^{2/3}$, the critical azimuthal wavenumber m_c to $Ta^{1/6}$, and an eastward drift frequency at critical ω_c to $Ta^{1/3}$. Gilman (1977) extended the numerical calculations at $Ta = 10^5$ to include non-linear effects. The finite-amplitude solutions show that as Ra rises above the overall Ra_c, the peak in the kinetic energy spectrum shifts from m near m_c to lower m, with a second peak at m = 0. The shift towards lower m represents the increasing importance of the polar modes so that convection begins to fill the sphere, though the tendency for a mid-latitude gap remains even for finite-amplitude convection. The peak at m = 0 represents the differential rotation.

It is impossible under terrestrial laboratory conditions to simulate a radial buoyancy force in a sphere or spherical shell (though see Hart *et al.*, 1986). However, the centrifugal force of a rotating fluid can simulate the component of the gravitational force perpendicular to the rotation axis, the s-component, with a change in sign. By switching the basic state temperature gradient within the fluid, one can simulate convection in a rotating fluid sphere or spherical shell, at least to the extent that the component of the gravitational force parallel to the rotation axis, the z-component, is dynamically unimportant. At least near Ra_c, this appears to be true. Using such a set-up, Busse and Carrigan (1976), Carrigan and Busse (1983), Chamberlain and Carrigan (1986), and Cardin and Olson (1992) confirmed the existence of columnar convection near Ra_c. (In addition, the conduction solution for this geometry presumably induces fluid motion for subcritical Rayleigh numbers, but none of these authors discuss this.)

Working with Taylor numbers in the range of 10^{11} and Pr = 7, Cardin and Olson (1992) found experimentally that at Rayleigh numbers even a few times critical, the pattern of steadily drifting, periodic columns degenerates into chaotic, time-dependent convection,

though the tendency towards z-independence remains. Their numerical calculations for Ta between 10^6 and 2.5 x 10^9 and Pr = 7, again using cylindrical gravity, confirmed that as Ra rises above Ra_c convection becomes aperiodically time-dependent and chaotic in planes perpendicular to the rotation axis. The columnar structure in the direction parallel to the rotation axis remains, however. Using a power law fit (Ra_c proportional to $Ta^{3/5}$) to their numerical results, they extrapolated Ra_c to the large Taylor number appropriate to the Earth's core (Ta = 10^{28}, see Table 1.1), well beyond what they could model numerically. This Ra_c, approximately 10^{18}, is ten orders of magnitude less than the Rayleigh number they presume in the core (Table 1.1), so that they conclude that the core convects in the chaotic manner so described. To obtain the larger, more steady features observed in the surface magnetic field, they suggest that either Lorentz forces or mean-field effects, such as the mean azimuthal flow, play a role.

Busse (1975, 1977) constructed a dynamo based on columnar convective motions. He argued that the Lorentz force in the Earth's core is not of primary importance, so that the basic state force balance is geostrophic. Treating the Lorentz force as a perturbation of the geostrophic balance, Busse showed that the toroidal magnetic field is of the same order of magnitude as the poloidal field, thereby justifying the original assumption of a geostrophic balance. Because the toroidal field remains of the same order of magnitude as the poloidal field, Busse's dynamo is a weak-field model. The convective motions of Figure 3.1 provide a means to generate the toroidal magnetic field. Associated with each convecting column is a flow in the z-direction induced by the Ekman pumping (Greenspan, 1968) that occurs at the intersection of the columns with the spherical surface. The direction of the Ekman flow within each column depends upon the sense in which the column is convecting. This poloidal motion provides the helicity (Moffatt, 1978) necessary to generate the poloidal magnetic field and complete the dynamo cycle.

Weak-field dynamos may be intuitively satisfying and analytically tractable, but they may not be geophysically plausible (Roberts, 1988). Although small magnetic field

strengths characterize weak-field dynamos, so do small length scales. These small length scales result in high electric currents that increase the Ohmic dissipation, which has led to the oft-quoted comment that 'if the Earth operated a weak-field dynamo, one could stand a kettle of water anywhere on the Earth's surface and have it boil in three minutes'. Soward (1979) showed that at all but very small (ungeophysical) magnetic field strengths, the weak-field dynamo is unstable and the system prefers a strong magnetic field in which the Lorentz force enters into the basic state force balance. This magnetostrophic state prefers large length scales and hence the Ohmic dissipation for the strong-field dynamo is less than that for the weak-field dynamo. Eventually, of course, the back reaction of the Lorentz force will limit the ultimate strength of the magnetic field (Malkus and Proctor, 1975).

Braginsky (1964, 1967, 1980) suggested that magnetic-Archimedean-Coriolis (MAC) waves might be responsible for the generation of the main magnetic field. These asymmetric MAC waves, riding on an axisymmetric basic state, would both break the force of Cowling's theorem and supply the α-effect necessary to maintain the poloidal magnetic field. In this view, the Lorentz force is of primary importance in the force balance, and the Earth operates a strong-field dynamo. A new class of instabilities are possible due to the presence of a dynamically important magnetic field. Hide (1966) considered diffusionless MC waves as a possible mechanism for the westward drift. Acheson (1972, 1973) studied the effects of the variation with cylindrical radius s of basic differential rotation (shear), toroidal magnetic field, and buoyancy on ideal (non-diffusive) MAC instabilities. Fearn (1983, 1984, 1985) confirmed the results of Acheson's local analysis numerically in an infinite annulus and Fearn and Weiglhofer (1991) confirmed the results in a sphere.

Acheson (1972, 1973) found that a basic state toroidal magnetic field can destabilize a fluid via the ideal field-gradient instability, provided B(s) increases faster than $s^{3/2}$, where the basic state toroidal magnetic field $\mathbf{B} = B(s)\hat{\phi}$, and $\hat{\phi}$ is the unit vector in the eastward direction. Typically these linear instabilities take the form of westwardly propagating waves, and a fluid shear can stabilize them. In addition to ideal instabilities, Roberts and

Loper (1979) investigated resistive instabilites that require finite electrical conductivity for their existence. Much as increasing fluid viscosity facilitates ordinary convection in a rotating fluid, the presence of Ohmic dissipation can actually lower the strength or functional increase with s of the basic state magnetic field (from which the energy derives) necessary for instability. Fearn (1984) found that in the limit of small magnetic diffusivity, resistive instabilities concentrate in the critical layer near a requisite zero in B(s). Resistive instabilities can propagate either eastwardly or westwardly, and shear has less effect. The buoyancy-catalyzed instability (Roberts and Loper, 1979) requires stratification (either stable or unstable!) and diffusion to break the rotational contraint and release the magnetic energy.

A different mechanism for instability, and possible explanation for magnetic secular variations with 60 year periods, was suggested by Braginsky (1970, 1984). This mechanism is that of torsional oscillations, which result when the magnetic extension of the Taylor-Proudman theorem, Taylor's condition (Taylor, 1963), is not satisfied. Taylor's condition requires that in the absence of diffusion and time-dependence, the ϕ-component of the Lorentz force integrated over a coaxial cylinder C(s) must vanish. When this force does not vanish, torsional oscillations occur through the action of the poloidal magnetic field weaving its way across different fluid cylinders. This imparts a certain rigidity to each fluid cylinder. In the model-Z dynamo (Bragisnky and Roberts, 1987), the field lines are primarily aligned with the z-axis, so that large geostrophic flows $\mathbf{v}_g = v_g(s)\hat{\phi}$ are possible without violating Taylor's condition. To the extent that it is violated, one expects torsional oscillations (and diffusive effects). Clearly, rotating, electrically conducting fluids allow a wealth of instabilites that may (or may not) play a role in generating the main magnetic field and its secular variation.

However, in this section we are ultimately interested in the instabilities driven not by an unstable magnetic field gradient, but by an unstable buoyancy gradient, as for Chandrasekhar's (1961) rotating plane layer permeated by a uniform magnetic field.

Unfortunately, unlike Busse's models, rotating magnetoconvection and strong-field dynamos in spherical geometry are not amenable to analytical progress because one can no longer treat the magnetic field as a perturbation. Eltayeb and Kumar (1977) numerically studied linear magnetoconvection in a rotating sphere permeated by a toroidal field $\mathbf{B} = s\hat{\phi}$. For small values of the Elsasser number El they found that critical convection takes the form of drifting rolls as Roberts (1968) and Busse (1970) predicted. As for the plane layer, the magnetic field facilitates convection so that the critical Rayleigh number Ra_c reaches a minimum for an Elsasser number El = O(1). The magnetic field increases the length scale of the convection, which now fills the sphere, but unlike for the plane layer, the spherical boundary causes overstability for all investigated values of the Prandtl number Pr and magnetic Prandtl number q. For q = O(1), as El exceeds O(1), the instability takes on the form of a diffusionless MAC wave.

Fearn (1979) found similar results for $q << 1$, as may be geophysically more realistic, except that as El exceeds O(1), the most unstable mode does not resemble a MAC wave in that it is eastwardly propagating. This 'exceptional' mode requires stable stratification and derives its energy from the basic state magnetic field. Fearn and Proctor (1983a, 1983b) studied the effects of differential rotation on modes driven by an unstable buoyancy gradient. They found that increasing shear, as measured by the magnetic Reynolds number $R_m = VL/\chi$, where V is a characteristic speed and L a length scale such as the core radius, increases Ra_c. For small q, as R_m rises above O(q), the differential rotation localizes the buoyancy perturbation at a critical point and at that critical point the phase speed of the instability approaches the fluid velocity. They suggest that the magnetic secular variation could represent a combination of the fluid motion and the phase speed of the wave relative to the fluid, particularly if a critical point exists near the outer core surface. Drew (1991) found that the addition of an inner core with radius η has little effect on Ra_c until η nears .5. In order to simulate compositional convection he employed a basic

state temperature gradient that is largest near the inner core, which he found increases the efficiency of convection over a uniform gradient.

Zhang and Busse (1987, 1988, 1990) and Zhang (1991a,b) studied the linear and non-linear development of rotating convection in a spherical shell of inner radius $\eta = .4$ for $Ta < 10^{12}$ and $(Ra-Ra_c)/Ra_c < 2$. They used a Galerkin method based on that of Cuong and Busse (1981) that allows for an azimuthal drift of the solution, so that the finite-amplitude solutions are stationary in the drifting reference frame. They found that for $Pr < O(1)$, the curve describing Ra_c as a function of Ta shows some unusual bends, which is apparently due to the most unstable mode switching from columnar convection to one more concentrated near the equator (Zhang and Busse, 1987, 1988). The columnar equatorial modes that occur for $Pr = O(1)$ near Ra_c spiral from mid-latitude to equator in the prograde direction (Zhang, 1991a). At $Pr = 7$, Cardin and Olson (1992) observed this experimentally. Zhang (1991a) noticed, as did Gilman (1977), that as the non-linearity increases the kinetic energy spectrum of the system shifts towards lower azimuthal wavenumbers. As Pr increases, the columnar modes at Ra_c exhibit less spiralling (Zhang, 1991a,b) and the mean azimuthal flow generated by the non-linear advective force decreases (see Equation (3.2) of this chapter, and Zhang and Busse, 1990). For infinite Pr, as Ra rises above Ra_c, the eastward drift rate is a strongly decreasing function of Ra (even becoming westward), and the non-linear solutions shift the convection to lower latitudes, where they can more efficiently convect heat to the surface.

Note however (Figure 9 of Zhang, 1991b), that for all $Ra > Ra_c$ the heat flux is large and positive near the equator and small and negative at mid-latitudes. His interpretation of 'hot' and 'cold' columns convecting heat via the Ekman flow in the direction along columns is therefore confusing. Rather (Bloxham *et al.*, 1992), the convective columns are out of phase in azimuth with the temperature perturbations, and the primary heat transport is via the convective overturning of the columns, which produces the maximum heat flux at the equator. At Ra_c this columnar convection is inefficient in a

sphere, and for cylindrical radii between the columns and the spherical surface the heat must diffuse. For supercritical Ra, the non-linearity helps break the rotational constraint and allows more efficient convection in the equatorial zone, as Zhang deduced. The origin of the negative heat flux at mid-latitudes remains uncertain.

Cuong and Busse (1981) studied convectively driven dynamos in the same spherical shell for Pr = 1 and Ta < 10^5. Their Galerkin formulation allowed them to examine the linear stability towards hydromagnetic perturbations of the stationary finite-amplitude hydrodynamic solutions. They obtain dynamo action when the magnetic Prandtl number, which they treat as an eigenvalue (rather than the more difficult but more physically sensible velocity amplitude), reaches a critical level q_c. Zhang and Busse (1988, 1989, 1990) extended the analysis to include finite-amplitude magnetic fields and the effects of the Lorentz force on the fluid motions, for a range of Pr and Ta < 10^6. For Ta = 3 x 10^4 and azimuthal wavenumber m = 2 they found sub-critical magnetic field generation, *i.e.*, a finite-amplitude magnetic field permitted dynamo action at a Rayleigh number lower than that at the onset of dynamo action, indicating that the magnetic field is facilitating convection and magnetic field generation. On the other hand, for m = 4, the length scale is small enough at this relatively low Taylor number so that rather than releasing the rotational constraint the magnetic field competes for the available energy and subcritical dynamo action is not possible. They found magnetic field generation concentrated in high latitudes, with an increase in the strength of the polar meridional convection (Zhang and Busse, 1990).

These studies all considered instabilities driven by laterally homogeneous boundary conditions, *i.e.*, free convection. If lateral temperature differences in the lower mantle help drive core flow, we must also study forced convection, about which very little is known. The study of forced convection requires one to specify the functional form and amplitude of the laterally inhomogeneous boundary condition. Zhang and Gubbins (1992) considered steady thermal convection driven by a laterally variable temperature on the CMB, with a

neutrally or stably stratified core. As mentioned in Chapter 2, they found that rotation induces an azimuthal phase shift between the thermal boundary condition and the flow, and allows the boundary driven motion to penetrate into the shell. Stratification supresses the radial flow, but has little effect on the surface toroidal flow. Their study did not include bottom heating (the mechanism for free convection) or Lorentz forces.

3.4 A method to find steady, finite-amplitude solutions

We have given a necessarily brief review of rotating convection and magnetoconvection, as well as an even briefer introduction to instabilities that are magnetically rather than buoyantly driven. Our review has completely omitted the other route towards an understanding of the fully self-consistent hydromagnetic dynamo problem: kinematic dynamo theory. This highly mathematical subject has made great progress (Moffatt, 1978), and has guided the work of those studying rotating magnetoconvection. We have seen that in the absence of a magnetic field, buoyancy driven flow in a rotating fluid shows some very unexpected behavior. In the presence of a magnetic field, or with the possibility of magnetic field generation, the mathematical and physical subtleties can be very difficult to assimilate. Given our primitive knowledge of the conditions in our planet's interior, it is even more difficult to know what is of geophysical interest and what is of purely mathematical interest.

Most of the work on magnetoconvection has been linear, rather understandable given the analytical and numerical difficulties of the problem. Thus, most studies in the field have been eigenanalyses of the conduction solution with an imposed toroidal magnetic field, with MAC waves representing the first bifurcation. Non-linear solutions have been at Rayleigh numbers only slightly above critical. This slight supercriticality permits stationary solutions in a steadily drifting (with respect to the rotating spherical shell) reference frame. Fully time-dependent calculations are computationally prohibitive. Many of the

computational problems are a result of the high Taylor number inducing small length scales. For those trying to model dynamo processes that occur over thousands to tens of thousands of years, the short time step that small length scales require in order to avoid numerical instability is a bitter pill.

In our rather unconventional approach, we remove the explicitly time-dependent terms from (3.1) - (3.4). As discussed, the motivation for looking for time-independent solutions to the convective equations is that the data indicate that there are certain motions that are nearly time-independent on the convective timescale. By removing the necessity to time step and looking directly for stationary solutions, we make our search for finite-amplitude solutions computationally easier. The price we pay of course is that time-dependent solutions are beyond our reach, and earlier work has shown that the most unstable freely convecting solutions contain a steady drift. At Ra above Ra_c the drift rate may be lower, though for higher Ra we certainly expect aperiodic time-dependence. Nevertheless, the data indicate that there is some steadiness in the core. This may be a function of a non-linear mean-field effect, or more likely, of inhomogeneous forcing. In their study of boundary forced flows, Zhang and Gubbins (1992) found steady solutions. Before we progress to inhomogeneous forcing, however, we will study homogeneous forcing to build confidence in the method. In addition, we hope to gain some insight into axisymmetric rotating magnetoconvection, for which we will see our method can successfully model.

Throughout these calculations, we use an infinite Prandtl number. If core convection is compositionally driven, this is a reasonable approximation given the extremely low rate at which chemical inhomogeneities diffuse. On the other hand, if core convection is thermally driven, $Pr \geq O(1)$ (Table 1.1). Moreover, if one bases an estimate for Pr on turbulent values rather than molecular values, a sensible choice for the Prandtl number might be $Pr = 1$. However, given that core convection is most likely compositionally driven (Gubbins, 1977, Loper, 1978), and that the qualitative form of

rotating convection may be insensitive to Pr once Pr > O(1) (Zhang and Busse, 1990), we feel there is ample justification for studying the system at infinite Pr. Moreover, an infinite Pr removes the added difficulty of the non-linear advection term $\mathbf{v}\cdot\nabla\mathbf{v}$ from equation (3.2). The magnetic Prandtl number q in the Earth's core is most likely $O(10^{-6})$ (Table 1.1), though again, using turbulent values rather than molecular values might imply q = O(1). Fearn (1979) found that the value of q plays a key role for magnetically driven instabilities, but for buoyantly driven instabilities he obtained results for $q = 10^{-6}$ similar to those of Eltayeb and Kumar (1977) for q = 1. Thus, to further reduce the parameter space we fix q = 1 for the remainder of the calculations.

Rather than use the second order equation (3.1), we found that we could achieve greater numerical accuracy by using the first order equations on a staggered grid, which we will soon present. Of course, this results in a larger system with more unknowns to solve for. Setting $\mathrm{Pr} = \infty$, q = 1, $\partial\mathbf{B}/\partial t = \mathbf{0}$, and $\partial c/\partial t = 0$, the equations we solve are

$$\nabla\times\mathbf{B} - (\mathbf{e} + \mathbf{v}\times\mathbf{B}) = \mathbf{0}, \tag{3.15}$$

$$\nabla\cdot\mathbf{B} = 0, \tag{3.16}$$

$$\nabla\times\mathbf{e} = \mathbf{0}, \tag{3.17}$$

$$-\nabla p + \nabla^2\mathbf{v} - \mathrm{Ta}^{1/2}\,\hat{\Omega}\times\mathbf{v} + \mathrm{Ra}\,c\hat{\mathbf{g}} + \mathrm{Ta}^{1/2}\mathrm{El}\,(\nabla\times\mathbf{B})\times\mathbf{B} = \mathbf{0}, \tag{3.18}$$

$$\nabla\cdot\mathbf{v} = 0, \text{ and} \tag{3.19}$$

$$\mathbf{v}\cdot\mathbf{f} - \nabla\cdot\mathbf{f} = 0, \text{ with} \tag{3.20}$$

$$\mathbf{f} - \nabla c = \mathbf{0}. \tag{3.21}$$

For the remainder of this chapter, we will concentrate on non-magnetic, non-rotating convection to introduce our method of solution and demonstrate its viability. Thus, we will solve (3.18) - (3.21) in a spherical shell of inner radius η and outer radius 1 with El = Ta = 0 and radial gravity $\hat{\mathbf{g}} = \hat{\mathbf{r}}$. We use a spherical coordinate system (r,θ,ϕ), with

$\hat{\mathbf{r}}$ the unit vector in the radial direction, $\hat{\theta}$ the unit vector in the colatitudinal direction, and $\hat{\phi}$ the unit vector in the eastward direction.

To force non-zero solutions to the system (3.18) - (3.21) there must of course be a buoyancy source. In most studies on core convection such as those we have discussed, that source is a fixed, high value for the buoyancy deficit c at the bottom of the system and some lower value at the top. The reasons for adopting such boundary conditions on c, whether temperature or composition, are primarily historical and for comparisons with prior work. However, if the release of light material at the ICB is driving core convection, a more realistic boundary condition at $r = \eta$ might be a fixed radial buoyancy gradient $\nabla_r c = \mathbf{f}_r = 1$ (in this non-dimensionalized system). The corresponding condition at $r = 1$ should be $\mathbf{f}_r = 0$, assuming no core material leaks into the mantle.

On the other hand, if convection is thermally driven, the proper boundary condition at $r = 1$ might be a fixed (but perhaps laterally variable) $\mathbf{f}_r$, representing the heat flux into the mantle at the CMB (King and Hager, 1989). At $r = \eta$, the proper thermal boundary condition is not so evident, so that it might be a fixed c or $\mathbf{f}_r$. In any case, boundary conditions on $\mathbf{f}_r$ that have a net non-zero buoyancy flux into or out of the system must necessarily be time-dependent, as one would expect for a fluid outer core that is gradually becoming enriched in ligher elements or gradually cooling (and in either case with η growing as a function of time). Although we are not inherently concerned here with these changes that occur on a timescale much longer than the convective timescale, we must pay heed to our boundary conditions if we have any hope of finding time-independent solutions. Thus, we have chosen to use fixed boundary conditions on $\mathbf{f}_r$ to supply buoyancy to the system, but we must assign $\mathbf{f}_r$ such that the net flux across the upper and lower boundaries of the spherical shell is zero.

We first break (3.18) - (3.21) into their scalar components, with (u,w,v) the velocity $\mathbf{v}$ and (f_r,f_θ,f_ϕ) the buoyancy gradient $\mathbf{f}$. In the r-θ plane we discretize the equations using a staggered grid, which we show in Figure 3.4. Such a grid allows one to

take central differences accurately. For more details on our finite differencing, see the appendix to this chapter. In the azimuthal direction, we assume exp imϕ dependence, where the azimuthal wavenumber m is an integer. We can then remove f_ϕ = imc from our set of unknowns and the ϕ-component of (3.21) from our set of equations. Because the problem is non-linear through the term **v**·**f** in (3.20), there will be coupling between solutions of different wavenumbers m. For instance, the interaction of sin mϕ and cos mϕ solutions will produce contributions to the m = 0 and sin 2mϕ and cos 2mϕ solutions. We include the interaction terms in the equations that govern the m = 0 solution, but we do not calculate the 2m solutions, an approximation we will later examine. Thus, for each variable at each grid point we compute an m = 0, cos mϕ, and sin mϕ solution. If our grid contains N points in radius and L points in colatitude, as measured by the points at which we define the pressure (Figure 3.4), then our system contains

$$K = 3[(N-1)L+(N-1)L+N(L-1)+NL+NL+(N-1)L+N(L-1)] \qquad (3.22)$$

unknowns.

We will compute solutions only for $0 < \theta < \pi/2$, and assume a symmetry about the equator in order to make computational savings. Again, because there can be non-linear coupling between solutions of different symmetries, this is not strictly correct, but for the weakly non-linear parameter range that we will consider, the symmetry approximation should be valid. We impose the following symmetry conditions for m = 0 and all $m \geq 2$:

$$\partial u/\partial\theta = v = w = \partial p/\partial\theta = \partial c/\partial\theta = \partial f_r/\partial\theta = f_\theta = 0 \text{ at } \theta = 0, \text{ and} \qquad (3.23)$$

$$\partial u/\partial\theta = \partial v/\partial\theta = w = \partial p/\partial\theta = \partial c/\partial\theta = \partial f_r/\partial\theta = f_\theta = 0 \text{ at } \theta = \pi/2. \qquad (3.24)$$

The symmetry conditions that we have imposed across the equator through (3.24) represent dipole symmetry, as opposed to the opposite symmetry conditions at $\theta = \pi/2$, which

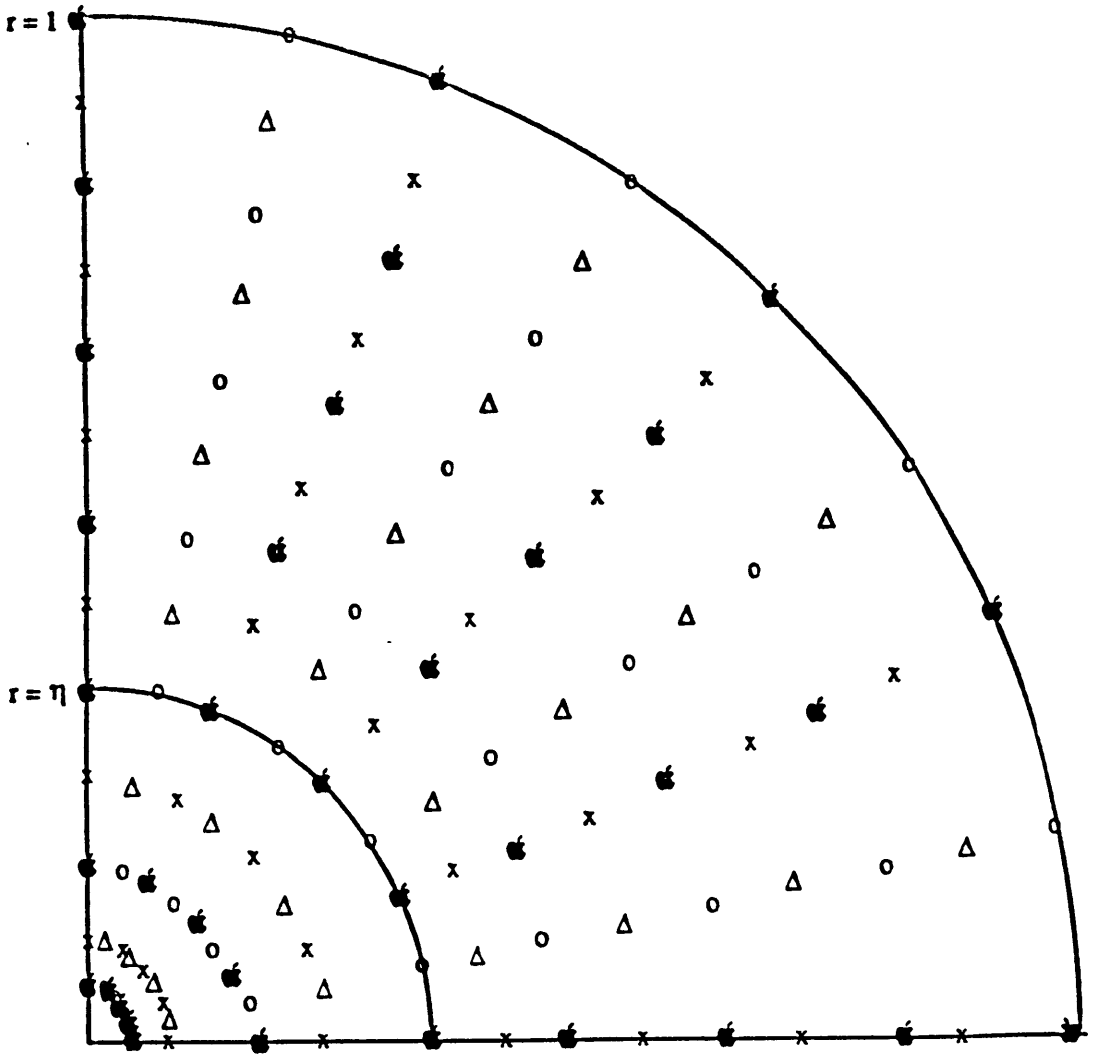

Figure 3.4 A schematic of the finite difference staggered grid that we use for the calculations. In this model, N = L = 4, and $N_i = 2$. The net is ungraded, and we omit grid points for r > 1.

KEY: o = u, v, f_r, b_θ, b_ϕ

x = w, f_θ, b_r

Δ = p, c, e_θ

● = e_r

represent quadrupole symmetry. We have studied only dipole symmetry in an effort to reduce the parameter space. For m = 1, in which there can be flow across the pole, we impose the following symmetry conditions:

$$u = \partial v/\partial\theta = \partial w/\partial\theta = p = c = f_r = \partial f_\theta/\partial\theta = 0 \text{ at } \theta = 0, \tag{3.25}$$

with the symmetry conditions at $\theta = \pi/2$ unchanged. Finally, we impose no slip and no normal flow at the rigid spherical boundaries, so that

$$u = w = v = 0 \text{ at } r = \eta \text{ and } r = 1. \tag{3.26}$$

Our solution method for the non-linear problem (3.18) - (3.21) with (3.23) or (3.25), (3.24), and (3.26) is an iterative one. For a linear system, one solves $\mathbf{A}\cdot\mathbf{x} = \mathbf{b}$ once, where **A** is the finite difference matrix operator, independent of the solution vector **x**, and **b** contains the sources. However, for a non-linear problem the operator **A** is a function of the solution vector **x**, *i.e.*, $\mathbf{A} = \mathbf{A}(\mathbf{x})$, and the system one must solve is $\mathbf{A}(\mathbf{x})\cdot\mathbf{x} = \mathbf{b}$. At iteration n we can set the vector of K unknowns $\mathbf{x}_n = \mathbf{x}_{n-1} + \Delta\mathbf{x}$, so that

$$\mathbf{A}(\mathbf{x}_{n-1}+\Delta\mathbf{x})\cdot(\mathbf{x}_{n-1}+\Delta\mathbf{x}) = \mathbf{b}. \tag{3.27}$$

Since we cannot solve (3.27) directly, we solve its approximation at iteration n,

$$\mathbf{A}(\mathbf{x}_{n-1})\cdot\Delta\mathbf{x} = \mathbf{b} - \mathbf{A}(\mathbf{x}_{n-1})\cdot\mathbf{x}_{n-1}. \tag{3.28}$$

Until $\Delta\mathbf{x} = \mathbf{0}$, when $\mathbf{x}_n = \mathbf{x}_{n-1}$, we have not satisfied the original system of equations (3.27). When $\Delta\mathbf{x} = \mathbf{0}$, we speak of a converged solution. In the absence of a converged

solution, the vector $\mathbf{x}_n$ is meaningless since it does not represent the solution to a physical problem, as would a numerical solution at a given time step.

In order to begin our iterative procedure to solve (3.27) we must start with a guess solution $\mathbf{x}_0$. We can then compute the operator matrix $\mathbf{A}(\mathbf{x}_0)$ as well as the right hand side of (3.28) so that we can solve (3.28) for $\Delta\mathbf{x}$, set $\mathbf{x}_1 = \mathbf{x}_0 + \Delta\mathbf{x}$, and repeat the procedure with $\mathbf{x}_1$ replacing $\mathbf{x}_0$. At each iteration we must solve a system $\mathbf{A}\cdot\Delta\mathbf{x} = \mathbf{d}$, where $\mathbf{d} = \mathbf{b} - \mathbf{A}(\mathbf{x}_{n-1})\cdot\mathbf{x}_{n-1}$. To solve $\mathbf{A}\cdot\Delta\mathbf{x} = \mathbf{d}$ we use damped least squares with preconditioning. Hence,

$$\Delta\mathbf{x} = (\mathbf{A}^T\mathbf{D}^{-1}\mathbf{A}+\varepsilon^2\mathbf{I})^{-1}\cdot(\mathbf{A}^T\mathbf{D}^{-1}\mathbf{d}), \tag{3.29}$$

where $\mathbf{A}^T$ is the transpose of $\mathbf{A}$, $\varepsilon^2\mathbf{I}$ is the diagonal damping matrix, and $\mathbf{D}$ is the preconditioning matrix. The matrix $\mathbf{D}$ is a diagonal matrix with element $D_{i,i} = \Sigma_j A_{i,j}^2$, where i is the row index and j the column index. In essence, the preconditioning normalizes the magnitude of the rows of $\mathbf{A}$ in order to reduce the eigenvalue spread and make the inversion of $\mathbf{A}^T\mathbf{A}$ more stable in the limit of small damping ε^2.

3.5 Solutions in a spherical shell for Ta = El = 0

In this section we demonstrate the method's use and its ability to find steady, finite-amplitude convective solutions in a spherical shell when Ta = El = 0. Unless otherwise noted the spherical shell has an inner radius $\eta = .35$, which is roughly the scaled radius of the Earth's inner core for a CMB with radius 1. We carried out program development and testing on an Apollo workstation DN 3500, while we performed the calculations presented throughout the remainder of this chapter and the next on a Cray X-MP. For most of the calculations we used a grid with N = L = 8, so that K = 1224, as according to (3.22). Later on we will compare the numerical accuracy of these solutions with those on larger

grids. Although the code can handle a graded net for which we can obtain finer resolution in boundary layers, we find for this non-rotating, non-magnetic problem that a graded net is unnecessary at the relatively low Rayleigh numbers that we search for solutions. Finally, for all matrix inversions (3.29) we used the LINPACK routines.

We begin with an intial guess solution $\mathbf{x}_0$ that consists of a field of ones and zeros (in the non-dimensionalized system), which we denote starting model 1. With the matrix **A** normalized to O(1) by the preconditioning, we set our initial damping $\varepsilon^2 = 10^{-6}$, which is much less than O(1) but still much greater than the $O(10^{-14})$ precision of the Cray X-MP. We proceed with the iterative procedure outlined above, solving the problem (3.28) via (3.29) at each iteration step, and updating $\mathbf{x}_n$. At each iteration step, we compute the root mean square of the fit, rms = $(d_{i,i})^{1/2}$. For an O(1) model such as model 1, the starting rms is O(1), and for a converged solution, $\Delta\mathbf{x} = \mathbf{0}$, so that the rms approaches zero (actually, machine error, $O(10^{-14})$). We have found that if we decrease the damping ε^2 beneath 10^{-6} too quickly, the solution $\mathbf{x}_n$ is difficult to control and the rms may not decrease smoothly . Thus, only as the rms decreases during an iteration sequence do we lower the damping ε^2. Typically, we require roughly 15 - 30 iteration steps to reach a converged solution (if we are to reach one), though this number will vary with the values of Ra, Ta, and El under study. We will further discuss the iteration sequence as we solve specific problems.

For boundary conditions such as those here, in which we have homogeneous forcing (f_r independent of θ and ϕ along both $r = \eta$ and $r = 1$), the linear conduction solution induces no motion and buoyancy simply diffuses for non-zero Ra. The conduction solution is a solution for all Ra, though as Chandrasekhar (1961) found, for $Ra > Ra_c$, the conduction solution is unstable and non-linear convection commences. Beginning each iteration sequence with $\mathbf{x}_0$ equal to model 1, the converged solution that we obtain for $m = 0$ (axisymmetric solution only), $m = 2$, or $m = 4$ for all $Ra < 2.2 \times 10^4$ is the conduction solution. However, for $Ra = 2.2 \times 10^4$, the iteration sequence converges not

to the conduction solution but to a solution in which the buoyancy gradients are no longer purely radial and O(1) motions are present. We have obtained a finite-amplitude, non-linear convective solution. Hence, for this problem $Ra_c = 2.2 \times 10^4$.

The solution that occurs at Ra_c is axisymmetric. In Figure 3.5 we show fluid velocity flux arrows in an arbitrary meridional slice of the northern hemsiphere. Even when we allow the possibility of an m = 2 or m = 4 (along with an m = 0) solution, the iteration sequence at $Ra = 2.2 \times 10^4$ always converges to the purely m = 0 solution. Moreover, we obtain the same Ra_c and the same solution at Ra_c for a variety of iteration sequences with different damping at each iteration step. Similarly, when we begin with $\mathbf{x}_0$ equal to model 2, which substitutes minus ones for the ones of model 1, or model 3, which substitutes tens for ones, we obtain the same Ra_c and the same solution at Ra_c.

In order to check the accuracy of the solutions we employ a finer mesh with N = L = 12. Beginning with $\mathbf{x}_0$ equal to model 1 and looking for axisymmetric convection, we find that at $Ra = 2.2 \times 10^4$ we converge to the conduction solution, unlike for the 8 x 8 grid. It is not until $Ra = 2.4 \times 10^4$ that we obtain a convective solution. For N = L = 14, we find Ra_c also equals 2.4×10^4, so our value for Ra_c on the computationally more manageable 8 x 8 grid is perhaps not more than 10% off its 'exact' value. The convective solutions that occur at $Ra = 2.4 \times 10^4$ for the three grids are qualitatively similar to that in Figure 3.5. The amplitude of the convection (as measured by the maximum flux) on the 8 x 8 grid is twice that on the 12 x 12 grid, which in turn is not quite twice that on the 14 x 14 grid. This variation represents the rapid growth of the amplitude of convection with Ra above Ra_c, and the apparent tendency of the coarser grid to overestimate the amplitude of the convection.

Figure 3.5 shows that latitudinal wavenumber $\ell = 2$ dominates the axisymmetric convection that commences at Ra_c for N = L = 8. Although Chandrasekhar (1961) studied convection with fixed buoyancy rather than fixed buoyancy gradient boundary conditions, our results are nevertheless in general agreement with his. Referring to his Chapter 6, Table

XXV, we find that for a shell of inner radius $\eta = .3$, $Ra_c = 1.8 \times 10^4$ with a critical latitudinal wavenumber $\ell_c = 2$, whereas for $\eta = .4$, $Ra_c = 2.8 \times 10^4$ with $\ell_c = 3$. For a thinner shell with $\eta = .6$ we obtain $Ra_c = 1.2 \times 10^5$ (for N = L = 8), which is again in reasonable agreement with Chandrasekhar's value $Ra_c = 1.1 \times 10^5$. Although $\ell = 2$ again dominates our axisymmetric convection, as opposed to his value $\ell_c = 6$, a closer inspection of Table XXV reveals that Ra_c is a very weak function of ℓ, so it is perhaps not surprising that we might obtain a different dominant ℓ at Ra_c.

Returning to the shell with $\eta = .35$, we follow the nature of steady solutions on the 8 x 8 grid as the Rayleigh number rises above Ra_c. As Ra rises through 3×10^4, the convective pattern remains m = 0 and $\ell = 2$, but the amplitude of the motions increases non-linearly with Ra (Figure 3.6). This of course represents the increasing importance of convection over conduction in the transport of buoyancy. Like Figure 3.5, we obtain Figure 3.6 independent of the model that we begin with for $\mathbf{x}_0$. At $Ra = 5 \times 10^4$ we obtain $\ell = 3$ axisymmetric convection for all starting models (Figure 3.7). In between $Ra = 3 \times 10^4$ and $Ra = 5 \times 10^4$, however, the iteration sequence becomes very difficult to control, with the rms not decreasing smoothly, even when heavily damped. Eventually, after some 30 iteration steps, we obtain a converged solution, but the solution we arrive at is the conduction solution! The iteration sequence behaves similarly for all starting models.

We interpret this behavior as follows. For $2.2 \times 10^4 \leq Ra \leq 3 \times 10^4$ the iteration sequences converge to m = 0, $\ell = 2$ convection. For $Ra \geq 5 \times 10^4$ but less than some as yet undetermined Ra the iteration sequences converge to m = 0, $\ell = 3$ convection. Clearly there is a bifurcation in between, so it should not surprise us that the iteration sequences should become difficult to control for $3 \times 10^4 < Ra < 5 \times 10^4$. In some sense it is as though an unconverged solution $\mathbf{x}_n$ cannot easily determine the direction in which it should move in order to further minimize its misfit. Conduction is a mathematically possible solution for all Ra, and at only roughly twice critical it is not improbable for an iteration sequence to converge to the conduction solution.

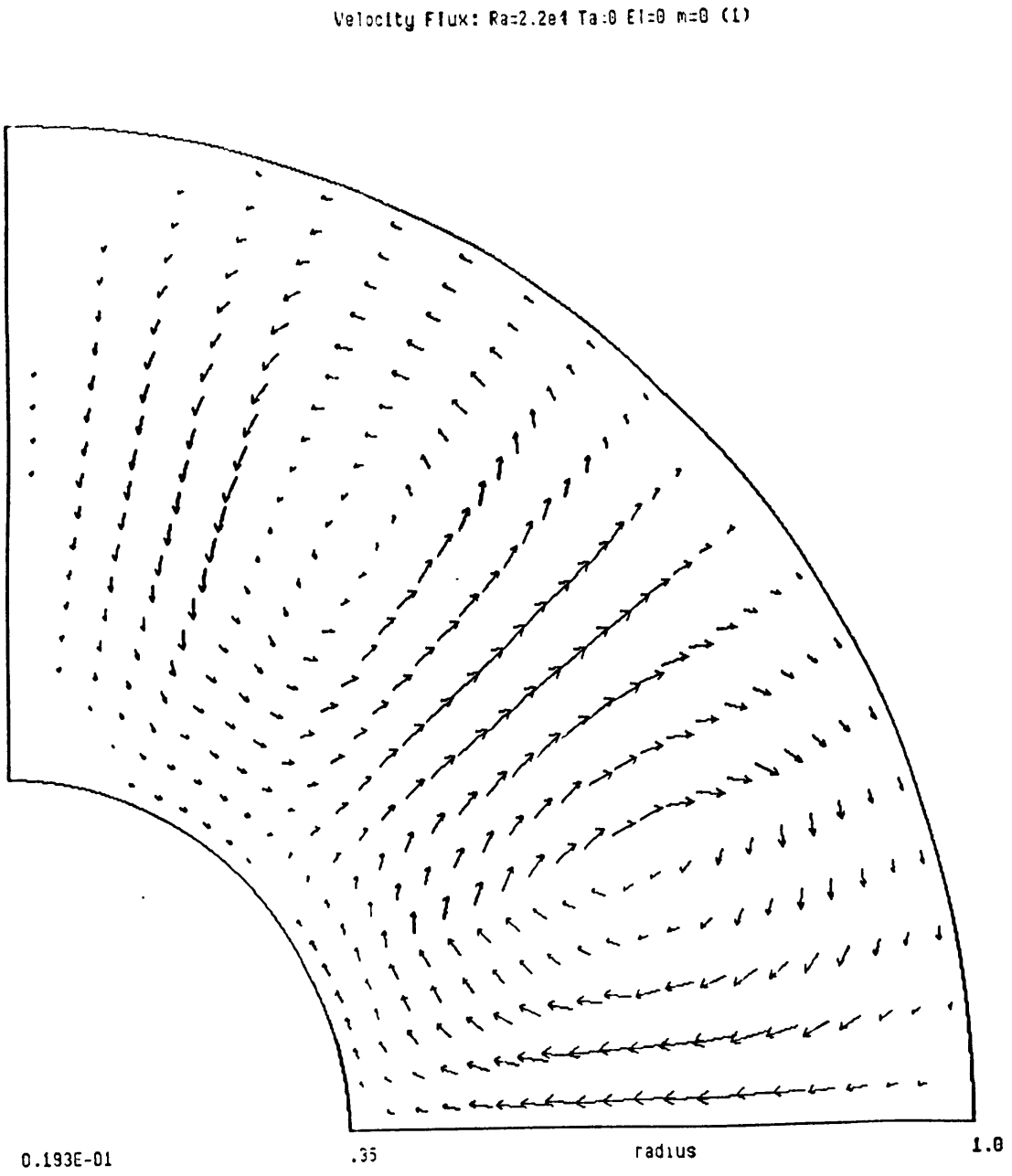

Figure 3.5 Axisymmetric fluid velocity flux arrows in a meridional slice of the northern hemispherical shell with $\eta = .35$ for $Ra = Ra_c = 2.2 \times 10^4$, $Ta = 0$, $El = 0$, and $Pr = \infty$ (starting model 1). The $m = 0$ flow has no component out of the meridional plane. For plotting purposes we linearly interpolate fluxes from the $N = L = 8$ grid. The number at the bottom left of the figure represents the maximum flux v_{max}. If the flux at a point is less than one-tenth v_{max}, we do not plot its flux arrow.

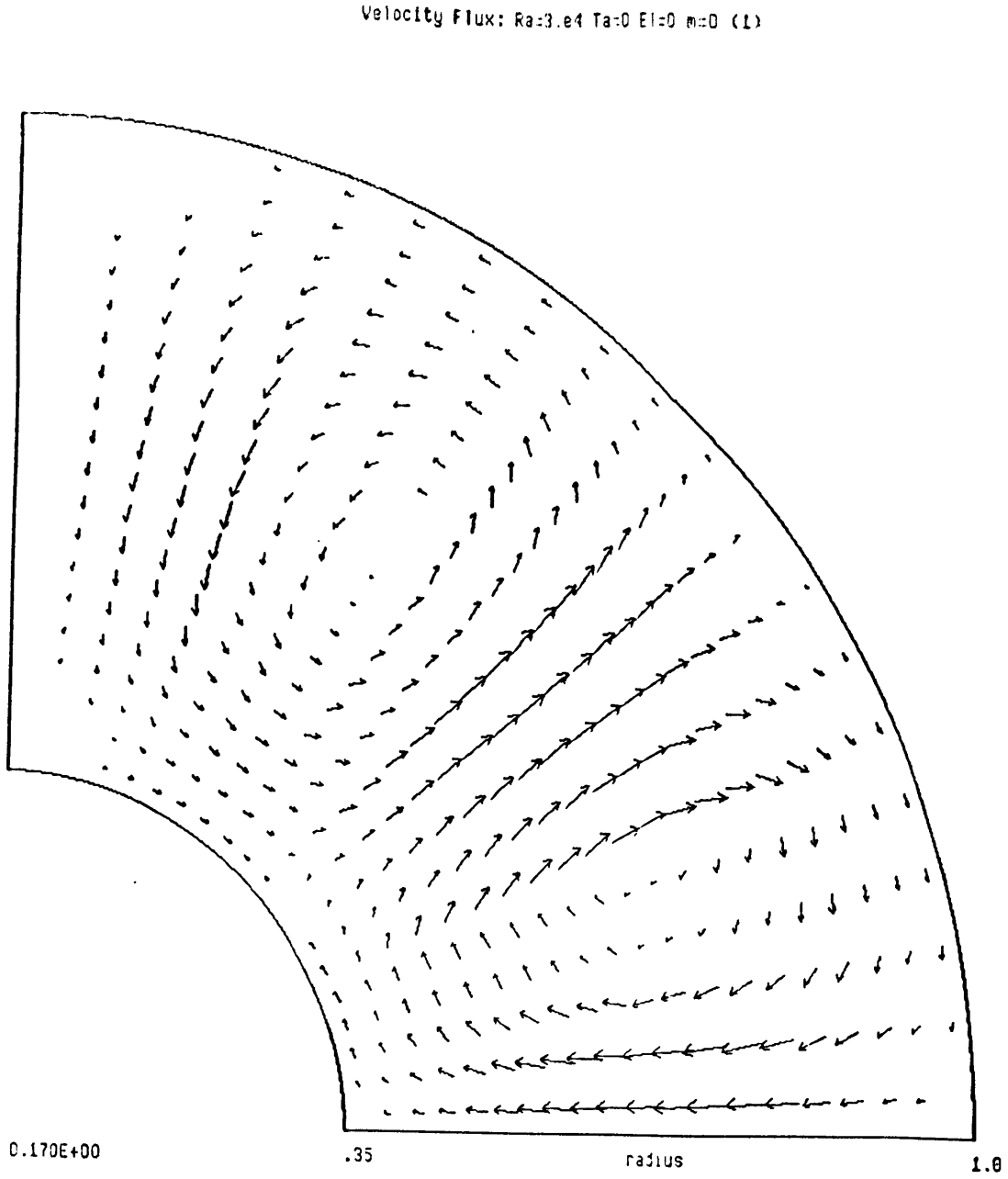

Figure 3.6 As for Figure 3.5, but with Ra = 3 x 10^4. The amplitude of the $\ell = 2$ flow has increased by nearly a factor of ten above its value at Ra = 2.2 x 10^4, as evidenced by v_{max}.

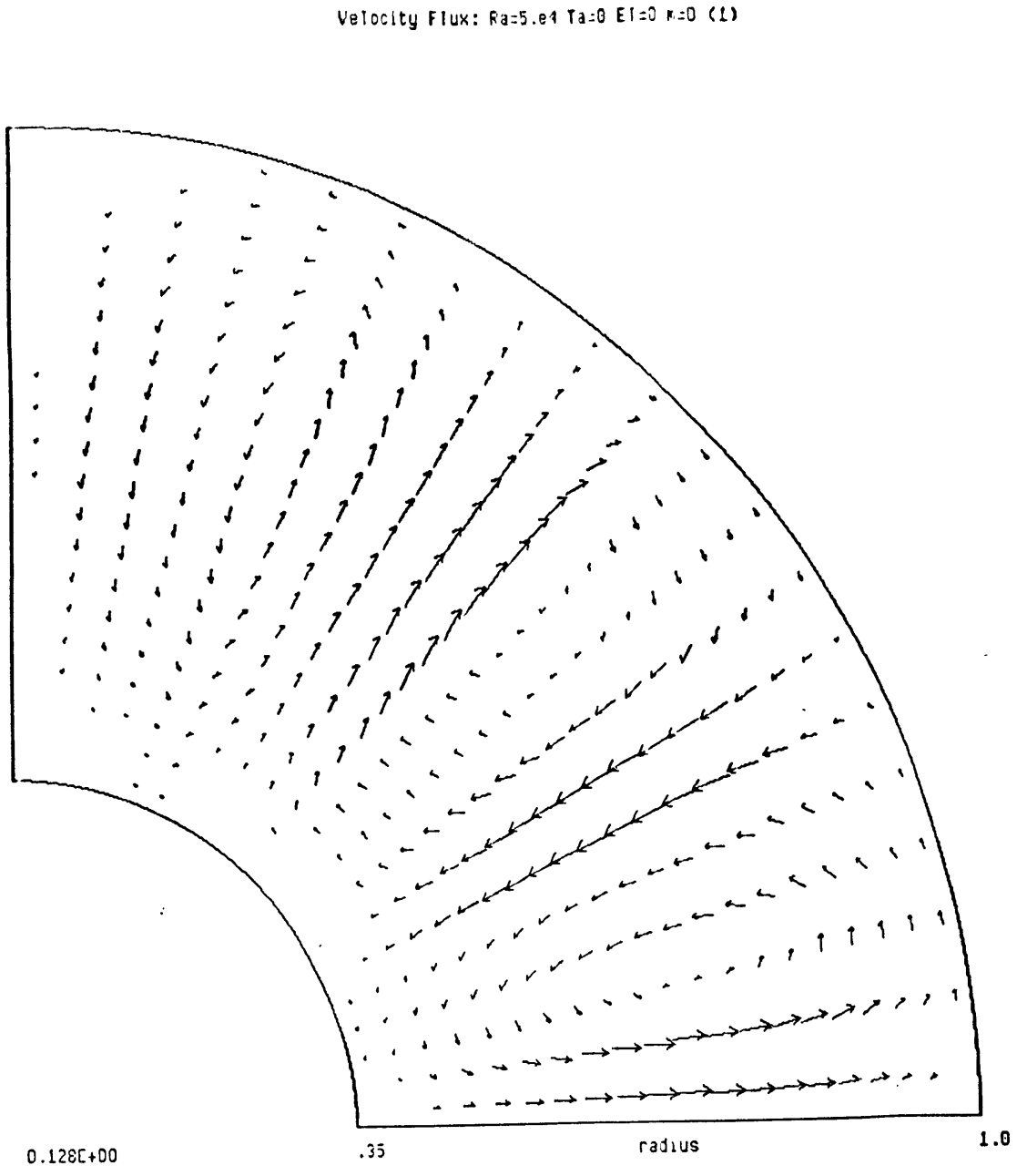

Figure 3.7 As for Figure 3.5, but with Ra = 5 x 10^4. The flow is $\ell = 3$.

At Ra = 1 x 10^5, we find converged solutions that depend upon the starting model and are thus non-unique. However, the final converged solution for a given starting model is not particularly sensitive to the damping at a given iteration step. Some of the solutions are three-dimensional. With $\mathbf{x}_0$ as starting model 1, we obtain axisymmetric convection even if we allow for an m = 2 or m = 4 solution. We show this axisymmetric solution, which is primarily $\ell = 4$, in Figure 3.8. In Figure 3.9 we show the more vigorous $\ell = 3$ axisymmetric convection that results with $\mathbf{x}_0$ as starting model 2, again independent of whether we allow an m = 2 or m = 4 solution. With starting model 3, however, we obtain different solutions if we impose axisymmetry, m = 2, or m = 4. If we impose axisymmetry, we obtain the same solution as in Figure 3.9. If we impose m = 2, we converge to the three-dimensional convection that we show in Figure 3.10a,b,c. Finally, if we impose m = 4, the solution reverts to the axisymmetric convection of Figure 3.8. Presumably, at this modest Ra the convection resists the small length scale of m = 4 by reverting to axisymmetry.

In order to obtain converged three-dimensional solutions we have had to operate at higher Ra. While this is not completely surprising, the method does appear to show some predilection towards finding axisymmetric solutions. As Ra rises further above Ra_c the iteration sequences become more difficult to control due to the increasingly non-linear solution surface becoming more complex. Moreover, the conduction solution surface becomes more difficult to reach at higher Ra, so we are less likely to obtain conduction as a converged solution. By Ra = 5 x $10^5 > 20\ Ra_c$ we cannot get the iteration sequence to converge within 40 iterations. Of course, this is not unexpected behavior from a physical standpoint: as Ra rises above critical, conduction becomes more remote, convection becomes smaller scale, and turbulence eventually develops. Accompanying the cascade to smaller scales we expect time-dependence, though this method cannot predict the time-dependence.

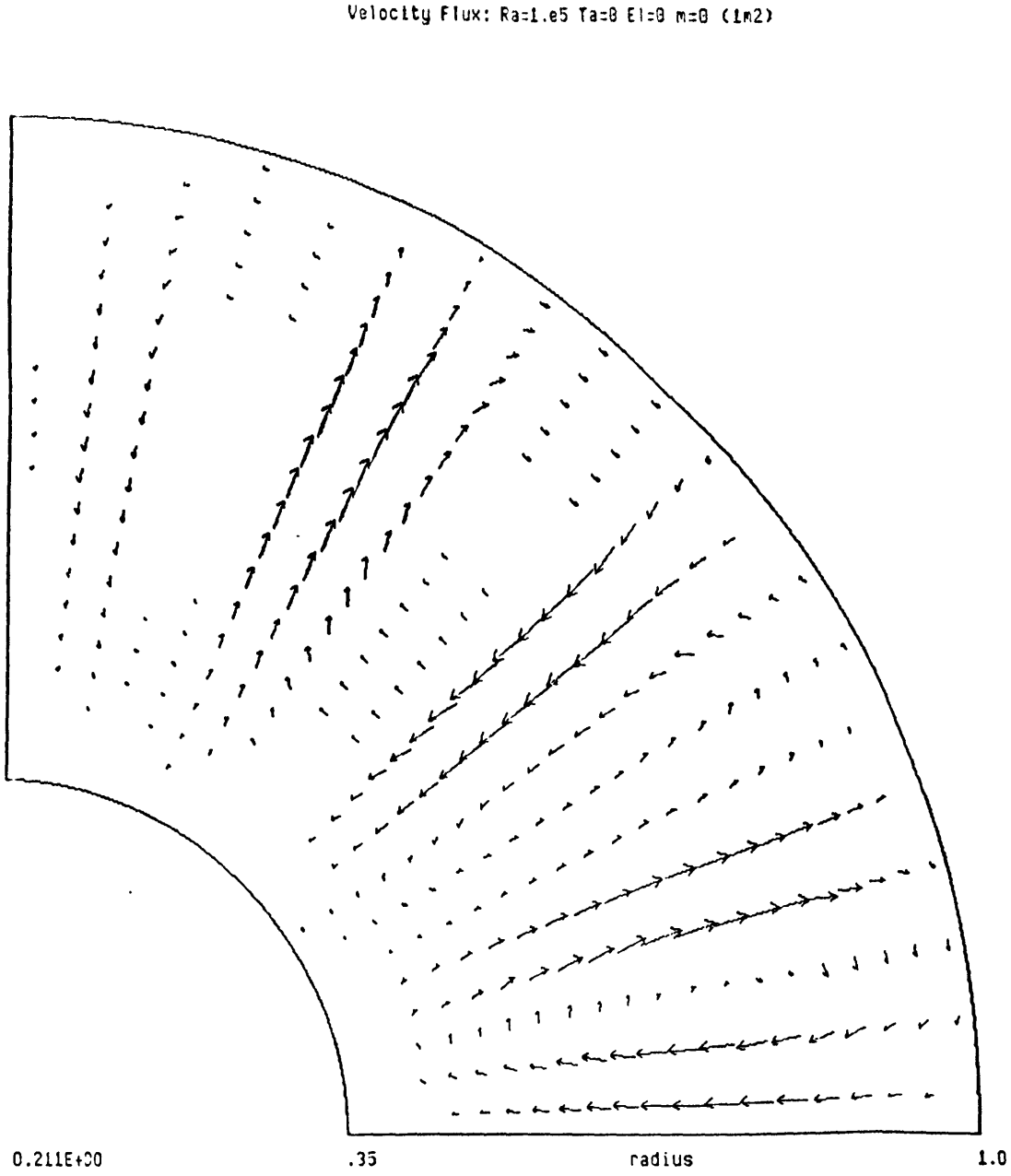

Figure 3.8 As for Figure 3.5, but with Ra = 1 x 10^5. The flow is $\ell = 4$.

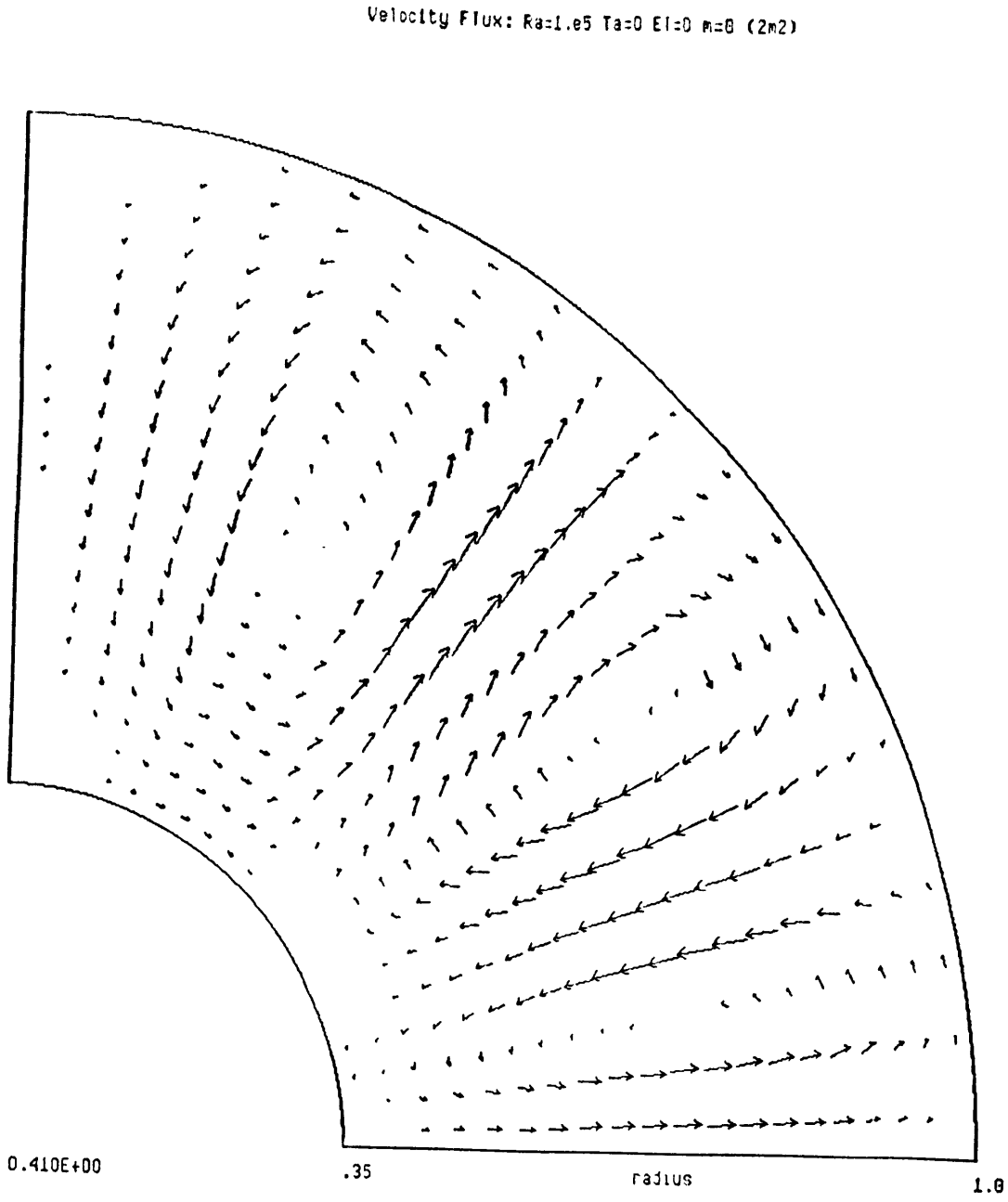

Figure 3.9 As for Figure 3.8, but with starting model 2. The flow is $\ell = 3$, though with greater amplitude than at Ra = 5 x 10^4. The $\ell = 3$ flow is more vigorous than the $\ell = 4$ flow of Figure 3.8, which is also at Ra = 1 x 10^5.

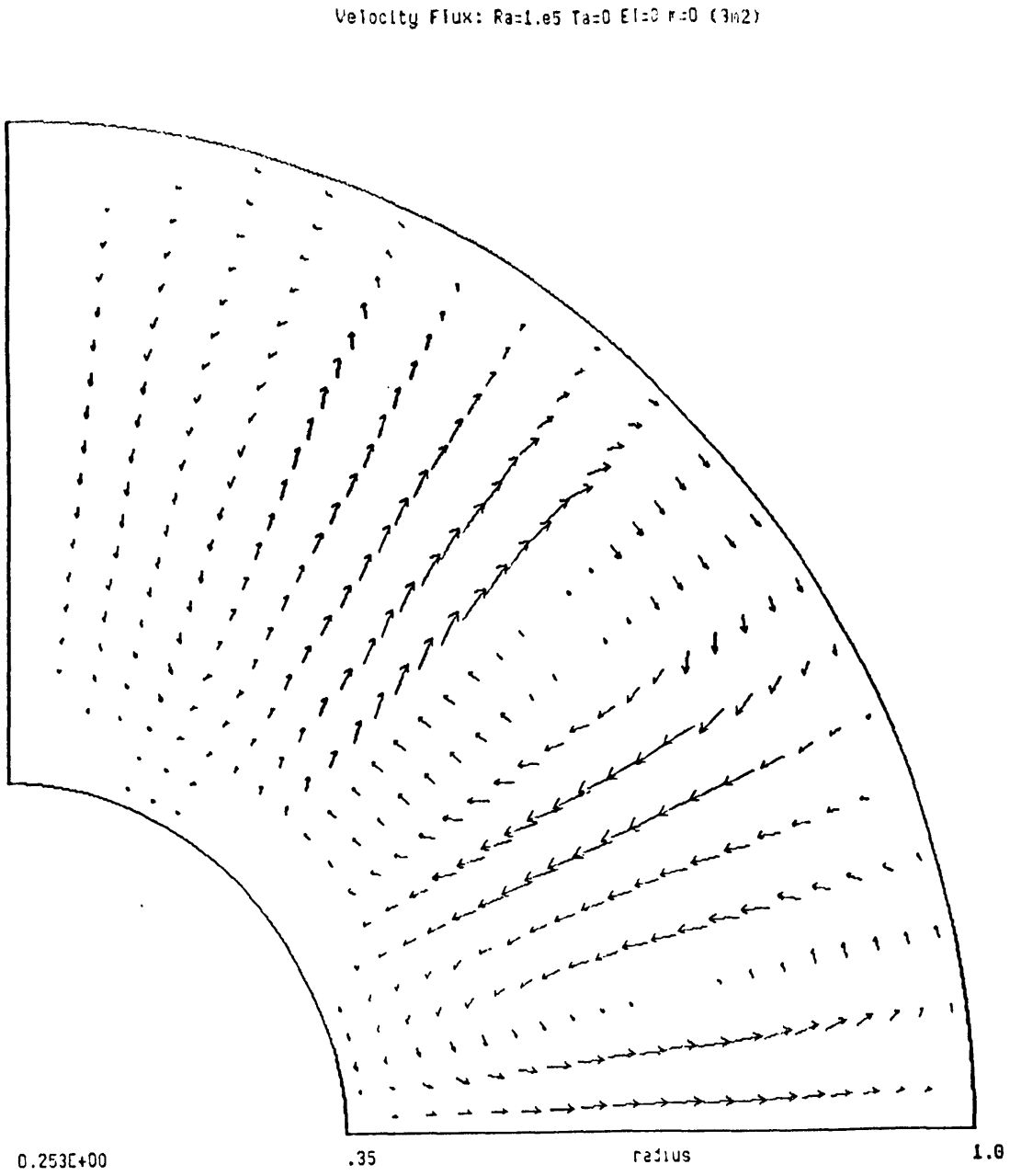

Figure 3.10 As for Figure 3.8, but with starting model 3. The convection contains **m = 2** flow in addition to axisymmetric flow.

a) The axisymmetric component. The flow is $\ell = 3$, though of lesser amplitude than thepurely axisymmetric flow of Figure 3.9.

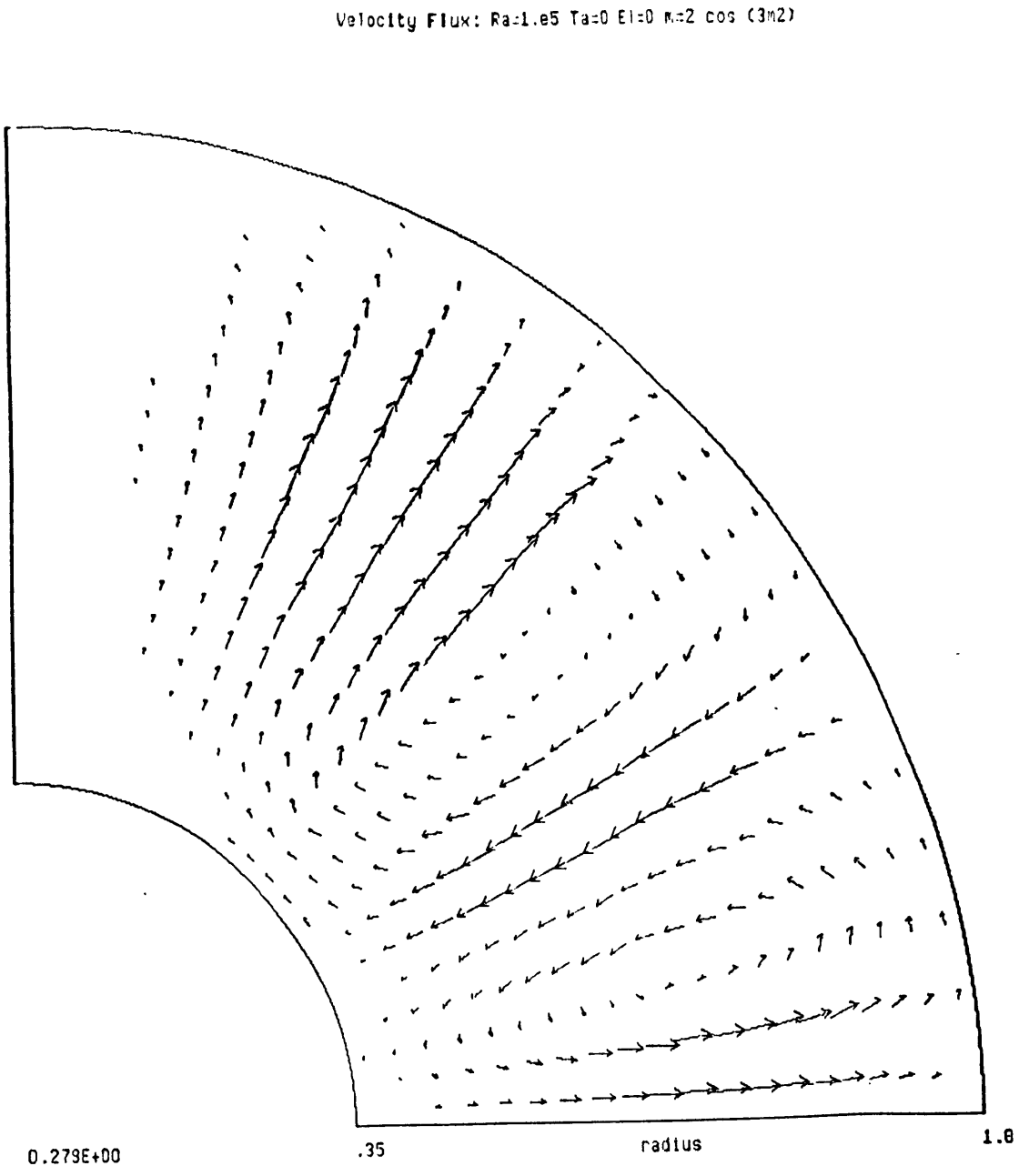

b) The cosine component of the m = 2 flow in a meridional slice at $\phi = 0$. We do not show the accompanying m = 2 azimuthal flow.

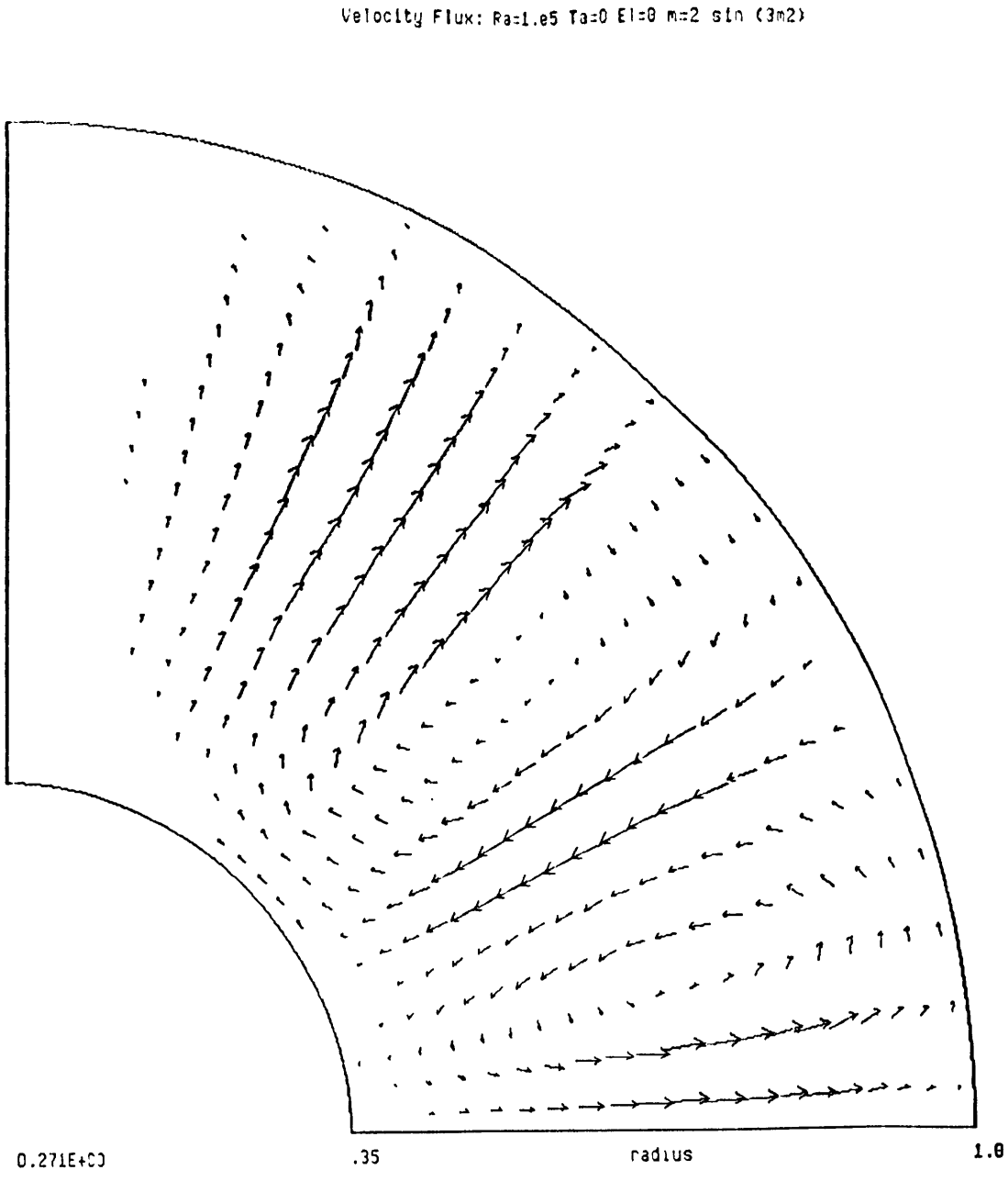

c) As for Figure 3.10b, but the sine component.

At higher Ra such as Ra = 10^5, the converged solutions, even the axisymmetric ones, are no longer unique. However, despite trying starting models other than 1, 2, or 3, and iteration sequences with different damping levels, we always obtain one of only a few different converged solutions (Figures 8 -10). In any case, as Ra rises above Ra_c, the omission of the explicitly time-dependent terms becomes more suspect. Although we may obtain a converged solution in the space domain, without the time-dependent terms we cannot be sure our solutions are stable in the space-time domain. Thus, much as the conduction solution is an exact solution that is unstable to perturbations in the space domain for $Ra > Ra_c$, our converged, stationary convective solutions in the space domain may be unstable to perturbations in the time domain.

Short of time-stepping, one could perform a linear stability analysis of our finite-amplitude solutions to determine the stability with respect to time perturbations. Although we have not done this yet, our general expectation for this non-rotating, non-magnetic problem is that the converged solutions that we have obtained with relative ease at moderate Ra are likely to be stable with respect to time. As Ra rises, our difficulty in finding converged solutions in the space domain is very likely related to the increasing importance of the time-dependence, which we have neglected. As we shall see in the next chapter, however, one cannot always be so confident about the stability of converged solutions, and a certain amount of physical intuition is necessary in lieu of the mathematical stability analysis. In any case, in this chapter we have demonstrated that the method can reproduce reasonably well the nature of stationary convection in a non-rotating, non-magnetic fluid.

References

Acheson, D.J., "On the hydromagnetic stability of a rotating fluid annulus", *J. Fluid Mech.* **52**, 529-541 (1972).

Acheson, D.J., "Hydromagnetic wavelike instabilities in a rapidly rotating stratified fluid", *J. Fluid Mech.* **61**, 609-624 (1973).

Bloxham, J. *et al.*, personal communication (seminar) (1992).

Braginsky, S.I., "Magnetohydrodynamics of the Earth's core", *Geomagn. & Aeron.* **4**, 698-712 (1964).

Braginsky, S.I., "Magnetic waves in the Earth's core", *Geomagn. & Aeron.* **7**, 851-859 (1967).

Braginsky, S.I., "Torsional magnetohydrodynamic vibrations in the Earth's core and variations in day length", *Geomagn. & Aeron.* **10**, 1-8 (1970).

Braginsky, S.I., "Magnetic waves in the core of the Earth. II", *Geophys. Astrophys. Fluid Dynam.* **14**, 189-208 (1980).

Braginsky, S.I., "Short-period geomagnetic secular variation", *Geophys. Astrophys. Fluid Dynam.* **30**, 1-78 (1984).

Braginsky, S.I., and Roberts, P.H., "A model-Z dynamo", *Geophys. Astrophys. Fluid Dynam.* **38**, 327-349 (1987).

Busse, F.H., "Thermal instabilities in rapidly rotating systems", *J. Fluid Mech.* **44**, 441-460 (1970).

Busse, F.H., "A model of the geodynamo", *Geophys. J. R. Astron. Soc.* **42**, 437-459 (1975).

Busse, F.H., "An example of nonlinear dynamo action", *J. Geophys.* **43**, 441-452 (1977).

Busse, F.H., and Carrigan, C.R., "Laboratory simulation of thermal convection in rotating planets and stars", *Science* **191**, 81-83 (1976).

Busse, F.H., and Cuong, P.G., "Convection in rapidly rotating spherical fluid shells", *Geophys. Astrophys. Fluid Dynam.* **8**, 17-44 (1977).

Cardin, P., and Olson, P., "Chaotic thermal convection in a rapidly rotating spherical shell: consequences for flow in the outer core", manuscript, (1992).

Carrigan, C.R., and Busse, F.H., "An experimental and theoretical investigation of the onset of convection in rotating spherical shells", *J. Fluid Mech.* **126**, 287-305 (1983).

Chamberlain, J.A., and Carrigan, C.R., "An experimental investigation of convection in a rotating sphere subject to time varying thermal boundary conditions", *Geophys. Astrophys. Fluid Dynam.* **35**, 303-327 (1986).

Chandrasekhar, S., *Hydrodynamic and Hydromagnetic Stability*. Dover Publications (1961).

Cuong, P.G., and Busse, F.H., "Generation of magnetic fields by convection in a rotating sphere. I", *Phys. Earth Planet. Inter.* **24**, 272-283 (1981).

Drew, S.J., "Thermal convection in a spherical shell with a variable radius ratio", *Geophys. Astrophys. Fluid Dynam.* **59**, 165-183 (1991).

Eltayeb, I.A., and Kumar, S., "Hydromagnetic convective instability of a rotating, self-gravitating fluid sphere containing a uniform distribution of heat sources", *Proc. R. Soc. London A***353**, 145-162 (1977).

Fearn, D.R., "Thermal and magnetic instabilities in a rapidly rotating fluid sphere", *Geophys. Astrophys. Fluid Dynam.* **14**, 103-126 (1979).

Fearn, D.R., "Hydromagnetic waves in a differentially rotating annulus I. A test of local stability analysis", *Geophys. Astrophys. Fluid Dynam.* **27**, 137-162 (1983).

Fearn, D.R., "Hydromagnetic waves in a differentially rotating annulus II. Resistive instabilities", *Geophys. Astrophys. Fluid Dynam.* **30**, 227-239 (1984).

Fearn, D.R., "Hydromagnetic waves in a differentially rotating annulus III. The effect of an axial field", *Geophys. Astrophys. Fluid Dynam.* **33**, 185-197 (1985).

Fearn, D.R., and Proctor, M.R.E., "Hydromagnetic waves in a differentially rotating sphere", *J. Fluid Mech.* **128**, 1-20 (1983a).

Fearn, D.R., and Proctor, M.R.E., "The stabilizing role of differential rotation on hydromagnetic waves", *J. Fluid Mech.* **128**, 21-36 (1983b).

Fearn, D.R., and Weiglhofer, W.S., "Magnetic instabilities in rapidly rotating spherical geometries I. From cylinders to spheres", *Geophys. Astrophys. Fluid Dynam.* **56**, 159-181 (1991).

Gill, A.E., *Atmosphere-Ocean Dynamics*, Academic Press (1982).

Gilman, P.A., "Linear simulations of Boussinesq convection in a deep rotating spherical shell", *J. Atmos. Sci.* **32**, 1331-1352 (1975).

Gilman, P.A., "Nonlinear dynamics of Boussinesq convection in a deep rotating spherical shell. I", *Geophys. Astrophys. Fluid Dynam.* **8**, 93-135 (1977).

Greenspan, H.P., *The Theory of Rotating Fluids*, Cambridge University Press (1968).

Gubbins, D., "Energetics of the Earth's core", *J. Geophys.* **43**, 453-464 (1977).

Hart, J.E., Glatzmaier, G.A., and Toomre, J., "Space-laboratory and numerical simulations of thermal convection in a rotating hemispherical shell with radial gravity", *J. Fluid Mech.* **173**, 519-544 (1986).

Hide, R., "Free hydromagnetic oscillations of the Earth's core and the theory of the geomagnetic secular variations", *Phil. Trans. Roy. Soc. London A***259**, 615-647 (1966).

King, S.D., and Hager, B.H., "Coupling of mantle temperature anomalies and the flow pattern in the core: interpretation based on simple convection calculations", *Phys. Earth Planet. Inter.* **58**, 118-125 (1989).

Loper, D.E., "The gravitationally powered dynamo", *Geophys. J. R. Astron. Soc.* **54**, 389-404 (1978).

Malkus, W.V.R., and Proctor, M.R.E., "The macrodynamics of α-effect dynamos in rotating fluids", *J. Fluid Mech.* **67**, 417-443 (1975).

Moffatt, H.K., *Magnetic Field Generation in Electrically Conducting Fluids*, Cambridge University Press (1978).

Proudman, J., "On the motion of solids in liquids posessing vorticity", *Proc. Roy. Soc. A***92**, 408-424 (1916).

Roberts, P.H., "On the thermal instability of a highly rotating fluid sphere", *Astrophys. J.* **141**, 240-250 (1965).

Roberts, P.H., "On the thermal instability of a rotating fluid sphere containing heat sources", *Phil. Trans. Roy. Soc. London A***263**, 93-117 (1968).

Roberts, P.H., "Future of geodynamo theory", *Geophys. Astrophys. Fluid Dynam.* **44**, 3-31 (1988).

Roberts, P.H., and Loper, D.E., "On the diffusive instability of some simple steady magnetohydrodynamic flows", *J. Fluid Mech.* **90**, 641-668 (1979).

Soward, A.M., "Convection driven dynamos", *Phys. Earth Planet. Inter.* **20**, 134-151 (1979).

Taylor, G.I., "Experiments with rotating fluids", *Proc. Roy. Soc. A***100**, 114-121 (1921).

Taylor, J.B., "The magnetohydrodynamics of a rotating fluid and the Earth's dynamo problem", *Proc. R. Soc. London A***274**, 274-283 (1963).

Zhang, K.K., "Parameterized rotating convection for core and planetary atmosphere dynamics", *Geophys. Res. Lett.* **18**, 685-688 (1991a).

Zhang, K.K., "Convection in a rapidly rotating spherical shell at infinite Prandtl number: steadily drifting rolls", *Phys. Earth Planet. Inter.* **68**, 156-169 (1991b).

Zhang, K.K., and Busse, F.H., "On the onset of convection in rotating spherical shells", *Geophys. Astrophys. Fluid Dynam.* **39**, 119-147 (1987).

Zhang, K.K., and Busse, F.H., "Finite amplitude convection and magnetic field generation in a rotating spherical shell", *Geophys. Astrophys. Fluid Dynam.* **44**, 33-53 (1988).

Zhang, K.K., and Busse, F.H., "Convection driven magnetohydrodynamic dynamos in rotating spherical shells", *Geophys. Astrophys. Fluid Dynam.* **49**, 97-116 (1989).

Zhang, K.K., and Busse, F.H., "Generation of magnetic fields by convection in a rotating spherical fluid shell of infinite Prandtl number", *Phys. Earth Planet. Inter.* **59**, 208-222 (1990).

Zhang, K.K., and Gubbins, D., "On convection in the Earth's core driven by lateral temperature variations in the lower mantle", *Geophys. J. Int.* **108**, 247-255 (1992).

Chapter 3 Appendix

In this appendix we present the finite difference operators that we use for our staggered graded net. In Figure 3.4 we show the grid points at which compute the various unknowns. We use this staggered grid because generally it allows us to take centered first derivatives. Thus, we compute the radial component of the Navier-Stokes equation, (3.19), about the o's in Figure 3.4, the colatitudinal component about the x's, and the azimuthal component about the o's. We compute both the divergence equation, (3.19), and the buoyancy equation, (3.20), about the Δ's (both for which the value of the staggered net is most apparent). Finally, we compute the radial component of (3.21) about the o's and the colatitudinal component about the x's.

Let f_o represent the value of a particular scalar unknown f at a grid point $x_o = (r_o,\theta_o)$. If f_+ represents the value of f at $x_+ = x_o + \Delta x$ and f_- the value at $x_- = x_o - \Delta x$, then the derivative of f with respect to the scalar direction x (r or θ) about the point x_o is

$$f_o' = (f_+ - f_-)/(x_+ - x_-). \qquad \text{(A3.1)}$$

Equation (A3.1) is accurate to second order (in the Taylor series expansion of f about f_o) for a centered first derivative (such as $\partial u/\partial r$ in the diverence equation), and holds for a graded net as well as for a uniform net. In order to obtain second order accuracy for a derivative that is not centered (such as $\partial u/\partial r$ in the radial component of the Navier-Stokes equation), we must replace (A3.1) with

$$f_o' = \frac{[(f_-)(x_+ - x_o)^2 - (f_+)(x_- - x_o)^2 - (f_o)((x_+ - x_o)^2 - (x_- - x_o)^2)]}{[(x_- - x_o)(x_+ - x_o)(x_+ - x_-)]}. \qquad \text{(A3.2)}$$

The second derivative of f with respect to x about x_0 is

$$f_o'' = \frac{2[(f_+)(x_- - x_o) - (f_-)(x_+ - x_o) + (f_o)(x_+ - x_-)]}{[(x_- - x_o)(x_+ - x_o)^2 - (x_+ - x_o)(x_- - x_o)^2]}. \qquad \text{(A3.3)}$$

Equation (A3.3) is accurate to second order and is also valid for a graded net as well as for a uniform net. Finally, we sometimes need to take a weighted average of an unknown f. Thus, to assign a value f_o at a point x_o at which f is not actually defined on the grid of Figure 3.4, we set

$$f_o = [(x_+ - x_o)(f_-) + (x_o - x_-)(f_+)]/(x_+ - x_-). \qquad \text{(A3.4)}$$

Chapter 4

Rotating Magnetoconvection: Steady Solutions, Free and Forced

4.1 Introduction

In Chapter 3 we developed an iterative method to find steady solutions in a spherical shell to the non-linear equations (3.1) - (3.4), which govern the buoyancy-driven convection of a fluid with Rayleigh number Ra, Taylor number Ta, Elsasser number El, Prandtl number Pr, and magnetic Prandtl number q. We then solved the system for infinite Pr and q = 1 (for reasons laid out in Section 3.4), and Ta = El = 0, in order to demonstrate the method's successes and limitations in studying free convection. The time-independent equations for infinite Pr and q = 1, (3.15) - (3.21), are once again

$$\nabla \times \mathbf{B} - (\mathbf{e} + \mathbf{v} \times \mathbf{B}) = \mathbf{0}, \tag{4.1}$$

$$\nabla \cdot \mathbf{B} = 0, \tag{4.2}$$

$$\nabla \times \mathbf{e} = \mathbf{0}, \tag{4.3}$$

$$-\nabla p + \nabla^2 \mathbf{v} - \mathrm{Ta}^{1/2}\, \hat{\Omega} \times \mathbf{v} + \mathrm{Ra}\, c\hat{\mathbf{g}} + \mathrm{Ta}^{1/2}\mathrm{El}\, (\nabla \times \mathbf{B}) \times \mathbf{B} = \mathbf{0}, \tag{4.4}$$

$$\nabla \cdot \mathbf{v} = 0, \text{ and} \tag{4.5}$$

$$\mathbf{v} \cdot \mathbf{f} - \nabla \cdot \mathbf{f} = 0, \text{ with} \tag{4.6}$$

$$\mathbf{f} - \nabla c = \mathbf{0}. \tag{4.7}$$

In this chapter we will continue our study of the non-magnetic problem (4.4) - (4.7) with El = 0, but for non-zero Ta. After applying our iterative method to find solutions to the full problem (4.1) - (4.7) in the simpler geometry of a cylindrical annulus in order to further test our method, we will return to solve (4.1) - (4.7) in a spherical shell. We will also solve (4.1) - (4.7) in a spherical shell with gravity in the cylindrically radial direction rather than

in the spherically radial direction, in order to observe the role of g_z, the component of gravity in the z-direction. Having built up an understanding of our iterative method through a study of free convection, we will then use the method to find steady motions forced by laterally inhomogeneous buoyancy flux boundary conditions, as may be appropriate at the Earth's core-mantle boundary (CMB).

4.2 Solutions in a spherical shell for non-zero Ta, El = 0

The value of Ta in the Earth's outer core is unknown, though it is certainly very large, perhaps $O(10^{28})$, because of the high rotation rate and small molecular fluid viscosity of the liquid metal in the outer core (Table 1.1). It is infeasible to numerically model at such large Ta because of the small length scales that occur in this parameter range (see Section 3.3). It is for this reason that there has been so much emphasis on the asympotic relationship of the critical Rayleigh number Ra_c, critical azimuthal wavenumber m_c, and critical drift frequency ω_c to Ta, as $Ta \rightarrow \infty$. Zhang and Busse (1987) found that by $Ta = 10^7$, the asymptotic relationship that Ra_c is proportional to $Ta^{2/3}$ is very closely approached. Thus, in order to get at least a qualitative sense of the role of rapid rotation, one needs to model with Ta approaching that range. For this reason we will primarily study solutions at $Ta = 10^6$, which is numerically manageable, and also some at $Ta = 4 \times 10^6$.

As for the non-rotating problem, we study free convection driven by a homogeneous buoyancy flux across $r = \eta$ and $r = 1$. Throughout this chapter we set $\eta = .35$. We again apply the symmetry conditions (3.23) - (3.25) and boundary conditions (3.26). We compute solutions with the number of grid points $N = L = 8$, except for a few checks on the accuracy of the solutions when we employ a finer mesh. Except for the addition of relatively rapid rotation, the problem is identical to that studied in Section 3.5. As for when $Ta = 0$, if Ra is lower than a certain value, Ra_c, the iteration

sequence converges to the conduction solution, independent of the choice of starting model x_0 and azimuthal wavenumber m.

At Ta = 10^6 we find Ra_c = 1.7 x 10^5, nearly a factor of ten higher than that for Ta = 0. We obtain this value for Ra_c for starting models 1, 2, and 3. Although we allow for m = 2, 4, 6, 8, or 10 components, the convective solution that we obtain at Ra_c is always axisymmetric, and ℓ = 1, as measured by the number of convective overturns. We show the poloidal motion in Figure 4.1. The effects of rapid rotation are evident. Firstly, convection does not commence until the buoyancy force, as measured by Ra, is large enough to overcome the rotational constraint - hence the higher Ra_c as compared with that for Ta = 0. Secondly, when convection does commence, the fluid motions tend towards two-dimensionality, independent of the coordinate parallel to the rotation axis. Thus, in the polar regions the motion is oriented in the z-direction, turning only in the boundary layers on r = η and r = 1. In the equatorial region, axisymmetric poloidal motion is absent except at radii near r = η, because such motion in the mainstream violates the Taylor-Proudman theorem. Hence, diffusion remains the primary means of buoyancy transport in the equatorial region, except near the inner boundary. The rapid rotation results in an axisymmetric azimuthal flow that we show in Figure 4.2. The flow is westward in regions where the flow is away from the rotation axis, and eastward in regions where the flow is decreasing its cylindrical radius.

The behavior of the iteration sequences at Ta = 10^6 as Ra rises above Ra_c is similar to those at Ta = 0. For Ra = 3 x 10^5, we obtain axisymmetric convection whether we start with model 1 (Figure 4.3) or model 3 (Figure 4.4). The solutions are very clearly different modes, although their effective buoyancy transports are similar. Beginning with model 1, we converge to axisymmetric ℓ = 3 convection at both Ra = 4 x 10^5 and Ra = 5 x 10^5 (neither shown). The mode we obtain for the two is the same, but the amplitude at Ra = 5 x 10^5 is greater than four times that at Ra = 4 x 10^5, demonstrating the rapid non-linear growth of the amplitude of convection with increasing Ra. Through their

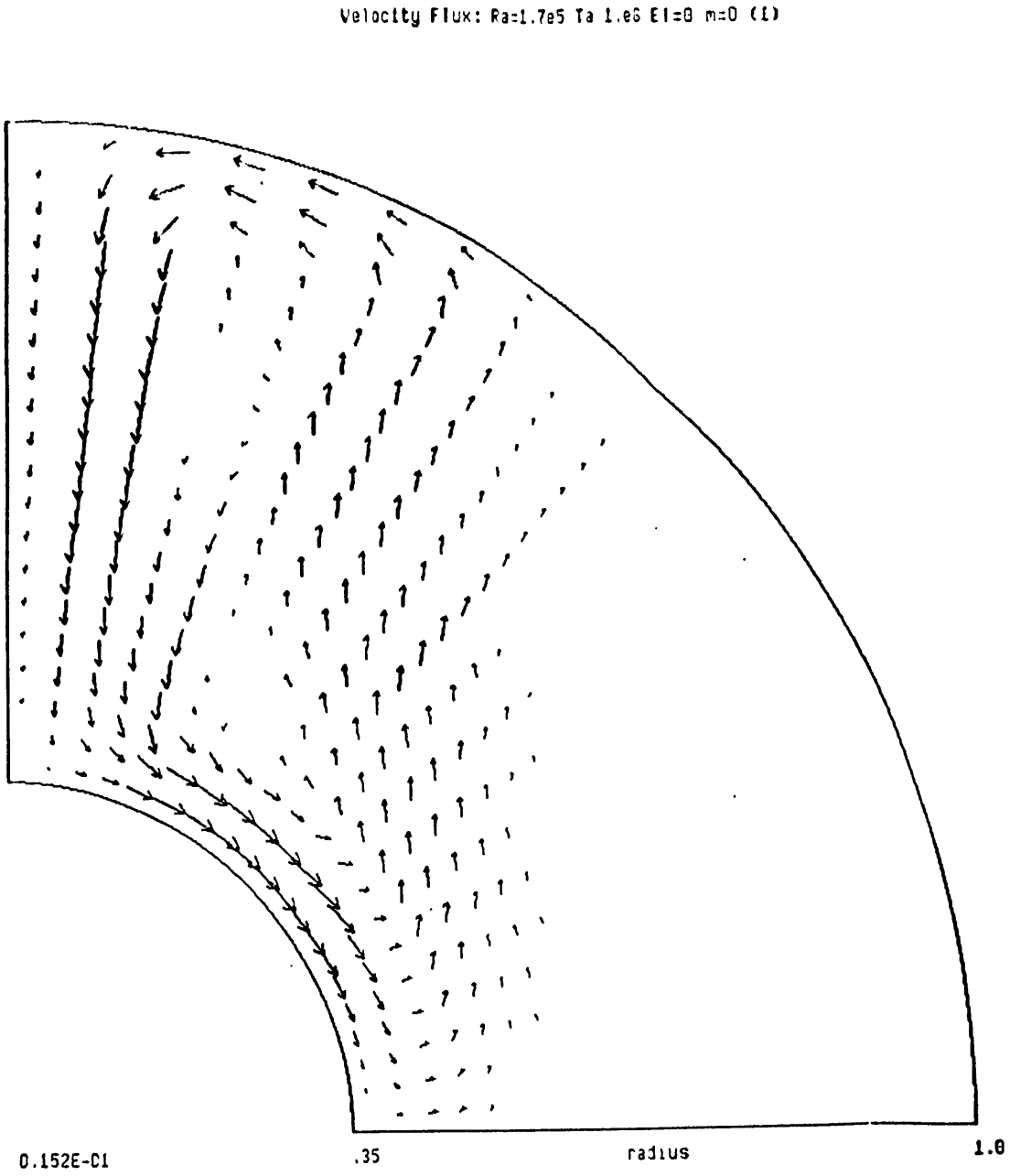

Figure 4.1 Axisymmetric fluid velocity flux arrows in a meridional slice of the northern hemispherical shell with $\eta = .35$ for $Ra = Ra_c = 1.7 \times 10^5$, $Ta = 10^6$, $El = 0$, and $Pr = \infty$ (starting model 1). The rotation induces an $m = 0$ flow out of the meridional plane. For plotting purposes we linearly interpolate fluxes from the $N = L = 8$ grid. The number at the bottom left of the figure represents the maximum flux v_{max}. If the flux at a point is less than one-tenth v_{max}, we do not plot its flux arrow. The effects of rapid rotation on this primarily $\ell = 1$ polar mode are clear.

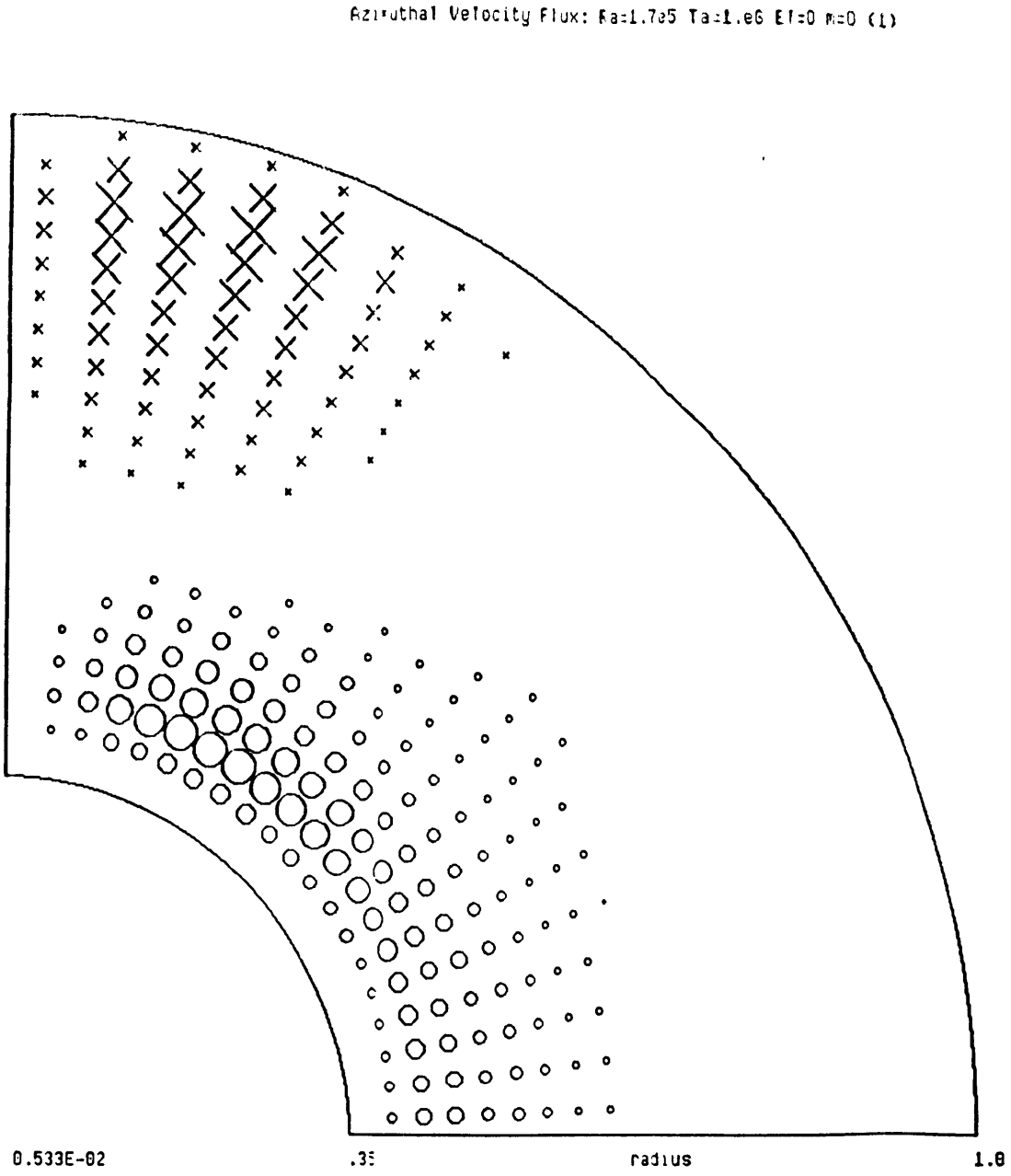

Figure 4.2 Axisymmetric azimuthal velocity flux in a meridional slice of the northern hemispherical shell for the parameters of Figure 4.1. The x's represent flow into the page (eastward flow) and the o's represent flow out of the page (westward flow). The flow is westward in regions where the flow is away from the rotation axis, eastward where it is towards.

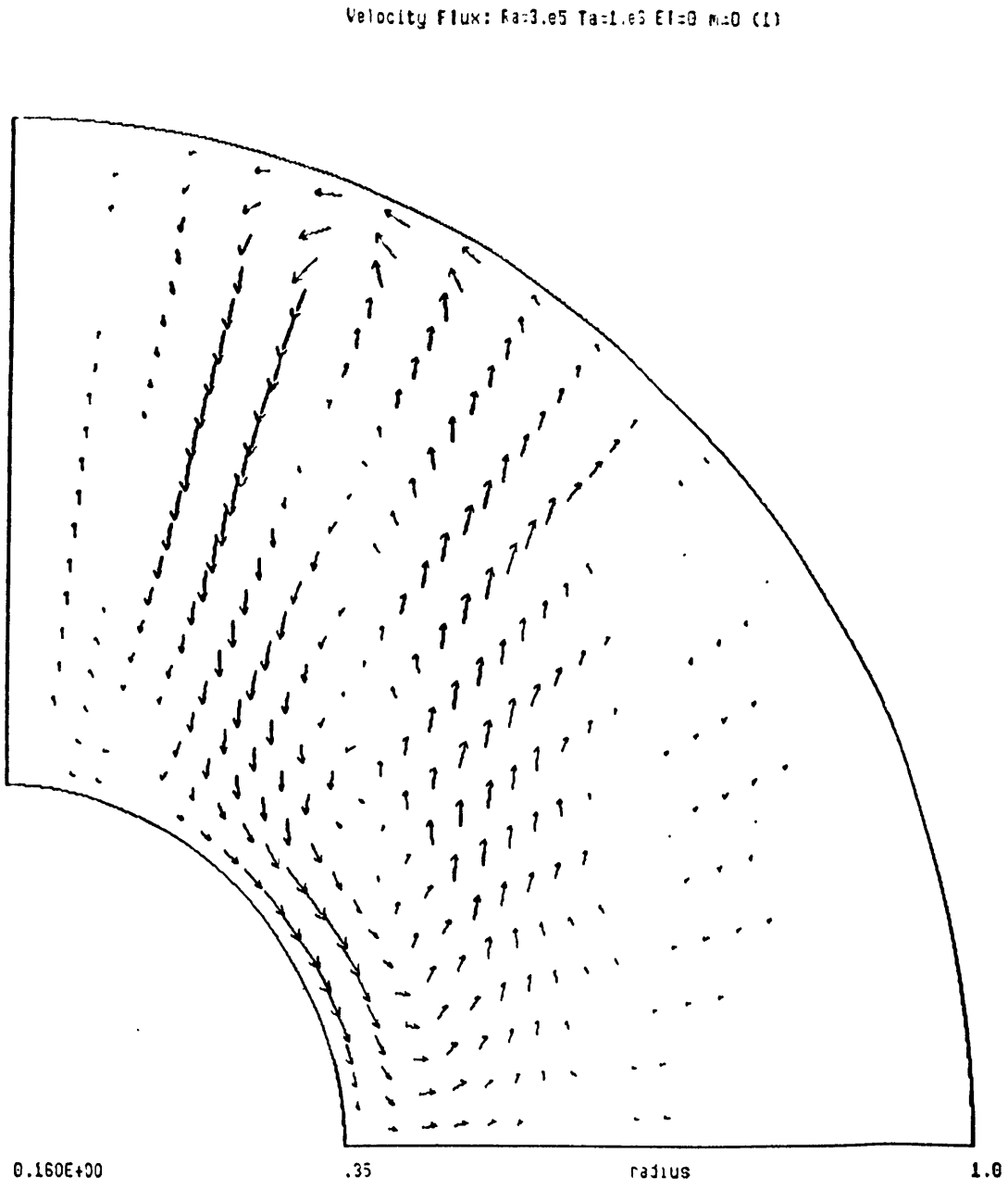

Figure 4.3 As for Figure 4.1 but for Ra = 3 x 10^5. The flow is primarily $\ell = 3$.

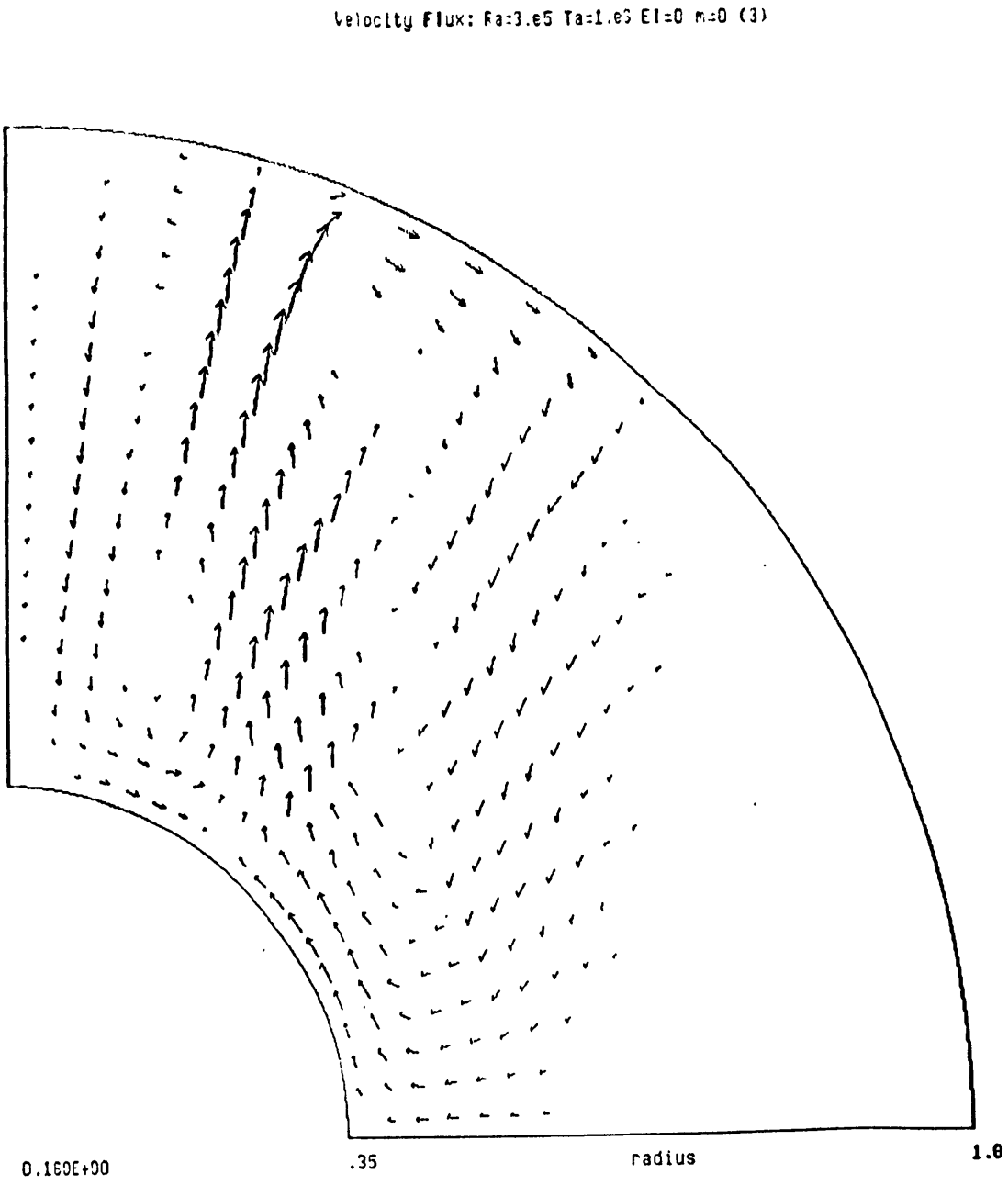

Figure 4.4 As for Figure 4.3 but using starting model 3 for x_0. Figure 4.4 clearly represents a different mode than does Figure 4.3.

z-independence and their prevalence in the polar regions, all converged modes show the effects of rapid rotation. As the Rayleigh number rises to $Ra = 10^6$, we are no longer able to obtain converged solutions, at least within 40 iteration steps. As for when $Ta = 0$, this is presumably due to a cascade to smaller scales, and the likely accompanying time-dependence.

When we increase the Taylor number to $Ta = 4 \times 10^6$, we observe behavior similar to that at $Ta = 10^6$, except that the rotational effects are yet more apparent. At $Ta = 4 \times 10^6$, the critical Rayleigh number rises to $Ra_c = 3.2 \times 10^5$. In Figure 4.5 we show the axisymmetric $\ell = 1$ convection that occurs at Ra_c. It is qualitatively similar to that at Ra_c for $Ta = 10^6$, except that it is perhaps more confined to the polar region, as one might expect. However, we can also begin to see the effect of numerical inaccuracy at this higher Ta, for which the length scale of motions becomes smaller. The $N = L = 8$ grid does not provide completely sufficient resolution of the small length scale, with the result that the solutions display spurious spatial ocillations. We can see this in Figure 4.5, particularly in that part of the convective cell in which fluid is rising.

For a finer grid with $N = L = 12$ we find $Ra_c = 2.2 \times 10^5$ at $Ta = 10^6$, as compared with $Ra_c = 1.7 \times 10^5$ on the 8×8 grid. As for at $Ta = 0$, a coarser grid tends to yield convection at a lower value of Ra than does a finer one. For $Ta = 4 \times 10^6$ the 12×12 grid yields $Ra_c = 4.6 \times 10^5$, thirty percent higher than $Ra_c = 3.2 \times 10^5$ on the 8×8 grid. In Figure 4.6 we show the convection that occurs at Ra_c for $Ta = 4 \times 10^6$ on the finer grid. Note that the finer grid eliminates the spurious spatial oscillations of the coarser grid. We can see that as the rotation rate increases an accurate solution requires a finer grid, as expected. We do not solve the equations (4.4) - (4.7) with non-zero Ta on a yet finer grid with $N = L = 14$, so we cannot yet be sure of the accuracy of our solutions. Nevertheless, we are quite confident that we have captured the essential behavior of the converged solutions.

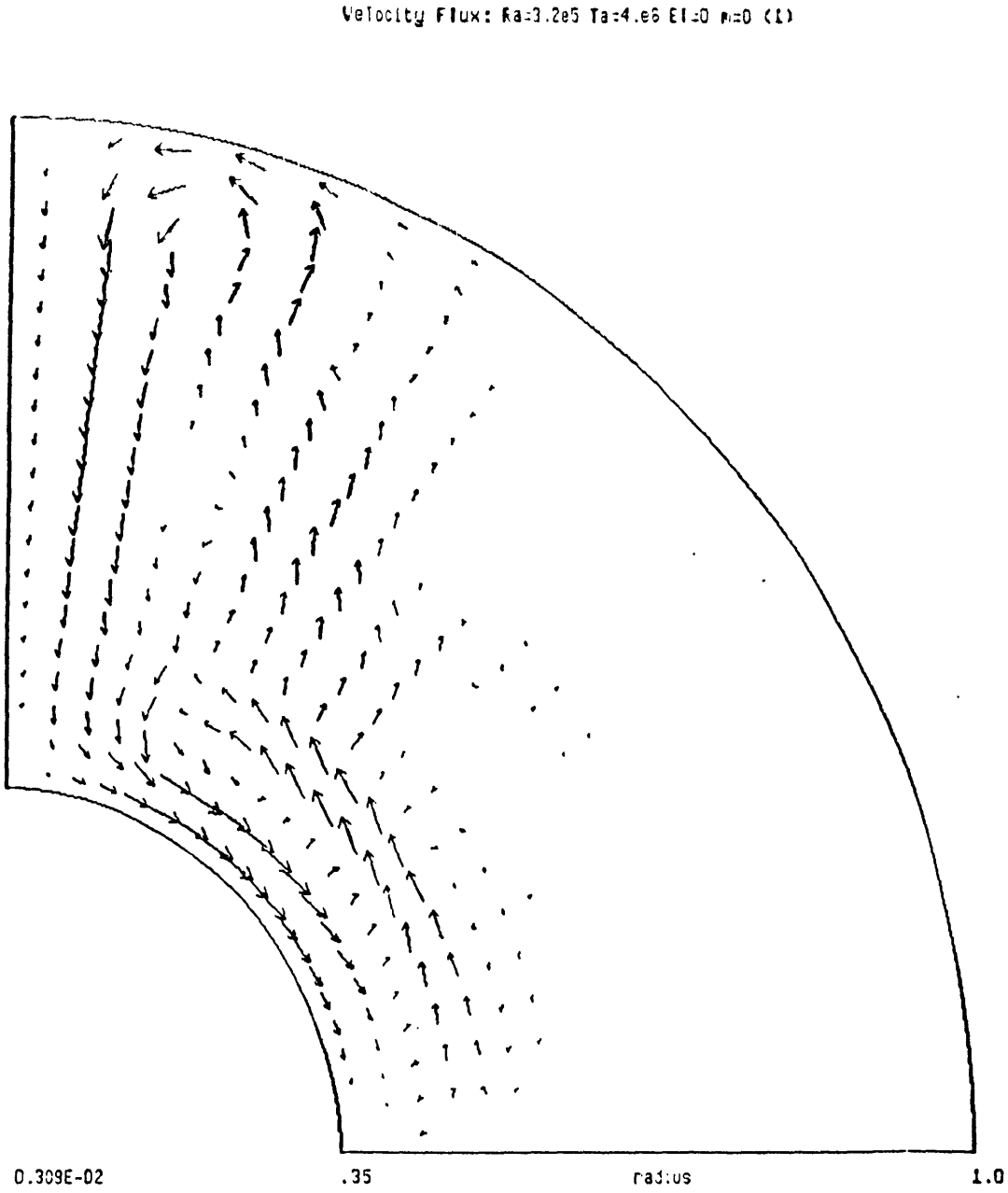

Figure 4.5 As for Figure 4.1 but with Ta = 4 x 10^6, so that Ra_c rises to 3.2 x 10^5. At this higher Ta the effects of numerical inaccuracy become apparent.

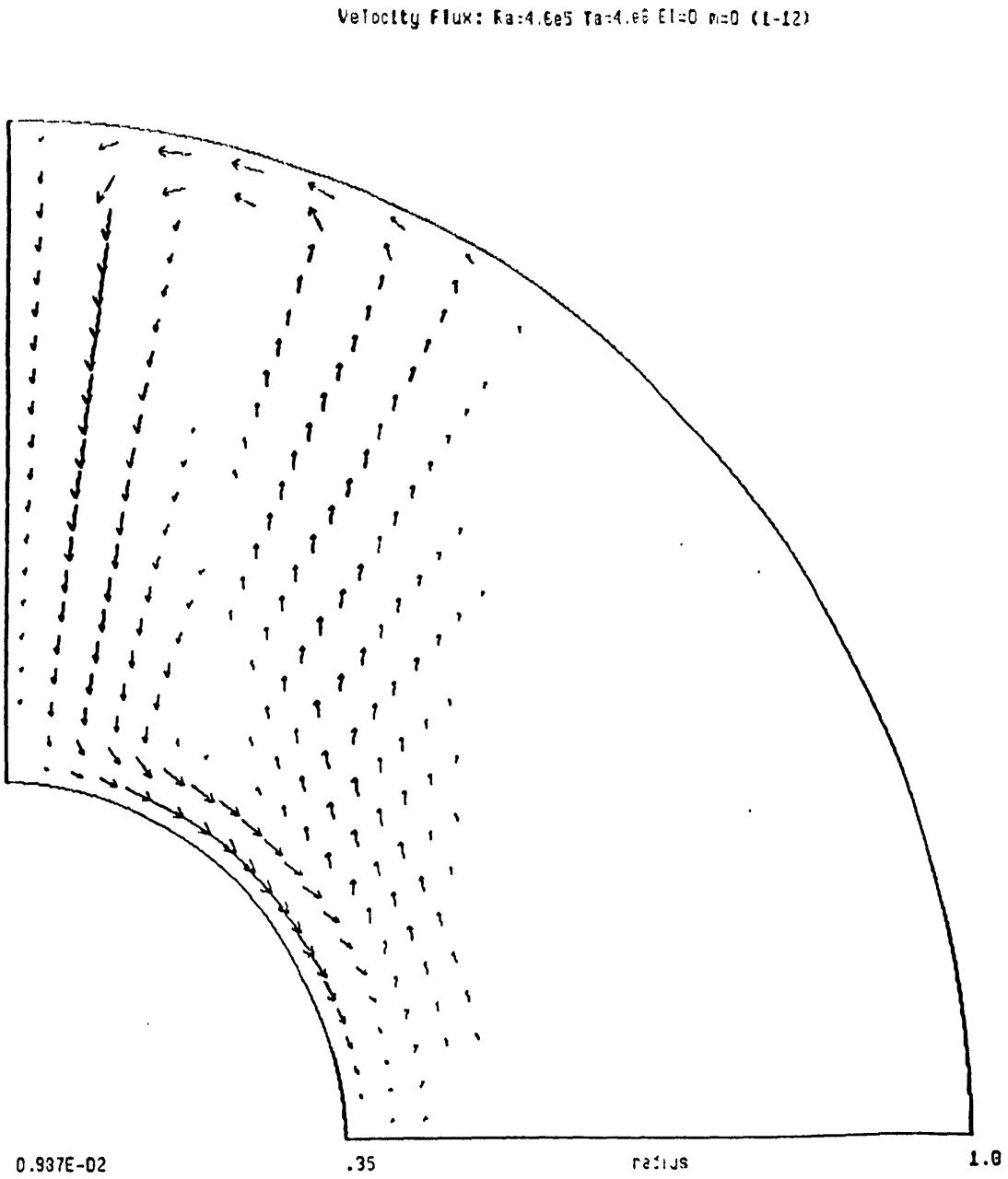

Figure 4.6 As for Figure 4.5 but with N = L = 12. For the finer grid $Ra_c = 4.6 \times 10^5$. The finer grid eliminates the spurious spatial oscillations of Figure 4.5.

Unlike at Ta = 0, we cannot obtain solutions with a ϕ-dependence, even as we progress to higher Ra. Although Busse and Cuong (1977) demonstrated that the columnar equatorial modes, which necessarily have a ϕ-dependence, occur for a lower Ra than do the polar modes, which can be axisymmetric (though must not necessarily be), we converge only to the polar modes. Why have we been unable to obtain any solutions with cos $m\phi$ and sin $m\phi$ components? The most likely explanation of course is that modes with a ϕ-dependence, *i.e.*, the columnar equatorial modes, are not time-independent, but rather, exhibit a drift. At infinite Prandtl number Pr, the only explicity time-dependent term is $\partial c/\partial t$, which we have dropped from (4.7). We can restore this term, assign a drift frequency ω, and search for converged, steadily eastwardly drifting equatorial modes. Looking for solutions near the critical Rayleigh number for the columnar equatorial modes (which we henceforth denote Ra_{ceq} to distinguish it from Ra_c that we find using our iterative procedure) at Ta = 10^6, we choose the appropriate ω_c from the asymptotic relation $\omega_c = .23\ Ta^{1/3}$ of Zhang (1991). However, we are still unable to obtain the equatorial modes, but instead, obtain the conduction solution.

Since we assign the drift frequency ω rather than have it come out of the analysis, even with guidance we must be extraordinarily lucky to pick the exact drift frequency that would yield the equatorial modes. Moreover, Zhang and Busse (1990) found that ω is a strong function of Ra at infinite Pr, so the guidance may be of somewhat limited help. However, there is second though related explanation for our inability to obtain steady equatorial modes. Cardin and Olson (1992) demonstrated experimentally and numerically that steadily drifting solutions persist only to within a few times critical (beyond the range of Zhang and Busse's steadily drifting solutions), beyond which the time-dependence becomes more complicated, eventually becoming aperiodic. Hence, the columnar convection that occurs near Ra_{ceq} (similar to Figure 3.1 in a sphere) may not persist for a very wide range in Ra. In some rough sense our inability to find the steadily drifting

equatorial modes using our iterative method may be related to the physical reality that these modes do not exist but for a very limited parameter range.

In light of the absence of equatorial modes, we must consider the stability with respect to time perturbations of the polar modes. Given that the equatorial modes occur for Ra lower than for the polar modes, it seems likely that our converged solutions are unstable with respect to time. Thus, the purely axisymmetric, steady polar modes that we have obtained as converged solutions are probably not physically realizable. On other hand, Gilman (1977) found that as Ra rises above Ra_{ceq}, there is a shift in the kinetic energy spectrum towards lower azimuthal wavenumber m (in addition to the Reynolds stress induced m = 0 differential rotation that occurs at finite Pr), and the convection begins to fill the sphere, both indicating that the polar modes are becoming increasingly important relative to the equatorial modes. Cardin and Olson (1992) did not obtain polar convection in their laboratory and numerical experiments in a spherical shell at large Ra because they simulated only the component of gravity perpendicular to the rotation axis. While a dynamically valid approximation near Ra_{ceq}, it is very likely not valid for Ra large enough such that buoyancy can overcome the rotational constraint at high latitudes.

4.3 Solutions in an infinite annulus

Spherical boundaries induce an azimuthal drift of convective columns via the Rossby wave mechanism of Figure 3.2. They also make the convective columns inefficient for transporting buoyancy by imposing a small radial length scale, which leads to the rapid onset with increasing Ra of highly time-dependent convection (Cardin and Olson, 1992). For one or both of these reasons we are unable to obtain three-dimensional convective columns in a spherical shell. We therefore feel it might be instructive to study rotating convection in an infinite annulus, which avoids interference from spherical boundaries, and forces convective solutions to have a ϕ-dependence. We will also study rotating

magnetoconvection in an infinite annulus. The main objective of this section is to establish our ability to find steady columnar convective solutions in the simpler geometry of an infinite annulus, and to understand the effect of a magnetic field on these 'equatorial' modes.

In the absence of a magnetic field, the equations governing steady convection at infinite Prandtl number in an infinite annulus remain (4.4) - (4.7), but we here solve them in cylindrical coordinates (s,ϕ,z), with $\hat{s}$ the unit vector in the cylindrical radial direction, $\hat{\phi}$ the unit vector in the eastward direction, and $\hat{z}$ the unit vector in the direction parallel to the axis of symmetry of the coaxial cylinders. As in the spherical shell, we flux buoyancy into the fluid uniformly along the inner cylinder $s = \eta = .35$, and remove a concomitant flux uniformly along the outer boundary $s = 1$. The rotation axis $\hat{\Omega} = \hat{z}$ lies along $s = 0$, and gravity $\hat{g} = \hat{s}$ is thus everywhere directed perpendicular to the rotation axis. The boundary conditions (3.26) remain unchanged on the rigid boundaries at $s = \eta$ and $s = 1$, where (u,v,w) now represent the velocity components in the (s,ϕ,z) directions. We again assume exp $im\phi$ dependence, and in the z-direction we assume exp ikz dependence, where k is the z-wavenumber, not necessarily an integer. As in the azimuthal direction, we allow for the interaction of sin kz and cos kz solutions to modify the $k = 0$ solution, but we ignore the sin 2kz and cos 2kz solutions. We thereby reduce the numerical problem to finding the s-dependence of the nine retained Fourier components for each of the scalar unknowns: the velocity (u,v,w), the pressure p, the buoyancy c, and the radial buoyancy gradient f_s. We find their s-dependence on a staggered grid with $N = 8$ radial points, using the same iterative procedure as for the spherical shell. For each iteration sequence we must choose Ra, Ta, m, and k.

At $Ta = 10^6$ we cannot find any convergent solutions that contain a non-zero k-component. This of course reflects the proclivity of the rapidly rotating infinite annulus to eliminate any z-dependence. Unlike in the sphere, we easily obtain non-drifting convection with non-zero m-components, *i.e.*, columns, provided Ra is high enough. The overall

lowest critical Rayleigh number occurs for m = 1, for which $Ra_{c1} = 2.0 \times 10^4$. As the assigned m rises, Ra_{cm} rises, so that $Ra_{c2} = 2.5 \times 10^4$, $Ra_{c4} = 3.6 \times 10^4$, and so forth. This preference for large scale flow in the annulus demonstrates the restrictive geometry of the sphere. Moreover, in the absence of spherical boundaries the presence and strength of rotation does not affect Ra_{cm}, with $Ra_{c1} = 2.0 \times 10^4$ at $Ta = 4 \times 10^6$, as at $Ta = 10^6$. As Ta rises, the pressure gradient simply rises to balance the increasing Coriolis force.

For a given Ra we can obtain convective solutions only for $m < m*$, and for $m > m*$ we obtain the conduction solution. The larger Ra is, the larger is $m*$. In Figure 4.7 we show the velocity flux in a one-quarter cross-section of the annulus for $Ra = 10^5$, $Ta = 10^6$, and m = 4. In this plan view the columnar structure of the flow is evident. The absence of a net azimuthal flow is a result of the infinite Prandtl number. The solution that we show in Figure 4.7 we obtain independent of the starting model and damping scheme. Within a few percent we also obtain the same solution on a grid with 12 radial points.

At $Ra = 10^6$, $Ta = 10^6$, and m = 4, and a starting model that consists of the converged solution at $Ra = 10^5$, we find a convergent solution that looks qualitatively like that of Figure 4.7, but with a larger amplitude. However, as discussed above and in Section 3.4, we have ignored the sin $2m\phi$ and cos $2m\phi$ part of the solution, an approximation whose validity we will now examine. At $Ra = 10^5$, $Ta = 10^6$, and m = 4, the ratio of the non-axisymmetric radial buoyancy gradient to the axisymmetric radial buoyancy gradient, $|f_{sm}/f_{so}|$, is less than one percent at each grid point, indicating that the non-linearity is not too great and that little power is transferred to the 2m wavelength. On the other hand, at $Ra = 10^6$, $|f_{sm}/f_{so}|$ is about one hundred percent in the interior of the fluid, so that considerable power is transferred to the smaller lengthscale, which we do not account for in our analysis. Moreover, if we begin with a more arbitrary starting model, we find a convergent solution at $Ra = 10^6$, $Ta = 10^6$, and m = 4 that exhibits a double columnar structure in radius (Figure 4.8), which is also clearly an attempt to achieve a

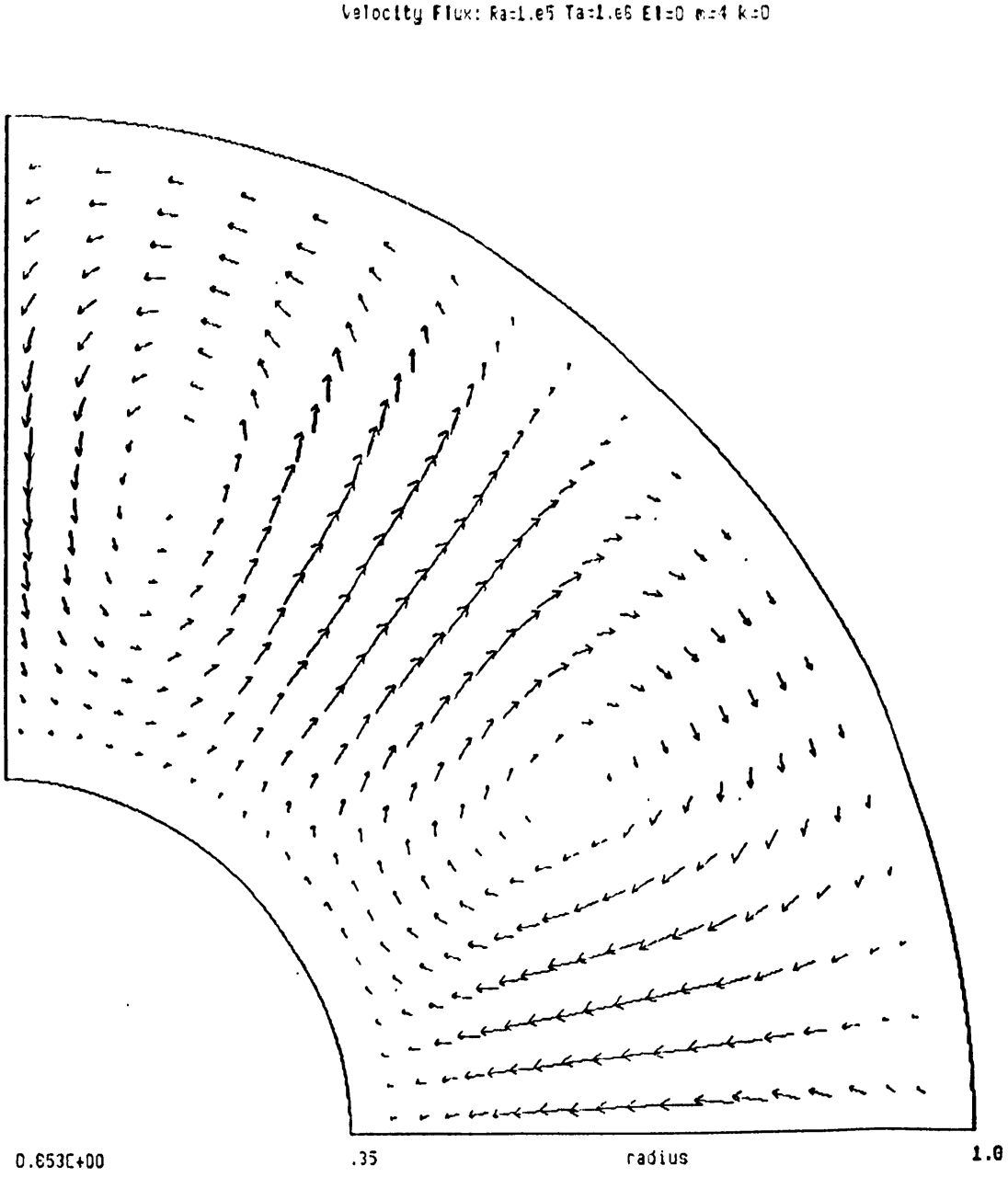

Figure 4.7 Fluid velocity flux arrows in a one-quarter cross-section of the cylindrical annulus with $\eta = .35$ for $Ra = 10^5$, $Ta = 10^6$, $El = 0$, and $Pr = \infty$. The $m = 4$, $k = 0$ flow has no component in the z-direction. For plotting purposes we linearly interpolate fluxes from the $N = 8$ grid. The number at the bottom left of the figure represents the maximum flux v_{max}. If the flux at a point is less than one-tenth v_{max}, we do not plot its flux arrow. The columnar nature of the flow is evident.

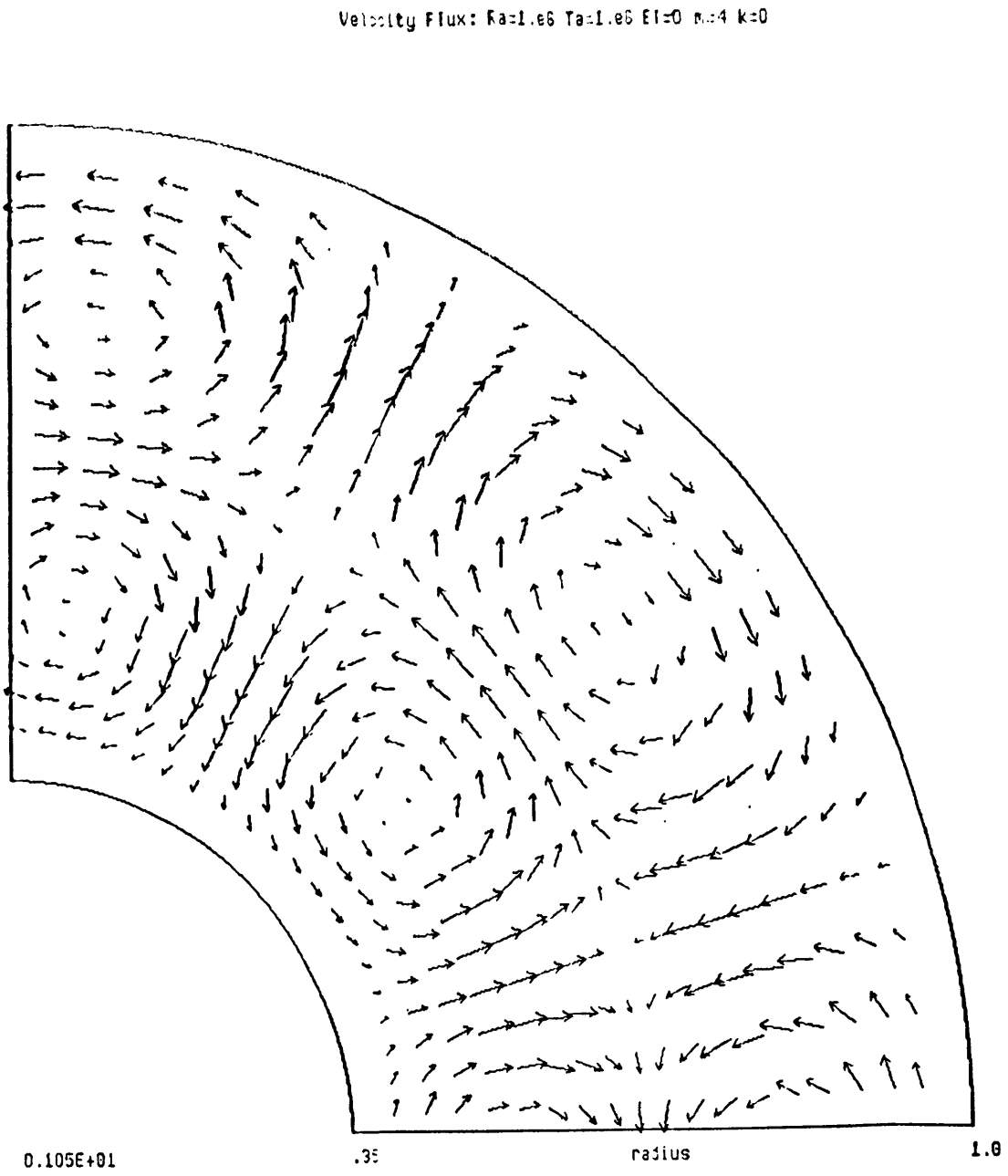

Figure 4.8 As for Figure 4.7 but for Ra = 10^6. We obtain this double columnar structure when we start with an arbitrary model $\mathbf{x}_0$, but when we start with $\mathbf{x}_0$ set to the converged solution at Ra = 10^5 we obtain a single columnar structure.

smaller length scale. In any case, for such large Ra we begin to doubt the stability of the steady, converged solutions with respect to time perturbations.

Before we study the effects of an imposed magnetic field on rotating convection in a spherical shell, we will study rotating magnetoconvection in an infinite annulus with $\eta = .35$ (and $q = 1$). The solid in $s < \eta$ and the fluid in $\eta < s < 1$ are of equal and finite electrical conductivity, and the solid in $s > 1$ is an electrical insulator. The finite electrical conductivity of the fluid adds the magnetic field $\mathbf{B} = (b_s, b_\phi, b_z)$ and electric field $\mathbf{e} = (e_s, e_\phi, e_z)$ as unknowns to the system. Thus, in the fluid in $\eta < s < 1$ we solve the three components of (4.1), the scalar equation (4.2), the ϕ-component of (4.3), and also the scalar equation

$$\nabla \cdot \mathbf{e} = 0, \tag{4.8}$$

in addition to the convective equations with the Lorentz force, (4.4) - (4.7). In $s < \eta$ we solve (4.1) with the fluid advection term $\mathbf{v} \times \mathbf{B}$ omitted, (4.2), the ϕ-component of (4.3), and (4.8). In the electrical insulator $s > 1$ the magnetic and electric fields must match to potential fields. Alternatively in $s > 1$, $\mathbf{B}$ and $\mathbf{e}$ must satisfy (4.1) with the term $(\mathbf{e} + \mathbf{v} \times \mathbf{B})$ omitted (*i.e.*, the electric current density $\mathbf{j} = \mathbf{0}$), (4.2), the ϕ-component of (4.3), and (4.8), with the condition that $\mathbf{B}$ and $\mathbf{e}$ approach zero as $s \to \infty$.

Although the potential fields in $s > 1$ have an analytic solution, we choose to numerically solve for $\mathbf{B}$ and $\mathbf{e}$ in this region using a graded net and requiring $\mathbf{B} = \mathbf{e} = \mathbf{0}$ at some arbitrarily large radius, such as $s = 100$. Although such a formulation increases the size of the matrix in (3.29) that we must invert at each iterative step, and although the impedance boundary conditions at $s = 1$ that follow from the analytic solution in $s > 1$ are relatively easy to implement in cylindrical geometry, they require a spectral transform for the colatitudinal direction in the spherical shell. Thus, for simplicity and in preparation for

the spherical shell we numerically find **B** and **e** in $s > 1$, as we will for $r > 1$ in the spherical shell. Across $s = 0$ the symmetry conditions for $m = 0$ and $m \geq 2$ are:

$$b_s = b_\phi = \partial b_z/\partial s = e_s = e_\phi = \partial e_z/\partial s = 0, \tag{4.9}$$

with the opposite conditions ($\partial b_s/\partial s = \partial b_\phi/\partial s = b_z = \partial e_s/\partial s = \partial e_\phi/\partial s = e_z = 0$) holding for $m = 1$. As before the fluid velocity (u,v,w) must satisfy the rigid wall, no slip conditions (3.26) on $s = \eta$ and $s = 1$. As for the purely hydrodynamical problem we assume exp $im\phi$ and exp ikz dependence, and numerically solve for the radial dependence on a staggered grid with four points (evenly spaced) in $0 < s < \eta$, eight points (evenly spaced) in $\eta < s < 1$, and six points (spaced geometrically larger with increasing s) in $1 < s < 100$.

Ideally we should not need to impose a magnetic field, but rather have one emerge as part of a steady finite-amplitude convective solution. However, creating a steady dynamo is not the main objective of this section. Hence we will impose a fixed magnetic field $\mathbf{B}_o$, though we retain all the non-linear terms in (4.1) - (4.8). We will impose two different magnetic fields: a uniform $\mathbf{B}_o = \hat{\mathbf{z}}$ and a toroidal field $\mathbf{B}_o = (1/s)\hat{\phi}$. Experimentally we could set up the former by building a solenoid about our rotating annulus and the latter by placing a wire along $s = 0$. Note that since we are primarily interested in convectively-driven instabilities and not magnetically-driven instabilities, the exact functional dependence of $\mathbf{B}_o$ is not crucial (Eltayeb and Kumar, 1977, Drew, 1991). As for the non-magnetic problem, $\hat{\Omega} = \hat{\mathbf{z}}$ lies along $s = 0$, and gravity $\hat{\mathbf{g}} = \hat{\mathbf{s}}$.

A fixed $\mathbf{B}_o = \hat{\mathbf{z}}$ should not affect the value of Ra_{cm} nor the the form of the convective columns at Ra_{cm} since $\mathbf{B}_o$ is parallel to $\hat{\Omega}$, both perpendicular to $\hat{\mathbf{g}}$. We observe this at $Ta = 10^6$ for both $El = 10^{-1}$ and $El = 10^0$ and $m = 4$ and $m = 6$. Moreover, the convection at $Ra = 10^5 > Ra_{c6} > Ra_{c4}$ remains aligned parallel to the z-axis, with no z-dependence (despite trying $k = 1$, 2, 4, and 10 and several starting models) and no flow

w in the z-direction. The convective columns create neither b_s nor b_ϕ, but simply drag b_z field lines independently of z. The non-linear interaction of $u(\phi)$ and $v(\phi)$ with $b_z(\phi)$ creates an axisymmetric b_z that effectively opposes the imposed $\mathbf{B}_0$ within the fluid. The regions of dense and sparse b_z field lines create no net Lorentz force to modify the fluid motions.

The choice of $\mathbf{B}_0 = (1/s)\hat{\phi}$ is more interesting in the infinite annulus. Once again, in the presence of rapid rotation we cannot obtain solutions that contain a non-zero k component, despite trying several z-wavenumbers and several starting models. At $Ta = 10^6$ we find that an azimuthal magnetic field at a non-zero El delays the onset of convection to higher Ra for both m = 4 and m = 6. Thus, whereas for El = 0, $Ra_{c4} = 3.6 \times 10^4$, for $El = 10^{-1}$, $Ra_{c4} = 9. \times 10^4$, and for $El = 4 \times 10^{-1}$, $Ra_{c4} = 3. \times 10^5$. Similarly, for El = 0, $Ra_{c6} = 8. \times 10^4$, but for $El = 10^{-1}$, $Ra_{c6} = 2. \times 10^5$. We observe consistent behavior for $Ra > Ra_{cm}$, in that an azimuthal magnetic field at a non-zero El lessens the amplitude of convection for a given Ra, Ta, and m. For instance, compare the amplitude of the velocity flux in Figure 4.9 at $El = 10^{-1}$ with that of Figure 4.7 at El = 0, both at $Ra = 10^5$, $Ta = 10^6$, and m = 4. In Figure 4.10 we show the total magnetic flux of the imposed field $\mathbf{B}_0$ plus that field created by the convective motions in Figure 4.9.

In the infinite annulus with gravity $\hat{\mathbf{g}} = \hat{\mathbf{s}}$ the rotation $\hat{\Omega} = \hat{\mathbf{z}}$ imposes no constraint on convection, and the presence of a magnetic field aligned perpendicularly to both $\hat{\Omega}$ and $\hat{\mathbf{g}}$ does not promote convection, but rather, inhibits it. This differs from the sphere, in which the combination of rotation and spherical boundaries limits the length scale and effectiveness of convection, so that an imposed toroidal magnetic field promotes convection (Eltayeb and Kumar, 1977, Fearn, 1979). Thus, it is both the presence of spherical boundaries and the relative orientation of $\hat{\Omega}$, $\hat{\mathbf{g}}$, and $\mathbf{B}_0$ near the equator that allows a magnetic field to enhance rotating magnetoconvection in a sphere. Through their absence, we have seen in this section the importance of spherical boundaries for limiting the length scale of rotating convection and for inducing the columnar convection that occurs near Ra_{ceq} to behave as a Rossby wave. We have also observed the inhibiting role that a

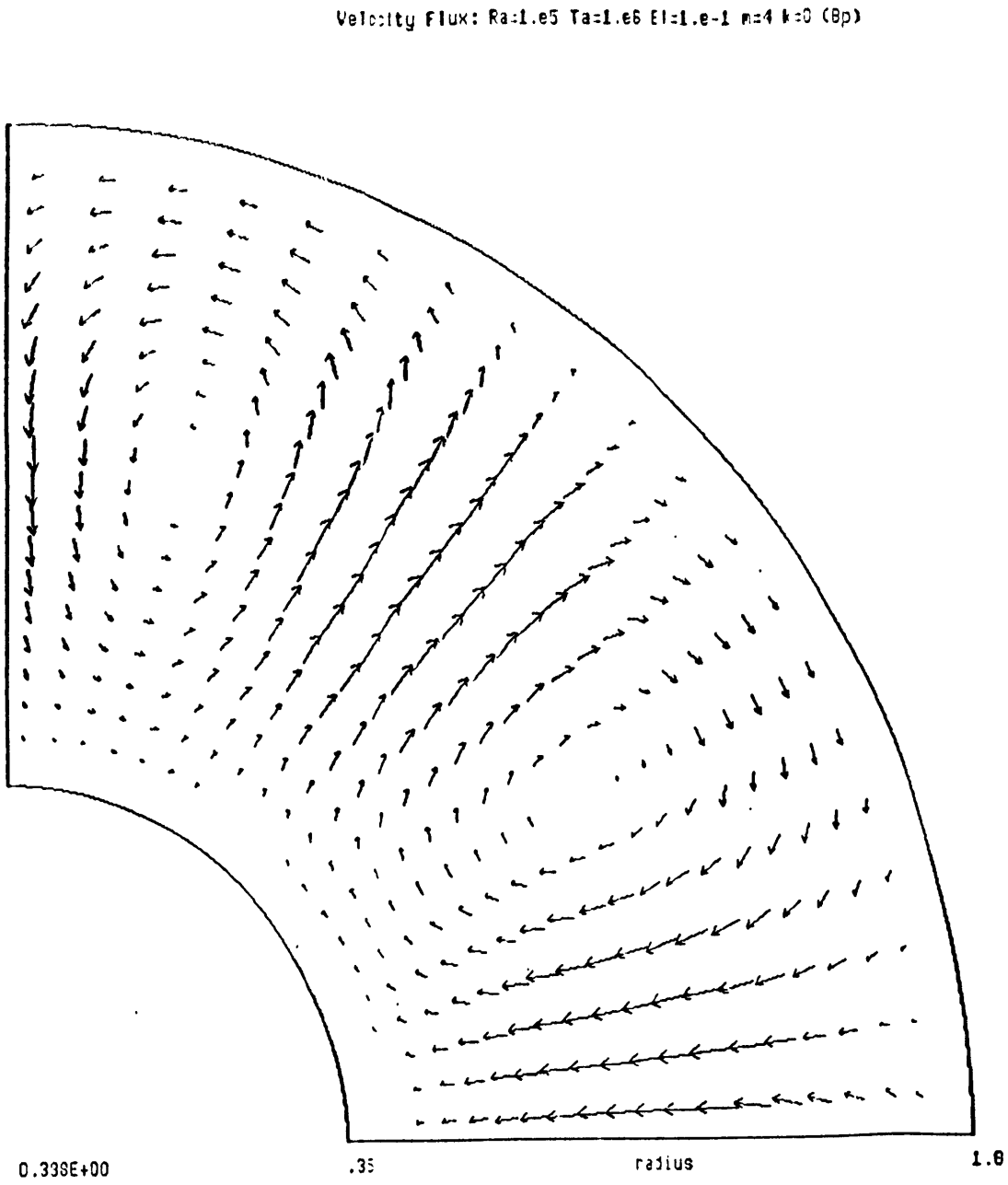

Figure 4.9 As for Figure 4.7 but for El = 10^{-1} and q = 1, and an imposed magnetic field $\mathbf{B_0} = (1/s)\,\hat{\phi}$. We compute the solution on a grid with four points in $0 < s < \eta$, eight points in $\eta < s < 1$, and six points in $1 < s < 100$. In the cylindrical annulus the toroidal magnetic field has a constraining effect on the columnar modes, which is most noticeable in the reduced fluid velocity flux from Figure 4.7.

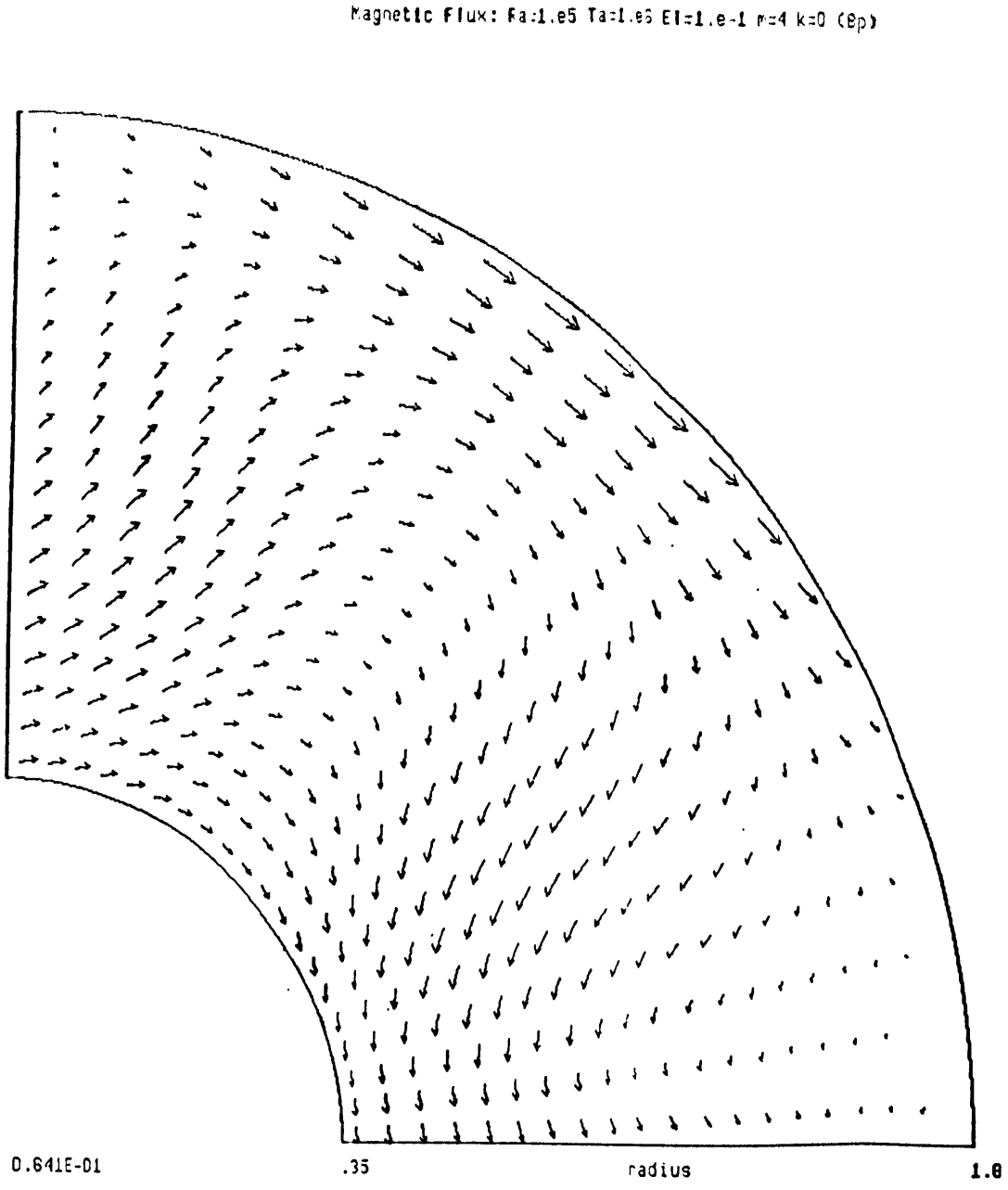

Figure 4.10 The total magnetic flux within the one-quarter cross-section of the fluid annulus for the parameters of Figure 4.9. The motions of Figure 4.9 create no magnetic flux in the z-direction.

magnetic field can have on rotating convection. Finally, we note here that our attempts to achieve dynamo action fail in that we are unable to find converged solutions that have a non-zero magnetic field when we do not impose a magnetic field. This failure reflects the lack of a z-velocity w that would give the convective columns the helicity necessary to generate dynamo action (Moffatt, 1978).

4.4 Solutions in a spherical shell for non-zero Ta and non-zero El

In this section we return to the study of free convection in a rotating shell, $\eta = .35$, but with an imposed magnetic field. In Section 4.2 we witnessed the difficulty of finding steady, non-axisymmetric solutions in a spherical shell with El = 0, but Ta non-zero. This difficulty may be due to convection near Ra_{ceq} appearing as a Rossby wave, or to the inefficiency and rapid onset of small scale, aperiodically time-dependent convection with increasing Ra. In either case, the time-dependence at even moderate Ra is a result of the spherical boundaries. Although an imposed toroidal magnetic field allows the convection in a rotating spherical shell near Ra_{ceq} to be larger scale, that convection appears as a MAC wave (Eltayeb and Kumar, 1977), so that finding steady, non-axisymmetric solutions still seems unlikely. We therefore concentrate on the influence of an imposed poloidal magnetic field on axisymmetric rotating convection, *i.e.*, the polar modes of Section 4.2. While Ra_c for the polar modes is greater than the critical Ra for the non-axisymmetric equatorial modes, Ra_{ceq} (at least in the absence of magnetic fields), the polar modes may play a role in supercritical convection (Gilman, 1977), so it is important to understand the influence an imposed magnetic field has on them.

In searching for steady, axisymmetric solutions we can set $e_\phi = 0$, since a non-zero e_ϕ would result in a non-zero $\nabla \times \mathbf{e}$ and hence a non-steady $\mathbf{B}$. Moreover, in the insulating region in $r > \eta$ we can set $b_\phi = 0$, since a non-zero b_ϕ would result in a non-zero electric curent density $\mathbf{j}$. In the electrically conducting solid in $r < \eta$ and the equally electrically

conducting fluid in $\eta < r < 1$ we solve the three components of (4.1) ($\mathbf{v} \times \mathbf{B}$ is of course zero in $r < \eta$), the scalar equation (4.2), and the ϕ-component of (4.3) for $\mathbf{B} = (b_r, b_\theta, b_\phi)$ and $\mathbf{e} = (e_r, e_\theta, 0)$. In $\eta < r < 1$ we must also simultaneously solve (4.4) - (4.7). In $r > \eta$ we simply solve $\nabla \cdot \mathbf{B} = \nabla \cdot \mathbf{e} = (\nabla \times \mathbf{B})_\phi = (\nabla \times \mathbf{e})_\phi = 0$, with the condition that $\mathbf{B}$ and $\mathbf{e}$ approach zero as $r \rightarrow \infty$ ($\cong 100$). We solve these equations numerically on the staggered grid in Figure 3.4 (with additional points in $r > 1$) using the iterative procedure discussed in detail in Section 3.4. The solutions we present are for $L = 8$ evenly spaced points in $0 < \theta < \pi/2$, and $N_i = 4$ evenly spaced points in $0 < r < \eta$, $N = 8$ evenly spaced points in $\eta < r < 1$, and $N_o = 6$ points whose spacing grows geometrically with r in $1 < r < 100$. For the axisymmetric problem this grid yields $K = 1146$ unknowns.

The fluid boundary conditions on $r = \eta$ and $r = 1$ are (3.26), the symmetry conditions about the pole (for $m = 0$) are (3.23), and the dipole symmetry conditions about the equator are (3.24). The electromagnetic boundary conditions (for $m = 0$) are $\mathbf{B} = \mathbf{e} = 0$ at $r = 100$ and $r = 0$. The $m = 0$ symmetry conditions about the pole are

$$\partial b_r/\partial\theta = b_\theta = b_\phi = \partial e_r/\partial\theta = e_\theta = 0 \text{ at } \theta = 0, \text{ and} \tag{4.10}$$

the dipole symmetry conditions about the equator are

$$b_r = \partial b_\theta/\partial\theta = b_\phi = \partial e_r/\partial\theta = e_\theta = 0 \text{ at } \theta = \pi/2. \tag{4.11}$$

Because the magnetic field due to a line current along $s = 0$, $\mathbf{B}_o = (1/r \sin\theta)\hat{\phi}$, contains a singularity within the fluid at $\theta = 0$ and is very large in the polar regions, it is not the best imposed magnetic field to work with. Previous studies (Eltayeb and Kumar, 1977, Fearn, 1979, Drew, 1991) have used an imposed field of the form $\mathbf{B}_o = (r \sin\theta)\hat{\phi}$. Such a $\mathbf{B}_o$ avoids any singularities, and is a simple toroidal field for which to study the linear

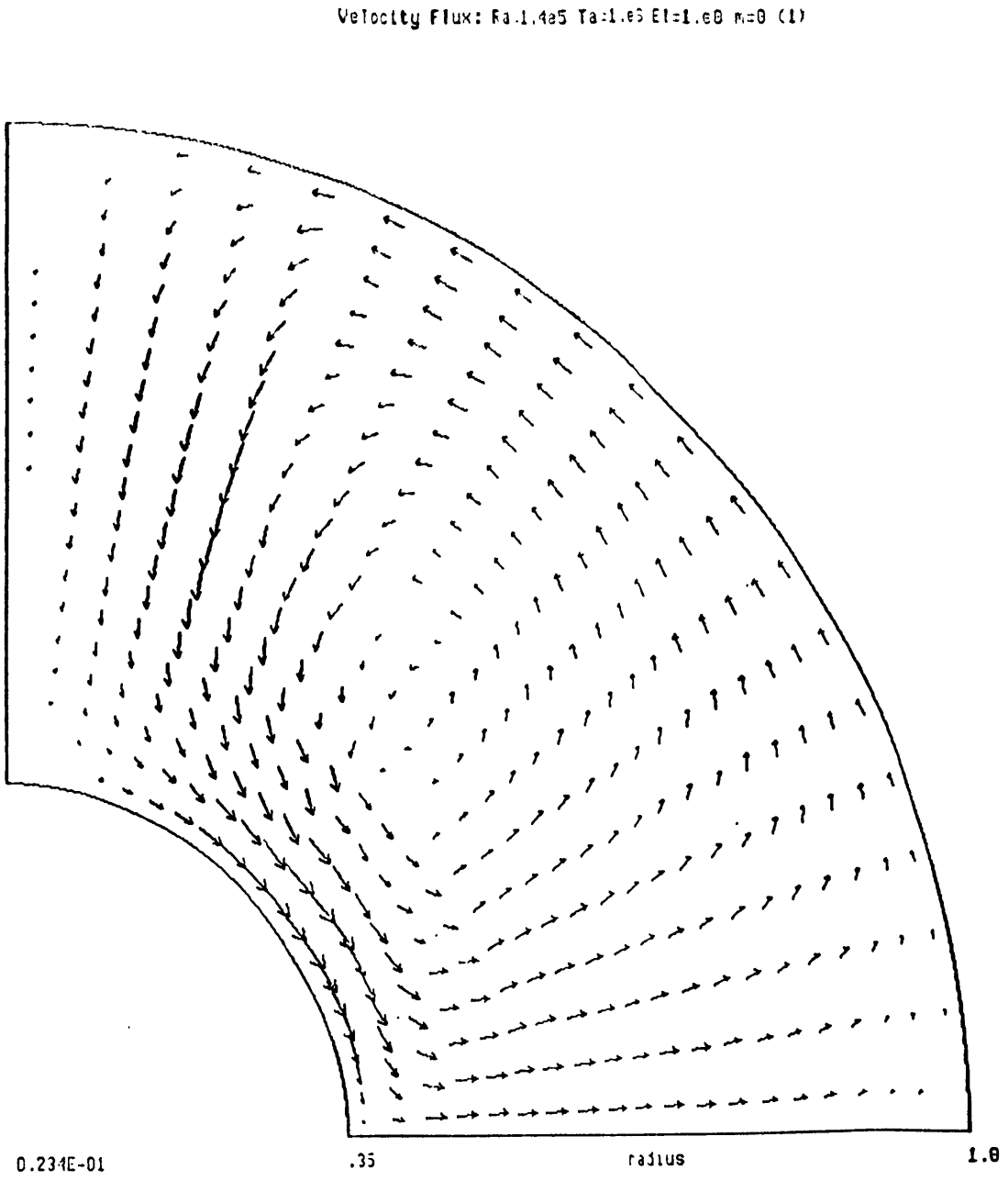

Figure 4.11 As for Figure 4.1 but for Ra = Ra_c = 1.4 x 10^5, El = 10^0 and q = 1 (and Ta = 10^6), and an imposed magnetic field $\mathbf{B}_0 = \hat{z}$. We compute the solution on a grid with four points ($N_i = 4$) in $0 < r < \eta$, eight points (N = 8) in $\eta < r < 1$, and six points ($N_o = 6$) in $1 < r < 100$, and L = 8. In the spherical shell the z-magnetic field has a liberating effect on the polar modes, which is most noticeable in the larger scale $\ell = 1$ flow than we picture in Figure 4.1.

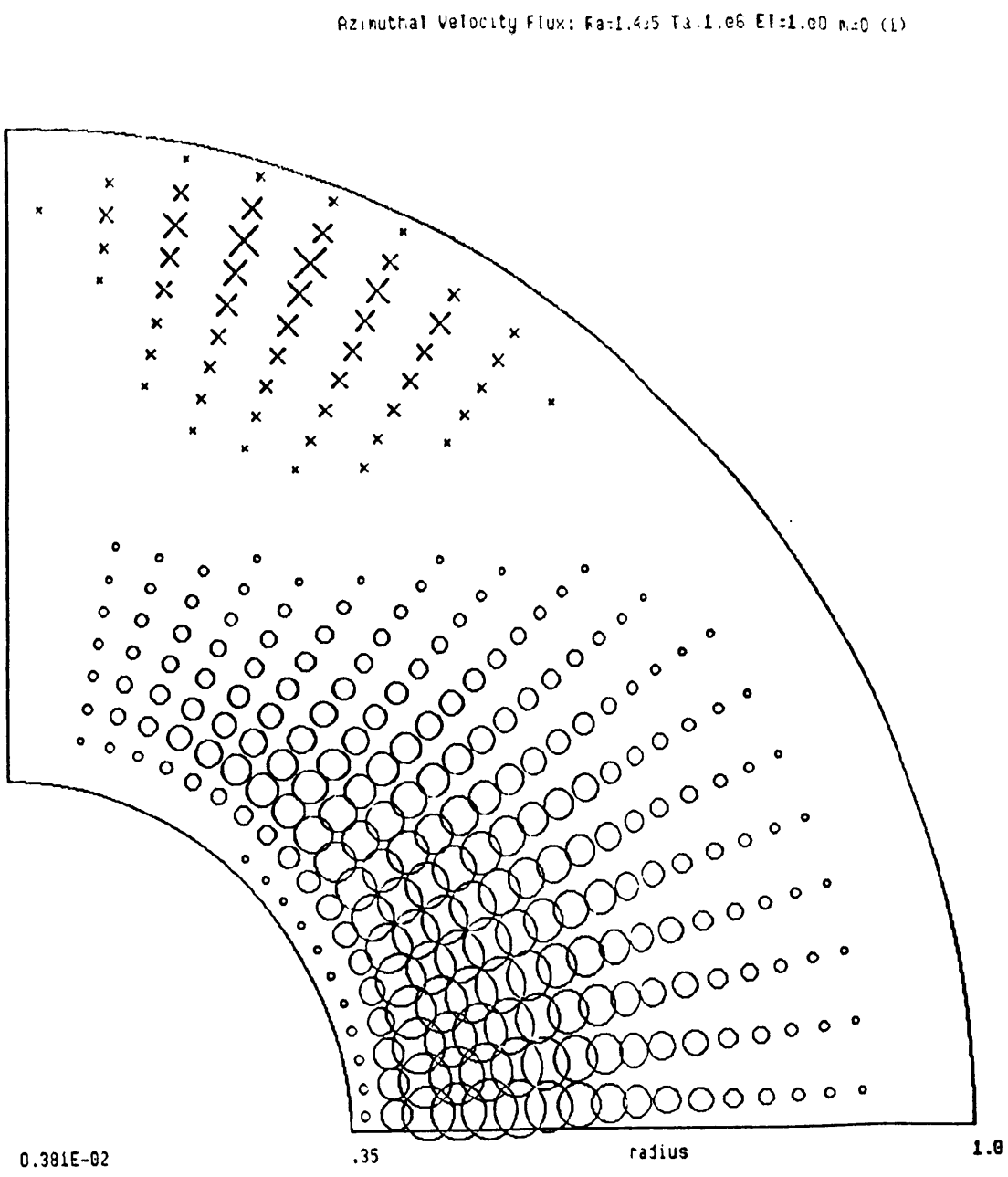

Figure 4.12 As for Figure 4.2, but for the parameters of Figure 4.11. With the addition of a magnetic field, the zonal velocity flux profile becomes smoother, and exhibits a net westward flow.

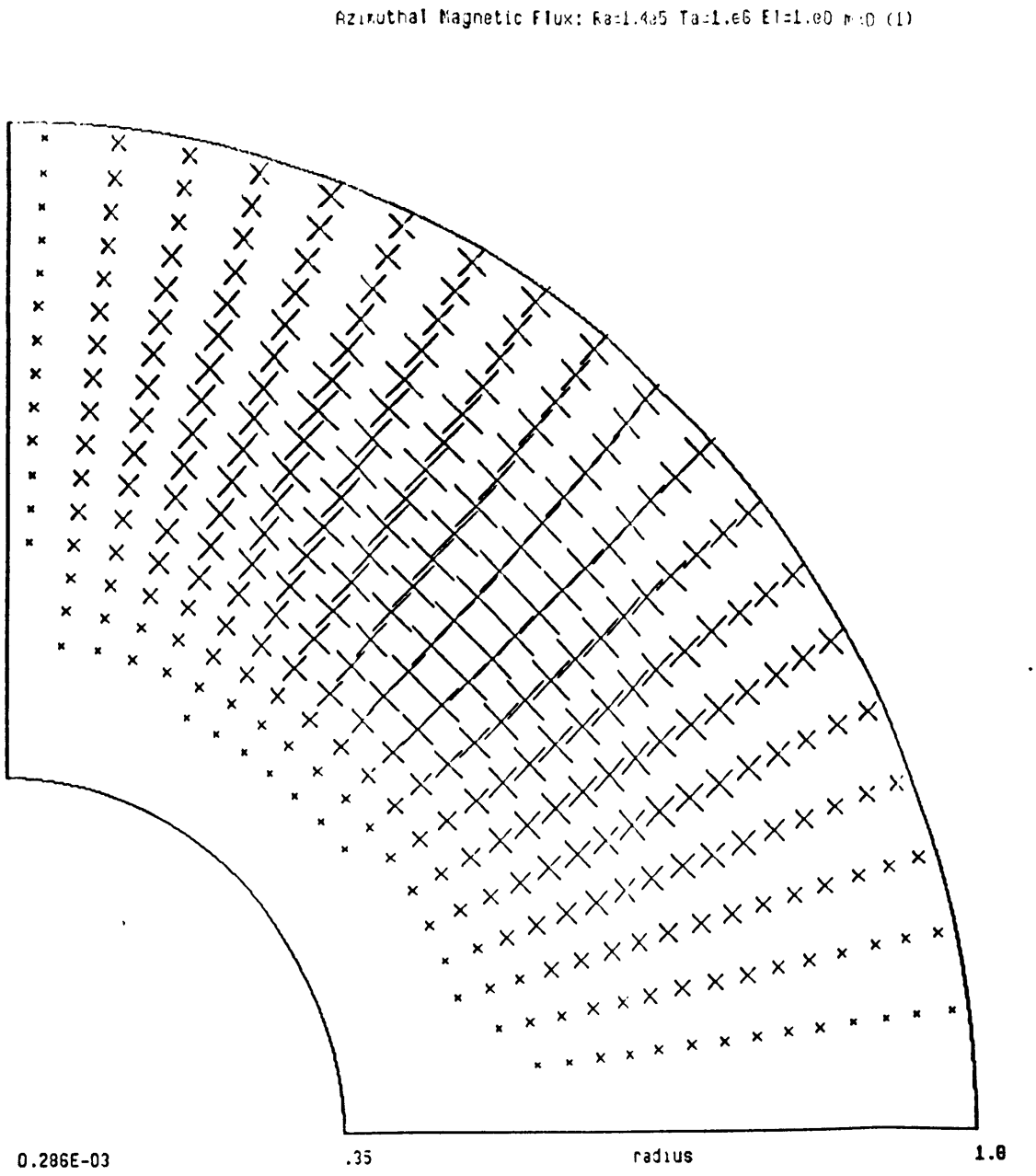

Figure 4.13 Axisymmetric azimuthal magnetic flux in a meridional slice of the northern hemispherical shell for the parameters of Figure 4.11. The x's represent eastward b_ϕ and the o's westward b_ϕ (none in this picture). Associated with b_ϕ is a j_r in the equatorial region, which acts with $\mathbf{B}_O = \hat{z}$ to yield a Lorentz force that opposes the Coriolis force, thereby allowing the broad profile of Figure 4.12.

stability of the conduction solution. However, it is not ideal for finite-amplitude studies because it requires an electric current that cannot be maintained in a physically plausible way. We therefore impose $\mathbf{B}_0 = \hat{z}$, which, since we are studying the influence of an imposed magnetic on the polar modes, is perhaps an interesting choice for $\mathbf{B}_0$ in light of the possibility of the model-Z dynamo (Braginsky and Roberts, 1987).

The presence of an imposed magnetic field $\mathbf{B}_0 = \hat{z}$ at non-zero El and Ta lowers Ra_c for axisymmetric convection from its value at zero El and non-zero Ta. Thus at $Ta = 10^6$, $Ra_c = 1.4 \times 10^5$ for $El = 10^0$, whereas $Ra_c = 1.7 \times 10^5$ for El = 0. For a weaker magnetic field, $El = 2.5 \times 10^{-1}$, or a stronger magnetic field, $El = 4.0 \times 10^0$, we converge to the conduction solution at $Ra = 1.4 \times 10^5$, supporting the idea that rotating magnetoconvection is most efficient at $El = 10^0$ (Fearn, 1979). Figure 4.11 shows the poloidal velocity flux in an arbitrary meridional slice of the northern hemisphere at Ra_c for $El = 10^0$. The $\ell = 1$ flow that occurs at Ra_c is large scale, and no longer aligned with the z-axis in the mainstream. The Lorentz force resulting from the cross-product of the radial electric current j_r (associated with the eastward b_ϕ that develops in the northern hemisphere from the westward advection of $\mathbf{B}_0$ (Figure 4.13)) with $\mathbf{B}_0$ opposes the Coriolis force, and radial flow in the equatorial zone becomes possible. The zonal velocity flux (Figure 4.12) associated with the increased radial flow exhibits a broader profile with more flow at larger radii than does the corresponding flow with El = 0 (Figure 4.2). We also note that a net westward azimuthal flow develops in response to the external torque due to $\mathbf{B}_0$.

Near Ra_c the converged solutions are independent of the starting model and details of the iteration sequence. However, as before, as Ra rises, the converged solutions become dependent on the starting model. Starting with the same model, let us compare supercritical solutions at $Ra = 4 \times 10^5$ and $Ta = 10^6$, for three values of El: $El = 2.5 \times 10^{-1}$ (Figure 4.14), $El = 10^0$ (Figure 4.15), and $El = 4.0 \times 10^0$ (Figure 4.16). For all three we obtain $\ell = 3$ convection, but once again we observe that $El = 10^0$ promotes convection most effectively. For Lorentz and Coriolis forces of comparable magnitude, the poloidal

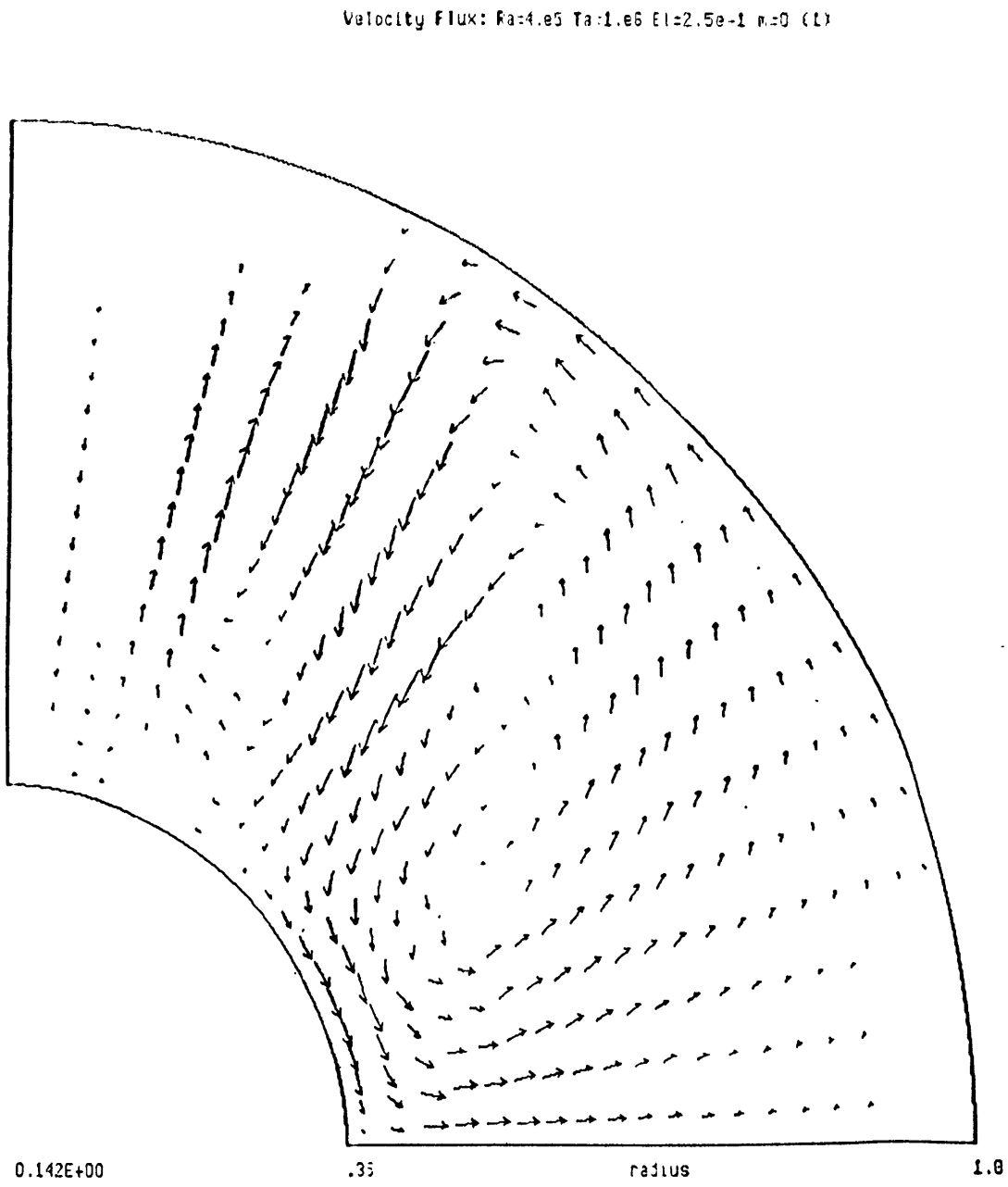

Figure 4.14 As for Figure 4.11 but for Ra = 4 x 10^5 and El = 2.5 x 10^{-1}. The $\ell = 3$ convection shows the dominant effect of rotation.

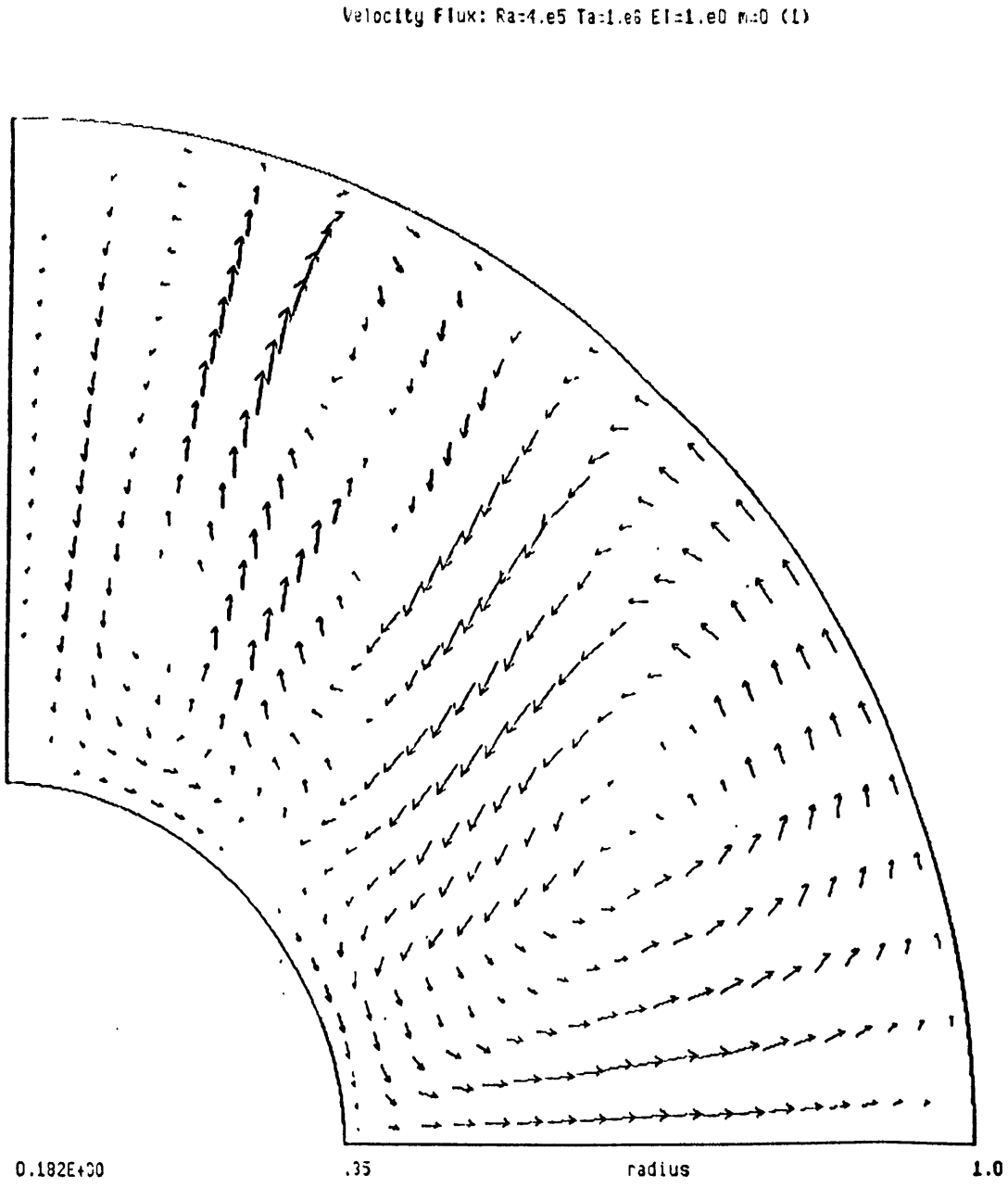

Figure 4.15 As for Figure 4.14 but for El = 10^0. The $\ell = 3$ convection effectively fills the sphere, most easily observed in the radial flow in the equatorial zone near r = 1.

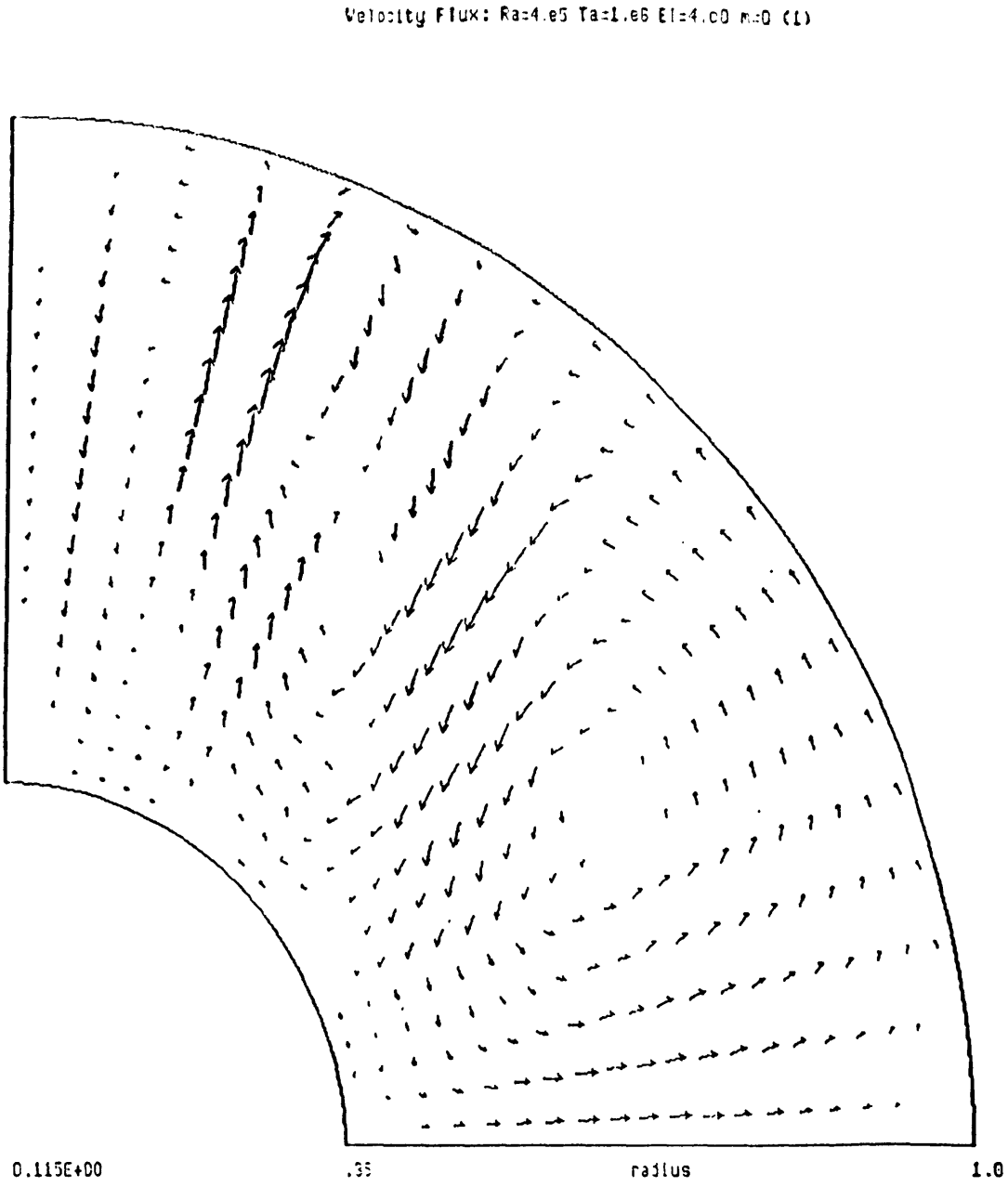

Figure 4.16 As for Figure 4.14 but for El = 4 x 10^0. The ℓ = 3 convection shows the dominant effect of $\mathbf{B}_0 = \hat{\mathbf{z}}$.

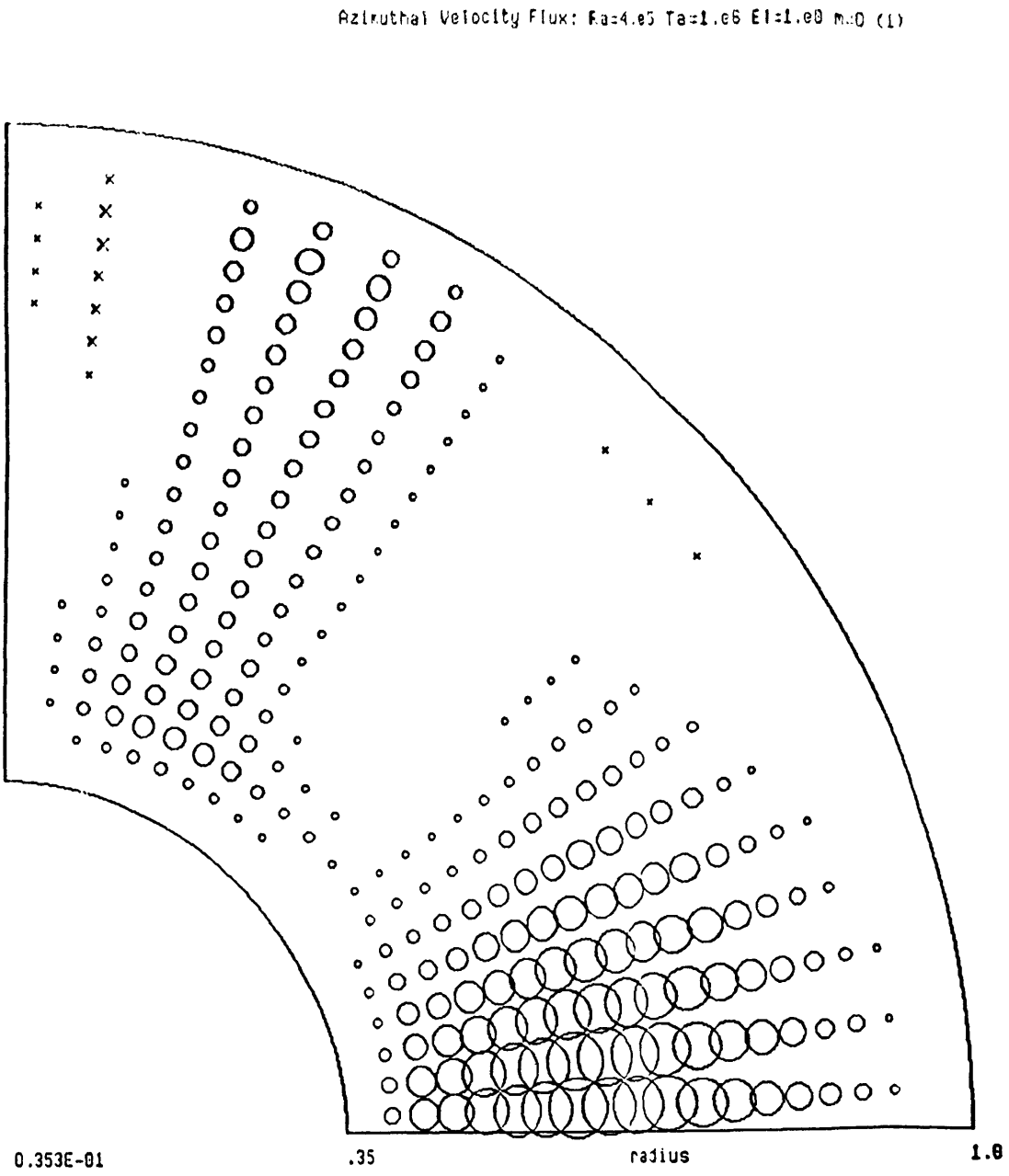

Figure 4.17 As for Figure 4.12, but for the parameters of Figure 4.15. In the equatorial zone, the westward flow extends to all radii, but remains largest nearer the bottom.

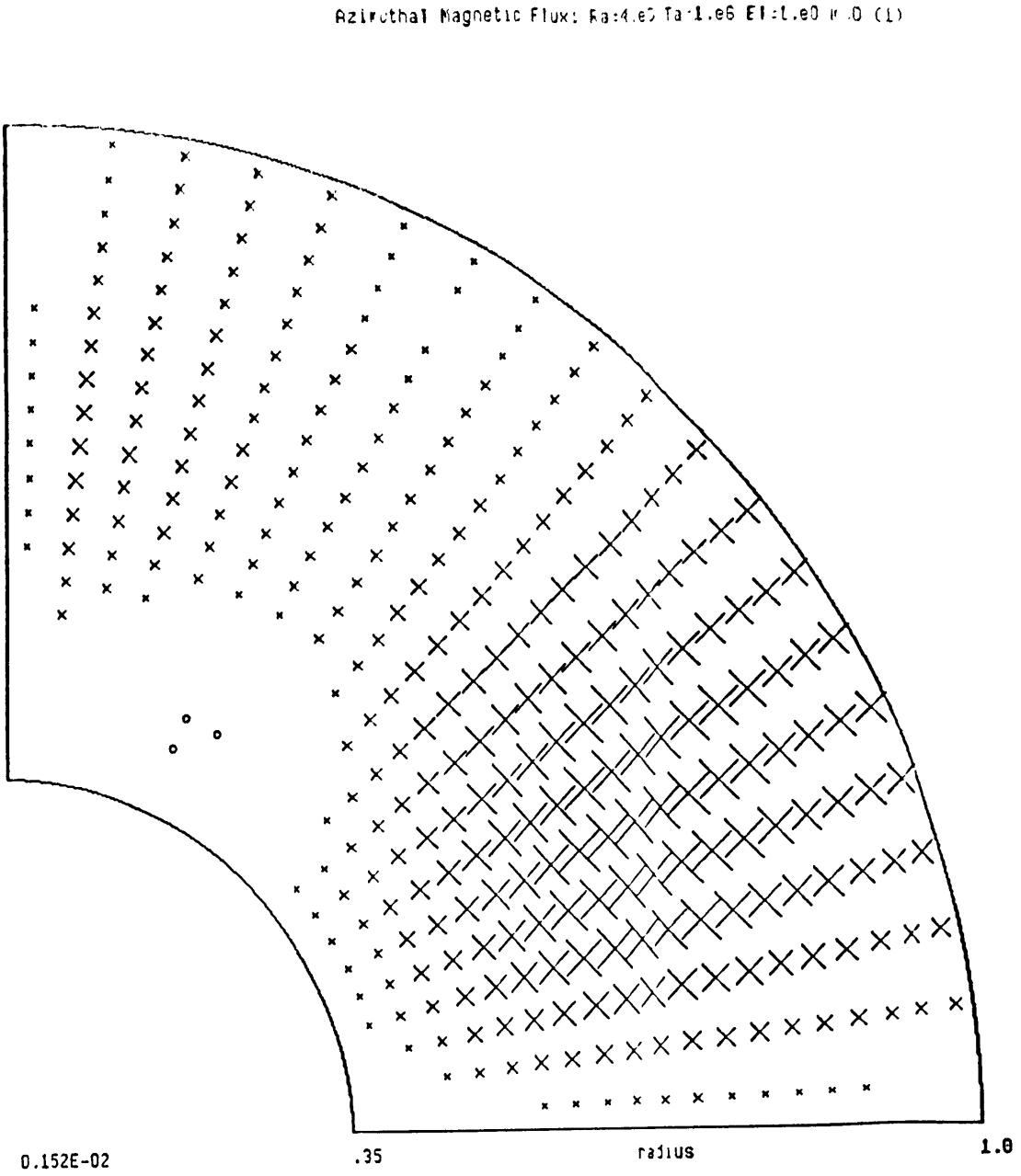

Figure 4.18 As for Figure 4.13, but for the parameters of Figure 4.15. The maximum b_ϕ shifts to lower latitude as Ra rises.

motions are largest in amplitude and the convection is largest in scale. Note that for either El = 2.5 x 10^{-1} or El = 4.0 x 10^{0}, the convection becomes more aligned with the z-direction, in the former case due to rotation and in the latter to $\mathbf{B_0} = \hat{z}$. Figure 4.15, and Figure 4.17, which shows the zonal velocity flux for El = 10^{0}, demonstrate that despite the liberating effect of the Lorentz force in the equatorial zone, convection remains more effective at smaller radii with conduction playing an important role nearer the outer boundary. Though we cannot be sure that conduction will remain important for larger Ra, the spherical geometry will most likely dictate that convection will continue to be more vigorous nearer the inner boundary.

A comparison of Figure 4.18 with Figure 4.13 shows that the maximum b_ϕ remains near $r = (\eta+1)/2$, but that maximum shifts to lower latitude with increasing Ra (even though with the imposed dipole symmetry b_ϕ is zero at the equator). This b_ϕ represents the largest magnetic field that the convection creates through advection (the ω-effect, Moffatt (1978)). At El = 2.5 x 10^{-1} the magnitude of b_ϕ is roughly 150% of the magnitude of $\mathbf{B_0}$ (= 1), at El = 10^{0} b_ϕ achieves 80% of the magnitude of $\mathbf{B_0}$, and at El = 4 x 10^{0} b_ϕ is only about 10% of the magnitude of $\mathbf{B_0}$. Although strong-field dynamos imply a toroidal magnetic field an order or two stronger than the poloidal field (Moffatt, 1978), we have only obtained an order one toroidal field via advection of the imposed poloidal field. At Ta = 4 x 10^{6}, we find an overall minimum Ra_c = 2.8 x 10^{5} at El = 10^{0}, whereas Ra_c = 3.2 x 10^{5} at El = 0. An interesting feature of the large scale $\ell = 1$ convection at Ra_c (Figure 4.19) is that despite the rapid rotation the spurious spatial oscillations of El = 0 convection have disappeared (compare Figure 4.19 with Figure 4.5), presumably due to the magnetic field increasing the length scale of the flow and reducing the need for high numerical resolution.

All of these solutions, Figures 4.11, 4.14, 4.15, 4.16, and 4.19, as well as others that we do not show, feature flow near the inner core moving towards the equator, with accompanying westward flow. Convection cells that have motion in the opposite sense are

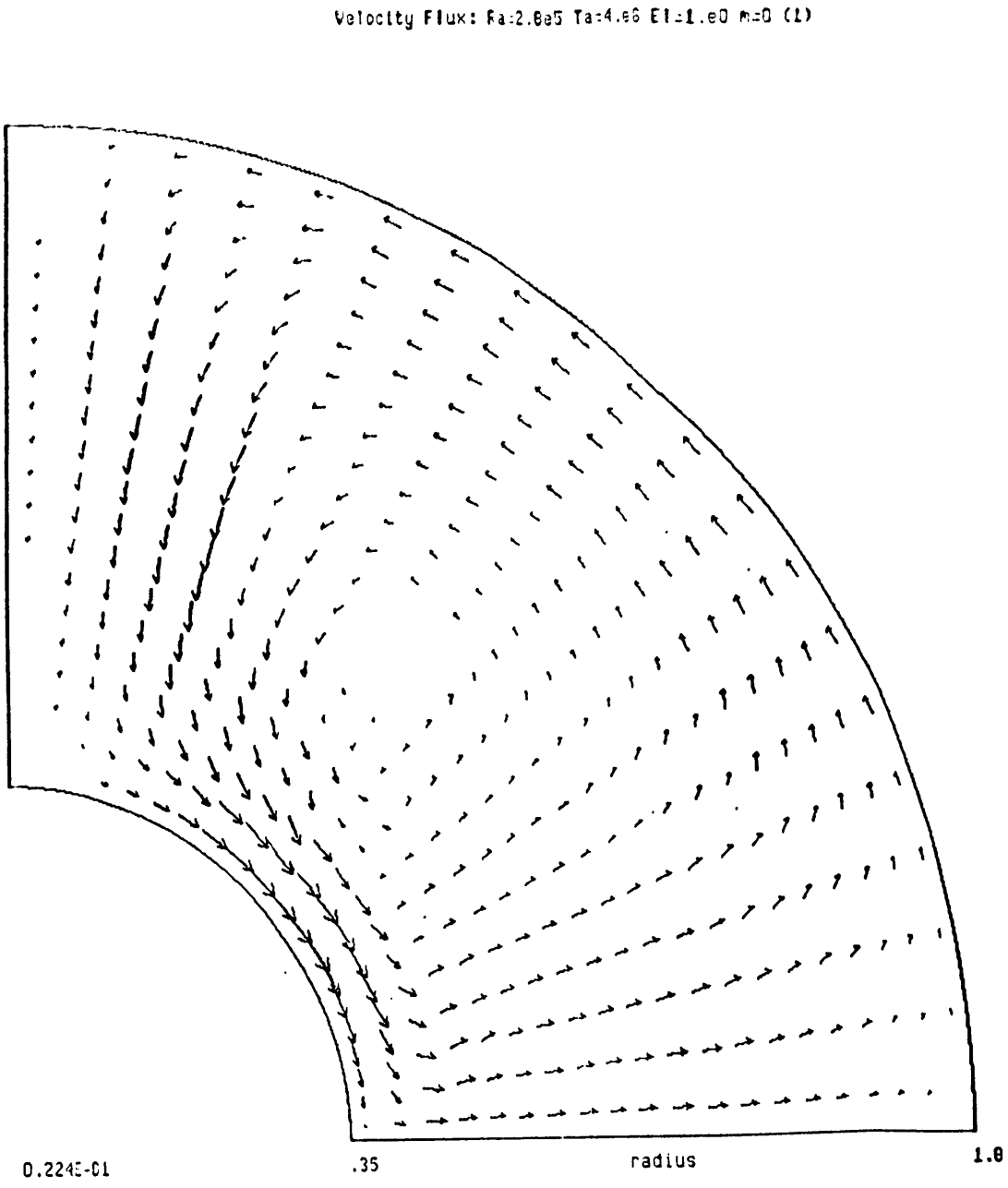

Figure 4.19 As for Figure 4.11 but for $Ra = Ra_c = 2.8 \times 10^5$ at $Ta = 4 \times 10^6$. Despite the increased rotation rate, numerical inaccuracy is not a problem with $El = 10^0$ as it is with $El = 0$ (Figure 4.5).

pushed to larger radii (Figures 4.14 - 4.16). This is unlike solutions with El = 0 (Figure 4.4) where there is no such bias. The preference for flow towards the equator at the lower boundary, with resulting radially outward flow at low latitudes, is a result of the non-linear interaction of the inward directed j_r with the eastward b_ϕ (Figures 4.13 and 4.18). Near the equator the Lorentz force due to these terms is in the direction towards the equator, thus re-enforcing the upward flow above the inner-outer core boundary. Consider now the converse flow: radially inward flow at low latitudes. Such flow causes eastward drift, resulting in a westward b_ϕ, an outward directed j_r, and a Lorentz force again towards the equator, which thereby opposes the radially inward flow. Thus, the non-linear flow near the lower boundary and near the equator is not symmetric with respect to radial upflow or downflow; radial upflow is preferred. The preference would be symmetric because of the opposite scenario near the upper boundary at r = 1, but for the demonstrated dominance of convection near the lower boundary and dominance of conduction near the upper boundary. This non-linear result is independent of the sign of $\mathbf{B}_0$ because $\mathbf{B}_0$ enters into equation (4.4) as the square.

Although the axisymmetric rotating magnetoconvective solutions of this section are large scale and fill the spherical shell, they appear to be the magnetic modification of the polar modes of Section 4.2. In that sense, and despite radial flow in the equatorial zone (an effect of the spherical geometry), their existence depends only on the z-component of gravity, and not on the s-component. In order to confirm this, in the next section we will search for solutions in the spherical shell with gravity in the s-direction rather than the r-direction. The observation that the modes are large scale and fill the spherical shell suggests that they effectively transport buoyancy. On the other hand, at least for an imposed toroidal magnetic field, linear stability theory predicts that the convection that commences at Ra_{ceq} appears as a non-axisymmetric MAC wave (Eltayeb and Kumar, 1977), for which the s-component of gravity plays an important role.

Nevertheless, for $Ra > Ra_c$ ($> Ra_{ceq}$), the polar modes may play a role in buoyancy transport, especially in the presence of a magnetic field.

4.5 Solutions in a spherical shell with cylindrical gravity

The equatorial modes that appear near Ra_{ceq} in a rotating spherical shell depend upon the s-component of gravity, g_s. For this reason, laboratory experiments using the centrifugal acceleration to replace g_s have been successful at confirming the theoretical predictions for Ra_{ceq} (Busse and Carrigan, 1976). However, they cannot obtain the polar modes that occur at higher Ra because they do not include the z-component of gravity g_z. By removing g_z we will confirm that the polar modes of Section 4.2 and the magnetically modified polar modes of Section 4.4 owe their existence to g_z. We remove g_z by setting $\hat{\mathbf{g}} = s\hat{\mathbf{s}}$, which simulates the centrifugal acceleration $\Omega^2 s\hat{\mathbf{s}}$, rather than setting $\hat{\mathbf{g}} = \hat{\mathbf{r}}$, which is more representative of the Earth's core and which we have used in our previous calculations. Other than this change in the buoyancy force, the problem formulation and solution method remains the same.

Because our method seeks time-independent solutions, and because the equatorial modes require non-axisymmetry and hence, because of the spherical boundaries, a time-dependence in the form of a drift (at the very least), we cannot hope to converge to columnar convective solutions. Since we presumably have also removed the engine for the polar modes, the only convergent finite-amplitude solutions we should find should be those driven by the axisymmetric thermal wind that results from the baroclinic conductive state (Cordero and Busse, 1992). Indeed, this is what we find. For $Ta = 10^6$, $El = 0$, and $Ra = 10^3$, 10^4, 1.7×10^5 (Figure 4.20), and 3×10^5 (Figure 4.21), we obtain converged $\ell = 1$ solutions that have a large westward flow in the equatorial zone and eastward flow in the polar regions. These solutions do not represent free convection, but merely the motion due to the non-alignment of surfaces of constant pressure and density. The motion occurs

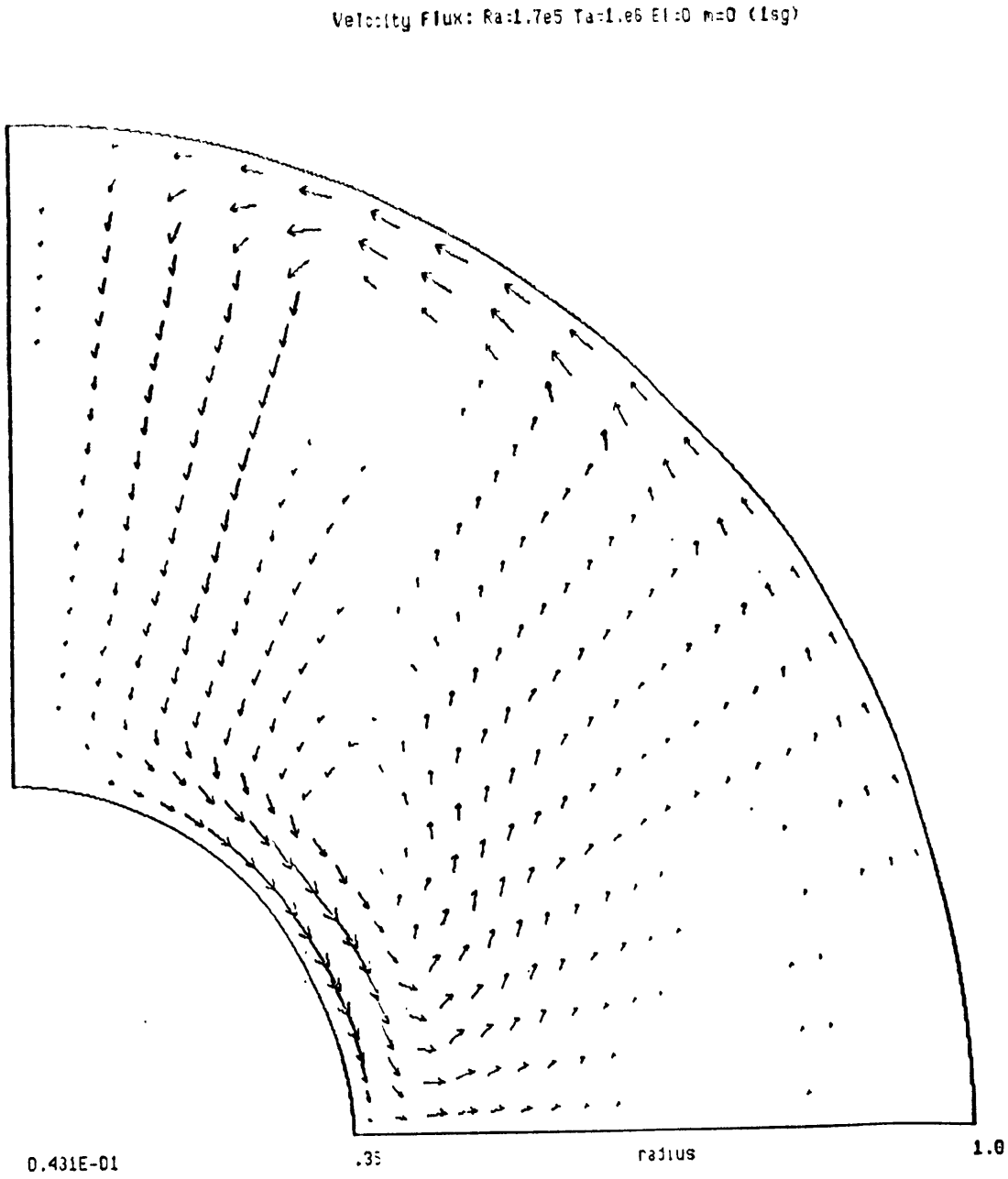

Figure 4.20 As for Figure 4.1 but for $\mathbf{g} = s\hat{\mathbf{s}}$. The motion is not due to the z-component of gravity (polar convection) but rather to the baroclinicity of the basic state.

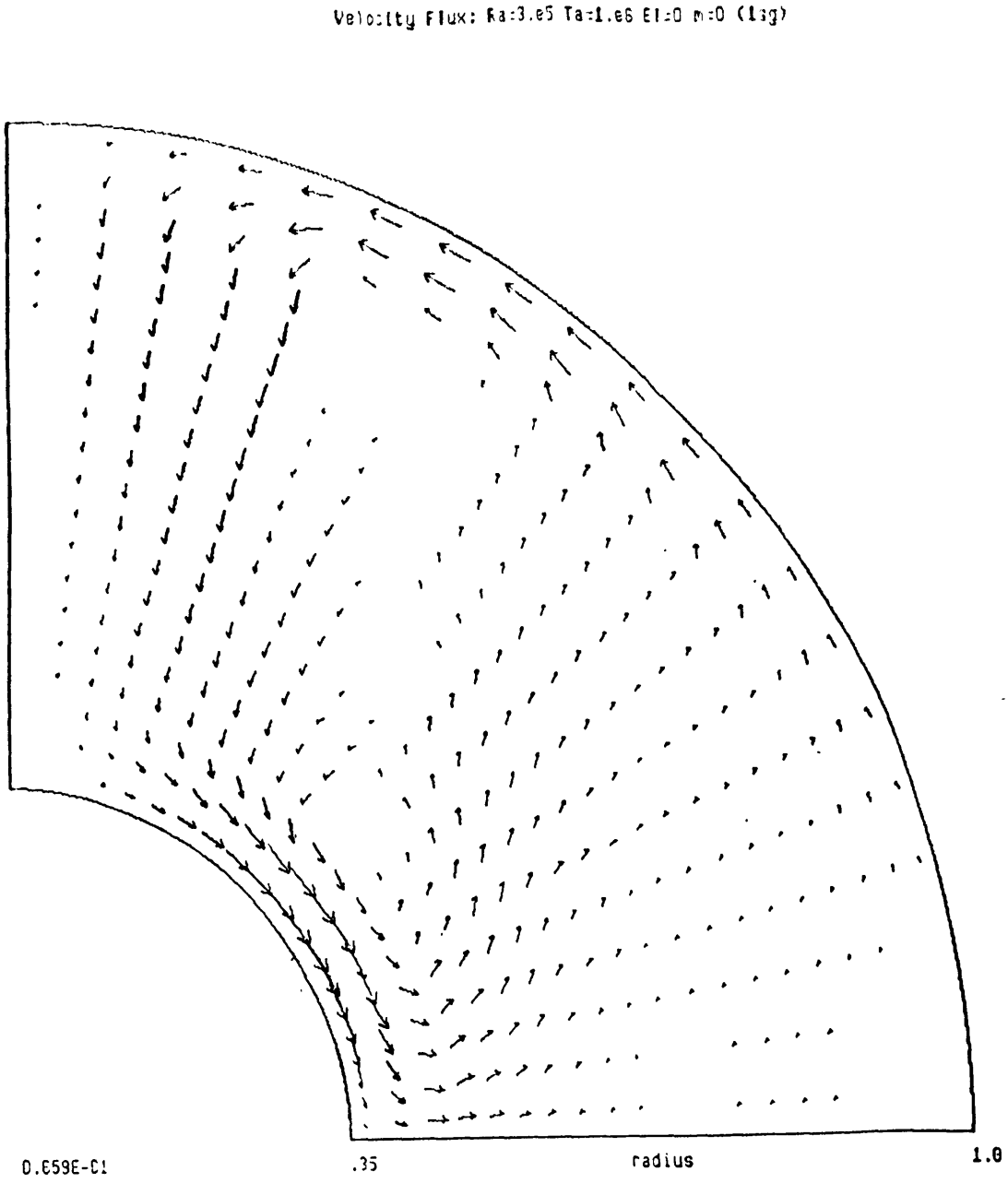

Figure 4.21 As for Figure 4.20 but at Ra = 3 x 10^5. Compare with Figures 4.3 and 4.4 for evidence that this motion does not represent a polar mode of free convection.

for all non-zero Ra, with the amplitude proportional to Ra rather than growing non-linearly beyond a particular bifurcation point, Ra_c. Moreover, the motion remains primarily $\ell = 1$ rather than switching to a higher latitudinal wavenumber as Ra increases (compare Figure 4.21 with Figures 4.3 and 4.4).

Eventually however, the non-linearity of the equations begins to make the iteration sequence difficult to control, and by $Ra = 10^6$ we are no longer able to reach a converged solution. For $Ta = 10^6$ and $El = 10^0$ (with $\mathbf{B_0} = \hat{\mathbf{z}}$) we observe similar behavior. At $Ra = 3 \times 10^4$, 3×10^5, and 6×10^5, we obtain converged $\ell = 1$ solutions, though of larger scale and decreased azimuthal flow from their El = 0 counterparts. By $Ra = 3 \times 10^6$ we can no longer find a convergent solution. It is interesting to note that at both El = 0 and $El = 10^0$, the amplitude of the polar modes near Ra_c is actually slightly less than the amplitude of the motions driven by the imposed baroclinic buoyancy state (compare Figure 4.20 with Figure 4.1). If the amplitude of the baroclinically driven azimuthal flow near Ra_{ceq} is of comparable magnitude with the azimuthal drift rate of columnar convection, it is perhaps not surprising that the laboratory experiments can accurately confirm the theoretical predictions for Ra_{ceq} but not the drift rate at Ra_{ceq} (Cordero and Busse, 1992). In any case, as Ra rises, the amplitude of the free convection rises much more rapidly than does that of the baroclinic motion (the ratio of the amplitudes of the solution in Figures 4.3 or 4.4 to 4.1 is much greater than that of Figure 4.21 to 4.20).

Clearly, in the absence of the z-component of gravity the polar modes do not exist in a rotating spherical shell. Even in the presence of a magnetic field $\mathbf{B_0} = \hat{\mathbf{z}}$ at non-zero El, for which the polar modes fill the sphere, the z-component of gravity remains the driving force. The s-component of gravity drives the columnar equatorial modes (Busse and Cuong, 1977), though we have been unable to obtain them in the spherical shell using our iterative approach to search for steady solutions. For El = 0 the equatorial modes have a lower critical Rayleigh number, Ra_{ceq}, than do the polar modes, Ra_c, though for $Ra > Ra_c$ one would expect that the z-component of gravity would become of dynamical importance

(Gilman, 1977). For El non-zero an imposed toroidal magnetic field lowers Ra_{ceq} for the equatorial modes (Eltayeb and Kumar, 1977), and an imposed z-magnetic field lowers Ra_c for the polar modes. Although those modes dependent upon g_s may still be the most unstable, one should not overlook the importance of g_z for rotating magnetoconvection for $Ra > Ra_c$.

Although core convection is undoubtedly time-dependent and non-axisymmetric, we have developed this iterative method to look for time-independent (and because of rotation and spherical boundaries, axisymmetric) solutions of the non-linear convective equations based on the observation that certain anomalous features of the Earth's magnetic field persist for much longer than the core convective time scale. Thermal anomalies in the lower mantle may provide this longer time scale. It seems unlikely that free convection cause the stationary features, but rather, motions driven via a laterally inhomogeneous boundary buoyancy flux do. We will examine this in the next section. However, we note that in developing and employing our method to obtain finite-amplitude solutions, we have observed that for $Ra > Ra_c$, as is likely in the core, g_z may be dynamically important.

4.6 Solutions driven by a laterally inhomogeneous boundary buoyancy flux

Although we have demonstrated that we can obtain steady, finite-amplitude convective solutions in a rotating, electrically conducting, fluid spherical shell, we can find such converged solutions only at Ra much less than that presumed in the Earth's outer core. On the other hand, we have used Ta much less than that appropriate to the core, so we cannot be sure by how much we underestimate (if at all!) the vigor and non-linearity of the convection. If the convection is in a turbulent state, we do not know if replacing the molecular values of the diffusivities with their eddy values in order to obtain a lower Ra yields a flow that is at all representative of the mean flow. Moreover, without a stability

analysis we cannot be sure our solutions could ever be attained. Nevertheless, we believe that the dynamical importance of g_z remains even for time-dependent solutions. In any case, it seems unlikely that free convection is responsible for the stationary features of the Earth's magnetic field, so we will now employ our method to find motions driven by a laterally inhomogeneous boundary buoyancy flux, which we call forced convection.

As we have seen in Chapter 2, there is some evidence that certain anomalous features of the Earth's magnetic field remain stationary for much longer than the convective time scale. Bloxham and Gubbins (1987) found that stationary regions of high magnetic flux across the CMB correlate with anomalously seismically fast mantle, *i.e.*, cold mantle, and stationary lows in the magnetic flux correlate with seismically imaged hot mantle. This suggests that the mantle, with its long thermal time scale, controls those features in the core that remain relatively stationary. They argued that regions in the lower mantle that are anomalously cold maintain a high heat flux from the core, which results from horizontally converging core fluid, bunching of magnetic field lines, and thus a high magnetic flux, and vice versa for hot mantle. This is in contrast to classical Rayleigh-Benard convection, for which a high heat flux implies upwelling. However, King and Hager (1989) argued that the proper boundary condition at the CMB is not the constant temperature boundary condition of Rayleigh-Benard convection, but rather variable heat flux, *i.e.*, a laterally inhomogeneous boundary buoyancy flux.

King and Hager (1989) studied convection driven by internal heating in a rectangular box, inifinite in one direction. They assumed thermally insulating bottom and side walls, and a prescribed variable heat flux along the top wall of the form

$$f_r = -1 - .5 \cos (n\pi x/2), \qquad (4.12)$$

where x is distance across the box and n is an iteger. A laterally inhomogeneous boundary buoyancy flux of the form (4.12) removes as much heat as the internal heating generates.

For moderate Ra (= 10^5), their results with (4.12) agree with the hypothesis of Bloxham and Gubbins (1987). At higher Ra (= 2.7×10^6), the convection becomes time-dependent, though statistically the downwellings tend to occur beneath regions of (imposed) high heat flux along the upper boundary. However, their calculations were for a box with side walls, rather than for a spherical shell, and they did not include the effects of rotation or a magnetic field. Zhang and Gubbins (1992) studied forced convection in a rotating spherical shell, but they did not include the effects of a magnetic field or free convection.

In this section we use the method of Section 3.4, but with variable rather than constant buoyancy flux conditions along $r = 1$. The boundary condition along $r = \eta$ remains the same. Whereas for our study of chemically driven free convection a homogeneous buoyancy flux is a reasonable model (at least along $r = \eta$), for a study of thermally driven forced convection, an inhomogeneous buoyancy flux along $r = 1$ is perhaps a better model than a homogeneous buoyancy flux. The results of King and Hager (1989) show that at high enough Ra, as may be appropriate to the Earth's core, the forced convection becomes time-dependent, though statistically there is a correlation between the convective patterns and the boundary conditions. Of course, our iterative approach cannot find time-dependent solutions, but we nevertheless hope that for moderate Ra we will find converged solutions that represent a mean solution. Whereas in a rotating spherical shell all non-axisymmetric free convective solutions exhibit a drift or more complicated time-dependence, not all motions forced by an azimuthally inhomogeneous boundary buoyancy flux will (Zhang and Gubbins, 1992). Indeed, the data seem to indicate that some such motions remain steady or maintain a mean (on the free convective time scale) in the mantle reference frame. Although the data show a ϕ-dependence, perhaps with an $m = 1$ dominance, so that it would be interesting to try and obtain steady, ϕ-dependent solutions, for simplicity we will continue our search for steady, axisymmetric solutions in order to understand latitudinal variations.

We first study motion in a spherical shell with $\eta = .35$ and $Ta = El = 0$. Throughout the following calculations we set

$$f_r = -1/(4\pi\eta^2) \text{ along } r = \eta. \tag{4.13}$$

Along $r = 1$ we try various boundary buoyancy flux conditions. In analogy with (4.12), we try

$$f_r = -1/(4\pi)(.5 + 2/\pi \sin\theta) \text{ along } r = 1. \tag{4.14}$$

Note that for (4.14), and for the choices of f_r that follow, the net buoyancy flux across $r = 1$ equals that across $r = \eta$ with (4.13). As for the solutions in a rotating spherical shell with s-gravity, baroclinic motion occurs at all non-zero Ra. For $Ra < Ra* \cong Ra_c$ (for Ra_c, see Section 3.5), this motion simply consists of downwelling near the equator, the region of high heat flux, and upwelling near the pole, the region of low heat flux, as King and Hager (1989) found (Figure 4.22 for motion at $Ra = 10^4$). The motion is essentially linear in that the amplitude is very nearly proportional to Ra. For $Ra > Ra*$ the iteration sequences converge to convective solutions not dramatically different from those of Section 3.5 (compare Figure 4.23 with Figure 3.7, both for motion at $Ra = 5 \times 10^4$). We obtain similar behavior for both

$$f_r = -1/(4\pi)(4/\pi \sin\theta) \text{ along } r = 1, \text{ and} \tag{4.15}$$

$$f_r = -1/(4\pi)(.5 + 3/4 \sin^2\theta) \text{ along } r = 1. \tag{4.16}$$

However, for

$$f_r = -1/(4\pi)(3/2 \sin^2\theta) \text{ along } r = 1 \tag{4.17}$$

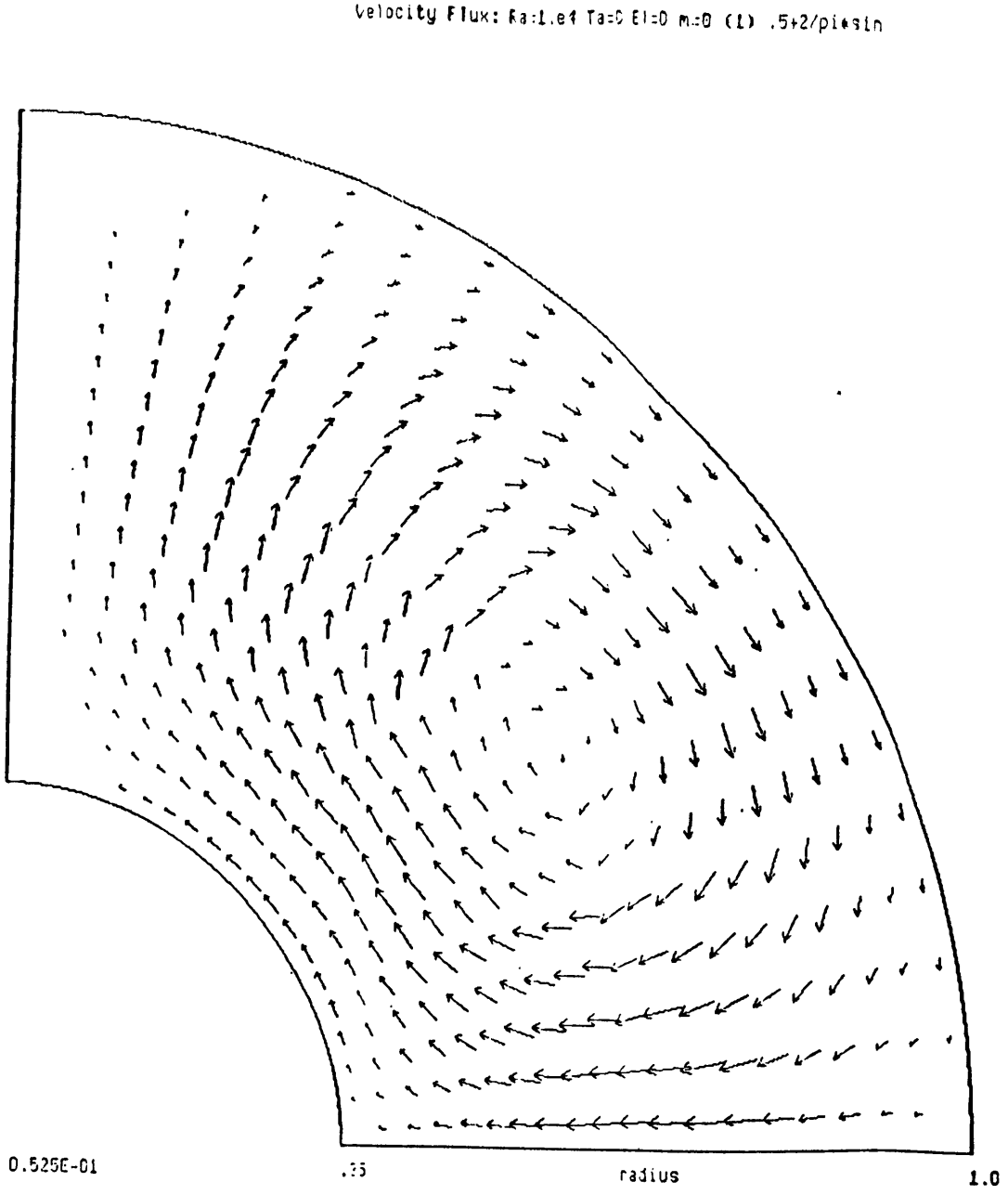

Figure 4.22 As for Figure 4.1 but for Ra = 10^4, Ta (and El) = 0, and the boundary condition (4.14) on f_r. The downwelling in the equatorial region is simply due to the baroclinicity of the basic state.

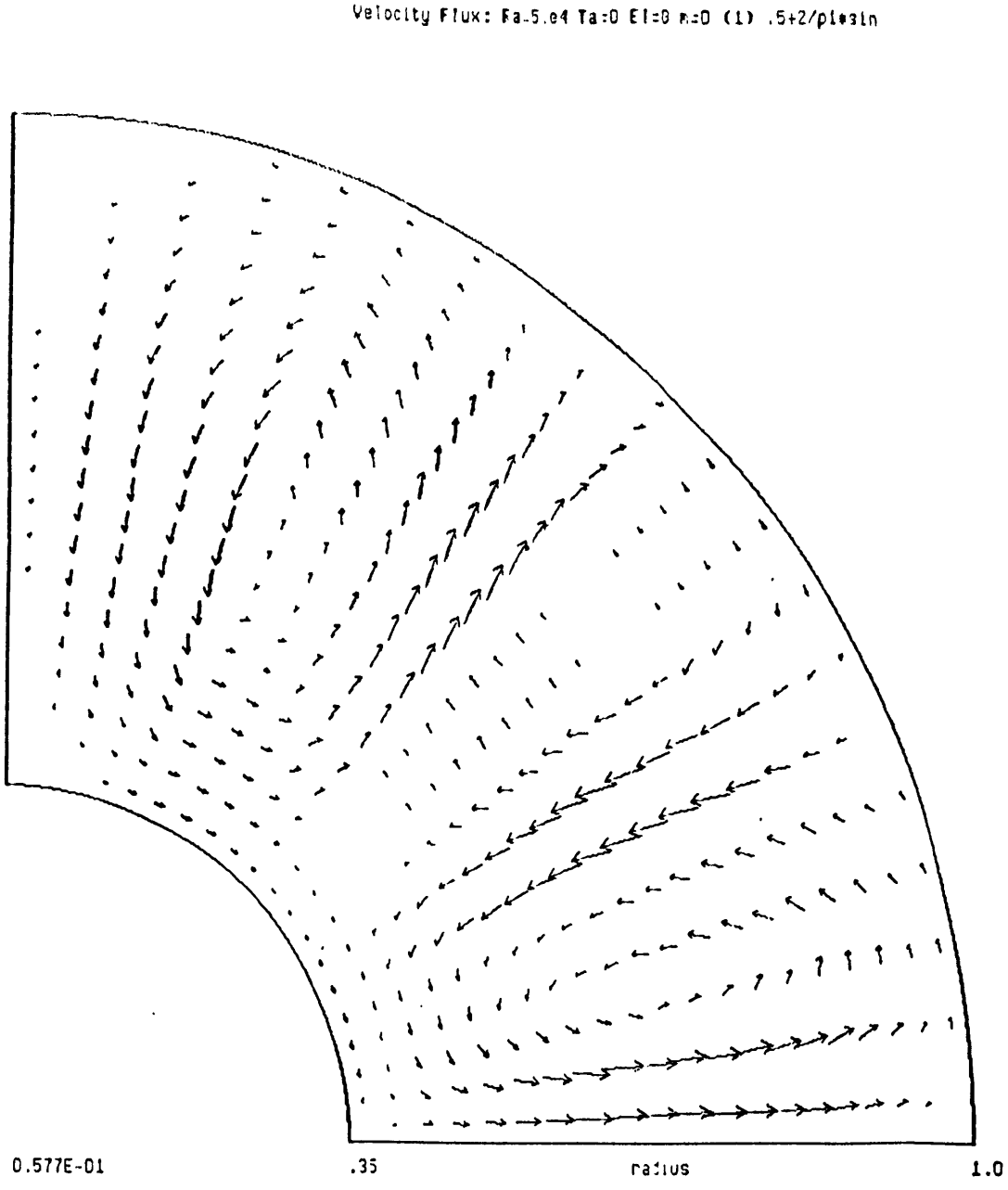

Figure 4.23 As for Figure 4.22 but for Ra = 5 x 10^4. A comparison with Figure 3.7 demonstrates that the boundary condition (4.14) does not yield a solution significantly different from that driven by a laterally homogeneous boundary buoyancy flux.

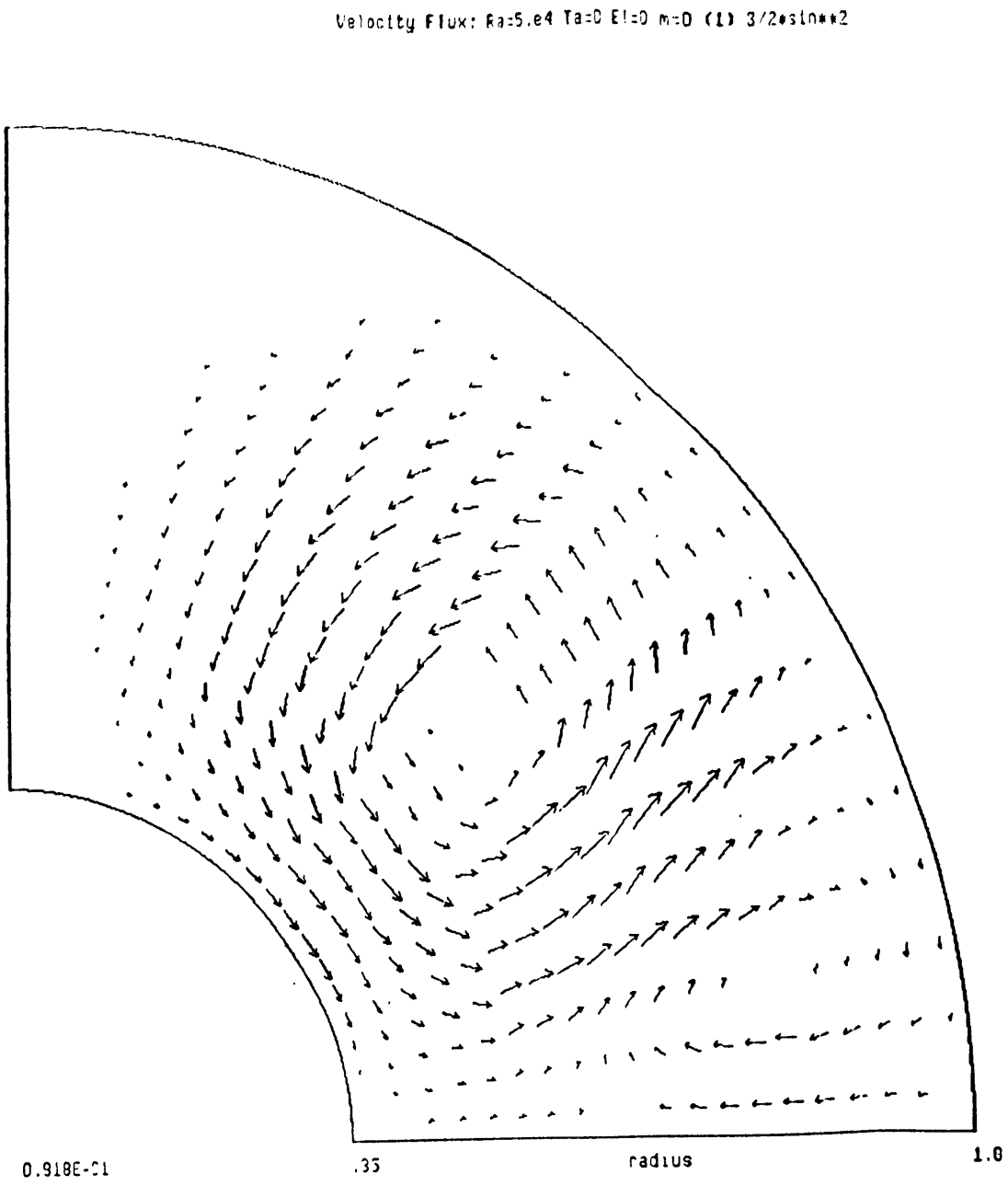

Figure 4.24 As for Figure 4.23 but for the boundary condition (4.17) replacing (4.14). The change in the nature of convection is evident, with a local downwelling occurring near the equator near r = 1.

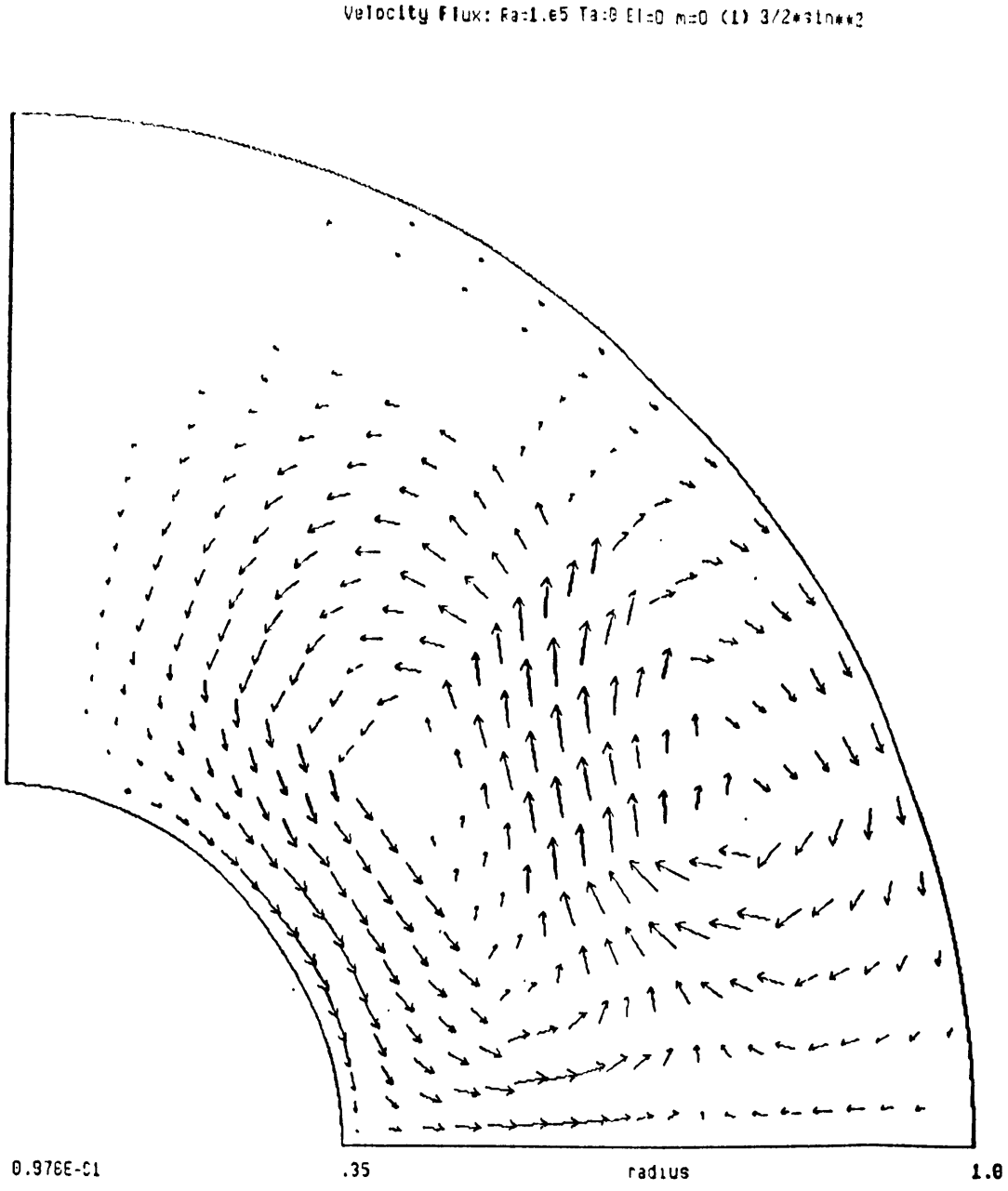

Figure 4.25 As for Figure 4.24 but at Ra = 10^5. The behavior at this higher Ra is similar to that at Ra = 5 x 10^4 (Figure 4.24), though the forced convection cell reaches to higher latitudes.

we obtain different behavior for Ra > Ra*. The converged solutions no longer represent free convection only slightly modified by the variable heat flux boundary condition. Rather, the concentrated and powerful boundary source (4.17) forces motion with the predicted sense near r = 1, and a separate convection cell forms deeper in the shell (Figure 4.24 for motion at Ra = 5 x 10^4). We obtain similar behavior at Ra = 10^5 (Figure 4.25), though by Ra = 5 x 10^5 we can no longer obtain a converged solution. The forced motion reaches further horizontally if not vertically into the core at larger Ra (compare Figure 4.25 with 4.24). It is tempting here to speculate that the effects of an inhomogeneous boundary buoyancy flux, *i.e.*, a variable heat flux into the mantle, reach only a fraction of the depth into the outer core. The forced motion, occurring in the upper fraction of the core, may be responsible for many of the observed stationary features in the secular variation field, whereas the free convection, occurring in the lower fraction, likely generates the dipole. (We speculate that a single convection cell with the proper sense is not likely to transport buoyancy efficiently enough at this moderately high Ra.) In order to produce a significant change from free convection for Ra > Ra* the forcing had to be concentrated and powerful. Whether this is realistic is not clear, given our uncertainty on the thermal conditions near the CMB.

We next add rotation and a magnetic field, looking for solutions in the spherical shell at Ta = 10^6 and El = 10^0. For our boundary condition on f_r we choose a function of the form

$$f_r = [-1 - y\,(3/2\,\sin^2\theta - 1)]/(4\pi) \text{ along } r = 1, \qquad (4.18)$$

where y is a real number. When y = 0 (4.18) reduces to a laterally homogeneous boundary buoyancy flux, and when y = 1 (4.18) reduces to (4.17). We will only examine solutions for 0 < y < 1, though y can take on any real value. For small Ra and non-zero y we obtain baroclinic solutions qualitatively similar to that in Figure 4.22. We interpret small as Ra <

$Ra*$, which we again define as roughly that value of Ra below which we obtain a solution dominated by conduction (for y = 0, $Ra* = Ra_c$, but for non-zero y there is not a clear bifurcation between conduction and convection). As Ra rises slightly above $Ra*$ ($\approx Ra_c = 1.4 \times 10^5$), for $y \leq .2$ the iteration sequences converge to solutions very similar to those in Section 4.4 (y = 0), but for $y > .2$ they do not converge.

However, for larger Ra, such as $Ra = 4 \times 10^5$, we can obtain converged solutions for a greater range in y. As before, for y = .1 we obtain a solution similar to that for y = 0 (Figure 4.15). On the other hand, for y = .5 (Figure 4.26) we obtain very different looking motion. With upwelling flow beneath the region of high boundary buoyancy flux, this motion does not represent the nearly linear conductive solution. Somewhat paradoxically, the motion at y = .7 (Figure 4.27) looks more similar to that in Figure 4.15 than does the motion at y = .5. We did not explore the uniqueness of the solutions with respect to the starting model (though Figures 4.26 and 4.27 result from the same starting model), so the solutions being different modes may be one possible explanation for the apparent paradox. Their net efficiency at transporting buoyancy is similar. For y = 1 at $Ra = 4 \times 10^5$ we cannot reach a converged solution.

Like in Figure 4.26, and unlike in Figures 4.24 and 4.25 (Ta = El = 0, y = 1), the motion near the equator in Figure 4.27 is still radially outward. Nevertheless, the upwelling near the core surface is reduced from that of Figure 4.15. This is more easily seen from Figures 4.28 and 4.29, which show the azimuthal velocity flux corresponding to the poloidal motion of Figures 4.26 and 4.27. In both Figures 4.28 and 4.29, the westward flow is pushed to smaller radii as compared with the flow in Figure 4.17. We propose that we could not obtain downwelling flow near the equator, despite the forcing, because of the strong effect of the non-linear interaction of j_r with b_ϕ near the lower boundary, which causes convective motion to prefer radial upwelling near the equator, as discussed near the end of Section 4.4. Nevertheless, we observe that the effect of the inhomogeneous boundary buoyancy flux is felt. Indeed, we hypothesize that we cannot

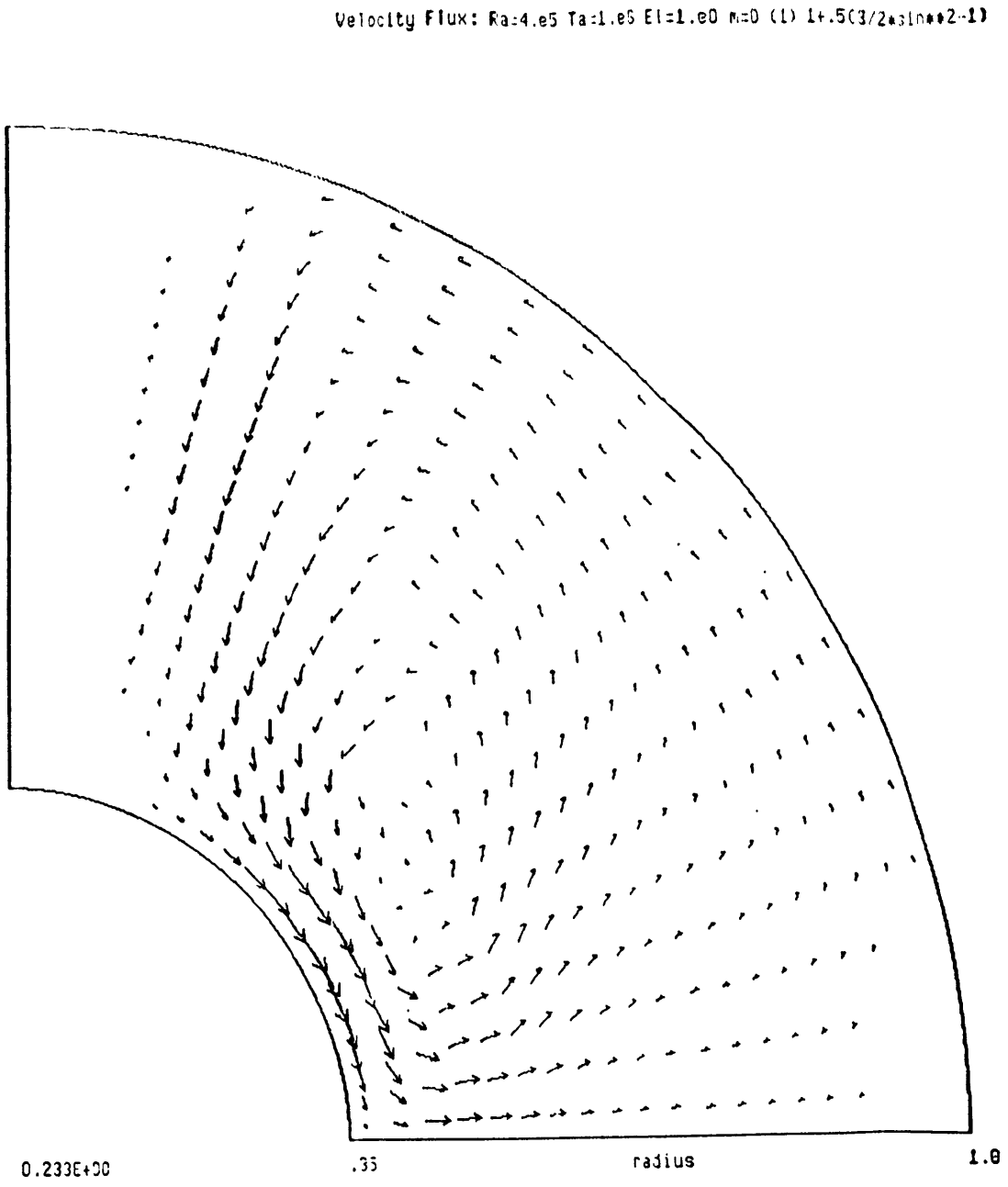

Figure 4.26 As for Figure 4.15 but with the boundary condition (4.18) on f_r, with y = .5. The solution represents neither the conductive solution nor the convective solution of Figure 4.15.

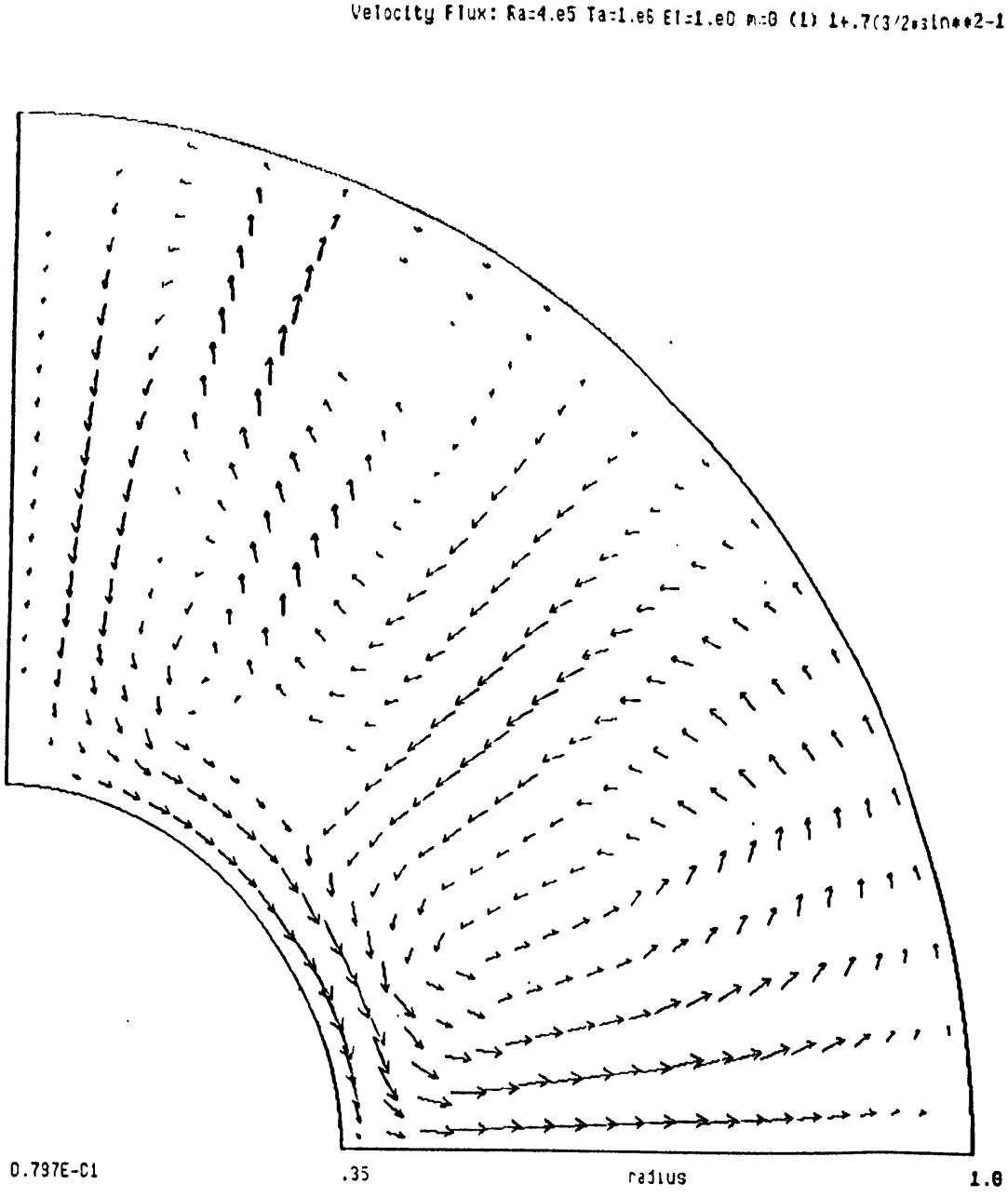

Figure 4.27 As for Figure 4.26 but with y = .7. For non-zero Ta and non-zero El we are unable to produce a steady local downwelling beneath the region of high heat flux out of the spherical shell (this figure and Figure 4.26).

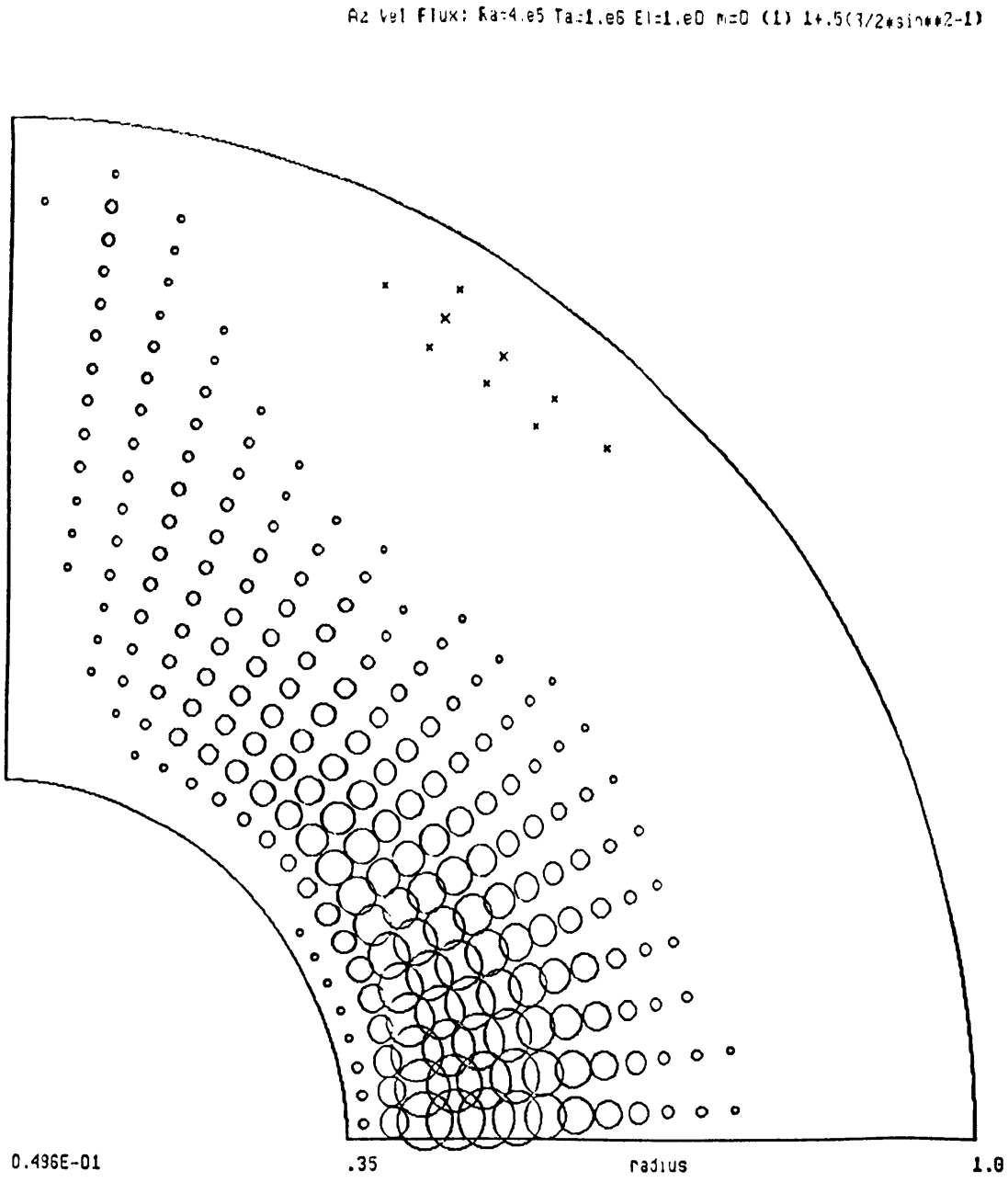

Figure 4.28 As for Figure 4.17, but for the boundary condition of Figure 4.26. The boundary condition forces the westward flow to smaller radii than for the free convection solution of Figure 4.17.

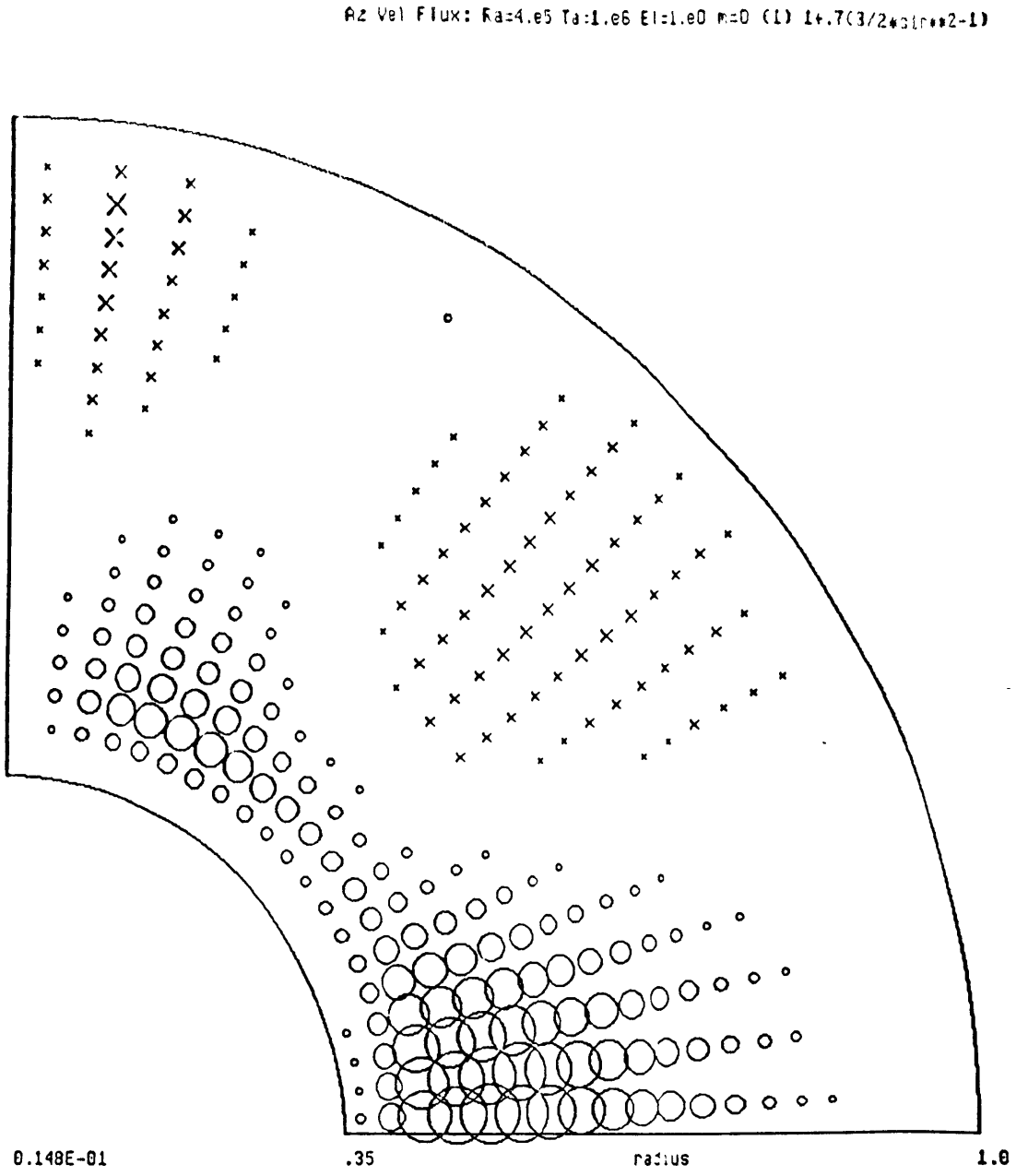

Figure 4.29 As for Figure 4.28, but for the boundary condition of Figure 4.27.

obtain converged solutions for $y > .2$ near $Ra*$ because of the difficulty the iterative procedure sometimes has in moving towards a solution near a bifurcation, in this case between conduction, with its equatorial downwelling, and convection, with its equatorial upwelling.

To test this hypothesis we set $y = -.7$, so that there is a high heat flux from the core into the mantle near the poles rather than near the equator. Near $Ra* = 1.4 \times 10^5$ we easily obtain a converged solution, which looks similar to Figure 4.11, but with an amplitude about three times as large. For this boundary condition (negative y), convection and conduction work together to produce downwelling at the poles and upwelling at the equator. At $Ra = 4 \times 10^5$ we obtain a converged solution that looks similar to the free convection solution of Figure 4.15, but with an amplitude nearly twice as large. Compare this with Figure 4.27 ($y = +.7$), in which the solution has an amplitude less than half that of Figure 4.15. Near $Ra = Ra*$, conductive and convective motions are of comparable strength, so we have difficulty obtaining a converged solution if they work in an opposite sense (positive y). For $Ra < Ra*$, conduction is prevalent, and for $Ra > Ra*$, convection is prevalent, though the boundary condition does modify the solution.

Although we have not always obtained a steady local downwelling beneath the region of high heat flux from the spherical shell for non-zero Ta and non-zero El, the boundary condition very clearly plays a role in governing the fluid motion and magnetic field generation. We have concentrated here on the effect of a latitudinally varying boundary condition. However, the variable heat flux from the core into the mantle is unlikely to be axisymmetric; neither will the resulting motions be axisymmetric (of course, they might not be even if the boundary conditions are). We have not yet studied the steady, non-axisymmetric motions in an electrically conducting, rotating spherical shell forced by a non-axisymmetric boundary heat flux. However, we know non-axisymmetric free convective solutions drift relative to the rotating frame, and the importance of MAC waves and of deterministic time-dependence for non-axisymmetric forced motions is unknown.

So too the role of non-deterministic time-dependence is unclear. Moreover, we have observed that the motions are rather sensitive to the exact functional form of the laterally inhomogeneous boundary buoyancy flux, which is imprecisely known near the CMB. Thus, before we can claim to understand the influence of the thermal boundary conditions at the CMB on core convection and magnetic field generation, we must make further observational and theoretical progress.

References

Bloxham, J., and Gubbins, D., "Thermal core-mantle interactions", *Nature* **325**, 511-513 (1987).

Braginsky, S.I., and Roberts, P.H., "A model-Z dynamo", *Geophys. Astrophys. Fluid Dynam.* **38**, 327-349 (1987).

Busse, F.H., and Carrigan, C.R., "Laboratory simulation of thermal convection in rotating planets and stars", *Science* **191**, 81-83 (1976).

Busse, F.H., and Cuong, P.G., "Convection in rapidly rotating spherical fluid shells", *Geophys. Astrophys. Fluid Dynam.* **8**, 17-44 (1977).

Cardin, P., and Olson, P., "Chaotic thermal convection in a rapidly rotating spherical shell: consequences for flow in the outer core", manuscript, (1992).

Cordero, S. and Busse, F.H., "Experiments on convection in rotating hemispherical shells: transition to a quasi-periodic state", *Geophys. Res. Lett.* **19**, 733-736 (1992).

Drew, S.J., "Thermal convection in a spherical shell with a variable radius ratio", *Geophys. Astrophys. Fluid Dynam.* **59**, 165-183 (1991).

Eltayeb, I.A., and Kumar, S., "Hydromagnetic convective instability of a rotating, self-gravitating fluid sphere containing a uniform distribution of heat sources", *Proc. R. Soc. London A***353**, 145-162 (1977).

Fearn, D.R., "Thermal and magnetic instabilities in a rapidly rotating fluid sphere", *Geophys. Astrophys. Fluid Dynam.* **14**, 103-126 (1979).

Gilman, P.A., "Nonlinear dynamics of Boussinesq convection in a deep rotating spherical shell. I", *Geophys. Astrophys. Fluid Dynam.* **8**, 93-135 (1977).

King, S.D., and Hager, B.H., "Coupling of mantle temperature anomalies and the flow pattern in the core: interpretation based on simple convection calculations", *Phys. Earth Planet. Inter.* **58**, 118-125 (1989).

Moffatt, H.K., *Magnetic Field Generation in Electrically Conducting Fluids*, Cambridge University Press (1978).

Roberts, P.H., "On the thermal instability of a rotating fluid sphere containing heat sources", *Phil. Trans. Roy. Soc. London A***263**, 93-117 (1968).

Zhang, K.K., "Convection in a rapidly rotating spherical shell at infinite Prandtl number: steadily drifting rolls", *Phys. Earth Planet. Inter.* **68**, 156-169 (1991).

Zhang, K.K., and Busse, F.H., "On the onset of convection in rotating spherical shells", *Geophys. Astrophys. Fluid Dynam.* **39**, 119-147 (1987).

Zhang, K.K., and Busse, F.H., "Generation of magnetic fields by convection in a rotating spherical fluid shell of infinite Prandtl number", *Phys. Earth Planet. Inter.* **59**, 208-222 (1990).

Zhang, K.K., and Gubbins, D., "On convection in the Earth's core driven by lateral temperature variations in the lower mantle", *Geophys. J. Int.* **108**, 247-255 (1992).

Chapter 5

Magnetic Rossby Waves in a Stably Stratified Layer near the Surface of the Earth's Outer Core

5.1 Introduction

In this chapter we study the magnetohydrodynamics of a stably stratified, electrically conducting, rotating, thin fluid shell as a model of the hypothetical stably stratified fluid layer at the top of the Earth's core. Though concerning the Earth's core, the topic is different from that studied in the previous two chapters, in which we considered free and forced rotating magnetoconvection in an unstably stratified thick fluid shell. The two are not necessarily contradictory, as it is possible that a thin stably stratified layer lies atop a thick unstably stratified layer (Fearn and Loper, 1981). On the other hand, if there is a strong laterally inhomogeneous boundary heat flux across the core-mantle boundary (CMB), it is not clear a stable layer can persist. Since we do not know the relative buoyancy of the stable layer to the variable buoyancy flux across the CMB, we cannot yet assess the stability of a stably stratified layer beneath the CMB. Although the stratification profile of the fluid outer core has been the topic of much discussion (Verhoogen, 1980) it nevertheless remains unknown.

A possible driving mechanism for core convection, and hence for the geodynamo, is compositional buoyancy (Braginsky, 1963), which depends upon the core not being a pure metal, but rather an alloy of a metal and a non-metal. In one scenario (Fearn and Loper, 1981), the metal preferentially freezes out at the inner-outer core boundary, leaving the remaining fluid enriched in the lighter non-metal component. In a cooling Earth with a sufficiently rapidly growing inner core, the diffusive state is unstable and convection occurs, most easily near the inner core. For the parameters given in Loper and Roberts (1981), and assuming the inner core has been steadily growing for three billion years,

Fearn and Loper (1981) estimated the entire outer core is convecting except for a diffusively stable layer some 70 km thick beneath the CMB. One problem with this scenario, as they realized, is that creating a stable layer of this thickness by diffusive processes would take several times the age of the Earth.

Alternatively, Loper (1989) hypothesized that it may be possible to have both stable stratification throughout the outer core and the movement of chemically buoyant material towards the CMB, a scenario known as penetrative convection. This suggestion rests in part on experiments on non-rotating, electrically insulating fluids (Turner, 1973), in which there is a buoyancy source at widely spaced intervals (relative to the container size) along the bottom of the system. The experiments indicate that as the buoyant material rises, it entrains surrounding material and becomes more dilute, and thus slightly heavier. Nevertheless, it always remains lighter than the surrounding material. Hence, the new material always rises to the top, with broad return of material everywhere else. In such a manner it might be possible to form a stably stratified compositional state in the outer core. Since stable stratification inhibits convective motions, which presumably regenerate the magnetic field, one might infer that stable stratification throughout the outer core is not compatible with the presence of a magnetic field. However, although penetrative convection implies a stably stratified core, the helicity of the rising blobs can provide the necessary dynamo action (Moffatt, 1988). Thus, an outer core with at least some stable stratification may not preclude dynamo action. In fact, there is some evidence (Gubbins *et al.*, 1990) that a stationary (perhaps stably stratified) fluid layer at the top of the core, some thirty percent of the core radius, can enhance dynamo action.

A different hypothesis on forming a stable layer at the top of the outer core invokes a CMB temperature that is constant with time (Gubbins *et al.*, 1982). From an initially convecting core, a constant temperature boundary condition will allow a subadiabatic region to develop beneath the CMB. The heat flux must conduct across this region, implying a relatively low rate of core cooling. For the parameters relative to the core, this

stable layer may be anywhere between 350 and 2000 km thick. However, the proper CMB boundary condition on temperature is not known, but a non-cooling mantle is unlikely (Loper, 1984). Moreover, these calculations are for a one-component fluid; compositional convection may very likely reduce the size of the stable region (Gubbins *et al.*, 1982, Fearn and Loper, 1981).

Yet another mechanism for establishing a stable layer beneath the CMB involves dissolving mantle material at the top of the outer core with subsequent downward diffusion (Stevenson, 1990). The experiments of Knittle and Jeanloz (1986) indicate that FeO becomes a metallic liquid at high pressures and temperatures, and that FeO in the outer core could react with oxides such as one would expect in the lowermost mantle. Thus, chemical reactions may be occurring at the CMB, so that material less dense than the bulk of the outer core might be accumulating at the top of the outer core. In summary, there are several hypotheses on how a stable layer at the top of the Earth's outer core might form, but we cannot yet prudently choose which, if any, have any validity. Moreover, the possibility of thermally forced motions disrupting a stably stratified layer has not yet been explored.

Unfortunately, geophysical observations have been unable to resolve the presence of a stable layer. Although the seismic data can rule out strong stratification, weak stratification with a buoyancy period of a few hours may be present, particularly near the top of the outer core (Masters, 1979, Bolt, 1982). Attempts to fit the magnetic secular variation data with purely toroidal flow, which stable stratification near the outer core surface implies, have also been inconclusive (Whaler, 1980, 1986). However, although the data appear to disfavor tangentially geostrophic toroidal flow, the possibility of magnetostrophic toroidal flow leaves open the question of stable stratification near the core surface (Bloxham, 1990). Crossley (1984) and Melchior and Ducarme (1986) suggested that superconducting gravimeters may be able to detect gravitational changes small enough to observe core modes, and hence determine the stratification structure of the core. However, despite claims by Aldridge and Lumb (1987) that they had identified particular

inertial modes in a spectral analysis of the data, Melchior *et al.* (1988) were not so confident that they could identify observed peaks in the residual gravimetric data as inertial modes in the fluid core.

Braginsky (1984) christened the hypothetical layer beneath the CMB the 'H' layer, and he (1984, 1987) began a theoretical investigation of its magnetohydrodynamics. It is the intent of this chapter to continue the investigation of the dynamics of the H layer. Unlike the work on internal waves in a thick shell (Olson, 1977, Friedlander, 1985, Friedlander, 1989), which are concerned primarily with the parameter regime in which the buoyancy frequency is small compared with the rotational frequency, we will be concerned with a fluid shell in which the two are comparable. This will allow us to make certain thin-layer simplifications in our study of the H layer, which are not possible in a nearly homogeneous, thick fluid shell. Unlike studies of the hydrosphere (Lindzen, 1967, Longuet-Higgins, 1968), we must also contend with the effects of the magnetic field.

Although there is no unambiguous geophysical evidence concerning stable stratification near the surface of the Earth's core, and although there are a variety of magnetohydrodynamic instabilities that occur in a nearly homogeneous thick shell that may manifest themselves through the short-period (years-decades) geomagnetic secular variation (Hide, 1966, Fearn and Proctor, 1983, Friedlander, 1989), the secular variation may likely have a relatively shallow source in the core. We intend to investigate the possibility that low frequency wave motions supported by a stable layer at the top of the Earth's outer core may be responsible for a portion of the secular variation, as Braginsky (1984) suggested. An alternative shallow mechanism for causing the short-period secular variation is an electric current instability associated with the large currents that result from the curvature of the magnetic field lines near the insulating mantle in the model-Z dynamo (Braginsky and Fishman, 1987). However, the large electrical currents are a feature of the model-Z dynamo, but not of the Taylor-state dynamo, so it is by no means certain that these large currents exist, given the uncertainty of the state of the dynamo (Roberts, 1989). In any

case, while it will be impossible to identify exact features in the secular variation field with the solution to any simple theoretical model, we hope to at least gain an understanding of the general spatial and temporal characteristics of waves in the hypothetical H layer.

In Section 5.2, we review Laplace's tidal equations, which govern the motion of a stably stratified, electrically insulating, rotating, thin fluid shell. Laplace's tidal equations rely on several assumptions, including a zeroth order hydrostatic balance, the Boussinesq approximation, inviscid flow, linear flow, the 'shallow-water' approximation, and the 'traditional' approximation, the last two relying on the primarily horizontal flow of a stably stratified, thin fluid layer. Lindzen (1967) and Longuet-Higgins (1968) have solved the Laplace's tidal equations, using a thin shell as a model for the Earth's atmosphere and oceans. For a homogeneous one-layer model with a free surface, the equations admit oscillations of the fluid surface known as the surface, or barotropic, mode. For a continuously stratified model with real buoyancy frequency N, the equations admit an infinite number of internal, or baroclinic, modes. Two classes of waves exist for both the surface and internal modes: the high frequency gravity waves and the low frequency Rossby, or planetary, waves.

If we are to apply the results to the H layer at the top of the Earth's magnetofluid core, we must also model the fluid as an electrical conductor. A dipole magnetic field will serve as a simple model for the core surface magnetic field. We modify Laplace's tidal equations to include the effects of the linearized Lorentz force due to this dipole field, and also add the linearized magnetic induction equation to our system of equations. In the limit of a thin-layer, the induction term is small compared with the advection and diffusion terms in the magnetic induction equation. We then extend the model from one shallow layer to two as an improved model for studying stratified flow in the core, and discuss the relevance of the first baroclinic mode of the two-layer model. We also introduce the 'rigid-lid' approximation that will enable us to represent the first baroclinic mode of the

two-layer model as the surface mode of the one-layer model, using the 'equivalent depth' and 'reduced gravity'.

In Section 5.3 we transform the spherical system to a Cartesian one, using the β-plane transformation. Since we are primarily interested in the magnetic analog of the low frequency Rossby waves, we make a further approximation that we denote the quasi-magnetostrophic approximation. In the quasi-magnetostrophic state, the Coriolis and pressure forces balance in the momentum equations, but the curl of the Lorentz force balances the curl of the Coriolis force in the vorticity equation. Using this approximation, we analytically solve the modified Laplace's tidal equations for magnetic Rossby waves on the β-plane, and compare the solutions with those for the well-understood non-magnetic problem. The eigenfunctions show that a magnetic field can break the equatorial waveguide that traps non-magnetic Rossby waves. However, for this thin-layer analysis the purely imaginary eigenfrequencies indicate that the solutions are overdamped due to the high Ohmic dissipation.

In Section 5.4, we numerically solve the modified Laplace's tidal equations on the sphere, and again compare the solutions with those for the non-magnetic problem. The solutions bear out the behavior predicted by the β-plane solutions. The solutions on the sphere also uncover a deficiency of the quasi-magnetostrophic approximation. In Section 5.5 we present a continuously stratified model, and review Braginsky's (1984, 1987) solutions. Finally, in Section 5.6, we discuss the limitations of the theory, and comment on the possible relevance of magnetic Rossby waves to the short-period secular variation. The notation that we use in this chapter differs slightly from that in the previous two, but we hope that we clearly define terms as we proceed.

5.2 Derivation of the modified Laplace's tidal equations

The Navier-Stokes equations governing the motion of an electrically conducting, rotating fluid are

$$\rho\left(\frac{D\mathbf{v}}{Dt} + 2\Omega \times \mathbf{v}\right) = -\nabla p + \rho\mathbf{g} + \nu\nabla^2\mathbf{v} + \frac{1}{\mu_o}(\nabla \times \mathbf{B}) \times \mathbf{B}, \qquad (5.1)$$

where $\mathbf{v}$ represents the fluid velocity, p the fluid pressure, ρ the fluid density, ν the kinematic viscosity, Ω the rotation vector, and $\mathbf{g}$ the gravitational acceleration. Associated with the magnetic field $\mathbf{B}$ is an electric current density $\mathbf{J} = 1/\mu_o(\nabla \times \mathbf{B})$, where μ_o is the permeability of free space. Moreover, for an incompressible fluid

$$\nabla \cdot \mathbf{v} = 0. \qquad (5.2)$$

In order to simplify the equations of motion (5.1) - (5.2), we must make additional assumptions. We assume a hydrostatic equilibrium state (p_o,ρ_o), about which we expand p, ρ, $\mathbf{v}$, and $\mathbf{B}$. For $\rho'/\rho_o << 1$, where ρ' is the perturbation density and ρ_o is the hydrostatic density, the Boussinesq approximation permits us to omit terms in ρ'/ρ_o except as they affect the buoyancy force. We will also assume inviscid flow, since we are concerned with low Ekman number flow of the mainstream.

Stable stratification tends to supress radial motions, so that in stably stratified regions of the core horizontal motions are dominant. For a system in which motions are primarily horizontal, the horizontal scale L is much greater than the vertical scale D. This scaling is natural for the thin spherical shells that comprise the Earth's atmosphere and oceans, but it is not obviously valid for a thick shell such as the Earth's outer core. However, in stably stratified regions of the core, the thick fluid shell behaves as many concentric thin fluid shells, so that D is perhaps order tens of kilometers and L is order hundreds of kilometers. We will next consider two approximations that take advantage of

the thinness (D << L) of the stratified layers. The first is the shallow-water (long wave) approximation.

We employ a spherical system with coordinates (λ,θ,r) representing the longitude, latitude, and radius. Consider first a homogeneous fluid layer of density ρ_0 ($\rho' = 0$ for a single homogeneous layer) bounded by a rigid sphere at $r = R$ and a free surface at $r = R+H+\eta$, with $\eta = \eta(\lambda,\theta)$. $H << R$ is the equilibrium thickness of the layer, and $\eta << H$ represents perturbations of the free surface from $r = R+H$. This is the simplest model that one might use to model the atmosphere or oceans. Of course, it is not a very good model for a stable layer at the top of the Earth's outer core, but we begin with it in order to introduce ideas. In a shallow system such as the thin spherical shell that we are considering, we can replace the continuity equation (5.2) with

$$\frac{\partial \eta}{\partial t} + \frac{1}{r\cos\theta}\left\{\frac{\partial[(H+\eta)u_\theta \cos\theta]}{\partial\theta} + \frac{\partial[(H+\eta)u_\lambda]}{\partial\lambda}\right\} = 0 \qquad (5.3)$$

where (u_λ,u_θ) are the eastward and northward velocities. This is the shallow-water approximation, which is valid under the conditions D << L, and $\eta << H << R$ (Gill, 1982). One consequence of the hydrostatic assumption and the shallow-water approximation is that $\nabla_H p = \rho_0 g \nabla_H \eta$, where p is now the non-hydrostatic pressure, and ∇_H is the horizontal gradient operator. We will make use of this in reducing (5.1)

The second approximation that relies on the shallow geometry is the traditional approximation, which allows one to substitute the variable radial coordinate r by the constant radius R of the spherical shell. In addition, one must also drop the terms in the horizontal components of (5.1) that are proportional to the radial velocity u_r in order to preserve the conservation of linear momentum principle that the equations should express (Phillips, 1966, Veronis, 1968). The resulting equations for horizontal motions are

$$\frac{Du_\lambda}{Dt} - (2\Omega + \frac{u_\lambda}{R\cos\theta})\, u_\theta \sin\theta = -\frac{1}{\rho_o R\cos\theta}\frac{\partial p}{\partial \lambda} + F_\lambda, \text{ and} \tag{5.4}$$

$$\frac{Du_\theta}{Dt} + (2\Omega + \frac{u_\lambda}{R\cos\theta})\, u_\lambda \sin\theta = -\frac{1}{\rho_o R}\frac{\partial p}{\partial \theta} + F_\theta, \tag{5.5}$$

where $\mathbf{F} = (F_\lambda, F_\theta)$ is the Lorentz force per mass density. Linearizing (5.3) and (5.4) - (5.5) with respect to u_θ, u_λ, and η, and substituting $\rho_o g \nabla_H \eta$ for $\nabla_H p$, we obtain the Laplace's tidal equations modified by (still undetermined) Lorentz forces. They are

$$\frac{\partial u_\lambda}{\partial t} - 2\Omega\, u_\theta \sin\theta = -\frac{g}{R\cos\theta}\frac{\partial \eta}{\partial \lambda} + F_\lambda, \tag{5.6}$$

$$\frac{\partial u_\theta}{\partial t} + 2\Omega\, u_\lambda \sin\theta = -\frac{g}{R}\frac{\partial \eta}{\partial \theta} + F_\theta, \text{ and} \tag{5.7}$$

$$\frac{\partial \eta}{\partial t} + \frac{H}{R\cos\theta}\{\frac{\partial [u_\theta \cos\theta]}{\partial \theta} + \frac{\partial u_\lambda}{\partial \lambda}\} = 0. \tag{5.8}$$

With $\mathbf{F} = \mathbf{0}$, the system admits longitudinally travelling wave solutions (Longuet-Higgins, 1968). These waves involve a fluctuation of the fluid surface η, and hence are known as surface modes.

Let us now examine the form of $\mathbf{F}$, which represents the Lorentz force contribution. $\mathbf{F} = 1/\rho_o\mu_o\, (\nabla \times \mathbf{B}) \times \mathbf{B}$, but hereinafter, we will absorb a factor of $(\rho_o\mu_o)^{-1/2}$ into $\mathbf{B}$, which will now represent the total magnetic field strength as measured by its Alfven velocity. Similarly, we will absorb a factor of $(\rho_o\mu_o)^{-1/2}$ into $\mathbf{E}$, the electric field intensity, and a factor of $(\mu_o/\rho_o)^{1/2}$ into $\mathbf{J}$, the electric current density. Let us set $\mathbf{B} = \mathbf{b}_o + \mathbf{b}$, with $\mathbf{b}_o >> \mathbf{b}$, and $\mathbf{e}_o = \mathbf{0}$, so that $\mathbf{E} = \mathbf{e}$. The linearized form of the Lorentz force is then $\mathbf{F} = (\nabla \times \mathbf{b}) \times \mathbf{b}_o + (\nabla \times \mathbf{b}_o) \times \mathbf{b}$. The toroidal component of the magnetic field, possibly quite large in the core's interior, is likely nearly zero at the CMB due to the low electrical conductivity of the mantle. Though it is possible that large electrical currents directly

underneath the CMB allow a large toroidal magnetic field very near the CMB, it is also possible that the poloidal component of the field dominates in this zone. We will thus choose the simplest poloidal field, a dipole, for $\mathbf{b}_o$.

In spherical coordinates, a dipole field takes the form

$$\mathbf{b}_o = BR^3/r^3\,(2\sin\theta\,\hat{\mathbf{r}} - \cos\theta\,\hat{\theta}), \tag{5.9}$$

where B is the magnitude of the dipole field. For this choice of $\mathbf{b}_o$, $\nabla \times \mathbf{b}_o = \mathbf{0}$, so that the linearized Lorentz force $\mathbf{F} = (\nabla \times \mathbf{b}) \times \mathbf{b}_o = \mathbf{j} \times \mathbf{b}_o$. The scaled, linearized form of Ohm's law for the perturbation fields (with $\mathbf{v}_o = \mathbf{0}$) is

$$\mathbf{j} = (1/\chi)\,(\mathbf{e} + \mathbf{v} \times \mathbf{b}_o), \tag{5.10}$$

where $\chi = 1/\sigma_e\mu_o$ is the magnetic diffusivity and σ_e is the fluid electrical conductivity. With $\mathbf{b}_o$ from (5.9), and $r \cong R$ across the thin layer,

$$\mathbf{j} \cong (1/\chi)\,(\,2u_\theta\,B\sin\theta + e_\lambda,\, -2u_\lambda\,B\sin\theta + e_\theta,\, -u_\lambda\,B\cos\theta + e_r). \tag{5.11}$$

Taking the cross product with $\mathbf{b}_o$ (with $r \cong R$) to form $\mathbf{F}$, and substituting into (5.6) - (5.7), we obtain

$$\frac{\partial u_\lambda}{\partial t} - 2\Omega\,u_\theta\sin\theta = -\frac{g}{R\cos\theta}\frac{\partial \eta}{\partial \lambda}$$
$$-\frac{B^2}{\chi}\,u_\lambda\,(3\sin^2\theta + 1) + \frac{B}{\chi}\,(e_r\cos\theta + 2e_\theta\sin\theta)\,, \text{ and} \tag{5.12}$$

$$\frac{\partial u_\theta}{\partial t} + 2\Omega\,u_\lambda\sin\theta = -\frac{g}{R}\frac{\partial \eta}{\partial \theta} - \frac{4B^2}{\chi}\,u_\theta\sin^2\theta - \frac{2B}{\chi}\,e_\lambda\sin\theta\,. \tag{5.13}$$

Equations (5.8), and (5.12) - (5.13) form a set of three partial differential equations in (t,θ,λ) for the unknowns functions u_λ, u_θ, and η. Because of the thin-layer approximations, the solution is independent of r. However, (5.12) - (5.13) also contain the unknown electric field, **e**, r-independent by assumption. In the absence of fluid viscosity, we allow free slip along the horizontal boundaries. We observe that $\mathbf{j} = \nabla \times \mathbf{b} = (1/\chi)\ (\mathbf{e} + \mathbf{v} \times \mathbf{b}_o)$ is then also not necessarily zero on these boundaries. But inside an insulator (the mantle will form one horizontal boundary in our final, more realistic model) $\mathbf{j} = \mathbf{0}$, so j_r must be zero everywhere since the radial component of the electric current density cannot suffer a discontinuity at a horizontal boundary. Thus by (5.11), $e_r = u_\lambda\ B \cos\theta$. However, we can say nothing about the horizontal components of **e**, since they relate to the horizontal components of **j**, which can suffer a discontinuity at the horizontal boundaries. We will later return to this issue.

In order to make the model more relevant to a study of the dynamics of a stably stratified layer at the top of the outer core, we must extend the model to two layers. Consider the two-layer model of Figure 5.1. The model has two homogeneous layers of thicknesses H_1 and H_2 with total thickness $H_1+H_2 = H$, and densities $\rho_1 > \rho_2$ differing by a small amount $\Delta\rho = \rho_1 - \rho_2$. The radial distance $r = R$ represents the rigid, lower boundary, $r = R+H_1$ the equilibrium level between the two layers, and $r = R+H_1+H_2 = R+H$ the equilibrium level above the two layers. The surface between the two layers lies at $r = R+H_1+h$ and the free surface above the two layers lies at $r = R+H+\eta$. Since $(\eta,h) << (H_1,H_2)$, and $(H_1,H_2) << L$, the characteristic horizontal length scale, we will from the outset assume the hydrostatic, shallow-water, and traditional approximations.

One can show (Gill, 1982), that the two-layer model admits two modes of oscillations, the barotropic mode and the baroclinic mode. In the limit for which we are concerned, $\Delta\rho/\rho \rightarrow 0$, the first two-layer mode, the barotropic mode, becomes the surface mode for the one-layer model of thickness H, and involves fluctuations of η. The second two-layer mode, known as the first baroclinic mode, is an internal mode, and does not exist

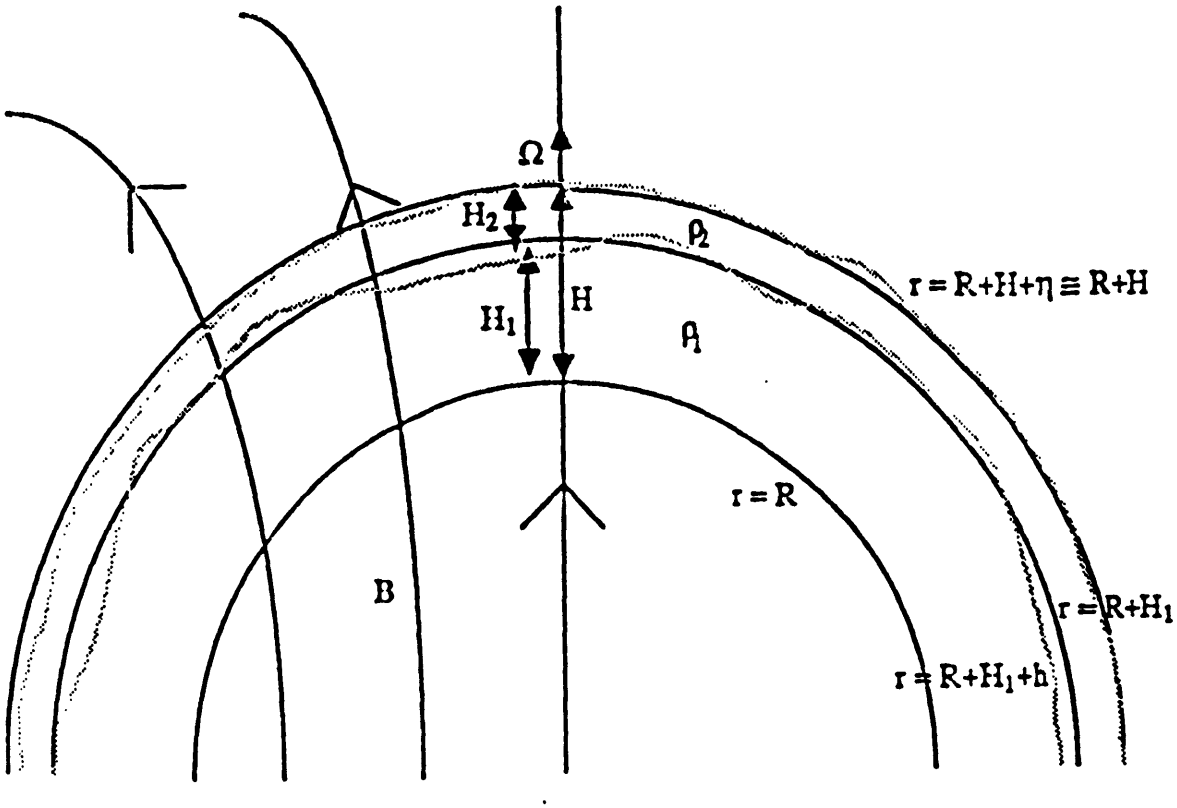

Figure 5.1 Sketch of the two-layer model that serves as a study for the H layer. For the linear, thin-layer approximations to be valid, the (dotted line) wave surfaces must be much less than the (solid line) equilibrium layer thicknesses, which must be much less than the (solid line) shell radius, *i.e.*, $(h,\eta) << (H_1,H_2) << R$. For the surface (barotropic) mode, $h << \eta$, and for the internal (baroclinic) mode of interest in this study, $\eta << h$, so that under the rigid-lid approximation we can associate $r = R+H+\eta$ with the mantle. The density $\rho_1 < \rho_2$, though $\rho_1 \cong \rho_2$. Ω is the rotation vector, and B is the zeroth order dipole field.

for a one-layer model. This mode has no radial surface motion at r = R+H, and involves only fluctuations of h. For this mode, we can associate r = R+H with the rigid mantle. One could, of course, extend the two-layer model to include infinitely many layers, *i.e.*, a continuously stratified fluid, which would have an infinite number of baroclinic (internal) modes. Internal modes in a continuously stratified fluid exhibit some vertical motion, characterized by the buoyancy frequency, N, where $N^2 = - (g/\rho_o)(d\rho_o/dr)$. Braginsky (1984, 1987) examined the problem of magnetohydrodynamic waves in a continuously stratified fluid, and we will later discuss his results.

Baroclinic modes in a continuously stratified fluid have no net flow across a vertical plane, but in a finite-layer model, baroclinic motion can have a net flow in a given fluid layer. Excitation of the first baroclinic mode of the two-layer model might therefore be a possible consequence of introducing fluid into an upper stable layer from underneath via penetrative convection, which is one proposed means for forming the H layer (Braginsky, 1987, Loper, 1989). In order to simplify the analysis, we must restrict the thickness of the lower layer. Nevertheless, since we are interested primarily in motion along the two fluid interface, we anticipate that the model will give some insight on magnetohydrodynamic waves in the H layer.

To study the first baroclinic mode, we will make the rigid-lid approximation. This consists of assuming $\partial\eta/\partial t << \partial h/\partial t$, and $\rho_1 \cong \rho_2 \cong \rho$. The positive density contrast $\Delta\rho$ is negligible except for the term involving g, the buoyancy term. This, of course, is simply the Boussinesq approximation for a two-layer model. The rigid-lid approximation assumes small upper surface displacements, with an imaginary rigid boundary (the mantle) providing the necessary pressure gradients. By manipulating the horizontal equations of motion and divergence equation appropriate to each layer (and using our knowledge of e_r), we obtain a system of three equations in the three unknowns h, $u_{\lambda *}$, and $u_{\theta *}$, where $u_{\lambda *} = u_{\lambda 2} - u_{\lambda 1}$, and similarly for $u_{\theta *}$, $e_{\lambda *}$, and $e_{\theta *}$. The resulting equations are

$$\frac{\partial u_{\lambda *}}{\partial t} - 2\Omega\, u_{\theta *} \sin\theta = -\frac{g}{R\cos\theta}\frac{\Delta\rho}{\rho}\frac{\partial h}{\partial \lambda} - \frac{4B^2}{\chi} u_{\lambda *} \sin^2\theta + \frac{2B}{\chi} e_{\theta *} \sin\theta \quad , \quad (5.14)$$

$$\frac{\partial u_{\theta *}}{\partial t} + 2\Omega\, u_{\lambda *} \sin\theta = -\frac{g}{R}\frac{\Delta\rho}{\rho}\frac{\partial h}{\partial \theta} - \frac{4B^2}{\chi} u_{\theta *} \sin^2\theta - \frac{2B}{\chi} e_{\lambda *} \sin\theta \quad , \text{ and} \quad (5.15)$$

$$\frac{\partial h}{\partial t} + \frac{H_1 H_2}{(H_1+H_2)\, R\cos\theta}\left\{\frac{\partial [u_{\theta *}\cos\theta]}{\partial \theta} + \frac{\partial u_{\lambda *}}{\partial \lambda}\right\} = 0 \quad . \quad (5.16)$$

Equations (5.14) - (5.16) are the dynamical equations appropriate for the first baroclinic mode of a rotating, electrically conducting, thin, two-layer fluid shell permeated by a dipole magnetic field. Although this system describes the first baroclinic mode of a two-layer model, it is mathematically identical to the system (5.6) - (5.8) that describes the surface mode of a one-layer model with equivalent depth $H_* = H_1H_2/(H_1+H_2)$, reduced gravity $g_* = g\,\Delta\rho/\rho$, and h replacing η. By our rigid-lid approximation, we have replaced the vacuum for $r > R+H+\eta$ with a solid, so our model now includes the rigid mantle. Of course, the lower layer must be unrealistically thin, and the solid bottom boundary precludes further fluid-fluid interactions, but following Braginsky (1987), we assume the density of forces is greatest in the H layer.

5.3 Derivation and solution of the β - plane equations

In order to solve (5.14) - (5.16), one must resort to a numerical approach. However, we will first transform the spherical Laplace's tidal equations to a local tangent plane, on which we can make analytical progress and gain insight into the full spherical problem. The transformation, well known and widely used in meterology and oceanography, is the β-plane transformation. It involves approximating the normal component of the rotation vector $f = 2\Omega\sin\theta$, which is the only component remaining after making the traditional approximation, by $f = f_o + \beta y$, where $f_o = 2\Omega \sin\theta_o$ and

$\beta = 2\Omega/R \cos \theta_o$. R is the radius of the spherical shell, and y represents the coordinate northwards from θ_o, the latitude at which the β-plane is tangent. In this Cartesian frame, x represents the coordinate in the locally eastward direction, and z the coordinate in the direction locally upward and normal from the tangent plane. The only effect of the Earth's sphericity that the approximation retains is to allow f to vary linearly with latitude. As the first term in an expansion of f, the approximation is valid only for motions limited in latitudinal extent. Hence, we must in general have $|y|/R << 1$ (Pedlosky, 1987).

Veronis (1963a,b) derived an additional condition on the validity of the β-plane to describe baroclinic motion, namely, that $D/L << \tan\theta$, where D and L are the characteristic vertical and horizontal length scales, respectively. Thus, one cannot expect accurate solutions within a narrow band of the equator. For the hydrosphere, with a characteristic shell thickness of 7 km and a radius of 6400 km, this excludes a band of a few degrees on each side of the equator. However, for the outer core, with a shell perhaps some 10 - 70 km thick and a radius of only 3500 km, this condition requires the exclusion of at least 5 degrees on each side of the equator. Despite these limitations on the applicability of the β-plane, we will nevertheless apply an equatorial β-plane, so that $\theta_o = 0$ degrees, $f_o = 0$, and $\beta = 2\Omega/R$. Moreover, for solutions on the equatorial β-plane to be valid under the condition that $|y|/R << 1$, they must go to zero as $|y| \rightarrow \infty$ (or more precisely, as $|y| \rightarrow R$).

Hide (1966) applied a mid-latitude β-plane analysis to a homogeneous, electrically conducting, rotating, thick fluid shell. Hide chose such a model to study magnetic-Coriolis (MC) waves and their possible relation to the secular variation. In his study of MC waves in a thick, homogeneous shell, Hide dropped $\chi\nabla^2\mathbf{b}$ in favor of $\partial\mathbf{b}/\partial t$. We have retained the diffusion term, however, because we are concerned with the smaller scale motions in a thin, inhomogeneous fluid layer. Moreover, the zeroth order magnetic field is different: like Fearn and Proctor (1983) and Friedlander (1989), Hide used a toroidal field, which may be more appropriate for the bulk of the core, rather than a poloidal field, which is perhaps a better model near the top.

Let us now apply the equatorial β-plane approximation to our system of equations (5.14) - (5.16). Under the equatorial β-plane approximation, we replace sinθ with θ and cosθ with 1, and set $f = \beta y$, where northward distance $y = R\theta$ and eastward distance $x = R\lambda$. We obtain

$$\frac{\partial u_x}{\partial t} - \beta y u_y = - g \frac{\partial h}{\partial x} - (4B^2/\chi)(y^2/R^2) v_x + (2B/\chi)(y/R) e_y, \qquad (5.17)$$

$$\frac{\partial u_y}{\partial t} + \beta y u_x = - g \frac{\partial h}{\partial y} - (4B^2/\chi)(y^2/R^2) v_y - (2B/\chi)(y/R) e_x, \text{ and} \qquad (5.18)$$

$$\frac{\partial h}{\partial t} + H \{\frac{\partial u_x}{\partial x} + \frac{\partial u_y}{\partial y}\} = 0, \qquad (5.19)$$

where (u_x,u_y) represents the velocity and (e_x,e_y) the electric field in the (x,y) direction. We have dropped the '*' subscripts on the velocity fields, g, and H, but it should be understood that for the first baroclinic mode of the two-layer model, the velocity fields are actually the differential velocity fields, g is the reduced gravity, and H is the equivalent depth.

If B, the magnitude of the zeroth order dipole field, and e_H, the horizontal electric field, equal zero, we obtain the β-plane approximation to Laplace's tidal equations (Lindzen, 1967). We can then reduce (5.17) - (5.19) to a single equation for u_y, and assume eastward propagating wave solutions of the form $u_y(x,y,t) = u_y(y) \exp [i (k_x x - \omega t)]$. The resulting ordinary differential equation that governs the latitudinal structure is

$$\frac{d^2 u_y}{dy^2} + (\frac{\omega^2}{c^2} - k_x^2 - \frac{\beta k_x}{\omega} - \frac{\beta^2 y^2}{c^2}) u_y = 0. \qquad (5.20)$$

This equation exhibits turning point behavior about the critical latitudes y_c, with $y_c^2 = (\omega^2 - k_x^2 c^2 - \beta k_x c^2/\omega)/\beta^2$. For $|y| < |y_c|$, equation (5.20) admits wavelike solutions,

but for $|y| > |y_c|$, only evanescent solutions exist. Hence, the equator acts as a waveguide, with the latitude varying Coriolis parameter trapping solutions in low latitudes.

Provided the dispersion relation

$$\omega^2/c^2 - k_x^2 - \beta k_x/\omega = (2n+1)\beta/c, \tag{5.21}$$

the solutions to (5.20) that are finite at $y = 0$ and vanish as $|y| \rightarrow \infty$ are

$$u_y(x,y,t) = 2^{-n/2} H_n\{ (\beta/c)^{1/2} y\} \exp(-\beta y^2/2c) \cos(k_x x - wt), \tag{5.22}$$

where H_n is the Hermite polynomial of integer order n. Solutions for which the term $\beta k_x/\omega$ in (5.21) is small, so that $\omega^2 \approx (2n+1)\beta c + k_x^2 c^2$, correspond to high frequency gravity waves. Gravity waves propagate both eastward and westward, symmetrically about $k_x = 0$. Solutions for which the term ω^2/c^2 in (5.21) is small, so that $\omega \approx -\beta k_x/(k_x^2 + (2n+1)\beta/c)$, correspond to low frequency Rossby (planetary) waves. Rossby waves, which owe their existence to the variation of the Coriolis force with latitude, propagate only westward. There are two waves in the large frequency gap between gravity and Rossby waves. The first is the non-dispersive Kelvin wave, which corresponds to $n = -1$ so that $\omega = k_x c$. It propagates eastward and involves motion only in the x-direction. The second is the mixed Rossby-gravity wave, which corresponds to $n = 0$ so that $\omega/c - k_x - \beta/\omega = 0$.

For B and $\mathbf{e_H}$ non-zero, we could again use (5.17) - (5.19) to eliminate two variables in favor of the third, say the fluid wave surface h, and repeat our procedure for non-magnetic waves. We have done this, and the result is a rather messy second order inhomogeneous differential equation, whose associated homogeneous equation does not have an obvious closed form solution. However, we are primarily interested in waves whose periods are on the years-decades time scale, *i.e.*, Rossby waves, whereas gravity

waves have periods of less than a day. We will therefore filter out the high frequency gravity waves, significantly simplifying the algebra.

For a study of long-period waves, the fluid is nearly in geostrophic balance. For a geostrophic balance, we can drop the inertial and Lorentz force terms in (5.17) and (5.18), yielding

$$- \beta y u_y = - g \frac{\partial h}{\partial x}, \text{ and} \tag{5.23}$$

$$\beta y u_x = - g \frac{\partial h}{\partial y}. \tag{5.24}$$

However, this geostrophic balance is degenerative (Pedlosky, 1987), in the sense that it cannot predict the velocity field's evolution with time, but only insure its Coriolis force balances the given pressure force. We must therefore go to a higher order of approximation by obtaining the z-component of the curl of (5.17) and (5.18), obtaining

$$\left(\frac{\partial}{\partial t} + \frac{4B^2}{\chi}\frac{y^2}{R^2}\right)\left(\frac{\partial v_y}{\partial x} - \frac{\partial v_x}{\partial y}\right) + \beta y \left(\frac{\partial v_x}{\partial x} + \frac{\partial v_y}{\partial y}\right) + \beta v_y - \frac{8B^2}{\chi}\frac{y}{R^2} v_x = - \frac{2B}{\chi}\frac{y}{R}\left(\frac{\partial e_x}{\partial x} + \frac{\partial e_y}{\partial y}\right) - \frac{2B}{\chi}\frac{1}{R} e_y \tag{5.25}$$

The vorticity balance, equation (5.25), examines the three-way balance between the curl of the Coriolis, inertial, and Lorentz forces. Using equations (5.19), (5.23), (5.24), and (5.25), it is now relatively easy to obtain an equation for h, with forcing terms e_x and e_y. Again looking for longitudinally travelling wave solutions, we set $h(x,y,t) = h(y) \exp [i (k_x x - \omega t)]$. The result is

$$\left(-i\omega c^2 + \frac{4B^2c^2}{\chi}\frac{y^2}{R^2}\right)\frac{d^2h}{dy^2} + \left(i\omega c^2/y + \frac{4B^2c^2}{\chi}\frac{y}{R^2}\right)\frac{dh}{dy} + \left(i\omega c^2 k_x^2 - \frac{4B^2c^2k_x^2}{\chi}\frac{y^2}{R^2} + ic^2\beta k_x + i\omega\beta^2 y^2\right) h = - \frac{2B}{\chi}\frac{H\beta y^2}{R}\left(\frac{\partial e_x}{\partial x} + \frac{\partial e_y}{\partial y} + \frac{e_y}{y}\right). \tag{5.26}$$

If we introduce solely the z-curl of the inertial term, *i.e.*, B = 0, (5.26) reduces to

$$\frac{d^2h}{dy^2} - \frac{1}{y}\frac{dh}{dy} + \left(- k_x^2 - \frac{\beta k_x}{\omega} - \frac{\beta^2 y^2}{c^2} \right) h = 0 . \qquad (5.27)$$

The form of this equation differs from (5.20) in the presence of the term -(1/y)(d/dy) and the absence of the term (ω^2/c^2). The cause of the absence of the latter term is that in setting the geostrophic balance from the outset, we have already filtered out gravity waves. Such a system is quasi-geostrophic in that it allows small deviations from the steady state geostrophic flow; these deviations are the Rossby waves. The second term presumably results from the small incompatability of (5.23) and (5.24) with (5.25). Nevertheless, at least for large y, away from the equator where the geostrophic balance must break down, (5.27) yields the expected behavior of Rossby waves.

For

$$\omega \Big/ \left(\frac{4B^2}{\chi} \frac{y^2}{R^2} \right) << 1 \qquad (5.28)$$

rearrangements of the magnetic field rather than inertial accelerations account for deviations from geostrophy. For a core surface magnetic field strength of about 10^{-4} T, B = 10^{-3} m/sec, and for an electrical conductivity $\sigma_e = 3 \times 10^5$ mho/m, $\chi = 1/\sigma_e\mu_o$ is approximately 10^0 m^2/sec, so that except for a band some tens of kilometers about the equator, the inequality (5.28) should hold for periods longer than a few years. Such a state we denote quasi-magnetostrophic since the Lorentz force rather than the inertial force enters into the force balance at this higher approximation. Although we have retained the time dependence through the continuity equation (5.19), we have filtered out the magnetic analog of high frequency gravity waves through our geostrophic approximation. Under the

quasi-magnetostrophic approximation we look for the low frequency magnetic Rossby waves.

If we apply the condition (5.28) to equation (5.26), it simplifies to

$$y^2 \frac{d^2h}{dy^2} + y \frac{dh}{dy} + (-k_x^2 y^2 + \frac{i\omega\beta^2\chi R^2}{4B^2c^2} y^2 + \frac{ik_x\beta\chi R^2}{4B^2}) h =$$
$$-\frac{1}{2B} \frac{HR\beta y^2}{c^2} (\frac{\partial e_x}{\partial x} + \frac{\partial e_y}{\partial y} + \frac{e_y}{y}) \quad . \qquad (5.29)$$

The equation governing non-magnetic Rossby waves, (5.20), is a Schrodinger equation; (5.29) is an inhomogeneous Bessel equation. Provided

$$\nu^2 = -\frac{i\, k_x\beta\chi R^2}{B^2}, \text{ and} \qquad (5.30)$$

$$k_y^2 = -k_x^2 + \frac{i\,\omega\beta^2\chi R^2}{B^2c^2}, \qquad (5.31)$$

a solution of the homogeneous equation ($e_H = 0$) associated with (5.29) is $h(y) = C_\nu(k_y y)$, where C_ν represents a Bessel function of order ν and k_y is the latitudinal wavenumber (Abramowitz and Stegun, 1964). Alternatively, we can rearrange (5.31) to obtain the dispersion relation for real, assigned k_y. The result is

$$\omega = -i\,(k_x^2 + k_y^2)\,\frac{B^2c^2}{\beta^2\chi R^2}. \qquad (5.32)$$

For validity of the β-plane, we must seek solutions $h(y) \to 0$ as $|y| \to \infty$, as well as solutions that are bounded at the origin, *i.e.*, the equator. The proper Bessel function is therefore that of the first kind, $J_\nu(k_y y)$, which is bounded at the origin. For fixed order ν and large $k_y y$, $J_\nu(k_y y) \sim (2/\pi k_y y)^{1/2} \cos(k_y y - \nu\pi/2 - \pi/4)$. Hence, as $|y| \to \infty$, the

solution amplitude oscillates and decays as $|y|^{-1/2}$. While this geometric decay with latitude is not as rapid as the exponential decay with latitude of non-magnetic Rossby waves, it nevertheless approaches zero at large |y|. Hence, our complete β-plane solution for quasi-magnetostrophic waves, valid for all y, is

$$h(x,y,t) = \mathrm{Re}\ \{\ \exp\ [i\ (k_x x - \omega t)]\ J_\nu(k_y y)\ \}, \qquad (5.33)$$

with ν given by (5.30) and ω by (5.32).

One consequence of a Bessel function solution is that the solution is not equatorially trapped, but is non-zero at all latitudes y, albeit with geometric decay near the poles. This is unlike the solution for non-magnetic Rossby waves, which has the form of a Hermite polynomial multiplying a decaying exponential. It is because of the wave nature of Bessel functions that we can define a wavenumber k_y in the latitudinal direction as in (5.31). Note too that because of the lack of a turning point as is present in the Schrodinger equation (5.20), the modes on the infinite interval $[-\infty,\infty]$ are not discrete, but rather form a continuous set as seen by (5.32). The breakdown of the equatorial waveguide by the Lorentz force is an example of the countering effects of rotation and a magnetic field.

In order to insure solutions that are bounded at the equator and go to zero near the poles, we had to allow that the eigenfrequencies ω might be complex. In fact, from (5.32) we see that they are purely imaginary. In the limit of zero horizontal electric field intensity e_H, magnetic Rossby waves in the H layer on the equatorial β-plane are overdamped; there is no propagation. Let us put representative numerical values into (5.32) to get an estimate of the damping time. For an equivalent depth $H_* = 10$ km (*e.g.*, for $H_1 = 15$ km and $H_2 = 50$ km, $H_* = 11.5$ km), a density contrast $\Delta\rho/\rho = 10^{-7}$ (Loper, 1989), and $g = 10$ m/sec^2, the squared non-rotational surface mode phase speed c^2 is about 10^{-2} m^2/sec^2. With R roughly 10^6 m and $|\Omega|$ about 10^{-4} sec^{-1}, $\beta = 2\Omega/R$ is approximately 10^{-10} (m-sec)$^{-1}$. Using an Alfven wave speed $B = 10^{-3}$ m/sec, and χ of the order

10^0 m^2/sec, we find $\omega = i\, O(k_x^2 + k_y^2)$. For disturbances with characteristic horizontal distances of the order of hundreds of kilometers, the characteristic damping time is roughly 10^2 years.

Braginsky (1987) found that the internal modes of the magnetic Rossby waves in a continuously stratified fluid are also heavily damped. In conjunction with his boundary conditions, by assuming $\partial \mathbf{b}/\partial t << [\nabla \times (\mathbf{v} \times \mathbf{b}_o), \chi \nabla^2 \mathbf{b}]$ in the magnetic induction equation, Braginsky implicitly set $\mathbf{e_H} = \mathbf{0}$. The neglected term in the induction equation, $\partial \mathbf{b}/\partial t$, results in a phase shift between ω and k_x that can indicate less Ohmic dissipation. Thus, although the eigenmodes in an infinitely thin layer are overdamped, the relevance of the solution (5.33) with (5.30) and (5.32) (and of Braginsky's solution) to a finite layer is unclear. In a finite layer, a non-zero $\mathbf{e_H}$ can approximately balance $-\mathbf{v} \times \mathbf{b}_o$. Unfortunately, the functional form of the electric field, and therefore of the inhomogeneous term, is unknown. It is unknown because of our failure to account for the radial (z) details of the magnetic field in the H layer. We cannot, however, incorporate these details into the r-independent (z-independent) thin-layer theory.

In obtaining the solution (5.33) we assumed a geostrophic balance in the momentum equations, which we know is not valid near the equator, and assumed the Lorentz force terms enter only into the vorticity equation. However, these Lorentz force terms in our β-plane model are proportional to y^2, so as y grows, they should become increasingly more important in the force balance. While we could not find an analytic solution to the full β-plane equations (5.17) - (5.19), we note that the forementioned differential equation analogous to (5.26) contains coefficients of d^2h/dy^2, dh/dy, and h with additional terms higher order in $(B^4/\chi^2)(y^4/R^4)/(\beta^2 y^2)$. Although these terms are small in the quasi-magnetostrophic limit, being higher order in y, they do weaken the case for the validity of the β-plane solution, which only decays as $y^{-1/2}$ even under the quasi-magnetostrophic approximation. Of course, on the sphere, the Lorentz force does not grow to infinity as a function of latitude. It would therefore be of some interest to solve

(5.14) - (5.16) numerically, with $e_H = 0$, and compare with the β-plane solution (5.33), with (5.30) and (5.32).

5.4 Solution of the modified Laplace's tidal equations

With B and e_H zero, the β-plane solutions quite successfully reproduce the essential features of the solutions on the sphere (Longuet-Higgins, 1968), including equatorial wave trapping. Following and extending the method of Longuet-Higgins (1968), we numerically solve equations (5.14) - (5.16) with zero e_H but non-zero B. The details of the numerical calculations are in the appendix to this chapter. As for the β-plane, we look for longitudinally propagating travelling waves of the form exp [i ($s\lambda - \omega t$)], where s is the longitudinal wavenumber and λ is the longitude. Three non-dimensional parameters central to the problem are the frequency scaled by the rotational frequency,

$$\sigma = \omega/2\Omega, \tag{5.34}$$

the squared ratio of the rotational speed to the non-rotational gravity wave speed,

$$\varepsilon = 4\Omega^2R^2/c^2, \tag{5.35}$$

where $c^2 = g(\Delta\rho/\rho)(H_1H_2)/(H_1+H_2)$, and a measure of the strength of the Lorentz to Coriolis force (essentially the Elsasser number of Chapters 3 and 4),

$$\alpha = 4B^2/2\Omega\chi. \tag{5.36}$$

For a study of baroclinic Rossby waves in the Earth's hydrosphere, where $c^2 = g_*H_*$ is in the range 10^0 - 10^4 m^2/sec^2 (Gill, 1982), a representative value of ε is in the range 10^4 - 10^0. The parameter α, of course, is zero. For a study of baroclinic magnetic

Rossby waves in the H layer, a representative value of ε is probably at least as large as 10^6, because c^2 is most likely less than 10^{-2} m^2/sec^2 due to the small density contrast of the layers. For B = 10^{-3} m/sec, $|\Omega|$ about 10^{-4} sec^{-1}, and χ order 10^0 m^2/sec, α is in the range 10^{-1} - 10^{-2} (demonstrating that the quasi-magnetostrophic approximation is reasonable). When α is non-zero, we must admit the existence of complex eigenfrequencies σ due to the introduction of Ohmic dissipation. For the magnetically damped westward Rossby modes, both Re(σ) and Im(σ) will be negative.

Figures 5.2 and 5.3 are log-log plots of the eigenfrequencies $|\sigma|$ vs. $\varepsilon^{-1/2}$ for s = 1, at $\alpha = 10^{-2}$ and $\alpha = 10^{-1}$ (and both for $e_H = 0$) respectively, that correspond to the low frequency modes of the non-magnetic system ($\alpha = 0$), which we also show for comparison. In Figure 5.2, we show the eigenfrequencies for the two lowest equatorially symmetric and antisymmetric modes, corresponding to the mixed Rossby-gravity mode (which is antisymmetric) and the first three Rossby modes. For small ε, the Re(σ) at $\alpha = 10^{-2}$ is essentially identical to the Re(σ) at $\alpha = 0$ for these low order modes (those modes with few latitudinal zeros). A small non-zero Im(σ) is also present at $\alpha = 10^{-2}$, not present at $\alpha = 0$. Although it is difficult to numerically obtain the low frequency Rossby modes that are of interest on the years-decades time scale (Re(σ) < 10^{-3}) for ε as large as 10^6, we can make asymptotic predictions. As at $\alpha = 0$, at $\alpha = 10^{-2}$ the Re(σ) for each mode appears to go asymptotically towards zero as a power of $\varepsilon^{-1/2}$, though the presence of a magnetic field does somewhat decrease the Re(σ) from their non-magnetic values. For large ε at $\alpha = 10^{-2}$, the Im(σ) achieves a constant value of about -5×10^{-3} for the lowest mode, and a slightly larger constant value for higher modes. Thus, for large enough ε, the eigenfrequencies become primarily imaginary, as the β-plane solution (5.32) predicts (though with a different dependency on $\varepsilon^{-1/2}$, which we shall later discuss). Presumably, the relative increase of the Im(σ) to the Re(σ) for a given mode at fixed α and an increasing ε is due to the smaller length scale, and hence higher Ohmic dissipation, associated with increasing rotation rate. Higher order modes show a decreasing Re(σ), and a slightly

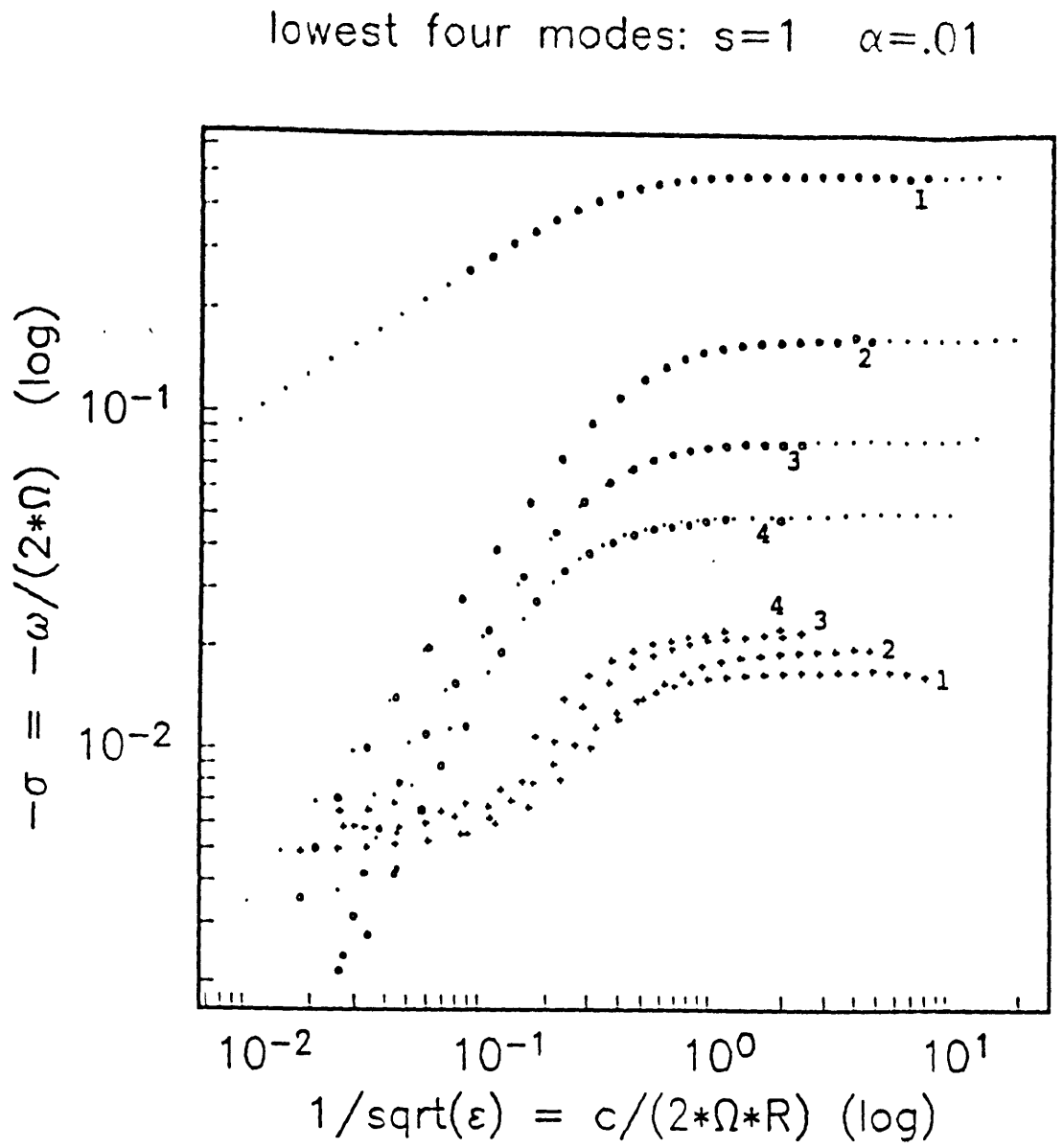

Figure 5.2 Log-log plot of the dispersion diagram, $|\sigma|$ vs. $\varepsilon^{-1/2}$, for the four lowest modes at s = 1. The circles represent the $Re(\sigma)$ at $\alpha = 10^{-2}$, and the plus signs represent the $Im(\sigma)$ at $\alpha = 10^{-2}$. For comparison, we show via dots the $Re(\sigma)$ at $\alpha = 0$ (Longuet-Higgins, 1968). The $Im(\sigma)$ is zero at $\alpha = 0$. We label the equatorially anti-symmetric mixed Rossby-gravity mode with a 1, the first symmetric Rossby mode with a 2, the first anti-symmetric Rossby mode with a 3, and the second symmetric Rossby mode with a 4.

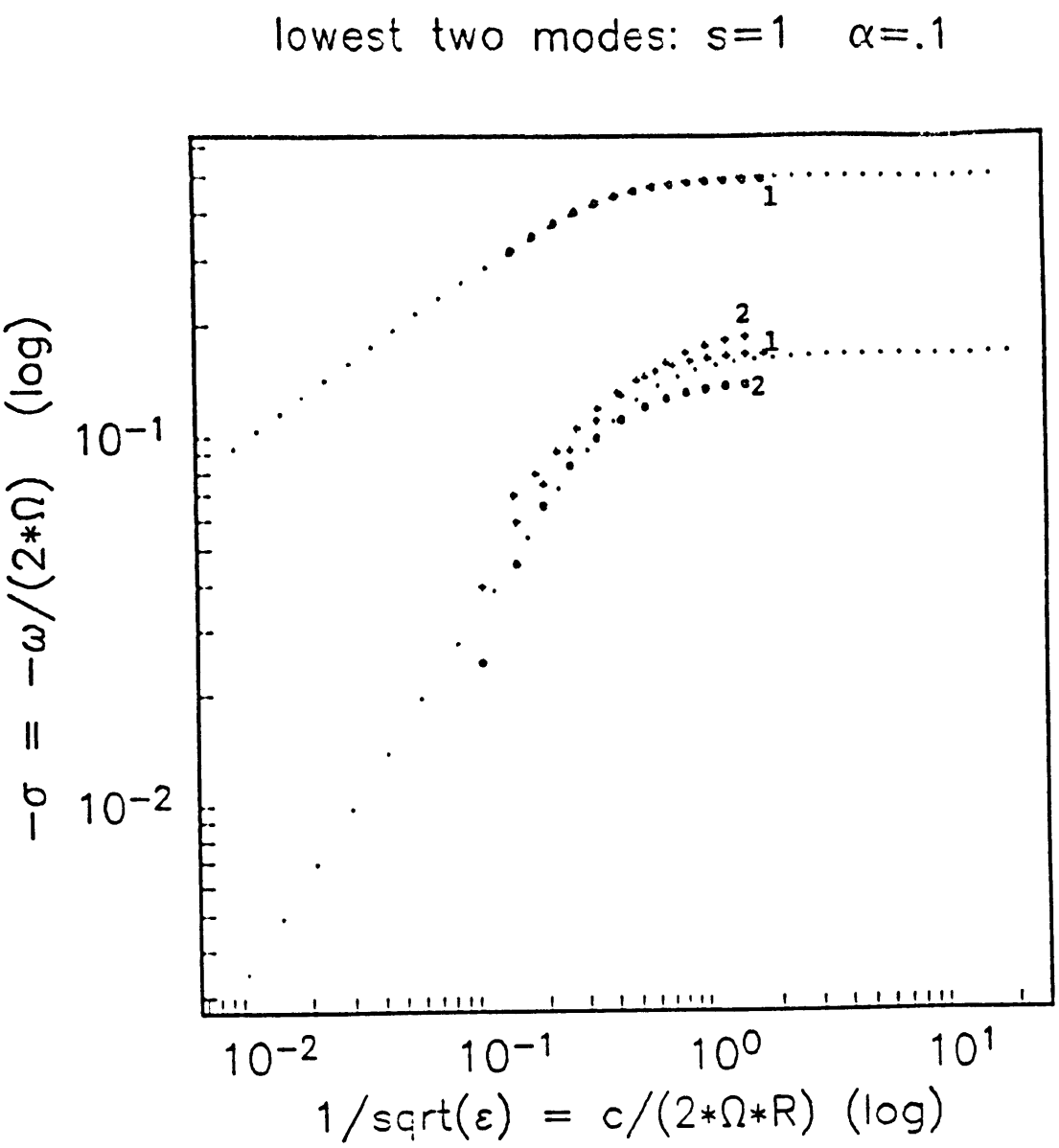

Figure 5.3 As for Figure 5.2, but for the two lowest modes at $\alpha = 10^{-1}$.

increasing Im(σ). This too is due to a smaller length scale, associated here with that of the higher order modes.

Figure 5.3 shows the effects of increasing the ratio of the strength of the Lorentz force to the Coriolis force. At $\alpha = 10^{-1}$, it is yet more difficult to calculate the eigenfrequencies at large ε, so for this reason, we show only the first two modes, and again the corresponding non-magnetic modes. The stronger magnetic field present at $\alpha = 10^{-1}$ than at $\alpha = 10^{-2}$ begins to decrease the Re(σ) for each mode from their non-magnetic values at a smaller ε, and continues to increase the Im(σ), as one might expect from (5.32). Unfortunately, it is rather difficult to ascertain the asymptotic values of Re(σ) and Im(σ) from the moderate ε that we have obtained. For these numerical solutions to the exact associated homogeneous equations (5.14) - (5.16), there is no reason in principle that α must be small; however, for α order one or greater, the β-effect is no longer dominant. Thus, for instance, we might not necessarily expect low frequency waves to travel westward, as do Rossby waves. Because near the core surface α is most likely 10^{-2}, and because we are interested in the magnetic analog of Rossby waves, we have studied the eigensystem only at small α.

In Figures 5.4 - 5.7, we examine the nature of the eigenfunctions of (5.14) - (5.16) for non-zero α (and $\mathbf{e_H} = 0$), and compare them with the eigenfunctions for $\alpha = 0$. Figure 5.4 shows the amplitude of the real and imaginary parts of the eastward fluid velocity $u_{\lambda *}$ of the first latitudinally symmetric Rossby eigenmode for s = 1 (for s =1, there is no symmetric mode with no latitudinal zeros), $\varepsilon = 10^2$, and $\alpha = 10^{-2}$, as a function of colatitude. We also plot the imaginary part of $u_{\lambda *}$ (the real part is zero) for the first symmetric mode for s = 1, $\varepsilon = 10^2$, and $\alpha = 0$. The normalization that we use here and throughout this work is that of Longuet-Higgins (1968), which seeks to keep the total kinetic plus potential energy of each mode constant, independent of σ, ε, or α. The imaginary parts of $u_{\lambda *}$ at $\alpha = 0$ and $\alpha = 10^{-2}$ are quite similar, but the finite electrical conductivity induces a phase shift with the introduction of a real part of $u_{\lambda *}$, which is

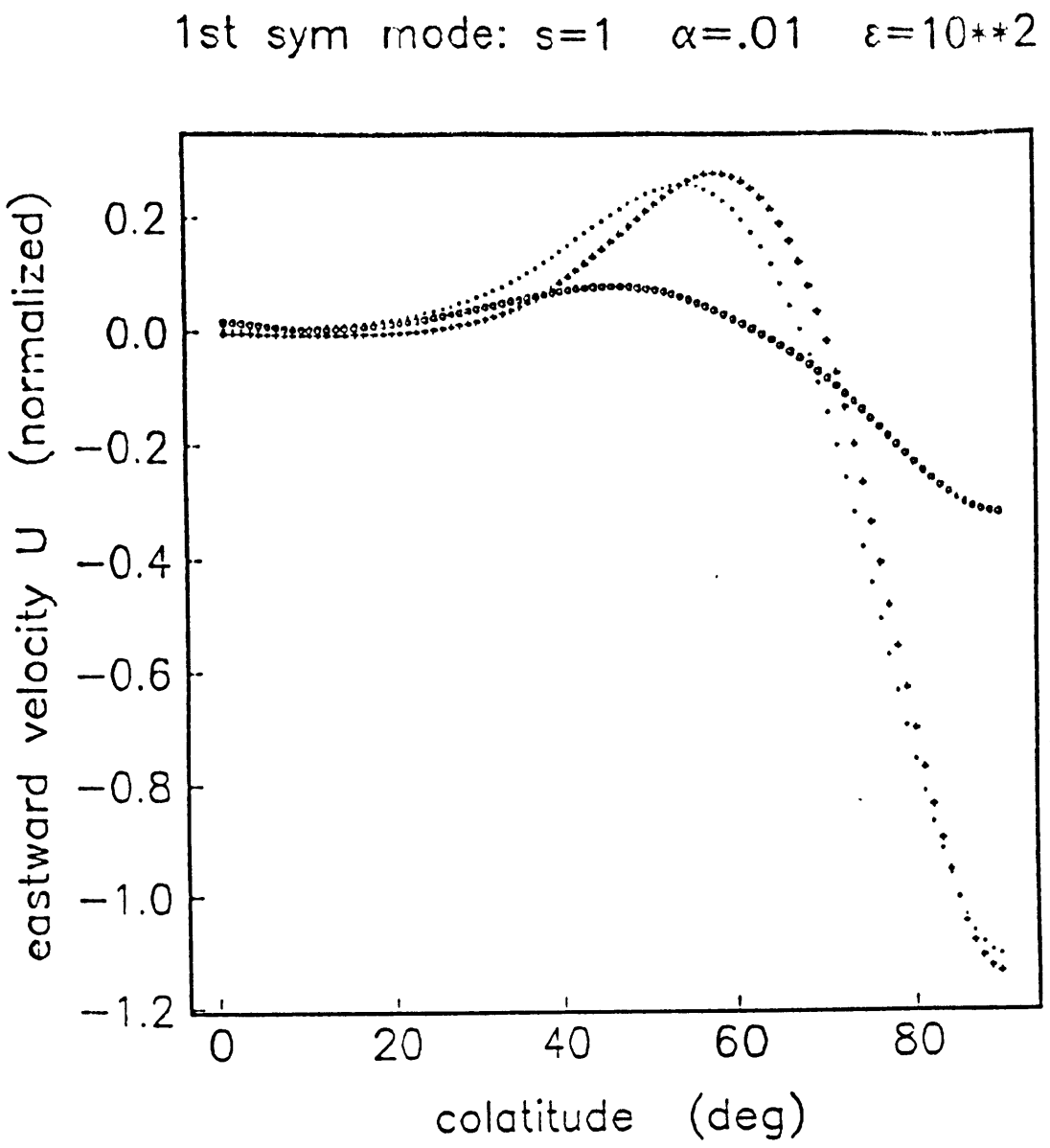

Figure 5.4 Normalized (see text) amplitude of the eastward fluid velocity $u_{\lambda *}$ reconstructed from the first symmetric eigenmode for s = 1 and $\varepsilon = 10^2$, as a function of colatitude. The circles represent the $Re(u_{\lambda *})$ at $\alpha = 10^{-2}$, and the plus signs represent the $Im(u_{\lambda *})$ at $\alpha = 10^{-2}$. For comparison, we show via dots the $Im(u_{\lambda *})$ at $\alpha = 0$ (Longuet-Higgins, 1968). The $Re(u_{\lambda *})$ is zero at $\alpha = 0$.

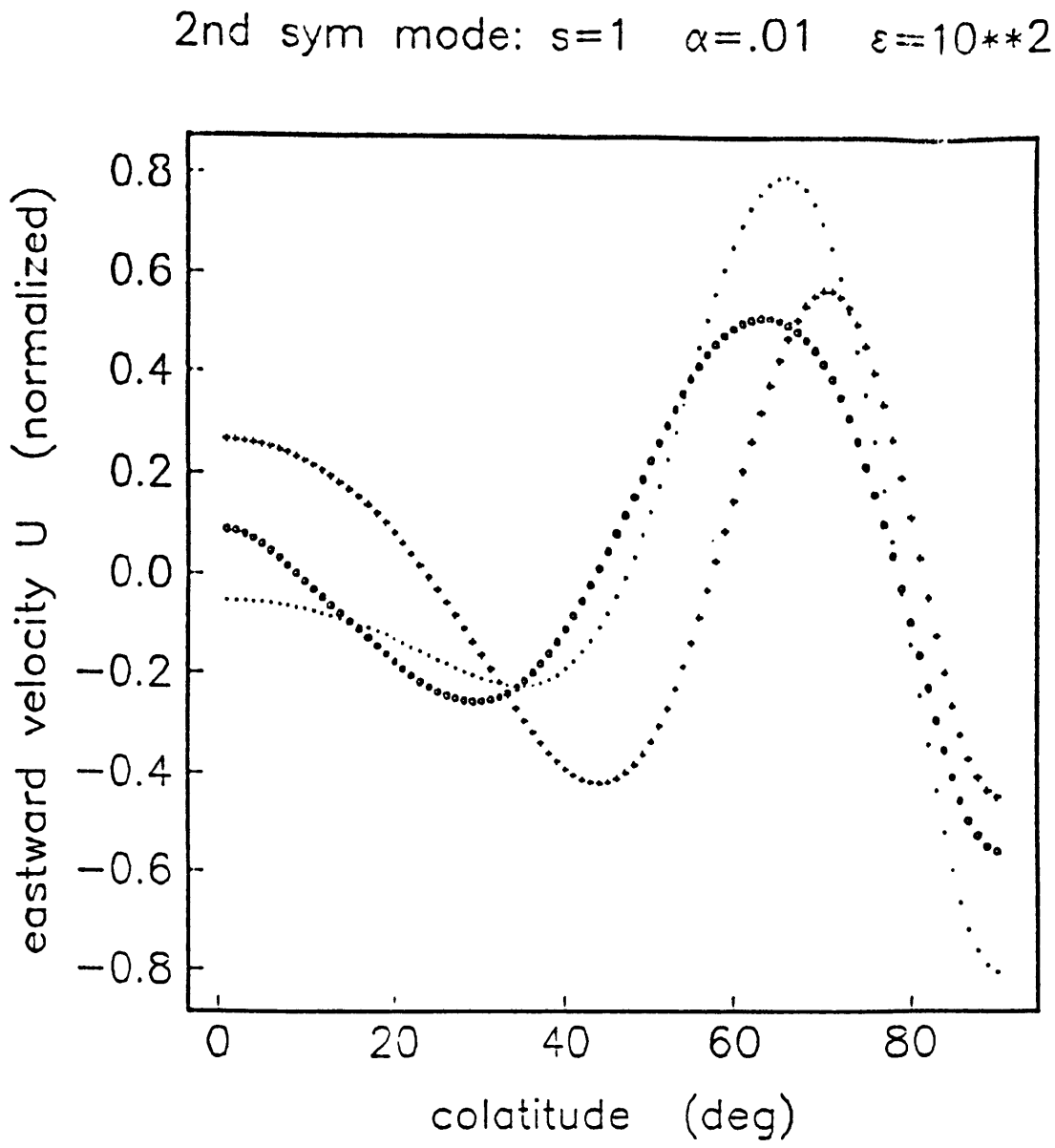

Figure 5.5 As for Figure 5.4, but for the second symmetric eigenmode.

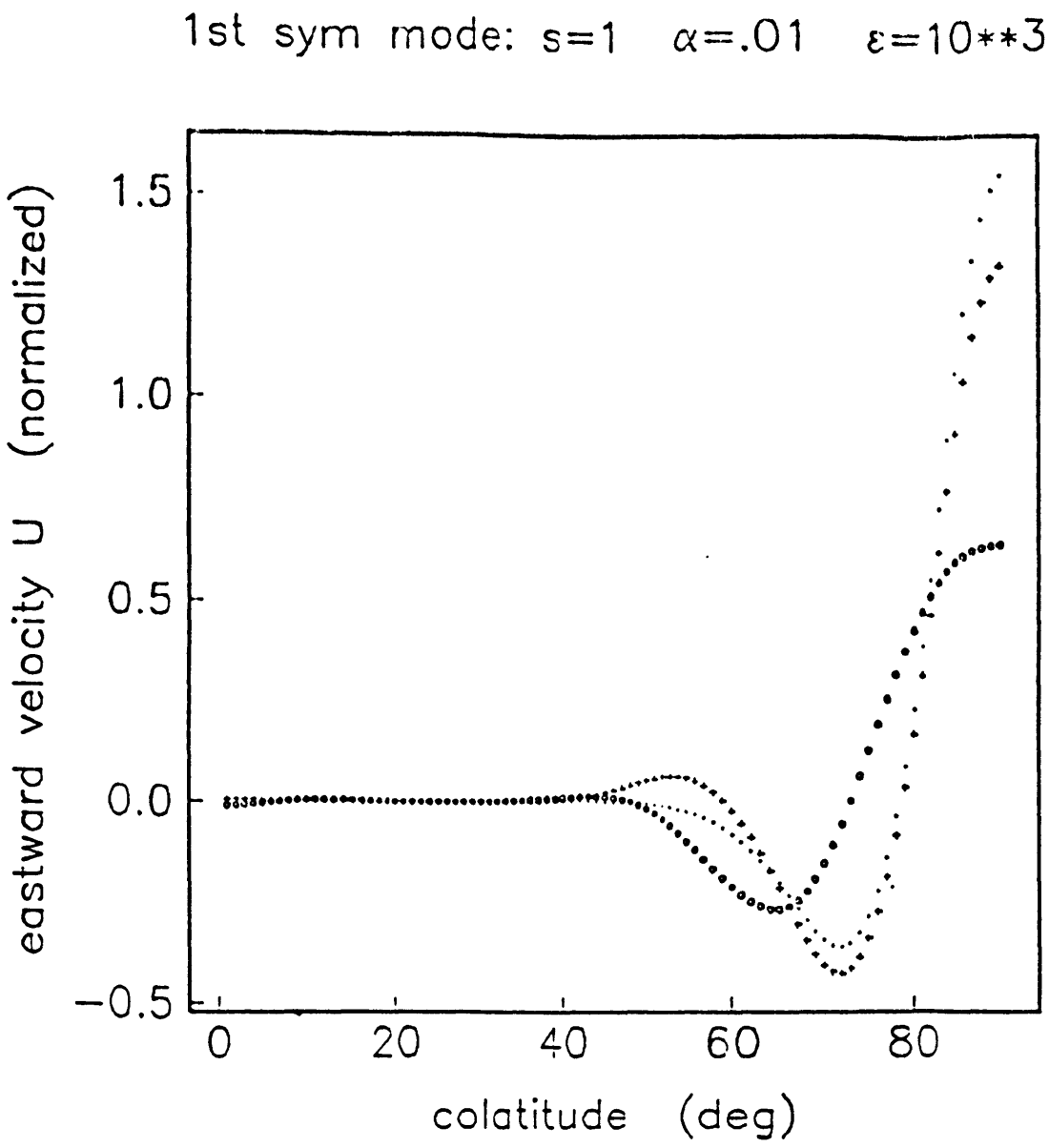

Figure 5.6 As for Figure 5.4, but for $\varepsilon = 10^3$.

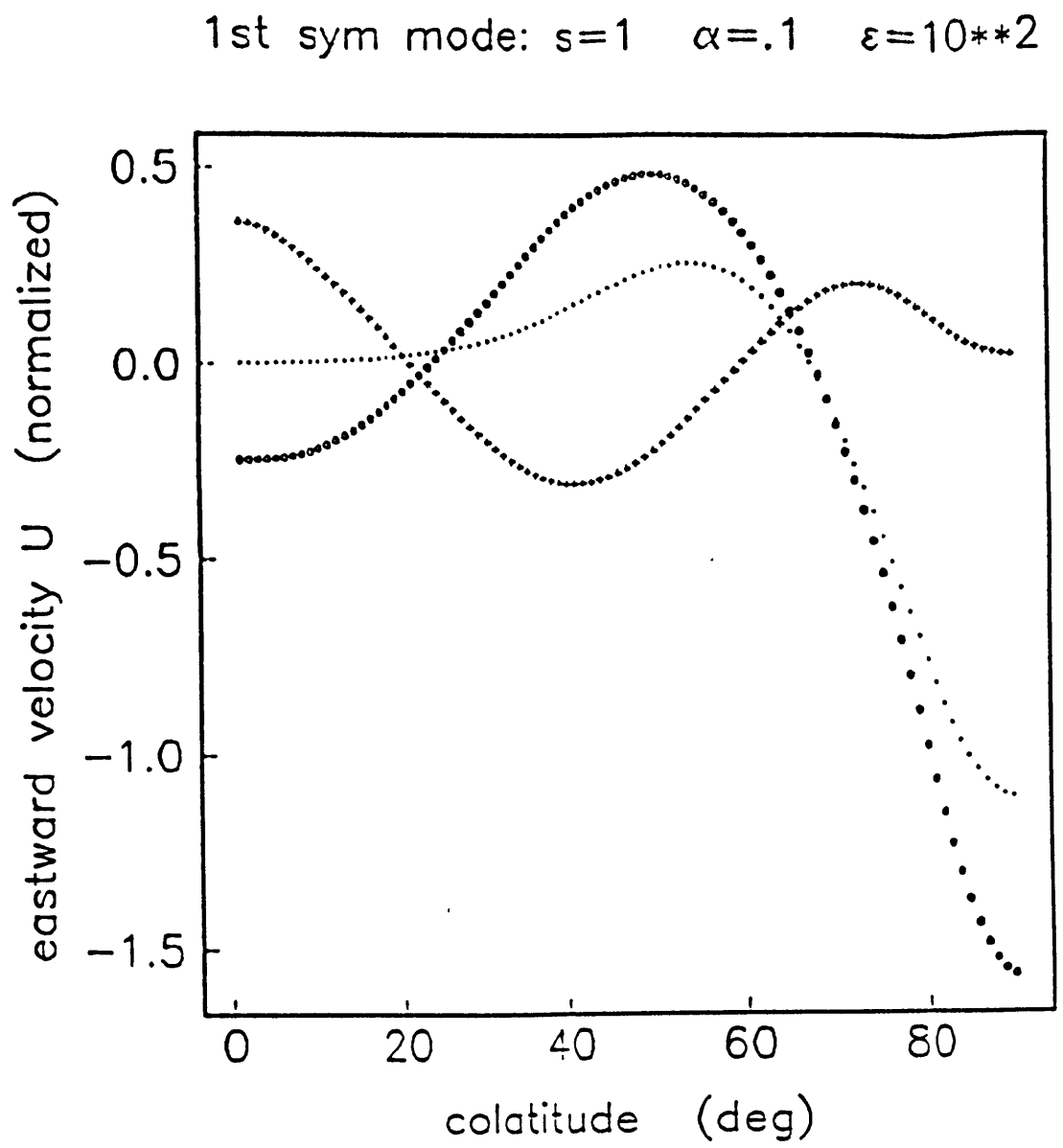

Figure 5.7 As for Figure 5.4, but for $\alpha = 10^{-1}$.

generally of lesser amplitude than the imaginary part of $u_{\lambda *}$. For this mode, a relatively small value of α does not break the equatorial waveguide. For the second symmetric mode (Figure 5.5), the phase shift is more significant, as one might expect for the smaller scale flow, and through the slightly larger amplitude near the pole there is some evidence of a breakdown of the equatorial waveguide.

At $\varepsilon = 10^3$ and $\alpha = 10^{-2}$, we could reliably obtain only the lowest symmetric eigenfunction, shown in Figure 5.6. For this lowest mode, the phase shift is again relatively small, and the magnetic field has almost no effect on wave trapping. At $\varepsilon = 10^2$ and $\alpha = 10^{-1}$, the effects of the magnetic field are much more apparent (Figure 5.7). Firstly, the stronger magnetic field much more effectively breaks the waveguide, with the equatorial amplitude no longer an order of magnitude greater than the polar amplitude. Secondly, the phase shift is nearly $\pi/4$ at most latitudes, indicating a diffusive solution. At this value of α, we could not reliably obtain higher modes or larger ε.

Unlike the infinite β-plane, which in the absence of turning points yields a continuous dispersion relation, the sphere, because of its bounded geometry, allows discrete modes. Nevertheless, from our limited numerical calculations, we can see the β-plane predictions are moderately successful. We can rewrite the β-plane dispersion relation (5.32) as

$$\sigma = \omega/2\Omega = - i (\alpha/\varepsilon) (k_x^2 + k_y^2) R^2. \qquad (5.37)$$

The β-plane predicts purely imaginary eigenfrequencies for large ε (and small ε, but the approximation (5.28) requires small ω and hence large ε) that are proportional to α and ε^{-1}. On the other hand, in the asymptotic limit of large ε, Figure 5.2 (and perhaps Figure 5.3) shows the $\mathrm{Re}(\sigma)$ is propotional to ε^{-1}, and the $\mathrm{Im}(\sigma)$ approaches a constant.

Thus, for large ε, both the β-plane analysis and the numerical calculations indicate dissipative behavior, but their predictions on the asymptotic dependence of σ on ε^{-1} differ. The lower limit on the $\mathrm{Im}(\sigma)$ of magnetic Rossby waves on the sphere as ε increases is

presumably related to the presence of Ohmic dissipation even in the limit of steady flow such that the $\mathrm{Re}(\sigma) = 0$, *i.e.*, geostrophic flow. Under the quasi-magnetostrophic approximation, on the other hand, the zeroth order state (5.23) - (5.24) is exactly geostrophic, so that in the steady limit, we might anticipate that both the $\mathrm{Re}(\sigma)$ and the $\mathrm{Im}(\sigma)$ would go to zero. Finally, while we did not perform extensive numerical calculations to examine the dependence of σ on α, Figures 5.2 and 5.3 bear out the β-plane prediction (5.37) that the $\mathrm{Im}(\sigma)$ is proportional to α, at least for moderate values of ε.

We can rewrite the condition for quasi-magnetostrophic flow, (5.28), as

$$\sigma/(\alpha\sin^2\theta) = \omega/(2\Omega\alpha\sin^2\theta) << 1. \qquad (5.38)$$

While the β-plane predicts that a magnetic field can break the equatorial waveguide, condition (5.38) reminds us that a sufficiently strong enough magnetic field is necessary if the Lorentz force is to supplant the inertial force and prevent wave trapping. Figures 5.4 - 5.6 show that for $\alpha = 10^{-2}$, the magnetic field is not yet strong enough to effectively break the equatorial waveguide. Figure 5.7, on the other hand, shows that there is non-zero amplitude at all latitudes for $\alpha = 10^{-1}$. Thus, the numerical calculations substantiate the β-plane prediction that a magnetic field can break the equatorial waveguide, and they also demonstrate that a sufficiently strong magnetic field is necessary.

Although there are encouraging similarities between the β-plane solutions and the numerical calculations, the accuracy of the β-plane predictions is not complete, particularly in regard to the $\sigma(\varepsilon^{-1})$ relation. In addition, due to the unknown horizontal electric field intensity $\mathbf{e_H}$ in both the analytical and numerical approaches, we do not know the relevance of the solutions to the H layer. The actual Ohmic dissipation rate is probably much lower than these models predict, and it is not clear the Lorentz force will be strong enough to break the equatorial waveguide. In order to include $\mathbf{e_H}$, we must release our assumption of

an r-independent solution. Unfortunately, this makes the problem considerably more complicated.

5.5 The internal modes

Braginsky (1984, 1987) examined waves in a thin, stably stratified layer on the core surface. For his study of the internal modes of a continuously stratified fluid, he assumed a zeroth order density deviation profile $\rho = -\rho_o \exp -\{2/H\,(R-r)\}$, where $H << R$ is the thickness of the thin, stably stratified layer. This density profile yields a real buoyancy frequency N, so that baroclinic motion is possible, and Braginsky (1984) assumed $N/2\Omega$ is order unity. Assuming, as have we, a quasi-magnetostrophic balance, Braginsky developed the equations governing the internal modes.

By dropping $\partial \mathbf{b}/\partial t$ in the magnetic induction equation, the r-dependence separates out, leaving functional dependence on λ,θ, and t. Looking for short wavelength perturbations, Braginsky made what is essentially the mid-latitude β-plane approximation about the latitude θ_o, and assumed $\exp [i\,(k_x\lambda + k_y y - \omega t)]$ dependence. Here, $k_x = m/s_x$, where m is an integer, and $s_x = R\cos\theta_o$ is the distance from the rotation axis. The square of the total horizontal wavenumber is $k_\tau^2 = k_x^2 + k_y^2$. The resulting local dispersion relation is

$$\varpi = \omega - k_x\zeta = \{\ (N^2H^2/a^2)\ (1/\beta_\theta R^2)\ \}\ \{\ -k_x - i\,k_\tau^2\,(B^2/\chi)\ /\ \beta_\theta\ \}, \qquad (5.39)$$

where a is the r separation constant ($a = 2.405$ is the first zero of the Bessel function J_o), $\beta_\theta = 2\Omega/R\cos\theta_o$, and the zeroth order magnetic field B is assumed constant. The velocity of differential rotation ζ is zero in our model. Equation (5.39) is equation (23) from Braginsky (1987), but in our notation. With the previously assumed numerical values, $\theta_o = 45°$, $m = 2$, and $k_\tau = \pi/600$ km^{-1}, $\mathrm{Re}(\varpi) \cong \mathrm{Im}(\varpi) \cong 60$ years^{-1}. Thus, Ohmic

dissipation also damps the internal modes rather strongly. Note, however, that (5.39) shows that the waves are less heavily damped in regions of small B.

We will now derive the solution and dispersion relation for the internal modes of quasi-magnetostrophic Rossby waves on the equatorial β-plane, and compare with Braginsky's mid-latitude β–plane solution, and with our solution for the first baroclinic mode on the equatorial β-plane. We adopt Braginsky's basic density deviation profile. The governing equations are the full continuity equation $(\partial u_x/\partial x+\partial u_y/\partial y+\partial w/\partial z) = 0$ replacing (5.19), (5.23) - (5.24) with the pressure p replacing the fluid boundary h, and the z-vorticty equation (5.25), with the electric current denisty $\mathbf{j_H}$ determined from the magnetic induction equation rather than Ohm's law. Thus, $\partial^2\mathbf{b_H}/\partial z^2 = -(B/\chi)(y/R)\,\partial\mathbf{v_H}/\partial z$, which is the horizontal part of the magnetic induction equation with $\partial\mathbf{b_H}/\partial t = \mathbf{0}$. This is equivalent to setting the horizontal components of $\nabla \times \mathbf{e} = \mathbf{0}$, and upon integrating this in z, to setting $\mathbf{e_H} = \mathbf{0}$. The equation governing the local vertical velocity w is $N^2w + \partial^2 p/\partial t\partial z = 0$ (Braginsky, 1987, Gill, 1982).

We combine the above into a single equation for w,

$$-\beta^2 y^2 \frac{\partial}{\partial t}\frac{\partial^2 w}{\partial z^2} - \frac{B^2N^2}{\chi R^2}\{\, y^2\nabla_H^2 + y\frac{\partial}{\partial y}\,\}w - \beta N^2\frac{\partial w}{\partial x} = 0, \qquad (5.40)$$

and set $w(x,y,z,t) = \psi(x,y,t)w(z)$. The function $w(z) = \sin(n\pi z/H)$, where n is an integer, satisfies (5.40) and the boundary conditions that the vertical velocity $w(z=0) = w(z=H) = 0$ (corresponding to both a rigid top and bottom). Setting $\psi(x,y,t) = \psi(y)\exp[i(k_x x - \omega t)]$, the resulting equation for ψ is

$$y^2\frac{d^2\psi}{dy^2} + y\frac{d\psi}{dy} + (-k_x^2y^2 + \frac{i\omega\beta^2\chi R^2}{4B^2c^2}y^2 + \frac{ik_x\beta\chi R^2}{4B^2})\,\psi = 0. \qquad (5.41)$$

This equation is the same as the homogeneous part of (5.29) for the first baroclinic mode of the two-layer model, but with $c^2 = N^2/(n^2\pi^2/H^2)$. Hence, we can simply use our results for the first baroclinic mode of the two-layer model to study the internal modes of a continuously stratified model by redefining the non-rotational phase speed c. However, the discussion near the end of Section 5.2 on excitation sources suggests that the two-layer model may be of more interest for geomagnetic secular variation studies.

We can compare our results on internal quasi-magnetostrophic waves on the equatorial β-plane with Braginsky's results on a mid-latitude β-plane. In analogy with (5.39), we can easily derive a local dispersion relation for large wavenumbers k_y. Assuming exp [i $(k_x x + k_y y - \omega t)$] dependence about a low latitude value of y_o in (5.41), we obtain

$$\omega = \{ (N^2H^2/n^2\pi^2)(1/\beta R^2) \} \{ - k_x (R^2/y_o^2) - k_y (B^2/\chi) / \beta y_o - i k_\tau^2 (B^2/\chi) / \beta \}. \quad (5.42)$$

Aside from the additional term due to propagation in the y direction, and the evaluation of β at $\theta = 0$ rather than at some mid-latitude, (5.42) is essentially identical to (5.39), but for the augmentation of the first term in the second bracket by a very large factor of R^2/y_o^2. This increase in the Re(ω) relative to the Im(ω) reflects, of course, the fact that in our model $\mathbf{b}_o$ increases linearly with y, and the Ohmic damping is proportional to $\mathbf{b}_o^2$. Thus, in regions of low $\mathbf{b}_o$ such as the low latitudes, we expect the magnetic Rossby waves to be less heavily damped. However, it is not clear these local dispersion relations for short latitudinal wavelengths are particularly valid, since the corresponding solutions do not satisfy the latitudinal boundary conditions.

5.6 Discussion

In the preceeding sections we developed a model for the hypothetical H layer at the top of the Earth's outer core. By invoking the hydrostatic, Boussinesq, linear, shallow-water, and traditional approximations, we reduced the general Navier-Stokes equations to the Laplace's tidal equations, which govern the primarily horizontal surface motion of a rotating, stably stratified, thin fluid layer, such as the Earth's hydrosphere. In order to model the H layer as a thin layer sitting above a 'homogeneous' core, we employed a two-layer model, and in particular, we examined the surface motion between the two layers. Under the rigid-lid approximation, the solution for the first baroclinic mode of the two-layer model, as such motion between layers is known, is the same as the solution for the surface mode of the one-layer model, with the use of a reduced gravity and an equivalent depth.

Laplace's tidal equations admit high frequency gravity waves that propagate both eastward and westward, and low frequency Rossby waves that propagate only westward. Due to the variation of the Coriolis parameter with latitude, the equator acts as a waveguide to trap these waves. Both a numerical solution to the full equations and a β-plane solution yield these properties. In the Earth's core, however, we must also model the fluid as an electrical conductor. To Laplace's tidal equations, we therefore added terms representing the linearized Lorentz force due to a dipole field, which as a simple poloidal field is a rough model for the magnetic field near the top of the outer core. We then transformed the equations from the sphere to the equatorial β-plane, and invoked the quasi-magnetostrophic approximation. This approximation enabled us to analytically examine the magnetic analog of Rossby waves, which because of their long periods, may be of some interest in secular variation studies.

Both the analytical β-plane results and the numerical calculations demonstrated that the addition of a magnetic field can release the equatorial wave trapping of Rossby waves,

provided the magnetic field is strong enough. Both analyses also demonstrated that the Ohmic dissipation of these waves is high, as Braginsky (1987) had also derived. However, they differed on the asymptotic decay rate in the limit of low frequency (high rotation). This discrepancy appears to be due to a limitation of the quasi-magnetostrophic approximation, which was necessary to find an analytic solution on the β-plane. Thus, for this highly dissipative system, one must be careful about dropping the inertial term even in the limit of small Re(ω), because Im(ω) can remain large.

While the β-plane and numerical solutions clearly demonstrate the counteracting effect of a strong magnetic field on rotation, the applicability of the dispersion relation (5.32) and the dispersion diagrams (Figures 5.2 and 5.3) to the H layer is unclear. This is due primarily to our having set $\mathbf{e_H} = \mathbf{0}$. Because of our thin-layer approximations, the electric field intensity remains unknown; however, in setting it to zero, we incurred a much higher electric current density than we would have had $\mathbf{e_H} \cong -\mathbf{v_H} \times \mathbf{b_o}$. Had we obtained smaller electrical currents, the dissipation would have been less, resulting in different dispersion relations. In the limit of an infinitely conducting fluid, of course, there would be no Ohmic dissipation, so that the eigenfrequencies would be purely real, as for the non-magnetic problem.

The terms in the magnetic induction equation $[\partial\mathbf{b}/\partial t, \nabla \times (\mathbf{v} \times \mathbf{b_o}), \chi\nabla^2\mathbf{b}]$ are of the order $[1/T, V/D, \chi/D^2]$, where T, V, and D are the characteristic time, velocity, and thickness scales. If we use $T \cong 10^8$ sec as a typical secular variation time scale (though the above discussion indicates the damping time scale could be less), $V \cong 10^{-4}$ m/sec as a characteristic fluid speed, and $D \cong 10^4$ m as a characteristic thickness, we find the three terms are in near balance with each other, in contrast with the assumption that $\partial\mathbf{b}/\partial t$ is small. Thus, the actual solution for waves on the H layer probably lies somewhere within the limits set by the solution for waves in the hydrosphere and the solution set forth here, with $\mathbf{e_H} = \mathbf{0}$. In order to determine $\mathbf{e_H}$, and hence the true solution, we must know the details of the radial dependence of the field variables.

Another weakness of the theory is that although the H layer may be thin, the underlying fluid layer is not. Unfortunately, we could not include fluid-fluid interactions beneath the H layer in our thin-layer model. A solid bottom boundary precludes the radial propagation of magnetic-Archimedean-Coriolis (MAC) waves and magnetic coupling to the bulk of the underlying fluid. Moreover, in the limit of an infinitely thin fluid layer the perturbation magnetic field due to the horizontal current is horizontal, *i.e.*, toroidal, so it would have no direct surface manifestation. For a finite layer a radial perturbation magnetic field would be present, so observation might be possible, but we do not know to what extent. The remedy to these shortcomings of the theory is again to relax the assumptions of thinness and of radial independence. But in abandoning the thin-layer approximations, we add enormously to the complexity of the problem. We will not here attempt to explore the two-dimensional eigenvalue problem. Finally, we have not considered the effects of a zeroth order differential rotation.

From Figure 5.2, we can roughly extrapolate the $\mathrm{Re}(\sigma)$ for the lowest symmetric mode to about 10^{-4} at $\epsilon = 10^{6}$. For $s = 1$, the westward phase speed $c_{ph} = \mathrm{Re}(\omega) / (s/R \cos\theta)$ near the equator is then approximately 10^{-2} m/sec, or several hundred km/year. Although our analysis shows that $\mathrm{Im}(\sigma) >> \mathrm{Re}(\sigma)$ in the limit of large ϵ, so that the instabilities are overdamped, the actual dissipation would be less if one allowed for a non-zero e_H. Of course, with the inclusion of a non-zero e_H the $\mathrm{Re}(\sigma)$ may change as well, but the $\mathrm{Re}(\sigma)$ appears to be relatively unaffected by a moderately weak magnetic field (see Figures 5.2 and 5.3). In any case, it appears premature to dismiss magnetic Rossby waves as unobservable based on their improperly derived high dissipation rates. For the relatively weak magnetic field strength appropriate for the top of the Earth's outer core, the equator may still act as a waveguide to trap wave amplitudes (see Figures 5.4 - 5.6), as in the hydrosphere.

Large accelerations of the westward drift such as the 1969 'jerk' (Courtillot and LeMouel, 1984) indicate that rapid changes in core flow can occur. Since it is unlikely that

any of the quantities associated with the basic state would have rapidly changed, we should probably associate such rapid secular acceleration with the forcing motion of sources, rather than with any resulting waves. If forced motions due to sources (such as the arrival of blobs in a penetrative convection scenario (Braginsky, 1987, Loper, 1989)) dominate the core surface motion field, they may swamp out any signals due to magnetic Rossby waves, even if the waves are relatively undamped. However, c_{ph} as we derived above is about 2 deg/year, faster than the typically assumed speed of .2 deg/year (Madden and LeMouel, 1982). Thus, were the geomagnetic data of sufficient quality and quantity, it might be possible to distinguish fast motion, due to magnetic Rossby waves, from the slower forced motions. An improvement in data quality, and a refinement of the theory presented here, may then eventually help us to determine the stability of the top of the Earth's outer core and magnetic Rossby waves' role in creating the secular variation.

References

Abramowitz, M., and Stegun, I.A., *Handbook of Mathematical Functions*, Dover Pub. (1964).

Aldridge, K.D., and Lumb, L.I., "Inertial waves identified in the Earth's fluid outer core", *Nature* **325**, 421-423 (1987).

Bloxham, J., "On the consequences of strong stable stratification at the top of Earth's outer core", *Geophys. Res. Lett.* **17**, 2081-2084 (1990).

Bolt, B.A., "The constitution of the core: seismological evidence", *Phil. Trans. Roy. Soc. London A***306**, 11-20 (1982).

Braginsky, S.I., "Structure of the F layer and reasons for convection in the Earth's core", *Dokl. Akad. Nauk SSSR* **149**, 1311-1314 (1963), (Engl. transl. *Sov. Phys. Dokl.*, 8-10).

Braginsky, S.I., "Short-period geomagnetic secular variation", *Geophys. Astrophys. Fluid Dynam.* **30**, 1-78 (1984).

Braginsky, S.I., "Waves in a stably stratified layer on the surface of the terrestrial core", *Geomagn. & Aeron.* **27**, 410-414 (1987).

Braginsky, S.I., and Fishman, V.M., "Investigation of the stability of the current layer in the terrestrial core at the boundary with the mantle", *Geomagn. & Aeron.* **27**, 710-714 (1987).

Courtillot, V., and LeMouel, J.L., "Geomagnetic secular variations impulses", *Nature* **311**, 709-716 (1984).

Crossley, D.J., "Oscillatory flow in the liquid core", *Phys. Earth Planet. Inter.* **36**, 1-16 (1984).

Fearn, D.R., and Loper, D.E., "Compositional convection and stratification of Earth's core", *Nature* **289**, 393-394 (1981).

Fearn, D.R., and Proctor, M.R.E., "Hydromagnetic waves in a differentially rotating sphere", *J. Fluid Mech.* **128**, 1-20 (1983).

Friedlander, S. "Internal oscillations in the Earth's fluid core", *Geophys. J. R. Astron. Soc.* **80**, 345-361 (1985).

Friedlander, S. "Hydromagnetic waves in a differentially rotating stratified spherical shell", *Geophys. Astrophys. Fluid Dynam.* **48**, 53-67 (1989).

Gill, A.E., *Atmosphere-Ocean Dynamics*, Academic Press (1982).

Gubbins, D., Thompson, C.J., and Whaler, K.A., "Stable regions in the Earth's liquid core", *Geophys. J. R. Astron. Soc.* **68**, 241-251 (1982).

Gubbins, D., Zhang, K., and Hutcheson, K., "Dynamics of the secular variation", *Abstracts for SEDI Symposium on Reversals, Secular Variation, and Dynamo Theory*, Santa Fe, New Mexico (1990).

Hide, R., "Free hydromagnetic oscillations of the Earth's core and the theory of the geomagnetic secular variation", *Phil. Trans. Roy. Soc. London* **A259**, 615-647 (1966).

Knittle, E., and Jeanloz, R., "High-pressure metallization of FeO and implications for the Earth's core", *Geophys. Res. Lett.* **13**, 1541-1544 (1986).

Lindzen, R.D., "Planetary waves on beta-planes", *Mon. Weather Rev.* **95**, 441-451 (1967).

Longuet-Higgins, M.S., "The eigenfunctions of Laplace's tidal equations over a sphere", *Proc. R. Soc. London* **A262**, 511-607 (1968).

Loper, D.E., "Structure of the core and lower mantle", *Adv. Geophys.* **26**, 1-34 (1984).

Loper, D.E., "Dynamo energetics and the structure of the outer core", *Geophys. Astrophys. Fluid Dynam.* **49**, 213-219 (1989).

Loper, D.E., and Roberts, P.H., "A study of conditions at the inner core boundary of the Earth", *Phys. Earth Planet. Inter.* **24**, 302-307 (1981).

Madden, T., and LeMouel, J.L., "The recent secular variation and the motions at the core surface", *Phil. Trans. Roy. Soc. London* **A306**, 271-280 (1982).

Masters, G., "Observational constraints on the chemical and thermal structure of the Earth's deep interior", *Geophys. J. R. Astron. Soc.* **57**, 507-534 (1979).

Melchior, P., and Ducarme, B., "Detection of inertial gravity oscillations in the Earth's core with a superconducting gravimeter at Brussels", *Phys. Earth Planet. Inter.* **42**, 129-134 (1986).

Melchior, P., Crossley, D.J., Dehant, V.P., and Ducarme, B., "Have inertial waves been identified from the Earth's core?", *Structure and Dynamics of Earth's Deep Interior*, Smylie, D.E., and Hide, R, ed., American Geophysical Union (1988).

Moffatt, H.K., "Liquid metal MHD and the geodynamo", *Proceedings IUTAM Symposium on Liquid Metal Magnetohydrodynamics*, Kluwer Academic Pub. (1988).

Olson, P., "Internal waves in the Earth's core", *Geophys. J. R. Astron. Soc.* **51**, 183-215 (1977).

Pedlosky, J., *Geophysical Fluid Dynamics*. Springer-Verlag (1987).

Phillips, N.A., "The equations of motion for a shallow rotating atmosphere and the 'traditional approximation'", *J. Atmos. Sci.*, **23**, 626-628 (1966).

Roberts, P.H., "From Taylor state to model-Z?", *Geophys. Astrophys. Fluid Dynam.* **49**, 143-160 (1989).

Stevenson, D.J., "Physical state of the core and the core-mantle boundary", *Abstracts for SEDI Symposium on Reversals, Secular Variation, and Dynamo Theory*, Santa Fe, New Mexico (1990).

Turner, J.S., *Buoyancy Effects in Fluids*. Cambridge University Press (1973).

Verhoogen, J., *Energetics of the Earth.* National Academy Press (1980).

Veronis, G., "On the approximations involved in transforming the equations of motion from a spherical surface to the β-plane. I. Barotropic systems", *J. Mar. Res.*, **21(2)**, 110-124 (1963a).

Veronis, G., "On the approximations involved in transforming the equations of motion from a spherical surface to the β-plane. II. Baroclinic systems", *J. Mar. Res.*, **21(3)**, 199-204 (1963b).

Veronis, G., "Comments on Phillips' proposed simplification of the equations of motion for a shallow rotating atmosphere", *J. Atmos. Sci.*, **25**, 1154-1155 (1968).

Whaler, K.A., "Does the whole of the Earth's core convect?", *Nature* **287**, 528-530 (1980).

Whaler, K.A., "Geomagnetic evidence for fluid upwelling at the core-mantle boundary", *Geophys. J. R. Astron. Soc.* **86**, 563-588 (1986).

Chapter 5 Appendix: Method of solution of Laplace's tidal equations

The method of solution of (5.14) - (5.16), with $\mathbf{e_H} = \mathbf{0}$, follows closely that developed by Longuet-Higgins (1968) to find the eigenvalues and eigenfunctions of the traditional Laplace's tidal equations over a sphere. The method is as follows. We first introduce into (5.14) - (5.16) a velocity potential Φ and a stream function Ψ, such that

$$u_{\theta *} = \frac{\partial \Phi}{\partial \theta} + \frac{1}{\sin\theta}\frac{\partial \Psi}{\partial \lambda}, \text{ and} \tag{A5.1}$$

$$u_{\lambda *} = \frac{1}{\sin\theta}\frac{\partial \Phi}{\partial \lambda} - \frac{\partial \Psi}{\partial \theta}, \tag{A5.2}$$

where θ is now the colatitude, and $u_{\theta *}$ is the southward velocity. We next form two new equations by taking the divergence $1/\sin\theta \{ \partial(5.14)/\partial\lambda + \partial(\sin\theta\ (5.15)\ )/\partial\theta \}$ and the curl $1/\sin\theta \{ \partial(5.15)/\partial\lambda - \partial(\sin\theta\ (5.14)\ )/\partial\theta \}$. Looking for waves travelling in the azimuthal direction, we assume the solutions Φ, Ψ, and h have $\exp[i(s\lambda - \omega t)]$ dependence.

Defining $\mu = \cos\theta$, $D_1 = -\sin\theta\partial/\partial\theta = (1-\mu^2)\partial/\partial\mu$, and $D_2 = \sin^2\theta\partial^2/\partial\theta^2 = (1-\mu^2)^2\partial^2/\partial\mu^2 - \mu D_1$ (using the chain rule on the definitions of D_1 and D_2 to obtain each of the second equalities), we perform some tedious algebra to obtain from the two new equations

$$\{ -i\omega(1-\mu^2)\nabla^2 + 2\Omega is(1-\mu^2) - \frac{B^2}{\chi}s^2 - \frac{3B^2}{\chi}s^2\mu^2 + \frac{4B^2}{\chi}\mu^2 D_2 - \frac{12B^2}{\chi}\mu^3 D_1 + \frac{8B^2}{\chi}\mu D_1 \}\Phi +$$
$$\{ 2\Omega\mu(1-\mu^2)\nabla^2 + 2\Omega(1-\mu^2)D_1 + \frac{B^2}{\chi}is(1-\mu^2)D_1 - \frac{8B^2}{\chi}is\mu(1-\mu^2) \}\Psi = \frac{g\Delta\rho}{R\rho}(1-\mu^2)\nabla^2 h, \tag{A5.3}$$

and

$$\{ -i\omega(1-\mu^2)\nabla^2 + 2\Omega is(1-\mu^2) - \frac{4B^2}{\chi}s^2\mu^2 + \frac{B^2}{\chi}D_2 + \frac{3B^2}{\chi}\mu^2 D_2 - \frac{9B^2}{\chi}\mu^3 D_1 + \frac{5B^2}{\chi}\mu D_1 \}\Psi$$

$$+ \{ -2\Omega\mu(1-\mu^2)\nabla^2 - 2\Omega(1-\mu^2)D_1 + \frac{B^2}{\chi}is(1-\mu^2)D_1 - \frac{6B^2}{\chi}is\mu(1-\mu^2) \}\Phi = 0. \tag{A5.4}$$

The third equation, (5.16), becomes

$$\nabla^2 h = \frac{i}{\omega}\frac{H_1H_2}{R(H_1+H_2)}\nabla^4\Phi, \text{ where} \tag{A5.5}$$

∇^2 is the horizontal Laplacian operator. We now eliminate h from (A5.3) and (A5.4) by use of (A5.5), and divide the two remaining equations for Φ and Ψ by $2\Omega i$. Using σ, ε, and α as defined by (5.34), (5.35), and (5.36), we can then write (A5.3) and (A5.4) as

$$\{ \sigma(1-\mu^2)\nabla^2 - s(1-\mu^2) + \frac{1}{\varepsilon\sigma}(1-\mu^2)\nabla^4 - i\alpha s^2 - 3i\alpha s^2\mu^2 + 4i\alpha\mu^2 D_2 - 12i\alpha\mu^3 D_1 + 8i\alpha\mu D_1 \}\Phi$$
$$+ \{ \mu(1-\mu^2)\nabla^2 + (1-\mu^2)D_1 + i\alpha s(1-\mu^2)D_1 - 8i\alpha s\mu(1-\mu^2) \}i\Psi = 0, \tag{A5.6}$$

and

$$\{ \sigma(1-\mu^2)\nabla^2 - s(1-\mu^2) - 4i\alpha s^2\mu^2 + i\alpha D_2 + 3i\alpha\mu^2 D_2 - 9i\alpha\mu^3 D_1 + 5i\alpha\mu D_1 \}i\Psi$$
$$+ \{ \mu(1-\mu^2)\nabla^2 + (1-\mu^2)D_1 - i\alpha s(1-\mu^2)D_1 - 6i\alpha s\mu(1-\mu^2) \}\Phi = 0. \tag{A5.7}$$

We now expand Φ and Ψ in a spherical harmonic series, so that their latitudinal representation is

$$\Phi = \sum_{n=s}^{\infty} A_n^s P_n^s(\mu) \text{ and} \tag{A5.8}$$

$$\Psi = \sum_{n=s}^{\infty} iB_n^s P_n^s(\mu), \tag{A5.9}$$

where $P_n^s(\mu)$ is the associated Legrendre polynomial of order n and degree s (Abramowitz and Stegun, 1964). Associated Legendre polynomials have several useful properties that we will take advantage of in solving for the unknown coefficients A_n^s and B_n^s, including

$$\nabla^2 P_n^s = -n(n+1)P_n^s, \tag{A5.10}$$

$$\mu P_n^s = \frac{n+s}{2n+1} P_{n-1}^s + \frac{n-s+1}{2n+1} P_{n+1}^s, \tag{A5.11}$$

$$D_1 P_n^s = \frac{(n+1)(n+s)}{2n+1} P_{n-1}^s - \frac{n(n-s+1)}{2n+1} P_{n+1}^s, \text{ and} \tag{A5.12}$$

$$D_2 P_n^s = -n(\mu^2+1)\, P_n^s - \mu(n+1)D_1\, P_n^s + 2\mu(n+s)\, P_{n-1}^s + (n+s)D_1\, P_{n-1}^s. \tag{A5.13}$$

Our procedure is now straightforward. We first choose an azimuthal wavenumber, thereby fixing s. Then, by successively using the recursion relations (A5.10) - (A5.13), and equating coefficients of like P_n^s to zero, we can reduce (A5.6) - (A5.7) to two infinite sets of independent algebraic equations (the even and odd n P_n^s uncouple from each other). One system corresponds to motions symmetrical about the equator, the other to motions anti-symmetrical about the equator. In practice, we must truncate each system at a finite number of $n = N_{max}$. For further details of the procedure as applied to the non-magnetic case, see Longuet-Higgins (1968).

It is evident from (A5.6) - (A5.7) that with the expansion (A5.8) - (A5.9) and the use of the recursion relations (A5.10) - (A5.13), our matrix equation, for either even or odd n, is of the form

$$[\sigma\mathbf{B} - \mathbf{C_o} - \alpha\mathbf{C} - 1/(\varepsilon\sigma)\mathbf{J}]\mathbf{x} = \mathbf{0}. \tag{A5.14}$$

In this system, the matrix **B** contains inertial effects, the matrix $\mathbf{C_o}$ Coriolis effects, the matrix **C** magnetic effects, and the matrix **J** buoyancy effects. **x** is the solution vector,

consisting of the coefficients A_n^s and B_n^s, at a chosen s. For a non-trivial solution vector, the bracketed term must have a determinant equal to zero. We would therefore like to find the eigenfrequencies σ that allow these non-trivial eigenvectors **x**. The matrix equation (A5.14) is not a standard linear eigenvalue problem, however, because for a given α and ε, σ appears in both the denominator and numerator.

Following Longuet-Higgins (1968), we set

$$\eta = 1/\varepsilon\sigma. \qquad \text{(A5.15)}$$

Setting $\mathbf{D} = \mathbf{C}_o + \alpha\mathbf{C} + \eta\mathbf{J}$, and multiplying by $\mathbf{B}^{-1}$ (provided **B** is invertible, which it is, since **B** represents the effects of $\sin^2\theta$ operating on a Legendre polynomial), we obtain a standard linear eigenvalue problem

$$\mathbf{Ax} = \sigma\mathbf{x}, \qquad \text{(A5.16)}$$

where $\mathbf{A} = \mathbf{B}^{-1}\mathbf{D}$. Of course, we have paid a price for our substitution (A5.15). For a given α and η, we obtain N_{max} eigenfrequencies σ, each corresponding to a different ε in order to keep η fixed in (A5.15). Increasing N_{max} increases the number of these eigenfrequencies that converge to a sufficient accuracy.

When $\alpha = 0$, **A** is real but not symmetric. Nevertheless, the N_{max} eigenfrequencies σ all turn out to be real (Longuet-Higgins, 1968). For real η, the corresonding ε are then all real, though some may be negative. The parameter ε is a measure of stable stratification, as (5.35) demonstrates. A negative ε corresponds to a negative value of c^2, implying a negative $\Delta\rho/\rho$ or a negative $H_1H_2/(H_1+H_2)$. Either of these possiblities represents unstable stratification, so that we must reject the free oscillations at eigenfrequencies that correspond to negative ε. The eigenfrequencies corresponding to negative ε play a role for forced motion, however, since in the expansion of an arbitary forcing function we might require eigenfunctions associated with these eigenfrequencies (Lindzen, 1967).

Given the nature of the non-linear eigenvalue problem, iteration over η is necessary. For the case in which $\alpha = 0$, this consists in theory of looping over all real η. In practice, one loops over a discrete number of points in η space, for each η obtaining the spectrum of N_{max} eigenvalues σ (not all of which will have converged to the desired degree of accuracy) and corresponding ε. Those eigenfrequencies corresponding to a real, positive ε represent the desired eigenfrequencies, after which one can compute the desired eigenfunctions. As a check of the computer code, we set s = 1 (as did we in all calculations), $\alpha = 0$, and $\eta = +/- (2^k)^{1/2}$ (k = 24,23,...,-20). Setting $N_{max} = 30$, we reproduced the work of Longuet-Higgins (1968).

When one includes Lorentz forces for a finitely electrically conducting fluid, α is non-zero, and A is no longer real, nor is it Hermitian. Thus, we must admit the existence of complex eigenfrequencies σ. Physically, of course, this is due to the introduction of Ohmic dissipation. For a physically realizable, stably stratified fluid, ε must be real and positive, hence for complex σ, η must be complex. In fact, with

$$\varepsilon_R + i\varepsilon_I = \frac{(\sigma_R\eta_R - \sigma_I\eta_I) - i(\sigma_R\eta_I + \sigma_I\eta_R)}{(\sigma_R\eta_R - \sigma_I\eta_I)^2 + (\sigma_R\eta_I + \sigma_I\eta_R)^2}, \qquad \text{(A5.17)}$$

it is evident that $\sigma_R\eta_I = -\sigma_I\eta_R$ for real ε. Once again, however, although the eigenfrequencies and eigenfunctions corresponding to a complex ε for a fixed and general η have no physical significance for the free oscillations, they are necessary for a complete eigenfunction expansion of forced motions.

When α is non-zero, we expect on a physical basis that both σ_R and σ_I will be negative for the damped westward modes. Hence, from (A5.17) we evidently need search only over the second quadrant of the complex η plane to obtain real, positive ε. The algorithm is simply to loop over this quadrant of the complex η plane, at each point

calculating N_{max} eigenfrequencies, keeping only those that correspond to real ε. We accomplish this daunting task by setting $\eta_R = -(2^i)^{1/2}$ and $\eta_I = +(2^j)^{1/2}$, where i and j are each a range of consecutive integers. In practice, we sped up the search by looking for η that caused a change in sign in ε_I, since a zero of ε_I should therefore have been nearby. Unfortunately, eigenfrequencies for the large ε that we are interested in are extremely difficult to obtain.

Chapter 6

Conclusions and Future Work

This thesis has illustrated some of the mathematical, geophysical, and physical difficulties of studying the Earth's core. The equations governing the motion of a rotating, electrically conducting fluid are mathematically formidable, necessitating approximations. The assumptions behind the approximations can be hard to gauge; the geophysical data do not always constrain the parameter range or the boundary conditions. Moreover, the geophysical data do not always provide a sufficient guide to the theoretician. This leaves the geodynamo problem somewhat vague and ill-defined, especially frustrating given the subtle physics. It is now clear why the non-dimensional number S defined in Chapter 1 is small. Nevertheless we feel we have made some progress towards gaining insight into the dynamics of the Earth's core.

In Chapter 2 we noted that certain features of the core magnetic field remain static, which, together with a possible correlation between the static features, thermal anomalies in the lower mantle, core-mantle boundary (CMB) topography, and virtual geomagnetic pole (VGP) paths, suggests that the mantle exerts a long timescale control over core flow. While questions remain about the resolution of the various data, the most apparent feature in all appears to be a difference between the equatorial region and the polar zones, perhaps with an azimuthal wavenumber m = 1 variation. This latitudinal dependence is not surprising - the grossest differences in both the thermal and motion fields in the Earth's hydrosphere are of course also between the equator and poles. In the Earth's hydrosphere these differences arise not only from differential solar heating between latitudes, but also from the different dynamics in the two regions, which results from the rapid rotation of the Earth.

In order to study steady fluid motions in a thick spherical shell driven by unstable buoyancy gradients, we developed in Chapter 3 an iterative method that searches for finite-amplitude, time-independent solutions. The method proved quite successful at predicting

the critical Rayleigh number Ra_c at which time-independent, non-rotating, non-magnetic convection commences, as well as the character of the finite-amplitude motion. As we raised Ra above critical, we experienced more difficulty in finding converged solutions. This is a result of the increasing non-linearity, with bifurcations in the space domain becoming denser. We would also expect that with this cascade to smaller spatial scales, our solutions would become more unstable with respect to time perturbations, eventually leading to chaotic convection. At least for moderate Ra, however, we believe our converged solutions yield correct time-averaged features.

In a rapidly rotating, electrically insulating, thick fluid shell with laterally homogeneous boundary buoyancy conditions, linear theory predicts that convection commences as azimuthally drifting columns (equatorial modes) tangent to the inner sphere, with g_s, the component of gravity perpendicular to the rotation axis, providing the driving force. With further increases in Ra, convection in the form of polar modes, which resemble the convective cells of a plane layer rotating about a normal axis, also occurs. These modes depend upon g_z, the component of gravity parallel to the rotation axis, for their existence, and although they are less unstable than the equatorial modes, it is necessary to include g_z for a proper understanding of supercritical convection. While the mode of convection between the equator and the poles differ, it is not obvious how, with homogeneous boundary buoyancy conditions, static features in the core magnetic field could arise that would correlate with the various anomalies in the lower mantle and CMB.

For a rapidly rotating, electrically conducting, thick fluid shell the free convection is larger scale and more efficient, whether it occurs as a magnetic-Archimedean-buoyancy (MAC) wave riding on an imposed toroidal magnetic field or as axisymmetric motion with an imposed z-magnetic field, as we studied in this thesis. The dynamical differences between the equatorial zone and the polar zones are a little more subtle than for the electrically insulating fluid. Using the method we developed in Chapter 3, we found in Chapter 4 that in conjunction with the greater vigor of convection nearer the inner core (due

to the spherical geometry), the non-linear interaction between the toroidal magnetic field and its associated radial electrical current leads to a bias towards equatorial upwelling flow. Although we have found this result through a study of the magnetic analog of the polar modes with a particular imposed magnetic field, the process by which the upwelling occurs is essentially a consequence of the ω-effect that is very likely responsible for the toroidal magnetic field in the core. We thus believe equatorial upwelling may be a general feature of the mean poloidal circulation due to free convection in the Earth's outer core.

On the other hand, it is possible that the mantle imposes thermal boundary conditions on the core with a latitudinal dependence, analogous to equatorial solar heating of the hydrosphere (though over many convective overturns of the mantle there is no dynamical reason why the present distribution should remain). The importance of north-south thermal boundary condition gradients at the CMB, with the accompanying thermal winds in the core, is not known. The results of Section 4.6 indicate that the ability of latitudinally variable boundary conditions to modify the motions of free convection depends not only upon the relative strength of the inhomogeneous lateral forcing to the homogneous vertical forcing (the size of the parameter y of Section 4.6), but also on the distribution of the inhomogeneity (the sign of y). We must therefore be careful about interpreting core surface flow as a direct result of core-mantle thermal forcing.

Through the Rossby or magnetic Rossby wave mechanism, all non-axisymmetric free convection solutions in a rotating spherical shell drift in azimuth. However, the data indicate that some features of the magnetic field do not drift, suggesting steady motions. Steady motions with an azimuthal variation must presumably result from azimuthally inhomogenous boundary conditions arising from conditions in the lower mantle. We have not yet studied azimuthally dependent solutions that arise from azimuthal variations in the boundary conditions. The importance of wave solutions in addition to steady solutions complicates such a study, and our iterative method may not be suitable. Indeed, the lack of

time-dependence is clearly the great limitation of our method, though the alternative, a three-dimensional time-stepping approach, is computationally prohibitive.

In Chapter 5 we studied magnetic Rossby waves in a hypothetical stably stratified layer at the top of the outer core. In the thin-layer limit we found analytically, using a β-plane approximation, and numerically that a sufficiently strong magnetic field can break the equatorial waveguide caused by rotation. The modes are highly dissipative, but this is a result of our neglect, necessary for the thin-layer approximations, of the electric field term in Ohm's law. For a finite-thickness layer the modes will be less dissipative so their relation to the magnetic secular variations remains unclear. The phase speed of magnetic Rossby waves is somewhat greater than the velocities generally inferred from secular variation studies. With an improvement in surface magnetic field data quality and quantity, it would be interesting to see if there were any evidence of signals of internal origin that resemble rapidly moving waves.

Finally, we conclude with a few remarks about future work that is a natural extension to this thesis. Firstly, a more detailed study of the relative effects of latitudinally variable versus vertical boundary buoyancy gradients would be desirable, as would further confirmation that the non-linear Lorentz force leads to a preference towards equatorial upwelling in the core. An extended study of the thesis work should include linear stability analyses of the steady, non-linear solutions. Secondly, a study of the motions driven by both an azimuthally variable upper boundary buoyancy flux and bottom forcing would be interesting, though extremely challenging, as the calculations must necessarily be three-dimensional, time-dependent, and non-linear. Concurrently, we hope to see further progress towards obtaining reliable maps of the lower mantle thermal structure and CMB topography, as well as continued paleomagnetic studies to determine the statistical significance of the VGP paths. Lastly, if strong enough, core-mantle thermal interactions are likely to disrupt a stably stratified layer at the top of the outer core, which is most likely a result of chemical (compositional) convection. A study of the thermal stability of a

chemically stratified layer could yield bounds on the thickness and buoyancy of a stable layer as a function of the size of lateral variations in the heat flux across the CMB. We hope to make progress on these topics in the near future.

Acknowledgements

Much as it sometimes seemed, I did not do the work in this thesis in a vacuum tube, but had the support, encouragement, and friendship of my fellow graduate students serving concurrent time. They are of course too numerous to name, but I would especially like to thank Justin Revenaugh, Greg Beroza, Lind Gee, Mark Murray, Dave Chester, Anne Sheehan, Will Wilcock, Carolyn Ruppel, Peter Puster, Jim Gaherty, and Steve Shapiro for fond memories and EAPS 'softball'. I'd also like to thank my officemates Andrew Gunstensen and Randy Mackie for generously supplying the office with a full complement of newspapers for my reading pleasure, as well as scintillating conversation.

Although their forecasts were lousy, I found the company of the meteorologists upstairs most enjoyable - especially Peter and Lyn Neilly, Rob Black, Josh Wurman, and Keith Groves, and by association, April Ratana and Imtiyaz Hussein. Perhaps it is appropriate here to thank Mount Pinatubo for providing an unusually cool summer of 1992 that allowed me to more easily complete this work.

Away from the Green Building, I found refuge playing with the Longwood Symphony, and I will miss the post-rehearsal Bertucci's crowd - Jordan Kaplan, Jack Dennerlein, Joel Hirschhorn, Christina Wipf, Eric Kawamoto, and John Little. So too living with the aspiring molecular biologists Alan Derman, Jared Silverman, and Marcia Belvin at lovely 5 Park Street was a welcome respite, and I hope we can continue housemate dinner in some rump form. I should thank the entire Belvin family as well, for adopting us on holidays. A few old friends deserve mention here, for reminding me of my time before grad school - Ed Dixon, Robin Cloues, and Jeff Fein and all the other Jeffs from high school.

To many on the 6th floor, it must have seemed as though my supervisor Ted Madden and I spent all our time arguing, and they were right! I nevertheless have the utmost respect for Ted's abilities as a scientist and above all, his integrity as a human

being. In addition to supplying reading material, Randy Mackie deserves credit for helping me to learn to deal with Ted's idiosynchrasies, helping me with numerous computer problems, and keeping up my morale. It is unpleasant for me to imagine what graduate school would have been like without his presence.

To Deborah, thank you for your support during the last stretch of late nights and bad moods, and for the comfort that in the end, it would all work out, and if it didn't, it didn't matter.

Finally, to my family and especially to mom and dad, thank you for a lifetime of support. Through all the miserable phone calls, you never hung up on me.

I should also like to thank the NSF and NASA for providing generous financial support during my tenure as a graduate student. Without it I could not have studied this arcane topic. Thanks are also due to Cray Research, Inc. for providing affordable computing time on the Cray X-MP. Dave Krowitz frequently helped me with computer problems (when Randy couldn't) and Terri Macloon with bureaucratic ones. My committee, Ted Madden, Jeremy Bloxham, Tom Jordan, and Sean Solomon, made helpful suggestions towards improving the thesis.